Dissertation zur Erlangung des Doktorgrades der Fakultät für Chemie und Pharmazie der Ludwig-Maximilians-Universität München

FLRTs: Regulator of cerebral cortex folding and a potential RGC marker in the mouse retina

Tobias Ruff

aus

Mühldorf am Inn, Deutschland

11.09.2018

Erklärung

Diese Dissertation wurde im Sinne von §7 der Promotionsordnung vom 28. November 2011 von Herrn Professor Rüdiger Klein betreut und von Herrn Professor Klaus Förstemann von der Fakultät für Chemie und Pharmazie vertreten.

Eidesstattliche Versicherung

Diese Dissertation wurde eigenständig und ohne unerlaubte Hilfsmittel erarbeitet.

München, Tobias Ruff, 03.12.2018

Dissertation eingereicht am: 11.09.2018

1. Gutachter: Professor Klaus Förstemann

2. Gutachter: Professor Rüdiger Klein

Mündlichen Prüfung am: 17.10.2018

Contents

List of Figures

List of Tables

List of abbreviations

AOS	Accessory optic system
APP	Amyloid precursor protein
aRG	Apical radial glia
ARX	Aristaless
bRG	Basal radial glia
CGE	Caudal ganglionic eminence
CNTN4	Contactin-4
CP	Cortical plate
DCC	Deleted in colorectal cancer
DCX	Doublecortin
DG	Dentate gyrus
dLGN	dorsal lateral geniculate nucleus
DRP	Density recovery profile
ECD	Extracellular domain
EPSC	Excitatory postsynaptic currents
GCL	Ganglion cell layer
GI	Gyrification index
GPR56	G-protein-coupled receptor gene
INL	Inner nuclear layer
IP	Intermediate progenitor
ipRGC	intrinsically photosensitive RGC
IZ	Intermediate zone
LED	Local edge detector
LGN	Lateral geniculate nucleus
Lpd	Lamellipodin
LRR	Leucine-rich-repeat
MGE	Medial ganglionic eminence
MPT	Medial pretectal nucleus
MTN	Medial terminal nucleus
MZ	Marginal zone
NMDA	N-methyl-D-aspartate receptor
NOT	Nucleus of the optic tract
ooDSGC	ON-OFF directionally selective ganglion cells
OPN	Olivary pretectal nucleus
osRGC	orientation sensitive RGCs
OSVZ	Outer subventricular zone
POA	Preoptic area
PP	Preplate
PPT	Posterior pretectal nucleus

PRL	Photoreceptor layer
PS1	Presenilin
PV	Parvalbumin
RELN	Reelin
RGC	Retinal ganglion cell
SAC	Starburst amacrine cells
SAP	Subapical progenitors
sbcRGC	suppressed by contrast RGC
SC	Superior colliculus
SCN	Suprachiasmic nucleus
Shh	Sonic hedgehog
SP	Subplate
SST	Somatostatin
SVZ	Subventricular zone
TCA	Thalamocortical axons
TUBA1A	Tubulin alpha 1A
VZ	Ventricular zone

Summary

The most prominent feature of the human brain is its large and folded cortex. The cortex is a laminar sheet of tissue that is organized into several layers and believed to control high level cognitive functions. During evolution, the cortex of many mammals expanded laterally much more compared to its increase in thickness. Since the surface area of the surrounding skull expanded less, the only way to fit the large cortical surface into the limited space was to fold it. Thus, today we can see gyrencephalic (folded, e.g. human) and lissencephalic (non-folded, e.g. mouse) mammalian brains. The precise mechanisms guiding cortical folding are still largely unknown. During brain development many neurons travel long distances from their birthplace to their final destination. To form the six layered structure of the cortex, newborn neurons migrate from the ventricular and subventricular zone all the way out into the cortical plate. The timing, speed, travel distance and direction of migration determines the neuron's final location and thus the overall morphology of the cortex. To date, all experimental evidence suggested an increased number of neural progenitors as the main cause of folding. However, several theoretical models proposed that cortical folding can be induced by rearranging the same number of cortical neurons. The distribution and organization of cells depend on a balance of intercellular adhesive and repulsive signalings. The Fibronectin Leucine-Rich Transmembrane (FLRTs) family of proteins can provide both signals by functioning as adhesive molecules and as heterotypic chemorepellents. The FLRTs (1-3) are regulators of early embryonic vascular and neural development. Mice with deletions of *Flrt1* and *Flrt3* show evidence that, cortical folding can be induced without increasing the number of neurons or neural progenitor cells. Instead removal of *Flrt1* and *Flrt3* alters neuronal migration and distribution. We consistently found bilateral clustering of mutant neurons normally destined to express FLRT3 in posterior cortical regions, which mostly coincided with the location of folds. Interestingly most folds appeared unilaterally on the left side in *Flrt1/3* DKO suggesting that cortical asymmetries favour folding on one side. Moreover, live imaging of embryonic cortex slices showed that neurons in *Flrt1/3* DKO mice were more likely to reach high migration speeds. The higher migratory speed was confirmed *in vivo* where more neurons reached the upper cortical plate too early and failed to mature their dendritic trees. Based on the observation that both an increase and reduction in FLRT expression in the developing cortex induces neuron clustering, simulations of neuronal migration showed that a tight balance between cell adhesion and repulsion is required for concerted neuronal migration. Simulations of neuronal migration with reduced cell adhesion favours the formation of a wavy cortical surface and may thus occasionally induce folding. In addition, we found reduced levels of *Flrt1/3* mRNA in humans and future sulcus regions of ferrets, suggesting that the fine-tuned balance between attractive and repulsive forces is a key regulator of folding.

The mammalian retina has the remarkable ability to dissect the visual scene into

distinct streams of information encoding color, luminosity, motion and contrast. Each stream is integrated by a subtype of cells in the ganglionic cell layer (GCL) and transmitted via parallel pathways to the visual centers in the brain. FLRT3 has been shown to act as a controlling factor of retinal vascular development. In order to distinguish vascular versus neuronal functions of FLRT3, we aimed to compare retinas totally depleted of FLRT3 by using SOX2-Cre with retinal ganglion cell (RGC)-specific Brn3b-Cre knock-out. Our results show that full depletion of *Flrt3* results in cataract formation, eye malformation, blindness and in one case specific loss of RGCs. Interestingly, all these phenotypes are not present when FLRT3 is removed specifically from RGCs, suggesting that its effects on the vascular system have a crucial role during retina and eye formation.

Analysis using genetic markers showed that all FLRTs (1-3) are also expressed in the retina postnatally and mainly in a subset of retinal ganglion cells (RGCs). Therefore, we asked whether FLRTs could represent potential markers for a functional subpopulation of that cell type. Functional analysis has identified more than 30 different RGC subtypes in the GCL so far. However, many of the functionally identified subpopulations lack a genetic marker to target these cells for full characterisation of each subpopulation. Histochemical studies showed expression of FLRT3 in a specific cell population within the GCL. Quantification revealed that 23% of the FLRT3+ cells are RGCs while the remaining 67% are displaced amacrine cells. The FLRT3+ RGC cell population represents only 6% of all RGCs. However, non-mosaic like FLRT3 RGC distribution and varying stratification depths within the inner plexiform layer revealed that the FLRT3+ RGC population consists of at least 6 morphologically defined subpopulations. The two biggest groups of FLRT3+ RGCs, which represent 78% of all reconstructed cells stratified within the ON layers 7-10, suggesting that those cells might react to increases in light intensity. Notably, 2 groups of ON-OFF bistratifying RGCs in layers 3/4 and 7/8 and a small population stratifying in the OFF layer 2 were identified. ON-OFF RGC specific CART immunostaining confirmed that 23% of all FLRT3-RGCs are indeed ON-OFF RGCs. Finally, 9 out of 83 RGCs showed a very diffuse stratification pattern. Retinofugal projection analysis of the whole FLRT3-RGC population showed no subregion specific targeting in the superior colliculus or ventral/dorsal lateral geniculate nucleus (LGN), which is usually found for ON, OFF or ON-OFF direction selective ganglion cells. This finding confirms the result that FLRT3+ RGCs consist of more than one functional subpopulation. Moreover FLRT3-RGCs innervate several nuclei of the accessory optic tract, which is important to control retinal image stabilisation. Interestingly FLRT3+ RGC projections were found in the medial terminal nucleus (MTN), which is the main target of ON direction selective ganglion cells (ON-DSGCs), thereby suggesting that at least a fraction of the FLRT3+ RGCs are ON-DSGCs. FLRT3+ RGCs completely avoided the intergeniculate leaf (IGL) and the suprachiasmatic nucleus (SCN), which excludes FLRT3-RGCs from being involved in circadian entrainment. Overall data supports the idea that FLRT3-RGCs are a mixtue of mostly ON but also some OFF and ON-OFF RGCs, which might be important for image stabilization.

Chapter 1

Introduction - FLRTs in cortex development

All nervous systems develop through 4 essential stages. First, progenitor cells proliferate into a epithelium. Second, they proliferate and differentiate into neurons and glia that will migrate and position themselves in a controlled manner. Third, neurons will mature and establish specific connections through the development of dendrites and the extension of axons. Finally, neurons will develop and refine chemical and electrical synapses with the support from glial cells [47].

1.1 Principles of mouse brain development

It takes around 19 days until the fusion of an egg cell and a sperm results in a newborn mouse that can survive outside a mothers protected uterus. The key processes that are needed to form a mouse from a single totipotent cell are simple. Embryonic cells need to divide or apoptose, sometimes migrate long distances, eventually specializing into a single cell type. However, all the mechanisms involved in such extraordinary events are not fully understood. A birth control system has to tell the cells exactly at what time and location they should divide or apoptose. They need clear signs that show them where to migrate and at what time they should start to do so. Finally, each cell needs to receive a signal that instructs them to differentiate- eg. into a neuron or a muscle cell.

Two developmental principles are repeatedly combined to organise proliferation, migration, differentiation and cell death: Asymmetry/polarity and embryonic induction. It all starts with the emergence of asymmetry.

The mouse oocyte is initially morphologically point-symmetric but eventually becomes an animal with three polarised axes. The cranial-caudal, the dorsal-ventral and left-right axis. Thus the developmental program needs to develop asymmetric poles.

But how does asymmetry emerge? Asymmetry has its molecular origins at the oocyte stage. Biomolecules and organelles distribute asymmetrically within the cell to build up a gradient that leads to the formation of the first body axis: the animal - vegetal axis [51, 135]. In the following rounds of cell divisions, the initial molecular gradient is successively converted into the morphologically asymmetric blastocyst. In the following process known as gastrulation the blastocyst forms the three germ layers endoderm, mesoderm and ectoderm. Subpopulations of cells from each layer then give rise to specific body parts. Neural induction is the key principle that directs cells towards their correct cell fate. As a consequence of the initial asymmetry of the blastocyst, a spacially restricted

subpopulation of cells begins to express a protein called factor X. Factor X either diffuses through the tissue or stays attached to the cell membrane. The neighbouring cells may or may not respond to factor X. The cellular response mainly depends on two factors: 1) the expression of the right receptor types that bind factor X or 2) the concentration of factor X. That means that even if all cells were exposed to factor X, they could react differently. In this case factor X would be called a morphogen. Morphogens induce the expression of different target genes in a concentration-dependent manner. Low threshold target genes become expressed even in cells far away from the release site of factor X while high threshold genes will only be activated in close proximity to the source of factor X. Depending on the combination of expressed target genes the cells then specify into distinct cell types [245].

1.2 Focus on cortex development

1.2.1 Neuron production

The fully developed mouse cortex contains around 49 different cell types that can be grouped into three main types: 19 glutamatergic excitatory pyramidal neurons, 23 GABAergic inhibitory interneurons and 7 non-neuronal types [261]. In the adult mouse cortex only about half of the cells are neurons. The remaining cells are astrocytes, microglia, oligodendrocytes, oligodendrocyte precursor, endothelial and smooth muscle cells [102]. In total, a mouse embryo generates and distributes 13.7 million neurons in a defined layered pattern across the cortex in approximately 8 days. [101]. All cells of the cerebral cortex develop from the telencephalic vesicle, the most rostral part of the neural tube. Initially the neural tube is only one cell layer thick. In the following rounds of symmetric progenitor cell divisions the neural tube enlarges laterally like a balloon to form the ventricular zone (VZ). At this stage all progenitor cells have a bipolar shape with one process touching each side of the neural tube (Figure 1.1). Around embyonic day 10 (E10.5) (in mouse) progenitor cells at the cortical VZ switch to asymmetric division to generate apical radial glia cells (aRGC) and neurons. These neurons then migrate out radially along the basal processes of the radial glia cells and form the preplate (PP). The preplate consists of Cajal-Retzius cells that mark the upper boundary (marginal zone, MZ) and subplate (SP) cells that line the lower boundary (SP) of the future cortical plate. Although most of the asymmetric divisions of radial glia form postmitotic neurons directly, some generate intermediate progenitor cells (IPs) that migrate to a region below the subplate called intermediate zone (IZ). Upon arrival at the IZ they continue to divide symmetrically to generate up to 8 postmitotic neurons. Indeed about 80% of all excitatory cortical neurons derive from those IPs [97, 175]. In addition to aRGC and IPs, subapical progenitors (SAPs) also contribute to the progenitor pool expansion during neurogenesis [175]. Within 7 days newly generated neurons follow the same path along radial fibers and form the cortical plate between the marginal zone and subplate. In the latest stages of neurogenesis some radial glia cells themselves start to migrate towards the cortical plate. After a final asymmetric division they detach from the VZ and translocate upwards to generate a basal radial glial cell (bRGC) [186]. The cortical plate is not a homogeneous tissue but organizes itself into 6 functionally defined layers (Figure 1.1). The layer which a neuron integrates into is determined by its birthdate [212]. Layer VI neuron generation peaks around E12.5 followed by layer V neurons at E13.5. Pyramidal neurons of layer IV are born around E14.5 and lastly upper layer neurons of layer II/III

at E15.5 [5, 32].

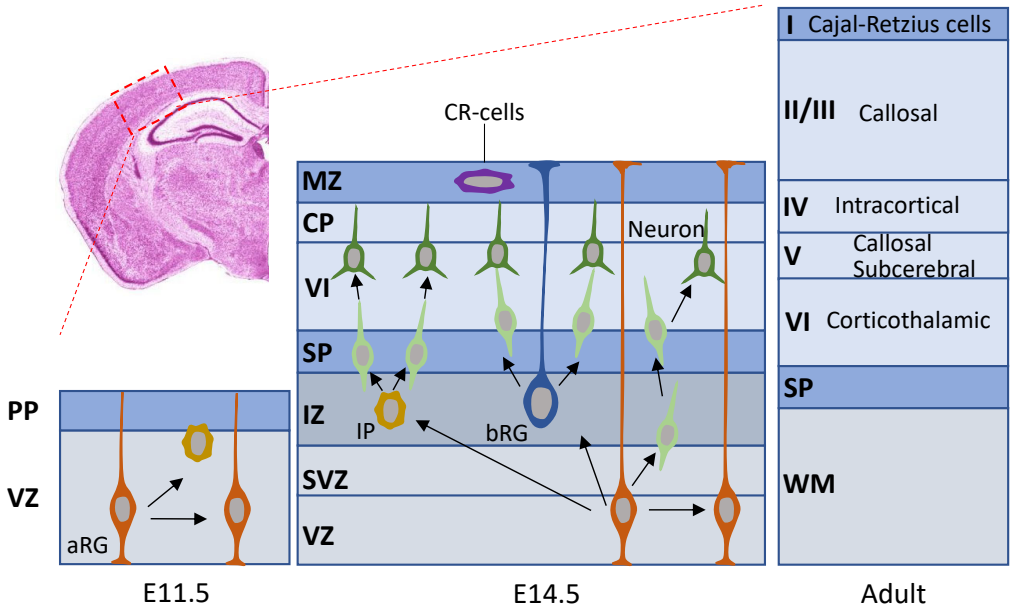

Figure 1.1: Cortical development. Initially aRGCs divide symmetrically to laterally enlarge the neural tube. From E12-E18 the cortex grows radially when aRGCs start to divide asymmetrically giving rise to neurons and intermediate progenitors. More than 80% of all excitatory cortical neurons are generated by symmetric division from those intermediate progenitor cells. IP: intermediate progenitors, aRGC: apical radial glia, bRGC: basal radial glia, VZ: ventricular zone, PP: preplate, SVZ: subventricular zone, IZ: intermediate zone, SP: subplate, CP: cortical plate, MZ: marginal zone, WM: white matter

While the cortical VZ is the main source of glutamatergic neurons in the cerebral neocortex, the second class of neurons, local circuit interneurons, are generated outside the cortical VZ. The majority of interneurons are born in the ventricular zone of two subcortical regions called the medial and caudal ganglionic eminence (MGE, CGE) and a smaller amount in the preoptic area (POA) [4, 160]. From there they travel long distances within the intermediate zone to reach their final destination in the cortical plate. In case of the MGE, birthdate determines laminar location of interneurons in the cortex and roughly matching those of the excitatory projection neurons. Early born interneurons (E12.5) integrate into deep layers while late born (E14.5-E16.5) neurons populate the upper layers [292]. Interneurons from the CGE however are born during late neurogenesis and do not follow the same rule. In the end interneurons comprise about 20% of all cortical neurons [44]. Local circuit interneurons are divided into 3 main subgroups, defined by the expression of parvalbumin (PV), neuropeptide somatostatin (SST) or 5HT3aR serotonin receptor [147]. The interneuron groups differ in their electrophysiological properties and connectivity. Malfunction of inhibitory interneurons may lead to overexcitation of associated neuronal networks and thus result in epilepsy, schizophrenia and autism. At E18, neurogenesis is mostly completed and neural progenitors switch to gliogenesis, generating oligodendrocytes and astrocytes. Indeed the increase in brain size during postnatal development can be mainly attributed to the production of new glial cells. Radial glia cells are therefore gradually restricted in their potential to produce neurons and change to glia production mode. So far only the proliferation of the radially migrating excitatory projection neurons has been associated with cortical folding.

As described above, the progenitor cells in the VZ continuously change their production line. First they amplify themselves to increase overall proliferative capacity. Then they switch to a neurogenic mode where they produce all different types of neurons within 7 days. And finally around birth the gliogenic production mode takes over to produce astrocytes and oligodendrocytes.

1.2.2 Neuronal migration

In complex nervous systems like the mouse CNS, the different types of neurons and glia are not produced at the location in which they will integrate into the neuronal circuit. Instead, all complex brains use distinct proliferative zones where each specialises in the production of a certain cell type. The consequence of that strategy is that the different cell types need to migrate, sometimes long distances, to reach their final destination. The acquisition of cellular migration is a hallmark of more complex nervous systems and its regulation is thus critical for its proper function. Neurons use two basic modes of migration: Radial and tangential. Radial migration can either be into the direction of the pial membrane (Cortical projection neurons) or away from it (e.g. cerebellar granule cells) [186, 210]. Tangential migration perpendicular to the radial axis can be either directed (e.g. interneurons of the IZ/SVZ) or undirected (e.g. interneurons of the MZ) [199, 260].

Migrating neurons are usually guided by molecular gradients. A concentration difference of only 6% between the front and back of a neuron is enough to orient them into the right direction [47]. Neurons follow two strategies to measure concentration gradients of attractive or repulsive guidance cues. The first is to use a single leading process pointing into the direction of migration. Lamelipodia and filopodia at the tip of the leading process randomly sense the guidance cues around them. Those branches that sense an attractive molecule get stabilised while the remaining branches retract [309]. In cortex development neurons with a single leading process are often closely attached to the radial fibers of the RGCs [211]. Interestingly the actin regulating protein lamellipodin (Lpd) enables neurons to distinguish between axonal and radial fibers. If Lpd is missing, the leading process attaches to axons instead, which orients the neurons perpendicular to the radial fibers along the tangential axons in the IZ [204]. A single leading process is usually used by straight migrating cortical projection neurons. Other neuronal types use branched leading processes as guiding sensors. The advantage over a single one is that the neuron can scan chemoattractant or repellent levels across a broader area [270]. Interneurons and other tangentially migrating neurons show the branched type of leading process [166]. Mutation experiments causing impaired cell adhesion at the leading process of migrating neurons, increases branching [69]. This suggests that pro-adhesive signals prohibit branching.

The leading process not only steers the neuron into the right direction but may also serve as the engine pulling neurons forward. There are two known mechanisms that drive neurons forward: Somal translocation and locomotion. In somal translocation a neuron has a long (60-96 µm) branched leading process that is attached to the pial surface. By contracting the leading process the soma gets pulled up very quickly towards the attachement site and stops when it reaches the branch point. In contrast to somal translocation, neurons in locomotion mode have short leading processes and migrate more discontinuously with alternating phases of fast and slow movements. The leading process is closely

attached to one of the radial fibers of the RGCs and it is used as a guide to pull the neuron into the preferred direction. In the early stages of cortical development when the cortical plate is only a few cell layers thick, the majority of migrating neurons rely solely on somal translocation to move upwards. However with increasing cortical thickness, the leading process of migrating neurons fails to reach the pial surface, so they require locomotion to move forward [182]. Between E12 and E18 few neurons migrate non-stop to the cortical plate (CP) after neurogenesis. Most newly generated neurons go through four phases of migration. The newborn neurons first acquire a bipolar shape and migrate rapidly from the VZ to the SVZ. Upon arrival in the SVZ/IZ they convert to a multipolar shape and remain there for about 24h. While a minority continues its migration to the CP afterwards, the majority of neurons first reverses direction towards the VZ. When their leading process touches the ventricular surface they keep the contact for about 10h. Afterwards they invert their polarisation and move upwards into the cortical plate by locomotion. The leading process that originally contacted the ventricular surface converts to the trailing process and a new leading process is protruded at the opposing pole. During upwards locomotion the trailing process elongates and grows tangentially within the VZ [186]. It later becomes the neuron's axon [234]. Interneurons in contrast only start to develop axons when they arrive at their final location [198, 174, 239]. Finally, as soon as the leading process touches the pial surface, the neuron switches migration mode and is pulled up to its final layer by somal translocation. However, in some cases one of the branches attached to the pia retracts, which leads to a final tangential movement towards the remaining branches [182]. Interestingly neurons generated by symmetric division from the same progenitor usually migrate together [186].

Now that I have described the mechanisms neurons use to move forward and sense their environment I will focus on the molecules that are involved in cortical migration. Guidance molecules like semaphorins, slits, ephrins, netrins and the chemokine SDF are involved in the control of neuronal migration [210]. Our understanding of the complex interactions between these molecules and all phases of migration are still not well understood. As a general rule, migrating neurons need to sense signals from the surrounding tissue and convert it into action. So far two signals have been found that are necessary to allow neurons to move into the cortical plate: Semaphorin3a and Reelin. Both molecules are secreted near the top of the cortical plate. Knockout of Sempahorin3a or Reelin in mice inhibits the multipolar-to-bipolar transition which is needed for radial migration [264, 39]. Multipolar neurons sense Reelin and ensure the cell surface expression of the adhesive N-cadherin. Too high or too low levels of N-cadherin inhibit neuronal migration [125, 121]. How correctly dosed levels of N-cadherin influences exit from the multipolar stage is still unknown.

1.2.3 Neuronal differentiation and function

The different types of neurons do not distribute equally across the whole cortical volume. It is assumed that the cortex consists of repetitive, modular columns, each representing a computational unit [164]. Within each column the cortex distributes and concentrates certain types in one of the six cortical layers. Although generally the neuronal composition within each layer is very similar there are regional differences especially between sensory and motor cortex. Ultimately, the connections of the different neuron types determines their function within the circuit. Layer II/III contains different types of commissural

neurons that establish cortico-cortico connections. Layer IV neurons receive sensory information and layer V contains different types of projection neurons that connect to the brainstem, spinal cord, superior colliculus and the striatum. Layer VI contains mainly callosal and corticothalamic projection neurons (Figure 1.1) [152]. Our knowledge about the function and how interneurons distribute across all layers in the cortex is very scarce. Interneurons are usually broadly subdivided into spiny pyramidal and spiny stellate cells [297]. Spiny pyramidal cells are excitatory glutamatergic neurons that reside in layer IV where they receive sensory inputs from the thalamus. Spiny stellate cells are a very diverse class of neurons that share inhibitory GABAergic properties. They differ in connectivity and firing properties but currently there is no classification for these cells [164].

How does the pool of progenitors establish such neuron diversity? Two opposing theories exist: One is a progressive competence-restriction mechanism, where the progenitor cells become more and more restricted in the type of cells they can produce. The second theory is the fate-restriction model in which different progenitor cell types produce a certain type of neuron. So far experimental evidence strongly supports the competence-restriction mechanism for excitatory neurons. When neural progenitor cells are grown in cell culture, the same progenitor can sequentially give rise to deep-layer and upper-layer neurons [159, 278]. If a late cortical progenitor is placed into a young cortex environment it cannot produce early progenitor neuron fates [77]. Most fate decisions occur during the progenitor stage development. However during early postmitotic stages other transcription factors continue to refine neuronal subtype identity. This refinement includes defining axonal projection targets, morphology and connectivity [152].

In the adult brain, glutamatergic projection neurons and GABAergic interneurons connect with each other such that the interplay of excitation and inhibition allows sensory signal processing and the establishment of motor actions. How each of those neurons connect to each other to form a functional circuit is not very well understood. Accumulating evidence suggests that the preference for connection to specific neuronal subtypes is defined by neuronal identity [25]. Moreover different functional outcomes of interneuron inhibition/excitation can be established by specifically targeting the soma, dendrites or the axon initial segment of the pyramidal neuron.

1.3 Structure and functions of the FLRT transmembrane receptor family

The family of FLRT proteins FLRT(1-3) was found in a screen for extracellular matrix proteins and have since then been studied by many labs. *Flrts* are expressed in many parts of the fetal and adult human body. FLRT2 and FLRT3 can be found in the pancreas, skeletal and heart muscle. Lung, liver and placenta show *Flrt1* and *Flrt3* expression. All three FLRTs are found in the brain [144].

The structurally homogeneous (41-55% sequence match) FLRT proteins are between 649 and 674 amino acids long and belong to type-I single-pass transmembrane proteins. At the N-terminus, their extracellular domains (ECD) contain a 10 leucine-rich-repeat domain (LRR) that is flanked by one highly conserved cysteine-rich region on each side (Figure 1.2 A). In general LRR domains have been implicated to be key sites for biologi-

cally relevant homo- and heterophilic protein-protein interactions and they are a common motif found in several other proteins [26, 138, 16]. These include Slit (midline crossing, dendrite arborization), Trk (axon growth/target selection), synaptic adhesion molecules (synapse formation) and LGl1 (synapse function) [24, 161, 137, 54, 288, 80, 81]. The proximal part of the FLRT ECD contains a fibronectin type III motif and a metalloprotease cleavage site (Figure 1.2 A). The short intracellular tail has no known functional domains but may be phosphorylated. FLRT proteins have the structure of single-pass transmembrane receptors and were shown to bind four different receptor classes: FGF receptors, Latrophilin3, Robo1 and Unc5s

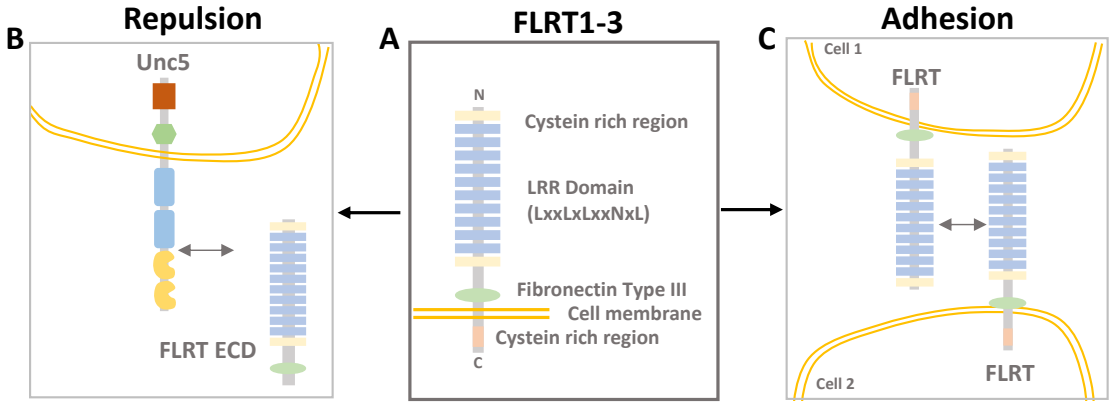

Figure 1.2: Repulsive and adhesive function of FLRTs. A: Structure of FLRT1-3 transmembrane receptors. B: FLRT3 extracellular domain is shed from the cell surface to repell Unc5 positive cells and axons. C: Homophilic binding between FLRTs mediates cell adhesion. ECD: extracellular domain.

In line with known functions of LRR domain containing proteins, FLRTs were shown to regulate neural, vascular and early embryonic (E6<) development [296, 67, 150, 163, 180, 193]. FLRTs are known to modulate FGF signaling which is essential for cell migration, proliferation and differentiation during development [114]. The interaction of FLRT2/3 at the Fibronectin type III domain with their corresponding FGF receptor (FLRT2 binds FGFR2, FLRT3 binds FGFR1+FGFR4a) induces FGFR signaling through the Ras/Raf/MAPK pathway. Interestingly *Flrts* seem to be induced by FGF-receptor signaling and serve as a positive feedback regulator of FGFR levels (Figure 1.3 C) [91, 23].

Moreover FLRTs are known to homophilically bind to each other via the LRR domain (Figure 1.2 C). Experiments on *Flrt* deletion constructs showed that the homophilic interaction works via the LRR domain and is independent of the fibronectin type-III domain or the cytosolic tail. The homotypic FLRT-FLRT interaction was shown to be important for homotypic cell sorting *in vitro* (293T cells) and *in vivo* (Xenopus embryos). Overexpression of *Flrt2* or *Flrt3* leads to a segregation of 293T cells or Xenopus embryonic cells [123].

During development FLRT-FLRT interactions are essential to ensure cell integrity. Mice that lack FLRT2 or FLRT3 show defects in the heart epicardium (*Flrt2 KO*) or the anterior visceral endoderm and basement membrane (*Flrt3 KO*) [67, 180]. As the structural homology suggests, FLRT2 and FLRT3 seem to have redundant functions [180]. In

addition to a role in cell-cell contact, FLRT2 mediates cell-matrix interaction by binding to the extracellular matrix protein fibronectin [75]. In contrast to the cell adhesive functions, FLRTs were shown to promote cell de-adhesion in Xenopus embryos. This effect is mediated via direct interaction of the intracellular tail with the small GTPase Rnd1 which is a modulator of the actin cytoskeleton. Moreover the cell adhesion protein C-Cadherin is internalized and thereby allows cell de-adhesion [189, 123]. To summarize, the LRR domain promotes homotypic cell adhesion and repulsion while the intracellular tail mediates cell de-adhesion. During development this dual functionality may allow cells to detach from their origin and migrate together in groups to their target location [123].

The brain is the only part of the body where all three FLRT receptors are found. However, the neurodevelopmental functions of FLRT receptors are still incompletely understood. First experiments indicated a growth promoting effect on developing and damaged neurons. In experiments where sensory nerves from rats were damaged, *Flrt3* was upregulated at the presynaptic axon terminals [224]. In *ex vivo* cultures of cerebral granule neurons, FLRT3 promoted neurite outgrowth while knock down of FLRT3 decreased the number and length of outgrowing neurites [269, 224]. Additionally, FLRT1 was shown to have a neurite promoting effect on primary hippocampal neurons [287]. Moreover FLRT3 was shown to modulate Netrin-mediated attraction in thalamocortical axons (TCA) (Figure 1.3 C). *Flrt3* is only expressed in rostral TCAs but not in intermediate TCAs. In presence of Slit1, the FLRT3-Robo1 interaction sensitizes rTCAs to the attractive guidance cue Netrin1. FLRT3 negative iTCAs are not attracted by Netrin1 [150].

Besides neural outgrowth FLRTs have been shown to facilitate synapse formation (Figure 1.3 B). Trans interaction of postsynaptic FLRT3 with the presynaptic G-protein coupled receptor latrophilin1 promotes glutamatergic synapse formation in hippocampal neurons. Knock-down of FLRT3 or latrophilin in cultured neurons, reduces excitatory synapse density. Similarly *in vivo* knock-down of FLRT3 in dentate gyrus granule cells reduces dendritic spine number which results in a decrease in excitatory postsynaptic currents (EPSCs) [193]. The interaction between FLRT and latrophilins has been confirmed by a crystal structure where the N-terminal part of the LRR domain of FLRT2 binds to the Olfactomedin domain of Latrophilin 3. It was also shown that the FLRT Latrophilin interaction mediates cell adhesion (Figure 1.3 B) [115, 155]. Moreover binding assays suggest that FLRT itself mediates the simultaneous binding between Unc5D and latrophilin3 to allow the formation of a ternary complex. Since the Unc5 and Latrophilin3 binding sites are at two opposing locations of the LRR domain, it allows the simultaneous binding of Unc5D and latrophilin3. While the FLRT2-latrophilin3 interaction mediates cell adhesion, the addition of Unc5D attentuates the cell adhesive effect. Further stochiometric analysis of the FLRT-Unc5-latrophilin complexes even suggests the formation of a quarternary complex where 2 latrophilin3 molecules bind to FLRT3 and Unc5D. Moreover mass spectrometry analysis proposes that those 2:1:1 complexes may even form dimers resulting in a Latrophilin3-FLRT2-Unc5D octamer (Figure 1.3 B) [116].

In contrast to the growth promoting effects on neurites and synapses, FLRT2 and FLRT3 were also found to have a repulsive effect on outgrowing axons during development (Figure 1.2 B). In primary mouse neuron cultures it was found that the extracellular domain (ECD) of FLRT1,2 and 3 can be shed from the receptor. The soluble FLRT ECD

can bind to Unc5 receptor expressing axons and thereby induce repulsion. Specifically it was found that in cortex/hippocampal cell cultures, FLRT2 or FLRT3 ECD induce growth cone collapse in Unc5D and Unc5B expressing axons and soma. *In vivo* experiments confirmed the repulsive interaction between FLRT and Unc5. Around embryonic day E15.5, the cortical plate shows high expression of *Flrt2* while neuroblasts and newborn neurons in the SVZ express Unc5D. Knockout of FLRT2 or Unc5D prevents repulsive FLRT2-Unc5D interaction and leads to a premature migration of Unc5D positive neurons into the cortical plate. Conversely an increase in Unc5D levels increased repulsion and thereby delayed neuronal migration (Figure 1.3 A) [296]. Also, in the retina, *in vitro* experiments and lamina specific expression pattern suggested a role for FLRT-UNC interactions in restricting dendritic arbours to defined sublaminae [275].

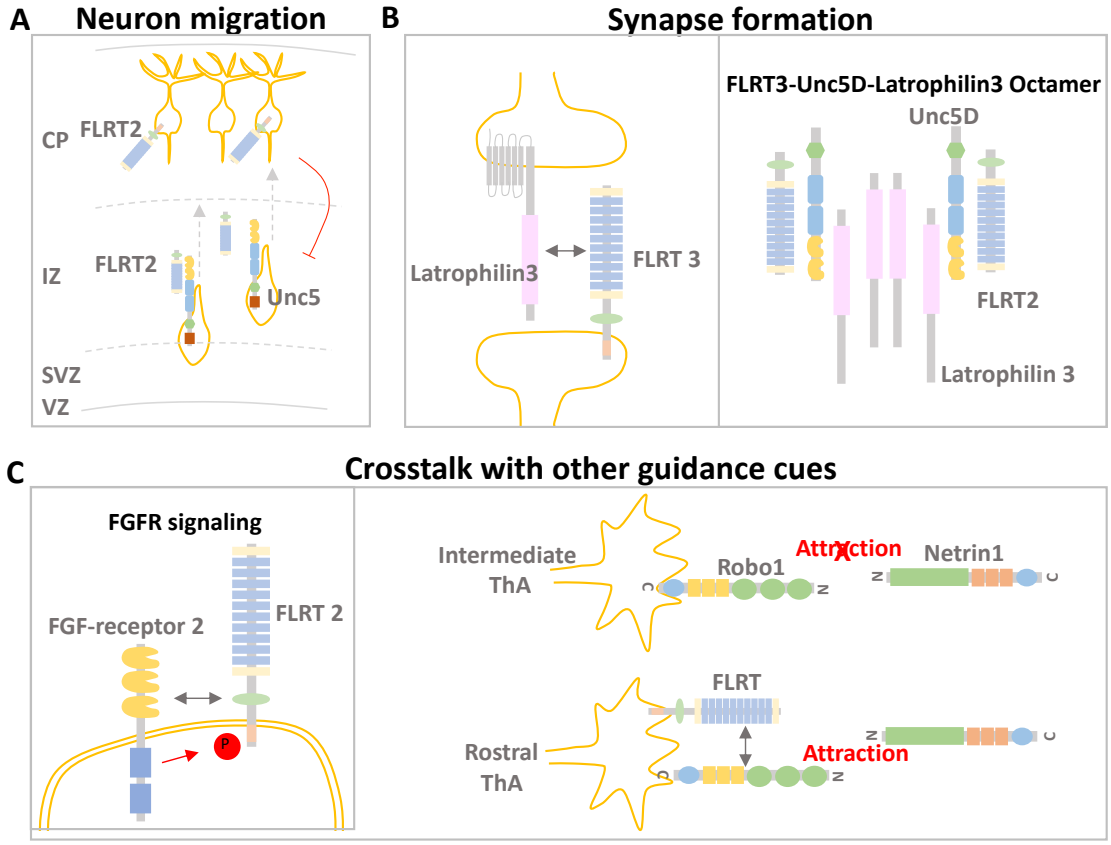

Figure 1.3: Different functions of FLRT interactions. A: Overexpression of FLRT2 or Unc5D reduces migratory speed. B: Latrophilin, FLRT3 and Unc5D interaction are involved in synapse formation. The supercomplex FLRT2-Unc5D-Latrophilin3 octamer (2:2:4) is probably mediating cell adhesion. C: FLRTs crosstalk with other signaling pathways. FLRT2 acts as a positive feedback regulator for FGF2 receptor. FLRT3 positive rostral ThA get attracted by Netrin1 while FLRT- intermediate ThA do not react to Netrin1. ThA: Thalamocortical axons, FGF: Fibroblast growth factors, IZ: Intermediate zone, SVZ: Subventricular zone, VZ: Ventricular zone, CP: cortical plate.

1.4 Current models of the mechanism of cerebral cortex folding

The human cerebral cortex is a 2.5 mm thin layered structure in which most of its volume is occupied by myelinated cortico-cortico, cortico-thalamic and cortico-spinal axons [1]. During evolution the cerebral cortex expanded laterally instead of growing radially by adding more layers of neurons (Figure 1.4). In order to fit the tangetially expanded cortical surface area of about 1600cm^2 into the human skull it had to develop large sulci (inward folds) and gyri (outward folds). In humans the cerebral cortex folds between 25 and 40 weeks of gestation.

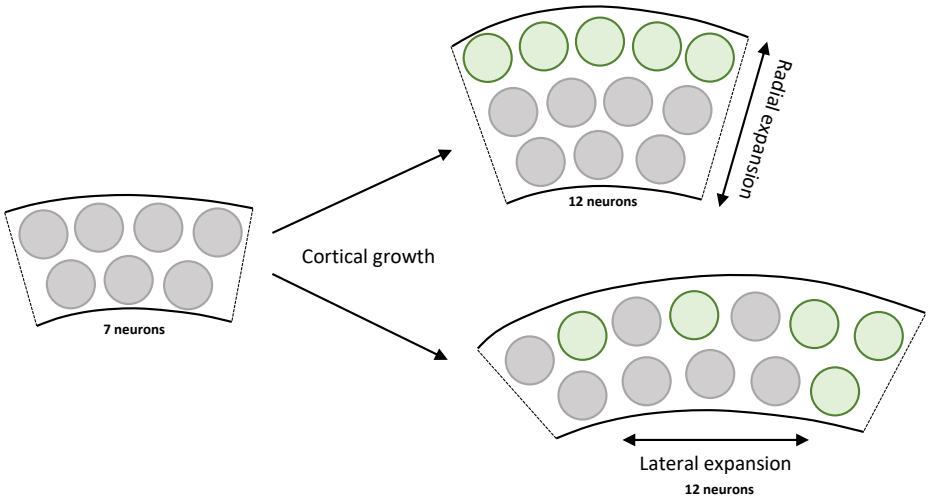

Figure 1.4: Radial vs. lateral cortical expansion. Cortical expansion requires the generation of new neurons which can be integrated in two ways. A: Neurons form a new layer, which expands the cortex radially. B: Neurons integrate into the existing layers, which expands the cortex laterally. In the end both cortices have the same number of neurons.

1.4.1 Evolutionary correlates of folded brains

The most evident difference between less and more folded mammalian brains is their size. As a general rule, bigger brains tend to fold more. The degree of cortical folding is usually described as the gyrification index (GI) which is the ratio of the cortical surface area including folds over total pial surface area (Figure 1.5) [310]. A high GI indicates more foldings.

Figure 1.5: Schematic representation of the gyrification index GI

By comparing the GI of over 100 mammalian species, it was shown that increased GI values (increased folding) in most species positively correlates (non-linearly) with brain weight, neuron number and neocortical volume. The increase in neuron numbers of bigger brains below a GI of 1.5 can be explained by an increase in the neurogenic period alone. If a brain exceeds the GI threshold of 1.5, however, it on average increases brain weight 14 times faster per gestation day compared to low GI brains. The difference between high and low GI brains cannot be explained by an increase of the neurogenic period alone which in humans (GI $>$ 1.5) is about 12 times longer compared to mice (GI $<$ 1.5). Additionally cell-cycle length in human neurons (45 h) is about 2.5 times longer than in mice (18.5 h) and makes it even more difficult to achieve the 1000 fold higher number of neurons in human (Figure 1.6). Thus beyond the GI threshold of 1.5 it becomes necessary and more cost-efficient to increase the proliferative potential of the neurogenic zones [149]. Indeed during development human brains show an expanded SVZ, which structurally divides into the inner SVZ (ISVZ) and outer SVZ (OSVZ). The OSVZ develops because of an increased number of basal progenitors (BPs). That pool of BPs consists mainly of two cell types: nonpolar basal intermediate progenitor cells (bIPs) that are not attached to any membrane and basal radial glia (bRG) that extend a radial fiber to the basal membrane. In mice BPs usually divide once to generate two neurons. In gyrencephalic species it is believed that BPs increase the progenitor pool size by symmetric and asymmetric self renewing divisions before specifying into neurons in a final division [149, 238, 92, 281].

Overall, data suggests that neocortical expansion below a GI of 1.5 was driven by increasing the neurogenic period, which beyond a GI of 1.5 was further boosted by a massive expansion of the neuroprogenitor pool size [149]. However, an increased cell proliferation does not automatically lead to cortical folding. The increased number of neurons in humans vs. mice lead to a disproportional lateral expansion of cortical surface (1000x) but only a minor increase in cortical thickness (10x) [73]. Thus, further theoretical and experimental work has attempted to solve the mechanisms that regulate the balance between radial and tangential cortical expansion.

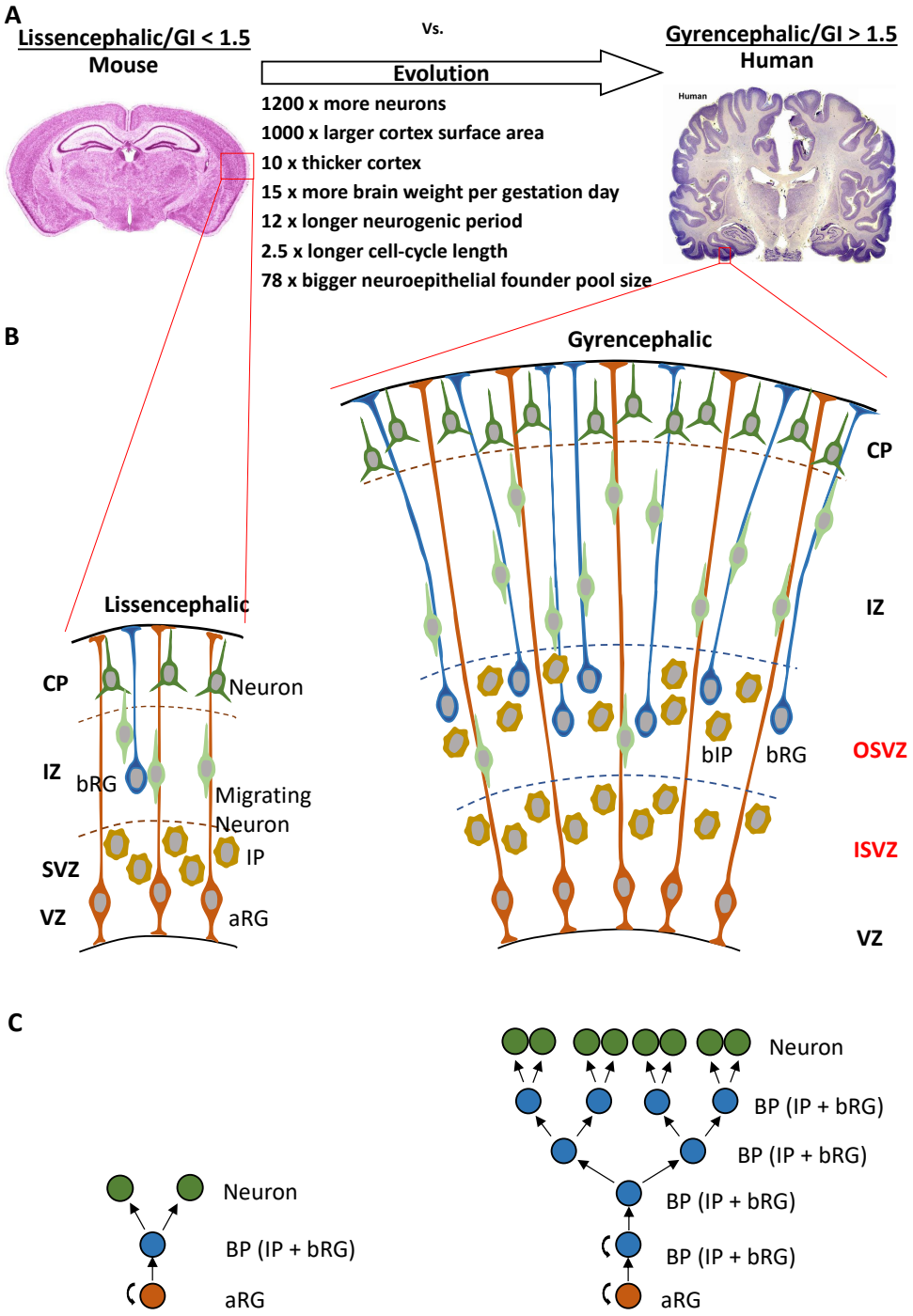

Figure 1.6: Evolutionary correlates between lissencephalic mouse and gyrencephalic human brain. A: Human cortex increased its size by expanding laterally instead of radially. B: On a cellular level the human cortex increased the thickness of the SVZ being subdivided into ISVZ and OSVZ. C: Gyrencephalic species like humans increased their pool of neuronal progenitor cells by symmetric division of basal radial glia cells to adapt to the increased number of neurons. SVZ: subventricular zone, ISVZ: inner SVZ, OSVZ: outer SVZ, bIP: basal intermediate progenitors, bRG: basal radial glia.

1.4.2 Theoretical ideas on cortical folding

The exact mechanisms by which gyrencephalic species develop folds during the phase of increased tangential expansion is still heavily disputed and several theoretical models have been proposed. Three questions are of major interest to solve the folding mystery. First, what biophysical properties of the cerebral cortex facilitate and correlate with folding? Second, what biological mechanisms do gyrencephalic species use to fold their brains? Third, is cortical folding just a byproduct of cortical expansion or genetically encoded?

To answer the first question, theoretical models simplify the cortex into a bilayer where the outer zone is the cortical plate and the inner zone represents the intermediate and ventricular zone [1]. Both layers may vary in their stiffness which defines how forces translate into tissue deformation. Although initial simulations proposed that the outer layer is required to be much stiffer than the inner layer in order to form folds, stiffness measurements of both layers showed that they are not so distinctly different [222, 285]. All mathematical models assume that the outer layer expands at higher speed than the inner layer. The outcome of those models was that initial geometry and the ratio of lateral vs radial expansion influence the folding pattern. Certain major folds are consistently found at the same location between human brains. Folding simulations in which the original brain shape of developing human fetuses was used showed that the initial cortical geometry, before its massive tangential expansion, influences the location of folds [258, 14]. Further, experiments in a 3D printed human brain model coated with an expanding polymer showed that a faster expanding outer zone induces folds that are very similar in size to the folds observed in humans [258]. This experiment also demonstrated that folds can appear even without an external constraint and thereby refutes the theory that folds may form due to external forces that restrict space for the expanding cortex [286]. Moreover a study comparing cortical morphometrics across different mammalian species showed that the degree of folding is a function of cortical thickness and surface area and does not correlate with the total number of cells. The more surface area and thinner the cortex, the higher degree of folding is observed [179]. Even in highly folded brains, the variations in the degree of local folding inversely correlates with the local thickness of the cortex [103].

Another early theory that has been experimentally tested, proposed intrinsic forces that are built up by the axons of migrating neurons. The so named "axon tension" theory suggested that forces from axons could pull at the regions where future sulci form and thereby induce cortical folding [271]. However experiments where axons in the developing gyri of ferrets were cut to measure the direction of forces concluded that there are not enough forces in the tangential direction that could pull the gyri together (Figure 1.7) [290]. The next section will focus on the biological mechanisms that may explain cortical folding (question 2).

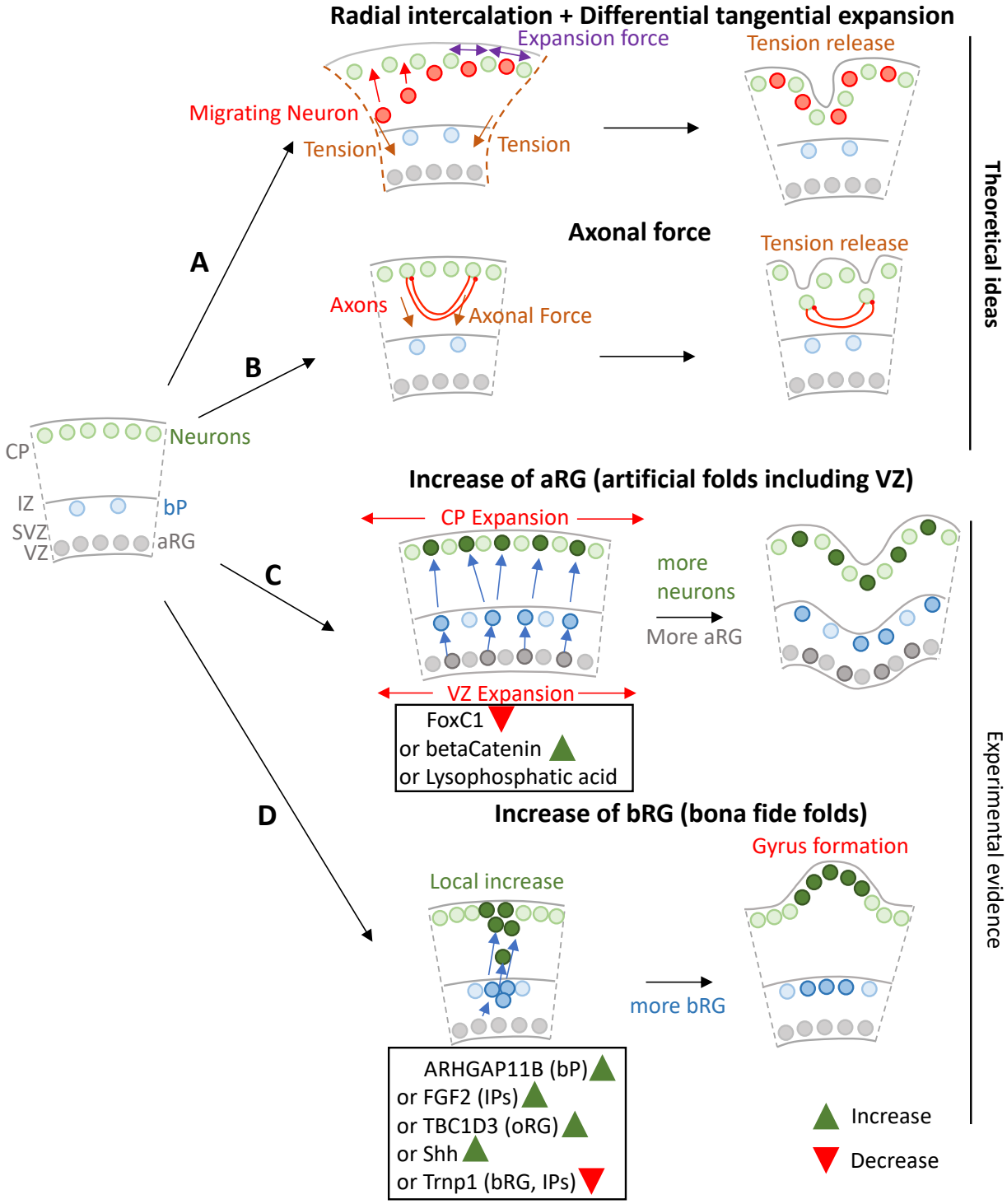

Figure 1.7: Theoretical models and experimental evidence on the mechanism of cortical folding. A: According to the radial intercalation hypothesis new neurons integrate into the same layer thereby producing laterally directed expansion forces only within the CP that results in folds. B: Axonal tension hypothesis suggests that intercortical axonal projections produce tension forces that induce sulci. C: Different molecules and genes were found to increase proliferation within the VZ that leads to expansion of both the ventricular zone and cortical plate. However, such expansion leads to aberrant folds that include the VZ. D: Local increase of bP and bRG cells induce gyri by increasing the number of neurons. CP: cortical plate, VZ: ventricular zone, SVZ: subventricular zone, aRG: apical radial glia, IPC: intermediate progenitor, bRG: basal radial glia, bPs: basal progenitors, IZ: intermediate zone

1.4.3 Molecular and cellular mechanisms in cortex folding

So far experimental data suggests that a local increase in the number of cells due to increased cell proliferation or reduced cell death induces folds. Although most theoretical models agree on differential tangential expansion as the main mechanism of folding, an increase in the number of cells alone cannot explain the specific massive lateral expansion of the outer zone. Importantly two experiments showed that lateral expansion of both the outer and inner zone does not lead to folds that resemble those of gyrencephalic species. In Foxc1 deficient mice in which the switch from lateral to radial VZ expansion is defective due to a loss of the meninges and its secreted factor retinoic acid, both the inner and outer zone expand immoderatily. That homogeneous expansion leads to folding of the VZ and the cortex which is contrary to the smooth VZ found in gyrencephalic species [240]. Similarly a transgenic mouse line expressing a stabilized beta Catenin exhibits an increase of the ventricular neural precursor cells, leading to a lateral expansion of the whole cortex. Again, the whole cortex including the VZ folded [43]. Lateral expansion of the cortex may lead to folds even without an external constraint. *Ex vivo* cultured cortex hemispheres that were treated with the proliferative factor lysophosphatic acid (LPA) again showed foldings of both the cortical plate and the VZ. Here a reduction in cell death rather than an increase in cell poliferation led to lateral cortical expansion [132]. Together with the modelling data, these experiments indicate that differential expansion of the developing cortex is essential for natural folding. Expansion of the ventricular neuroepithelial precursor cells alone leads to a homogeneous lateral expansion of both the inner and outer zone which causes abnormally folded brains (Figure 1.7).

One distinct hallmark of human cortex is its highly expanded outer subventricular zone (OSVZ) which is populated by an increased number of basal progenitors. It was hypothesized that the increased number of BPs in the OSVZ gives rise to more neurons and thereby laterally expands the cortex. Thus, recent work has focused on identifying genes that are preferentially expressed in human bRGs that could be tested for a developmental role in cortex folding (Figure 1.7) [209, 262, 157].

The general approach was to introduce specific genes expressed in gyrencephalic mammals or mimick their expression levels into mouse cortices. Human fetal cortices were found to have a pattern of high and low levels of the DNA binding molecule Trnp1 which contrasts with the high but homogeneous expression found in the mouse. Local knockdown of Trnp1 in the neural progenitor cells of the mouse VZ was found to reduce stem cell self renewal and promote an increase in the numbers of basal radial glia and intermediate progenitor cells leading to folding of the smooth mouse cortex. It was concluded that Trnp1 functions as a switch controlling both tangential (high levels) and radial (low levels) expansion [247].

Others identified the gene ARHGAP11B that does not exist in mice but is expressed in human radial glia cells. Local ectopic expression of ARHGAP11B in the developing mouse embryo led to an increase in basal progenitors that caused occasional foldings in adjacent regions [76]. Interestingly some experiments indicate that the location of cortical folds may not be coincidental but genetically programmed. Injections of the fibroblast growth factor 2 into the ventricles of developing mice caused a rostrocaudal increase in intermediate neural progenitors and neurons. In the same region the brains showed bilateral gyri and sulci that persisted into adulthood [214]. Consistent bilateral folding of

the cingulate cortex and other cortical regions could also be induced by constitutive activation of Sonic hedgehog signalling (Shh). Mechanistically, overactivation of Shh leads to an expansion of upper cortical layers by increasing bRGs and IPCs in the SVZ. Interestingly, restricting Shh signalling to medial cortical areas also restricted folding to the same region. In humans Shh signalling is highly active in aRGs and inactivation of Shh in human cortical organoids leads to a reduction of bRGs [279].

In ferrets, the location of future gyri can be predicted by local expansion of the oSVZ. Interestingly a thicker oSVZ positively correlated with increased Shh activity [53]. Another gene, TBC1D3, segmentally duplicated on human chromosome 17 around the time of hominoid evolution [119], reduces the delamination of aRGs in human fetal brain slices when downregulated. In line with this result, its overexpression in the mouse cortex induces the delamination of aRG cells and increases the numbers of bRGs. These effects lead to the generation of local folds that persisted until P3 (Figure 1.7) [122]. Further work in the ferrets has shown the contribution of the OSVZ to cortical folding. Ferrets are gyrencephalic species that develop their folds postnatally. Reducing or enhancing proliferation of bRGs in the OSVZ lead to reduced or increased degree of folding respectively [220, 167]. bRGs each have a radial fiber attached to the basal membrane. In gyrencephalic species the radial fibers of bRGs below future gyri diverge like a fan. Since neurons migrate along those fibers it is believed that the divergent projections leads to an increased lateral expansion by laterally distributing newborn neurons [156]. Although the aforementioned work nicely shows the importance of OSVZ, bRGs and with less evidence also IPCs in cortical folding, it is not clear how neurons distribute laterally instead of radially by expanding cortical layers. Indeed, in the macaque visual cortex a doubled abundance of OSVZ progenitor cells increases the numbers of upper-layer neurons without increasing folding [158]. Also a general increase of basal progenitors in the mouse does not always lead to foldings, suggesting that other mechanisms participate in such complex process [187].

The most accepted hypothesis states that is the combination of basal progenitor amplification with divergent radial migration that contributes to the expansion of the cortex in radial and tangential axes, and then its folding [220, 22]. In fact, the way neurons migrate in the cortex is quite different between lissencephalic (mouse) and gyrencephalic species like the ferret. In the mouse, newborn neurons mostly follow and adhere to their mother aRG cell leading to low lateral dispersion [185], which means that their birthplace dictates their final position in the lateral axis. However, in the ferret new born neurons originated from the OSVZ are able to switch several RG fibers and disperse laterally up to several millimeters (Figure 1.8). Currently, the mechanisms by which migrating neurons can disperse laterally in gyrencephalic species are unknown. During recent years, growing evidence supports the involvement of neuronal migration in cortex folding. For example, the role of most of the genes linked to abnormal cortical folding in humans has been associated with neural migration rather than with progenitor proliferation in both mouse and ferret experimental paradigms [176, 74]. Recently, elegant work by Shinmyo and co-workers, showed that solely impairing the migration of upper cortical neurons by downregulation of Cdk5, leads to a reduced degree of folding in ferret cortices [237]. These studies support the notion that neuronal migration is a key process during cortex folding because it affects the distribution of neurons which in turn alters the biophysical properties of the tissue.

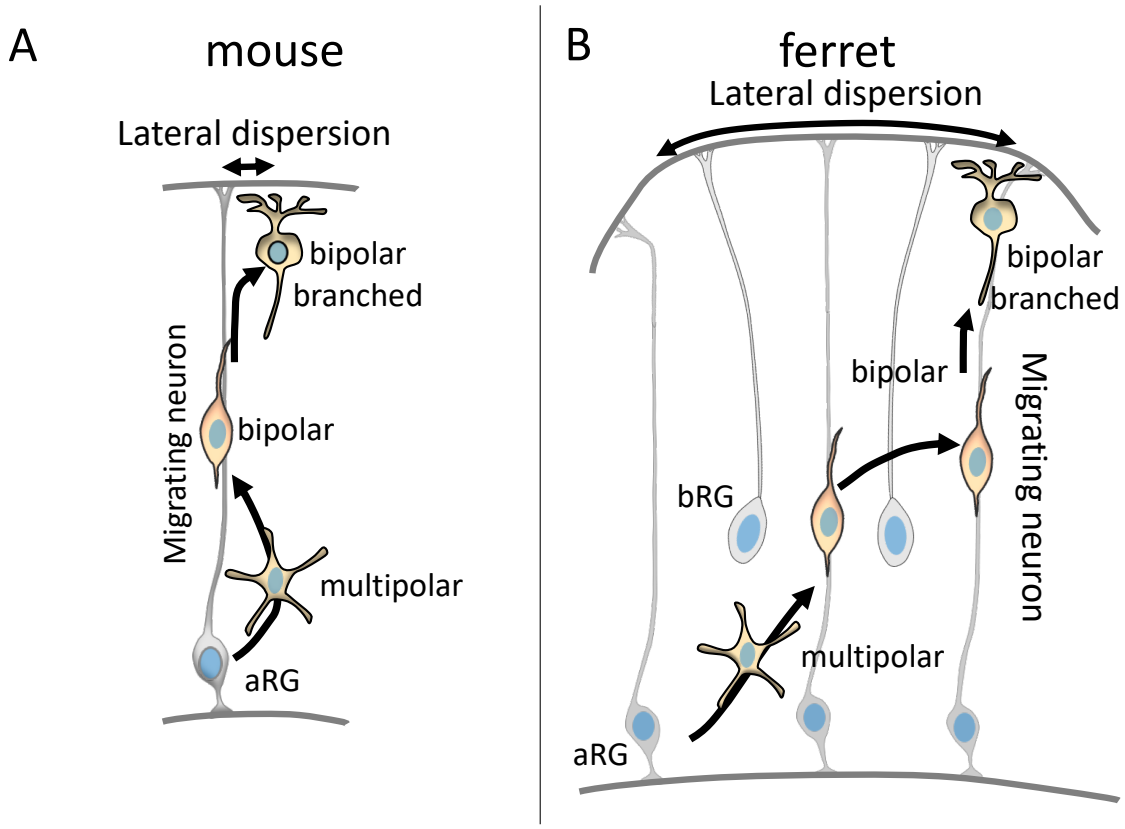

Figure 1.8: Mouse vs. ferret cortical migration. A: In the mouse neurons migrate radially without lateral dispersion. B: In ferrets, neurons can disperse laterally several millimeters on their way up into the cortical plate

The radial intercalation hypothesis proposes that the cortex expands laterally by squeezing new neurons into the same layer. The force to squeeze new neurons between existing neurons is generated by the leading process contractraction when in contact with the basal membrane, thereby pulling the neuron up into its final location (Figure 1.7) [250]. One shortcoming of this theory is that the phase of neuronal migration and intercalation is almost complete when the cortex starts to fold [280, 136]. Cortical folding however overlaps with cytoarchitectural differentiation. Thus, it was proposed that the expansion of dendritic and axonal arbours could provide enough forces to explain the lateral expansion of the cortex [222, 250]. In ferrets however at the onset of the exponential increase in cortical folding, the dendritic arbors in layer 2/3 and 4 are still very poorly developed but expand exponentially when folding already reached its plateau [21, 29]. This timing discrepancy suggests that glial cells and interneurons that populate the brain after neurogenesis, could participate in the generation of tangential expansion forces. However, no experimental evidence so far supports this idea.

1.4.4 Folding patterns: random or predetermined?

At a first glance, the folding pattern of the human cortex looks random. However certain patterns are strongly conserved between individuals. The deep primary folds in humans always develop at the same location while secondary, less deep folds are less well conserved [153]. The most shallow tertiary folds develop randomly across the whole cortex

[20]. Ferrets have only primary cortical folds that have a very defined and conserved pattern. This suggests that at least primary folds are in some way predetermined. Genetic mechanisms have been suggested based on transcriptomics analysis of the germinal layer in developing ferrets. In the OSVZ, several genes were found highly expressed in regions that will form gyri and downregulated in future sulci (and vice versa) [53]. Trnp1 is one such gene that is differentially expressed in germinal layers of future gyri and sulci [247]. Additionally, the initial shape and thickness might determine the size of folds and their location. Supporting evidence comes from models of folded paper and plastic brains that were coated with an expandable hydrogel. The later study showed that major primary folds reproducibly built at the same location and was attributed to the initial shape of the brain [258]. To summarize, the exact pattern of cortical folding seems to be a mixture of genetics that predefine the initial shape and biomechanical forces that finally fold the cortex based on the underlying shape. Smaller gyri and sulci however develop randomly since they vary between individuals and even genetically identical twins [154].

1.5 Aberrantly folded brains in humans

Cortical folding is essential for a normal working brain. Individuals with abnormally folded brains suffer from severe mental and emotional retardation, epileptic attacks, autism and schizophrenia [94, 188, 93, 197, 230, 50]. Two morphologically distinguishable cortical missfoldings are known. Lissencephaly and Polymicrogyria (Figure 1.9).

1.5.1 Lissencephaly

There are two subtypes of lissencephaly. Type I lissencephaly describes brains with a reduction (pachygyria) or complete loss (agyria) of the normal folds. Those brains often show microcephaly, fewer cortical neurons and have only 4 instead of the typical 6 layers. Lissencephalic patients suffer from severe mental retardation and epilepsy [197]. Five genes have been associated with the classical type 1 lissencephaly. LIS1 (Lissencephaly1), DCX (Doublecortin), TUBA1A (Tubulin alpha 1A), ARX (Aristaless) and RELN (Reelin) [84, 221, 208, 127, 19]. Interestingly, mutations in all of those genes disturb normal neuronal migration, mostly by affecting the neuronal cytoskeleton. DCX protein normally stabilises microtubules and LIS1 regulates neuronal forward translocation of the cell soma[106]. Thus, LIS1 mutated neurons have a lower cell motility [72]. TUBA1A protein is a brain-specific alpha tubulin and a main component of the microtubule system. TUBA1A mutations are assumed to disrupt interactions with other microtubule binding proteins (doublecortin and kinesin KIF1A) [177]. ARX is a homeobox gene. Homeobox genes are known to regulate the expression of a variety of different gene complexes during development. Thus, the exact molecular pathway that causes lissencephaly in ARX mutated brains is unknown. On a cellular level ARX mutations lead to defects in radial and tangential migration of cortical neurons [46]. Reelin is a signalling glycoprotein that is released by the Cajal-Retzius cells at the surface of the cortical plate. Reelin was shown to be a migration stop signal that is important for proper cortical layering. Loss of Reelin leads to an inversion of the cortical layers where later born neurons form deeper layers [33].

Type II lissencephaly (also Cobblestone lissencephaly) describes a condition with a disorganized cerebral cortex where neurons migrate too far into the pial surface to form

extracortical layers. These overmigrations are then responsible for agyria and/or cobblestone phenotypes. Patients suffer from mental retardation, epilepsy, congenital muscular dystrophies and ocular deficits. The mechanism involves mutations that lead to a disruption of the outermost layer of the brain, the glia limitans. Alpha dystroglycan seems to be a key molecule in a variety of genetic mutations. Alpha dystroglycan is a highly glycosylated receptor for extracellular matrix molecules and thereby maintains stability of the cell surface. Mutations in genes like POMT1, POMT2, POMGnT1 and Fukutin all affect the O-glycosylation of the alpha-dystroglycan [197, 49, 303, 265]. In mice, Golgi transmembrane protein Presenilin1 (PS1) deficiency was found to show cortical dysplasia that are similar to human cobblestone lissencephaly. PS1 deficient mice fail to maintain an intact pial basement membrane, which results in a loss of Cajal-Retzius neurons and subsequent overmigration or premature termination of migration [95]. Similarly, a loss of the basement membrane constituent integrin linked kinase leads to a cobblestone phenotype [83]. In general disruptions of the basal lamina seem to be the key mechanisms that cause the cobblestone lissencephaly.

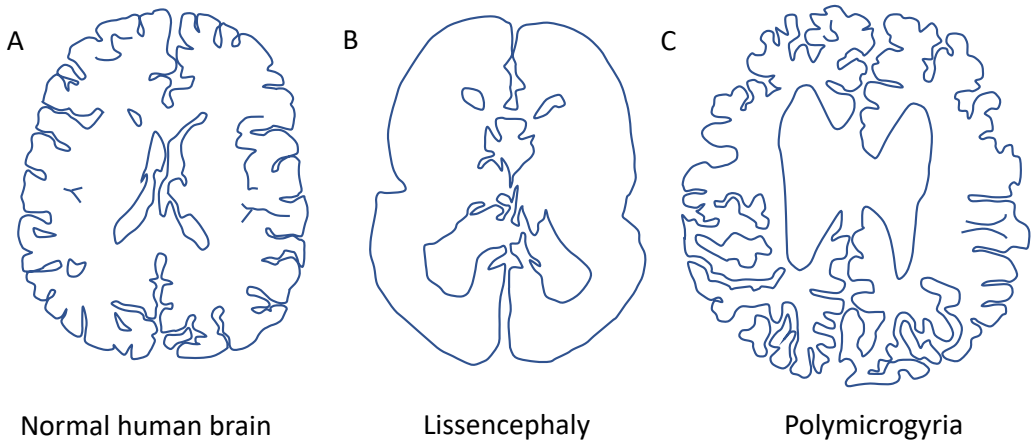

Figure 1.9: A: Contour scheme of a normal human brain. B: Lissencephalic brain. C: Polymicrogyric brain.

1.5.2 Polymicrogyria

Polymicrogyria describes a condition where the cortex has an excessive number of small gyri that are separated by small sulci. Depending if the cortex is unilaterally or bilaterally affected, patients suffer from focal seizures, cognitive impairments and various other symptoms that depend on the locations that are involved [83, 31]. In some cases the cortex is abnormally thick or thin [197]. Bilateral frontal and parietal polymicrogyria were found to be associated with mutations in the G-protein-coupled receptor gene (GPR56) [202, 203]. The gene is expressed in neural progenitor cells at the VZ and SVZ and is assumed to play a role in regional organization of the brain [197]. The gene GRIN1 that encodes a subunit of the N-methyl-D-aspartate receptor (NMDA) was also linked to extensive bilateral polymicrogyria. Mutations in GRIN1 alters the *in vitro* activity of the NMDA receptor [79].

1.6 Open questions and aims of the folding project

Gyrencephalic brains are in general bigger and therefore require the production of more neurons. Interestingly, while human cortical surface area expanded 1000 times, cortical thickness only increased by factor 10 leading to a lateral expansion and folding [73]. Current experimental data and comparative analysis showed that by adding an additional proliferative zone (OSVZ), gyrencephalic species like humans can increase their proliferative capacities to keep up with the higher neuronal demand. Forcing local increases in cell proliferation by producing more bRGs in mice could occasionally induce bona fide-like folds of the cortical plate. The question that remains to be solved is how the increased number of cortical neurons is arranged in a thin cortical layer and how that induces folding. Understanding cortical migration is therefore the key to fully understand folding. Previous work from our lab showed that members of the FLRT protein family can regulate the speed and radial distribution of neurons (FLRT2) and also their lateral distribution (FLRT3). Given that cortical migration can impact and regulate cortex folding, we were interested in analyzing double mutants to minimize the effects of redundant functions shared by members of this family. We focused on FLRT3 because its role in lateral dispersion of neurons but also with FLRT1, due to its high expression and overlap with FLRT3 during cortex development.

Chapter 2

Introduction - FLRTs in the mouse retina

2.1 Principles of retina development

The main aim of this thesis was to understand the role of FLRTs in the retina because of their specific expression in this structure. Here, this thesis will give an overview of three relevant points of the current knowledge of retina development that are related to our research. First, as described in a previous chapter, FLRTs have been shown to play a role in synapse formation, neuronal migration and axon guidance [193, 296, 150]. The retina itself is a piece of outsourced brain tissue. It has three distinct cellular layers (like the cerebral cortex) that form cell type specific connections between each other. The different cell types in each layer distribute equally across the retina to cover the whole visual space and the retinal ganglion cells (RGCs) must send axons to the right target regions. Since FLRTs have adhesive and repulsive functions and also can be shed from the cell surface, we hypothesized they could be involved in one of those developmental processes. Second, the developmental program wires the retinal circuit before eye opening at P15 and thus determines retinal signal processing. Third, taking into account all the potential functions of FLRTs in retina development, I will outline the four main steps required to generate a functional retina. The first step is to generate the right numbers of the seven main neuronal types in the retina. Second, those neurons need to migrate to their target location and distribute homogeneously. Third, all neurons need to form connections between each other to integrate into the circuit and connect to the brain. In a final step, neurons refine their connections.

2.1.1 Retinal layering

The retina consists of three defined nuclear layers: The photoreceptor layer (PRL), the inner nuclear layer (INL) and the ganglion cell layer (GCL). Like in the cortex, retinal neurons are not born at their final target location. Multipotent progenitor cells divide at the ventricular surface (the side of the future PRL) and generate neuroblastic precursors that migrate to their future layer [218]. All seven different cell types in the retina are produced in a temporal sequence. First, starting around E10.5 RGCs are produced, then horizontal cells, cones and amacrines and lastly rods and bipolar cells [218]. The sequence of neuronal production is fixed and multipotency declines over time. That means after a cell has started producing the next type in the sequence it cannot produce the previous

any more [289]. Two distinct modes have been described by which the newly born neurons reach their target location. Compared to neocortical migration, where neurons have to migrate long distances, migration in the retina is much shorter and does not rely on any radial glia that provide a fiber network to support radial migration [218]. RGCs, rods and bipolar cells attach their leading and/or trailing process to the retinal margins and use nuclear translocation to move towards the target region [173, 207]. Amacrines and horizontal cells however adopt a bipolar morphology and migrate without attachment to the ventricular or basal surface [85, 233, 111].

2.1.2 Retinal mosaic formation

The retina consists of a variety of different cell types, each performing a specific function in visual signal processing. About 30 different RGC types extract specific visual features like motion direction or contrast. To ensure that each of the about 30 visual features can be read out in every location of the retina, RGCs (as well as other cell types) from the same subpopulation distribute homogeneously in a non-random mosaic like fashion and their dendritic arbors show either constant overlap or tiling [283, 273]. The molecular mechanisms controlling this regular distribution are thus essential to ensure proper functional tiling of the retina. Despite its importance, no molecular mechanisms are known that homogeneously distribute RGCs across the retina. Findings from amacrine cells showed that adhesion and repulsion seem to be key processes in the formation of retinal mosaics. Interestingly, FLRT transmembrane receptors are known to have adhesive and repulsive functions during cortex development and may therefore represent possible candidates [296]. At least three different mechanisms have been proposed that would explain retinal mosaic formation. First, cell death was found to contribute to dopaminergic amacrine cell, alpha and M1 ganglion cell mosaics [215, 118, 42]. Second, lateral induction of newly generated cells could ensure homogeneous cell mosaics. However such mechanism has not been described yet *in vivo* [105]. Third, lateral migration of newly integrated neurons to distribute equally has been described for ON-starburst amacrine cells and horizontal cells. Homophilic repulsive interactions between the transmembrane multiple epidermal growth factor-like domains protein Megf10 or Megf11 were shown to be a molecular mechanism that repell amacrine and horizontal cell soma from each other [217, 82].

2.1.3 Stratification within the inner plexiform layer

At the inner plexiform layer (IPL) about 60 different types of bipolar cells, amacrine cells and RGCs from the inner nuclear and ganglion cell layer connect to each other at one of the about five defined strata [241]. Each cell type stratifies in one or more strata and ensure functional connections to the right cell type. The different subtypes either directly stratify into the correct lamina or establish a less restricted dendritic tree that gets pruned into the right lamina over time [129, 181]. Lamination is regulated by both neurotransmission dependent or independent interactions [105]. Blockage of photoreceptor terminals causes bipolar and horizontal cells to sprout into the outer nuclear layer and ablation of a specific bipolar cell type causes the corresponding RGC type to stratify in the wrong layer [216, 64, 190]. The neurotransmission independent mechanisms are based on heterotypic repulsive or homotypic adhesive cues. The repulsive interaction between the guidance ligands Sema5A/5B and their receptors PlexA1/A3 was shown

to restrict amacrine cell and ganglion cell dendrites within the IPL [168]. Heterotypic signalling between Sema6A and PlexA4 confines stratification of M1 RGCs and dopaminergic amacrine cells to the outermost IPL layer [169]. The homotypic adhesion molecules Dscam, DscamL, Sidekick1/2 and Contactins 1-5 were shown to regulate laminar specificity of certain amacrines and RGCs [293, 294, 295]. All three FLRTs have already been shown to have defined non-overlapping expression patterns in the IPL. *Flrt1* is expressed by cells that stratify in layer S1, *Flrt2* in layer S2 and S4 and *Flrt3* in layer S3. Immunostainings have revealed that *Flrt2* is expressed by ON starburst amacrine cells (SAC) in the GCL, OFF SACs in the INL and by about half of all ON-OFF direction selective RGCs (CART+). Moreover, stripe assays have suggested that repulsive FLRT-Unc5 interactions are involved in neuronal subtype recognition and thus the formation of defined strata [275]. However, knock out experiments are needed to confirm the *in vivo* relevance of those findings.

2.1.4 Retinofugal projections

RGCs collect and transmit all visual information to different retinorecipient regions in the brain. At around E11.5, RGC axons leave the retina through the optic disc at the center of the retina. The growth cones of RGC axons sense the guidance molecule Netrin1 released from the optic disc via their receptor DCC (Deleted in colorectal cancer) [55]. Additionally, repulsive cues from the peripheral retina (e.g. chondroitin sulfate proteoglycans) direct axons towards the center [251, 243]. The axons of each eye enter the optic nerve and arrive at the ventral midline of the diencephalon to form the optic chiasm at around E12.5 [71, 162]. Axons originating from RGCs at ventrotemporal regions of the retina project ipsilaterally while axons outside the ventrotemporal region cross the midline to project contralaterally [162]. The decision between ipsi- and contralateral projections is enabled by the expression of repulsive (ephrinB2) and attractive (Sempahorin6D, NrCAM, PlexinA1) guidance molecules in the optic chiasm. Ipsilaterally projecting RGCs express the kinase receptor EphB1 (induced by Zic2 transcription factor) which enables them to respond to the repulsive ephrinB2 [200]. Contralaterally projecting RGCs in turn can be identified by Islet2 and SoxC and are attracted to cell adhesion molecules like NrCAM and Plexin-A1 [194, 143]. After RGCs choose to go ipsi- or contralateral at the optic chiasm they are faced with the challenge of finding the right retinorecipient target. More than 40 distinct image-forming (e.g. dorsal lateral geniculate nucleus (dLGN), superior colliculus (SC)) and non-image forming targets have been identified in the brain [178]. The molecules regulating target specificity are still largely unknown. A few cell adhesion molecules were found to regulate target specificity in the non-image forming system. Cadherin6 regulates targeting of RGC axons to the olivary pretectal nucleus (OPN), Contactin-4 (CNTN4) or amyloid precursor protein (APP) to the optic tract (NOT), Semaphorin6 or PlexinA2/A4 to medial terminal nucleus and disabled-1 or Reelin to the dorsal lateral geniculate and intergeniculate nucleus [301, 191, 192, 58, 253].

Within a target region, axons of every specific RGC subtype show laminar-specific innervation refinement. [104, 126, 130, 60, 61]. This feature is most prominent within the SC and dLGN [235]. However, to date, no molecule has been found to regulate laminar targeting specificity [235]. Some work suggests that the dorsal/ventral sorting of RGC axons in the optic nerve, before they even reach the dLGN or SC, could already predestine axons to establish themselves the correct layer [34, 206]. After the axons reach

their right layer within the target, they have to connect to the correct retinotopic location [235]. The EphA/ephrin-A receptor/ligand system is known to map the nasal-temporal location of RGCs onto their target regions while EphB/ephrinB is assumed (although this point is still under discussion) to map the dorsal-ventral axis [268, 172]. Ipsilateral projecting RGCs use the Ten-m3 and Ten-m4 homophilic transmembrane glycoproteins to ensure correct retinotopic mapping [304, 62, 145]. Moreover, neuronal activity from the retina was found to play a role in retinotopic mapping. Since subcortical retinotopic map formation develops before eye opening, visually driven activity can be excluded from the mechanism. Instead another non-molecular mechanism was found. Spontaneous activity of RGCs that repeatedly spread in waves across the retina induce retinotopic map formation in the dLGN and SC and appear to be essential for eye-specific segregation of axon terminals in the dLGN [291, 201, 88, 308, 27]. All together, while the initial targeting of RGC axons depends on molecular cues, further refinement to establish and maintain retinotopic maps and eye-specific segregation in the target areas seem to be activity dependent [56, 38, 139].

2.2 Retinal signal processing

The retina senses light through photoreceptors at the outermost layer of the retina. However, the retina does not directly encode and transmit the information from each photoreceptor to the brain. Instead two additional cell layers, the inner nuclear layer (INL) and the ganglion cell layer (GCL) compress, filter and extract certain visual features of the raw signals before different types of RGCs transmit each feature in a separate stream to the brain. About 14 different morphologically defined bipolar cells within the inner nuclear layer (INL) connect the photoreceptors to the retinal ganglion cells in the GCL [15]. Bipolar cells react either to increases (ON) or decreases (OFF) in light intensity levels. All bipolar cells preferably stratify in one of the five layers of the inner plexiform layer. OFF bipolar cells stratify within layer 1 and 2 while ON bipolar cells stratify within layer 3,4 and 5 [15]. Depending on which layers RGCs connect to the bipolar cells, they compute either ON, OFF or ON-OFF features. Amacrine cells in the INL and GCL are responsible for special features like direction selectivity [300]. The advantage of that external visual preprocessing in the retina is that it dramatically reduces the amount of information that needs to be sent and processed by the brain. In the past years, the number of identified RGC subpopulations has increased suggesting that each one could compute and provide new visual features to the brain [10].

2.3 Known retinal ganglion cell types

2.3.1 Neuronal cell type classification

The genetically identified RGC population that I describe in my work raises three questions: First, how does similarity based clustering of cells help us to understand a neuronal circuit especially since no neuron is the same? Second, does the genetic *Flrt* marker label an homogeneous cell population? And third, does this cell population represent a new cell type or can I match them to an already known cell type? To answer the first question one needs to keep in mind that the retina consists of more than 60 different types of neurons that together extract about 30 different features from the visual input. To

allow each of those features to be detected across the whole visual space, neurons and their circuits providing that information need to repeatedly distribute across the whole retina. So especially in the retina, we may assume that structurally, morphologically and/or molecularly similar neurons also provide a similar function in the circuit. Thus molecular, structural and functional properties are often used to classify retinal neurons. However, there are no common rules for such classifications.

The homogeneity of a cell population is thus dependent on the personally set threshold at which one considers a neuron to be different enough to separate into a different class. Without such a threshold, one could continuously refine classification steps until one ends up having one "class" for each neuron, which would render the approach useless [307]. Another challenge in neuronal classification is the selection of the most suitable properties (e.g. morphology, physiology or molecular profile) and their hierarchical ordering. Certain molecular features are thought to be good candidates for first order classification since they not only determine neuronal features such as morphology, physiology and connectivity during development, but often maintain a cell's identity throughout life [276, 57]. One gene or molecule will unlikely be enough to define a single cell type but a combination of two to three markers could be sufficient to describe a functionally homogeneous cell population. And lastly, certain neuronal properties may stochastically change over time which may or may not influence the neuron's circuitry. Even if two neurons receive the same extrinsic or intrinsic developmental instructions, stochastic events and environmental influences may result in two different neurons [18, 3]. Moreover, some genes that determine certain characteristics are expressed only transiently during development and are not available for cell identification later on [227]. To summarise, cell classification is not a straightforward approach and needs careful evaluation of the selected features, hierarchies and classification thresholds below which further subdivisions do not improve our understanding of the neuronal circuit.

2.3.2 Alpha RGCs

So far four different alpha retinal ganglion cells have been identified [196, 140]. Alpha RGCs share large cell bodies, thick axons and wide mono-stratified dendritic fields. All four types respond to expanding stimuli (Figure 2.1 B) but can be distinguished by a combination of molecular markers and their response to expanding stimuli (OFF - sustained/transient or ON - sustained/transient) (Figure 2.1 A,B) [140]. That property suggests that they function to warn animals about fast approaching predators. This idea is further supported by their thick axons which allows them to transmit that critical information very quickly to the brain. Alpha RGCs do not respond to direction selective stimuli. Some alpha RGCs were shown to have blue-green spectral opponency which might contribute to color vision in mice [37].

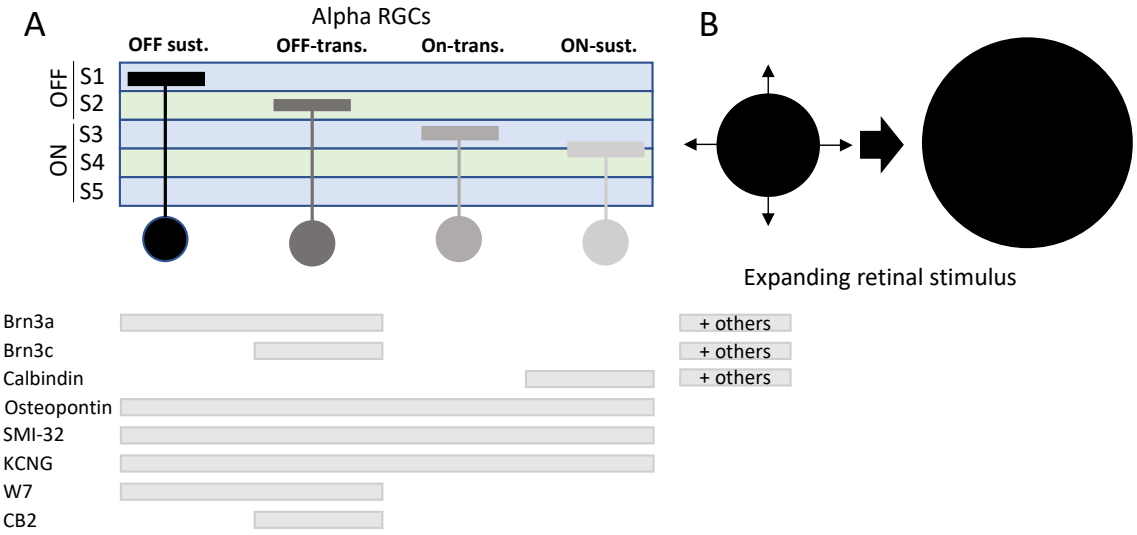

Figure 2.1: A: Stratification pattern and known molecular markers that distinguish the 4 different alpha RGC types. B: Alpha RGCs react to expanding stimuli. Sust., sustained; trans., transient

2.3.3 Local edge detectors/W3 cells

Local edge detectors (LEDs) were first discovered in the rabbit retina. Later W3 cells were found in the mouse retina that shared many properties of the LEDs suggesting them to be the same type [308]. In mice they represent about 13% of all RGCs and are one of the most numerous RGC types. They share a small (100 µm) but strongly branched dendritic arbor that stratifies near the center of the inner plexiform layer (Figure 2.2 A) [231]. Exposing the LEDs to natural scenes recorded with a camera showed that they remain silent most of the time but only fire at high contrast edges (Figure 2.2 A) [308]. W3 cells have On-Off receptive field centers that are activated by increasing and decreasing light intensities. This observation is in line with the stratification of the dendritic arbor at the intersection of ON and OFF inner plexiform layers. For many RGC types the stimulation in the center is opposed by stimulation in the surrounding regions. In W3 cells a blinking spot that increases in size causes the cell to turn completely silent (Figure 2.2 C) [308]. One biological function of this RGC type could be the detection of flying predators that when far away appear as a dot on a featureless background [308].

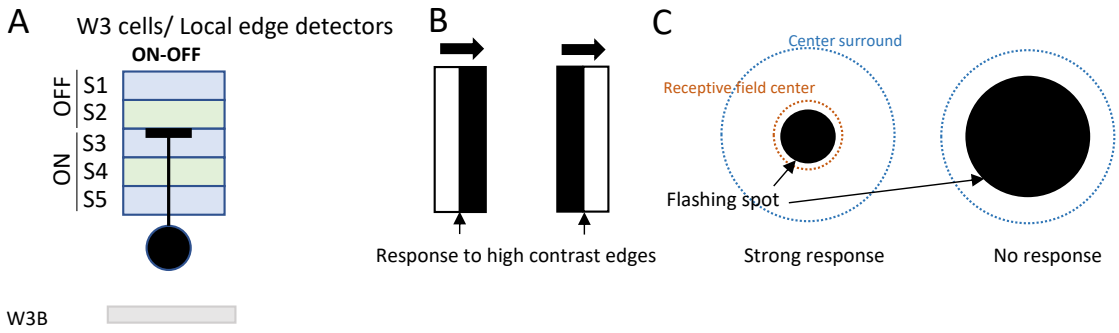

Figure 2.2: A: Stratification pattern and known molecular marker that label W3 RGCs in mice. B: W3 RGCs detect motion of small dark objects. Sust., sustained; trans., transient

2.3.4 J-RGCs (OFF DSGC)

J-RGCs (also OFF DSGCs) are identified by expression of an immunoglobulin superfamily protein JAM-B. Most of those RGCs have a characteristic asymmetric dendritic arbour which is aligned along the dorsal-ventral axis and stratifies in Layer 1 of the IPL (Figure 2.3 A). As with all functional RGC subtypes they also distribute in a regular mosaic across the retina. The asymmetric dendritic arbor combined with an OFF center and ON surround gives them their direction selectivity in the soma - dendritic arbor direction (Figure 2.3 B). Since all stimuli reaching the retina are inverted by the lens, that feature corresponds to an upward direction selectivity. J-RGCs project mostly to the superior colliculus and some also to the dorsal lateral geniculate nucleus. However, no projections could be seen in the accessory optic system where most other direction selective ganglion cells project to [130]. Additionally, smaller versions of the J-RGCs which do not express JAM-B but have the same asymmetric dendritic morphology were later found and molecularly defined [226].

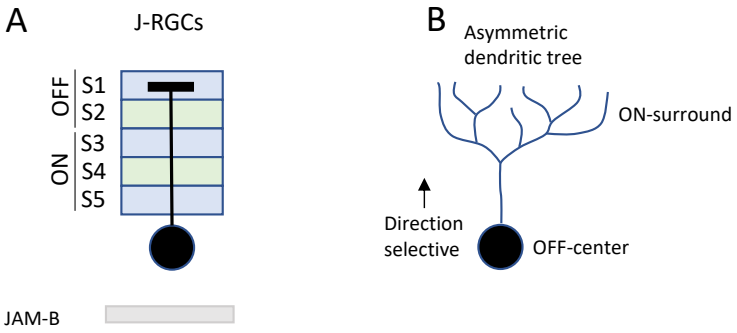

Figure 2.3: A: Stratification pattern and known molecular markers that label J-RGCs in mice. B: Alpha RGCs have OFF center and ON surround responses that make them direction selective in the soma to dendrite direction. In mouse J-RGCs respond to upwards moving stimuli.

2.3.5 F-RGCs

F-RGCs share expression of the Foxp2 transcription factor and represent about 20% of all RGCs in the Retina. Similar to the J-RGCs, F-RGCs also have an asymmetric dendritic tree oriented in the vertical axis. The observation that they do not distribute in a mosaic-like fashion suggested that F-RGCs are not a single subpopulation. Indeed, when Foxp2 is combined with different markers (FoxP1, Brn3b, Br3c) they can be subdivided into 4 different RGC populations that distribute in a mosaic-like fashion. Based on their dendritic size and function they were named F-mini-OFF, F-midi-OFF, F-mini-ON and F-midi-ON. F-midi/mini-OFF cells both stratify in layer 1 and F-midi/mini-ON cells have a broader stratification in layer 3/4/5 respectively layer 2/3 (Figure 2.4 A). Despite their direction selectivity, F-RGCs project only to image forming regions within the lateral shell of the dLGN and layers 2 and 3 of the superior colliculus. F-mini ON/OFF cells show direction selective responses while F-midi ON/OFF cells have no preferred direction [226].

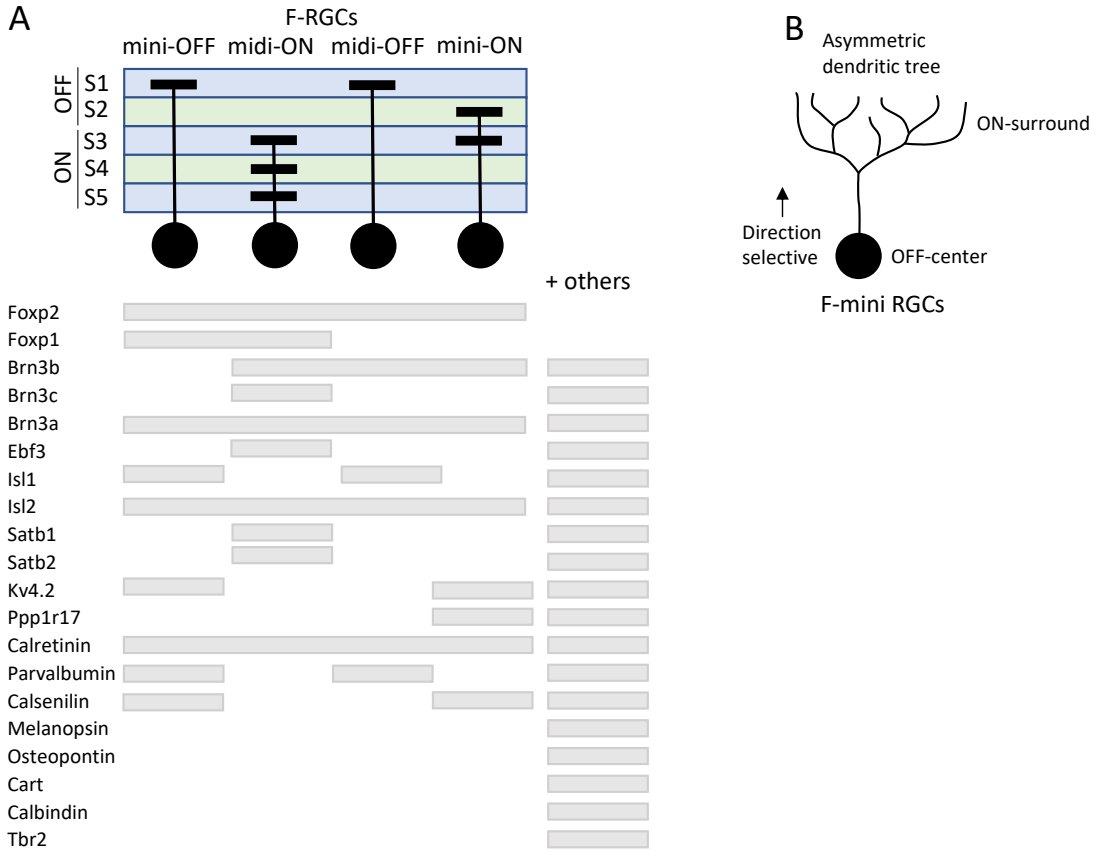

Figure 2.4: A: Stratification pattern and known molecular markers that distinguish four types of F-RGCs: midi-OFF/ON and mini-OFF/ON. B: F-mini-RGCs all have an asymmetric dendritic tree that gives them their direction selectivity. F-midi-RGCs don't show any direction selectivity.

2.3.6 ON-OFF directionally selective RGCs

Four different types of ON-OFF directionally selective ganglion cells (ooDSGCs) have been identified so far. They all respond to a light or dark stimulus moving in one of the four directions: upward, downward, backward and forward [70]. The direction selectivity is independent of object size and occurs even with stimuli smaller than the receptive field [12]. The mechanism for direction selective RGC repsonses involves directionally selective dendritic processes of starburst amacrine cells but it is still incompletely understood [274, 284, 300]. OoDSGCs all share bistratified dendritic trees that co-stratify with the Chat bands in layer 2 and 4 (Figure 2.5). The 4 ooDSGCs types exclusively express the neuropeptide CART and can be distinguished with a combination of Cadherin6, MMP17 and Collagen25a1. Moreover 3 transgenic lines (W9, BD and DRD4) were found to label nasal, ventral or dorsal/ventral ooDSGCs (Figure 2.5). All ooDSGCs project to the dorsal lateral geniculate nucleus while the ventral and dorsal ooDSGCs additionally project to the medial terminal nucleus and the nucleus of the optic tract [110, 126, 223, 267].

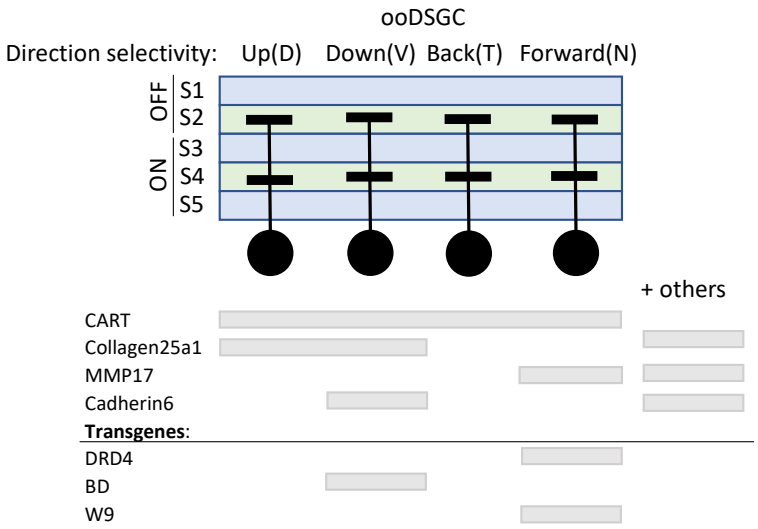

Figure 2.5: ON-OFF directionally selective ganglion cells (ooDSGC). Stratification and molecular identity of the four ooDSGC subtypes. Each of the four ooDSGCs prefers movement of a light/dark object in one of the four directions ventral, dorsal, nasal and temporal. V, ventral; D, dorsal; N, nasal; T, temporal; ooDSGC.

2.3.7 ON directionally selective RGCs

ON directionally selective ganglion cells respond to movements of one of the three directions: up, down and nasal. Fstl4 positive ON DSGCs in the ventronasal region of the retina respond to upwardly moving stimuli, while Fstl4 negative ON DSGCs prefer downwardly moving stimuli [302]. Compared to ON-OFF DSGCs, ON DSGCs only respond to light spots and edges (increases in light intensity) and remain silent for dark stimuli. Moreover, ON DSGCs respond best to slower moving bright objects. In line with their response properties they co-stratify with the ON Chat band in layer S4 (Figure 2.6) [255]. ON DSGCs project exclusively to the accessory optic system (AOS). The AOS was shown to be important for the optokinetic reflex which is crucial to stabilize the self-motion induced image shifts on the retina along the posterior, anterior and horizontal axes, which also matches the three semicircular canals of the inner ear that respond to the same axes of head movement [242, 301]. The different nuclei of the AOS specifically respond to forward (NOT-DTN), upward (dorsal MTN) or downward (ventral MTN) motion [242, 301]. Retrograde virus tracings showed that RGCs that project to the medial terminal nucleus (MTN) are purely ON DSGCs [58]. The nucleus of the optic tract (NOT) which is known to detect forward horizontal movement, receives input from both, the ON and ON-OFF DSGCs [301, 58]. This suggests ON DSGCs are important for mediating the optokinetic reflex [301]. Moreover Hoxd10 (knock-in mouse) was shown to label all ON DSGCs that respond to forward motion and all project to the AOS, representing about 3-5% of all RGCs [58]. Interestingly 35% of the cells labelled by the Hoxd10 mouse were ON-OFF DSGCs that do not express CART which was supposed to label all ON-OFF DSGCs [126]. The Hoxd10 positive ooDSGCs respond to lower speed forward moving objects similar to the ON-DSGCs [58]. The remaining Fstl+ cells outside the ventrotemporal region of the retina also project to dLGN, SC and the AOS [302].

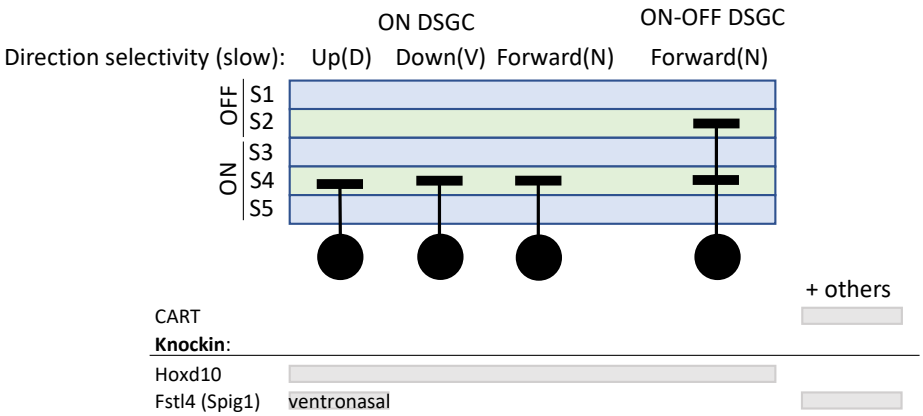

Figure 2.6: Three types of ON DSGCs can be distinguished based on their preference to light but not dark stimuli moving dorsal, ventral or nasal. Fstl+ ON DSGCs in the ventronasal retina respond to upward movement while Fstl- ON DSGCs prefer downwards movement. Using the Hoxd10 mouse all 3 ON DSGC subtypes are labelled. Moreover another CART negative ON-OFF DSGC was found in the Hoxd10 mouse that responds to forward motion. In contrast to ON-OFF DSGCs, all Hoxd10 positive cells respond best to slower moving stimuli.

2.3.8 Intrinsically photosensitive RGCs

Intrinsically photosensitive RGCs (ipRGCs) consist of 5 subtypes (M1-M5) that all express melanopsin which gives them the unique ability to respond to light directly without input from the photoreceptors. Light sensitivity is triggered by melanopsin through the activation of a signaling cascade that opens cation channels in the RGCs. IpRGCs distribute sparsely across the whole retina and can be distinguished based on their dendritic morphology, stratification, melanopsin expression and function (Figure 2.7). M1 cells are the main ipRGC type, have the highest melanopsin expression and stratify in the OFF layer S1. Their projections to the non-image forming suprachiasmic nucleus (SCN) are important for synchronizing the circadian clocks to the daily light-dark cycles [78, 195, 107]. Moreover the M1 and M2 cells both project also to the OPN which is important for controlling the light dependent constriction of the pupillary (pupillary light reflex) lucas2003diminished,baver2008two. The subtypes M2 to M5 also contribute to image forming vision which is reflected in their projections to the dLGN and SC [107]. M2 and M4 cells stratify mainly in the ON layer S5, M3 bistratify in the ON and OFF sublayers [13]. Interestingly about half of the previously described SMI32-positive alpha RGCs that express melanopsin belong to the M4 type and were shown to be essential for high contrast detection [232]. M5 cells have a uniquely small dendritic field size and stratify within the ON layer S5. They are excited by UV light and inhibited by green light, which is in contrast to other ipRGC types [246]. Due to the high variation in their projections within the brain suggests ipRGCs to be involved in a great variety of visual functions [112].

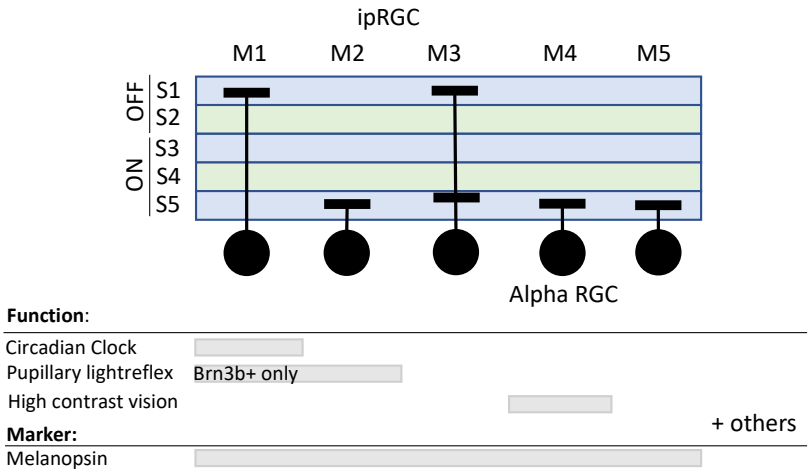

Figure 2.7: Intrinsically photosensitive retinal ganglion cell ipRGC (ipRGCs) can be divided in five subclasses M1-5. They can be distinguished based on function, stratification and markers.

2.4 Incompletely characterized RGCs

2.4.1 Orientation-sensitive RGCs

Orientation selectivity describes the property of cells to preferentially respond to a moving elongated visual stimulus aligned to a specific axis and to be inhibited by a stimulus orthogonal to the preferred axis [108]. Orientation selectivity was first discovered in the cat visual cortex [108]. Later orientation-sensitive RGCs (osRGCs) were found in the retina of pigeon, rabbit and later also in the mouse [170, 148, 40]. So far seven functionally different osRGCs have been identified for vertical, horizontal and orthogonal orientation of a flashing bar [9, 183, 184]. They represent about 14.5% of all RGCs in mouse [9]. Despite their exclusive ON responses, the ON vertically and horizontally tuned RGCs (vsRGC, hsRGC) both bistratify in the OFF layer S1 and ON layer S5 (Figure 2.8) [183]. While ON vsRGCs have a symmetric dendritic tree, ON hsRGCs have an oriented morphology. The OFF vertical and horizontal RGCs stratify both in OFF layer S1 (Figure 2.8) but can be distinguished again by the highly asymmetric dendritic morphology of the OFF vsRGC [184]. The horizontal and vertical ON-OFF and the ON oblique tuned cells were found in a functional screen using Calcium imaging [9]. Interestingly the OFF vsRGCs are labelled using the JAM-B Cre line, which has previously been report to label RGCs that have direction selective properties [184, 130]. All OFF vsRGCs tested by Nath et al. in the JAM-B Cre line showed vertical orientation selectivity but only weak direction selectivity that completely disappeared under photopic conditions [184]. Since the direction selectivity in the JAM-B cells originates from the center surround receptive field asymmetry, the direction selective response depends on features like background light intensity, color, contrast and speed of the moving object [184]. Genetic markers for the remaining cell types are still unknown.

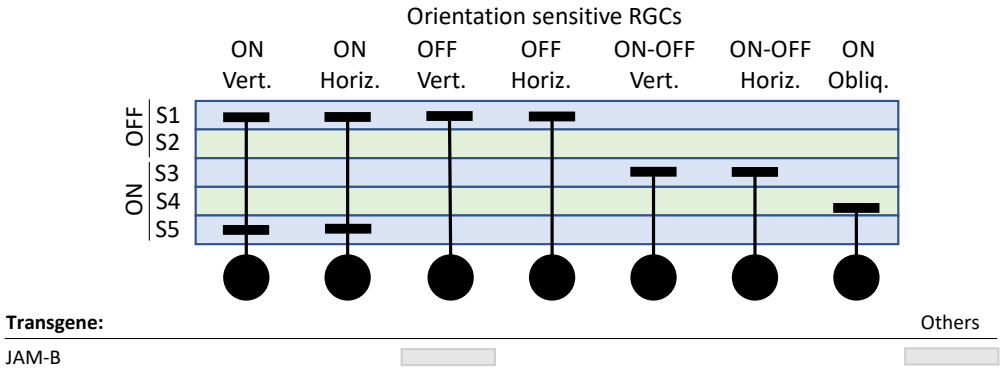

Figure 2.8: To date, seven functionally different orientation sensitive RGCs (osRGCs) have been identified in the mouse retina. OsRGCs respond preferentially to a stimulus along a specific axis. OFF-vertical osRGCs can be labelled with the JAM-B transgenic line. Vert, vertical; Horiz, horizontal; Obliq, oblique.

2.4.2 Suppressed-by-contrast RGCs

Suppressed-by-contrast RGCs (sbcRGC) were initially named uniformity detectors. Usually RGCs respond to increments or decrements of light by increasing their firing rate. SbcRGCs however are suppressed by high contrasts falling onto their receptive field center. So far, calcium population recordings indicate two types of sbcRGCs: On and OFF sbcRGCs [263, 9]. However only OFF sbcRGCs can be genetically labelled using a Cck-ires-Cre mouse line [263]. In line with their strong ON and weaker OFF response of the ON sbcRGCs, they show strong stratification in the ON layers S4/5 and weak stratifications in layer S1 (Figure 2.9). ON sbcRGCs were found to stratify in on layer S5 or sometimes also across the whole IPL [9]. ON-OFF sbcRGCs are suggested to provide a population signal for self-generated visual stimuli such as saccadic eye movements and blinking [263].

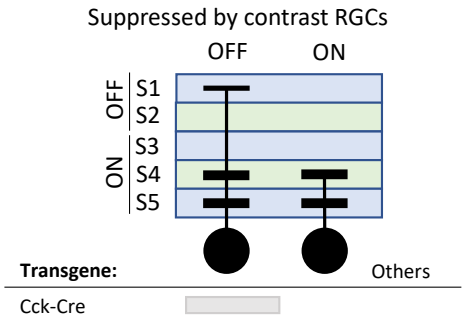

Figure 2.9: ON-OFF suppressed by contrast RGCs are silenced upon high contrast visual stimuli such as increases or decreases in light intensity. SbcRGCs show strong ON and weaker OFF suppression which matches their stratification pattern in layer S4/5 and S1.

2.4.3 Chromatically sensitive RGCs

Compared to humans, mice are dichromatic animals that express two types of opsins that have peak absorptions at middle wavelength (S-opsin) or ultraviolet (L-opsin) light.

The cones that express S and M-opsins represent only about 3% of all photoreceptors in mice [117]. Color distinction experiments confirmed that mice can indeed distinguish colors [117]. Interestingly there is no complete segregation of S and M-opsin expression in most of the cones. Only 4% of all cones express just S-opsin and distribute equally across the whole retina [98]. Most cones however co-express both opsins in varying ratios along a dorsoventral axis. M-cones are more frequently found in the dorsal half of the retina while the ventral retina contains mainly S-cones [257]. Consequently, the dorsal region can process S versus M chromatic information, while the ventral region is mostly restricted to monochromatic information processing [298]. The distribution of S and M-opsins is also reflected in the chromatic response properties of RGCs. Most RGCs responded to both UV (360 nm) and green (520 nm) light, however UV excitation was usually more dominant [68]. Some RGCs only respond to UV light (S-ON or S-OFF) and are connected to a bipolar cell type that receives input exclusively from S-cones [68, 151]. The genetic identity or stratification pattern of blue-sensitive RGCs in mouse has not yet been determined.

2.4.4 Beta RGCs (Pixel detectors)

Little is known so far about the beta RGCs. They were originally found in cats and later also in monkey (midget cell) and rabbit (brisk-sustained cell). Beta RGCs are more frequent and have a smaller receptive field compared to the alpha RGCs and are thought to be important for acute vision. There are probably two types of Beta RGCs: One large and one small beta RGC with either ON or OFF receptive field centers and an antagonistic surround [225, 249, 28, 231]. The existence of beta cells in mouse is not yet confirmed but a cell with similar antagonistic receptive fields has been found and could represent the beta RGCs found in cats, monkeys and rabbits [249, 228]. More recently a pixel-encoder ON retinal ganglion cell (PixON-RGC) has been genetically identified in a Grik4-Cre mouse [120]. Aside from labelling ON and ON-OFF DSGCs, the Grik4-Cre line also labelled small sized PixON-RGCs in the ventral retina. PixON-RGC receive only excitatory input in their receptive field center and only inhibitory input from their receptive field center surround. This combination allows PixON-RGCs to linearly encode local contrast and illumination. The responses are independent of light wavelength. PixON-RGCs stratify between layer 4 and 5 (Figure 2.9) and project mainly to the dLGN and may thus contribute to vision [120].

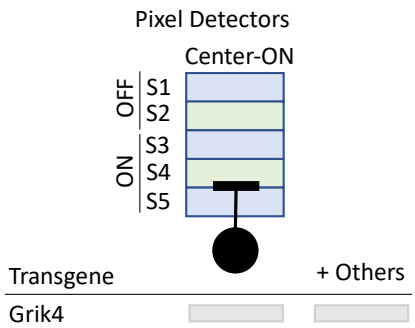

Figure 2.10: pixON-RGCs have small receptive field, stratify between layer 4 and 5, and respond linearly to increases in light within the receptive field center.

2.4.5 RGC types that lack a genetic marker

In line with the idea that stratification depth of RGCs determines their function, it was shown that the stratification pattern can discriminate 22 different RGC types [252]. For 6 out of those 22 RGC types no genetic marker has been identified [231]. Moreover, a functional screen of the whole retina by calcium imaging revealed over 30 functionally distinct RGC classes of which only few have a genetic marker to specifically target them [9]. Other studies found morphological distinct subpopulations of Calbindin/Calretinin, Parvalbumin and Brn3 positive [89, 146, 131, 8]. A more recent paper combined functional calcium imaging with electron microscope morphology reconstruction and found six previously not described RGCs [10].

2.5 Visual processing and feature extraction beyond the retina

Many of the previously described RGCs have a preferred projection pattern in the brain. Often RGCs of the same population do project to multiple targets in the brain but the relevance of that divergence is still unknown [59]. In general brain regions receiving direct input from the retina are divided into image and non-image forming brain regions. Non-image forming regions such as the supra-chiasmatic nucleus (SCN) or the olivary pretectal nucleus (OPN) receive input from different subtypes of intrinsically photosensitive RGCs and were shown to control the pupillary light reflex (OPN) and the circadian clock (SCN) [90, 96, 86, 86].

Another important brain region not involved in image formation is the accessory optic system (AOS). The AOS is responsible for generating eye movements that stabilize retinal images during head and body movements, also known as the optokinetic reflex [301]. Four nuclei, the medial, and lateral terminal nuclei (MTN and LTN) and the nucleus of the optic tract and the dorsal terminal nucleus (NOT/DTN) of the AOS were found to contribute to the horizontal and vertical image slip compensation [301]. On and On-Off DSGCs provide direct input to the nuclei of the AOS. On-DSGCs are one of several rare RGC types that specifically target the AOS without projections to the SC or dLGN [59, 301]. The contribution of each subtype to the optokinetic image stabilization still requires the identification of genetic marker to label each subtype individually.

Image forming regions are the dLGN and the SC. Both regions were shown to receive input from specific RGC subpopulations that project to specific subregions. The SC receives topographically mapped information from most of the RGCs in the retina. Each neuron in the SC receives input from about 6 RGCs [35]. The most superficial part of the SC is innervated by the W3 cells which are responsible for object motion [308]. The ON-OFF and OFF upward direction selective RGCs extend their projections to deeper layers of the SC [110, 129, 130]. The center-surround alpha RGCs project only to the deeper layers of the SC [109].

In the dLGN the different cells react to specific visual features [205, 256]. Each dLGN neuron may receive input from up to 10 different RGCs. The dLGN consists of a shell and a core region. LGN Calcium imaging and electrode recordings showed that direction and orientation selective cells are found mainly in the shell region while non-directionally tuned center-surround cells localize in the core region [165, 205]. In line with the recorded direction selectivity in the shell region, DSGC preferentially project to the shell region of

the dLGN while non DSGCs prefer the deeper core LGN [130, 110, 223, 129, 109].

The aforementioned brain regions are just a few of over 40 different RGC brain targets [178]. The functions of those RGC projections remain largely unknown. However current knowledge suggests that the parallel streams of visual information each have a preference to one or sometimes more specific brain regions. The genetic identification and definition of new RGC subpopulations is essential to further dissect the RGC type specific targets in order to help understand visual processing.

Chapter 3

Publications

3.1 First publication

3.1.1 Regulation of Cerebral Cortex Folding by Controlling Neuronal Migration via FLRT Adhesion Molecules

Article

Cell

Regulation of Cerebral Cortex Folding by Controlling Neuronal Migration via FLRT Adhesion Molecules

Graphical Abstract

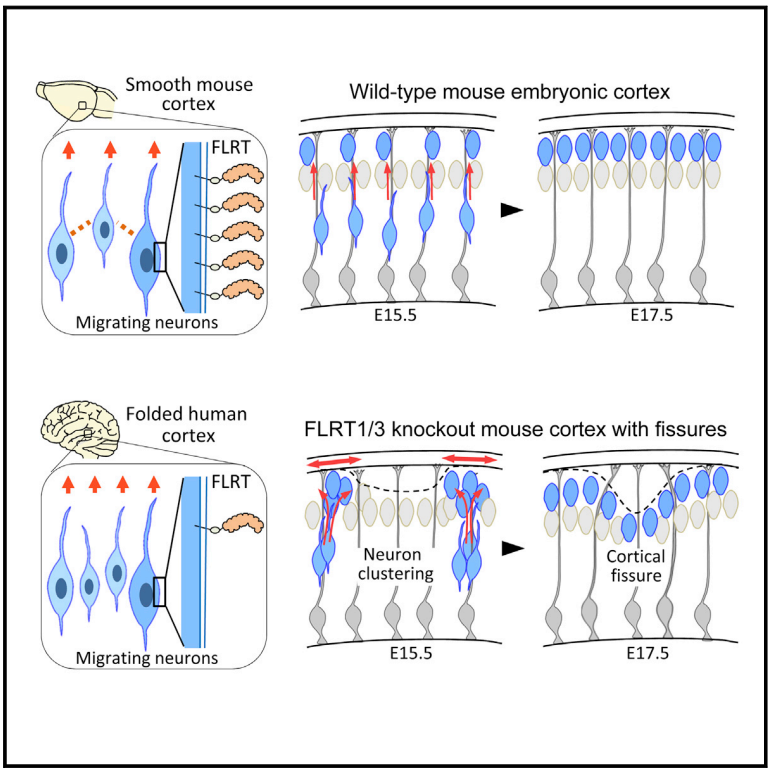

Authors

Daniel del Toro, Tobias Ruff, Erik Cederfjäll, Ana Villalba, Gönül Seyit-Bremer, Víctor Borrell, Rüdiger Klein

Correspondence

rklein@neuro.mpg.de

In Brief

Physical migration of neurons can create the folded cortical surface characteristic of primate brains.

Highlights

- *Flrt1/3* double-knockout mice develop macroscopic cortical sulci
- Cortex folding in mutant mice does not require progenitor cell amplification
- Absence of FLRT1/3 reduces intercellular adhesion and promotes immature neuron migration
- FLRT1/3 levels are low in the cortices of human embryos and future sulci of the ferret

del Toro et al., 2017, Cell *169*, 621–635
May 4, 2017
http://dx.doi.org/10.1016/j.cell.2017.04.012

CellPress

Article

Cell

Regulation of Cerebral Cortex Folding by Controlling Neuronal Migration via FLRT Adhesion Molecules

Daniel del Toro,[1,4] Tobias Ruff,[1,4] Erik Cederfjäll,[1] Ana Villalba,[2] Gönül Seyit-Bremer,[1] Víctor Borrell,[2] and Rüdiger Klein[1,3,5,*]

[1]Max Planck Institute of Neurobiology, Am Klopferspitz 18, 82152 Martinsried, Germany

[2]Instituto de Neurociencias, Consejo Superior de Investigaciones Científicas and Universidad Miguel Hernández, 03550 Sant Joan d'Alacant, Spain

[3]Munich Cluster for Systems Neurology (SyNergy), 80336 Munich, Germany

[4]These authors contributed equally

[5]Lead Contact

*Correspondence: rklein@neuro.mpg.de

http://dx.doi.org/10.1016/j.cell.2017.04.012

SUMMARY

The folding of the mammalian cerebral cortex into sulci and gyri is thought to be favored by the amplification of basal progenitor cells and their tangential migration. Here, we provide a molecular mechanism for the role of migration in this process by showing that changes in intercellular adhesion of migrating cortical neurons result in cortical folding. Mice with deletions of FLRT1 and FLRT3 adhesion molecules develop macroscopic sulci with preserved layered organization and radial glial morphology. Cortex folding in these mutants does not require progenitor cell amplification but is dependent on changes in neuron migration. Analyses and simulations suggest that sulcus formation in the absence of FLRT1/3 results from reduced intercellular adhesion, increased neuron migration, and clustering in the cortical plate. Notably, FLRT1/3 expression is low in the human cortex and in future sulcus areas of ferrets, suggesting that intercellular adhesion is a key regulator of cortical folding across species.

INTRODUCTION

The cerebral cortex is a central region in the brain that controls high-level cognitive functions (Geschwind and Rakic, 2013). During evolution, the cortex has undergone an enormous expansion that mostly accounts for the increase in brain size across mammalian species (Finlay and Darlington, 1995). Because the cerebral cortex is a laminar sheet of tissue, its expansion coincides with the formation of folds consisting of gyri and sulci. Based on cortical folding, mammals can be classified into gyrencephalic species (such as ferrets and most primates), which have folded brains, and lissencephalic species (such as mice), which have smooth-surfaced cortices.

Mechanistically, cortex folding is promoted by regional cortical growth together with tangential expansion (Borrell and Götz, 2014; Borrell and Reillo, 2012; Reillo et al., 2011). This model is based on the finding that one of the germinal zones of the cortex, the subventricular zone (SVZ), is subdivided into an inner (ISVZ) and outer (OSVZ) subventricular zone in gyrencephalic but not in lissencephalic species, (Reillo et al., 2011). The OSVZ is a proliferative region that contains transit-amplifying basal progenitors (BPs) that expands concomitant with the onset of cortical folding (Hansen et al., 2010; Lui et al., 2011). Recent observations have shown that local amplification of BPs can lead to gyrus formation in the smooth mouse cortex (Florio et al., 2015; Rash et al., 2013; Stahl et al., 2013; Wang et al., 2016), whereas a decrease of the BP pool reduces the gyrification index in the ferret (Reillo et al., 2011; Toda et al., 2016), indicating that expansion of BPs represents a key event to induce gyration of the mammalian brain. Interestingly, new findings have challenged this model regarding its predictive power on the gyration of the cortex. Recent studies have shown that increasing proliferation of BPs in the mouse SVZ per se increased the cortical thickness or surface but was not sufficient to cause gyrification (Nonaka-Kinoshita et al., 2013; Thomson et al., 2009; Wagenführ et al., 2015). Notably, the prevailing hypothesis proposes that it is the combination of BP amplification with divergent radial migration that contributes to the expansion of the cortex in radial and tangential axes and then its folding (Borrell and Reillo, 2012; Fernández et al., 2016; Lui et al., 2011; Reillo et al., 2011). According to this model, migrating neurons do not follow strictly parallel pathways but, instead, follow divergent trajectories, dispersing in the lateral axis, which leads to tangential cortical expansion and folding. Failure in neuronal migration causes severe abnormalities in cortical folding that result in human lissencephaly (Moon and Wynshaw-Boris, 2013). Moreover, recent findings directly support the radial divergence hypothesis by showing that, in the ferret cortex, migrating neurons do not follow strict radial pathways but, instead, follow more tortuous migration routes concomitant with the start of cortical folding (Gertz and Kriegstein, 2015). However, molecular mechanisms that affect neuronal migration and modulate this trajectory divergence, resulting in cortex folding, have not been found. Moreover, no mouse gene has yet been identified whose genomic or global modification (rather than acute and local) favors folding of the smooth mouse cortex.

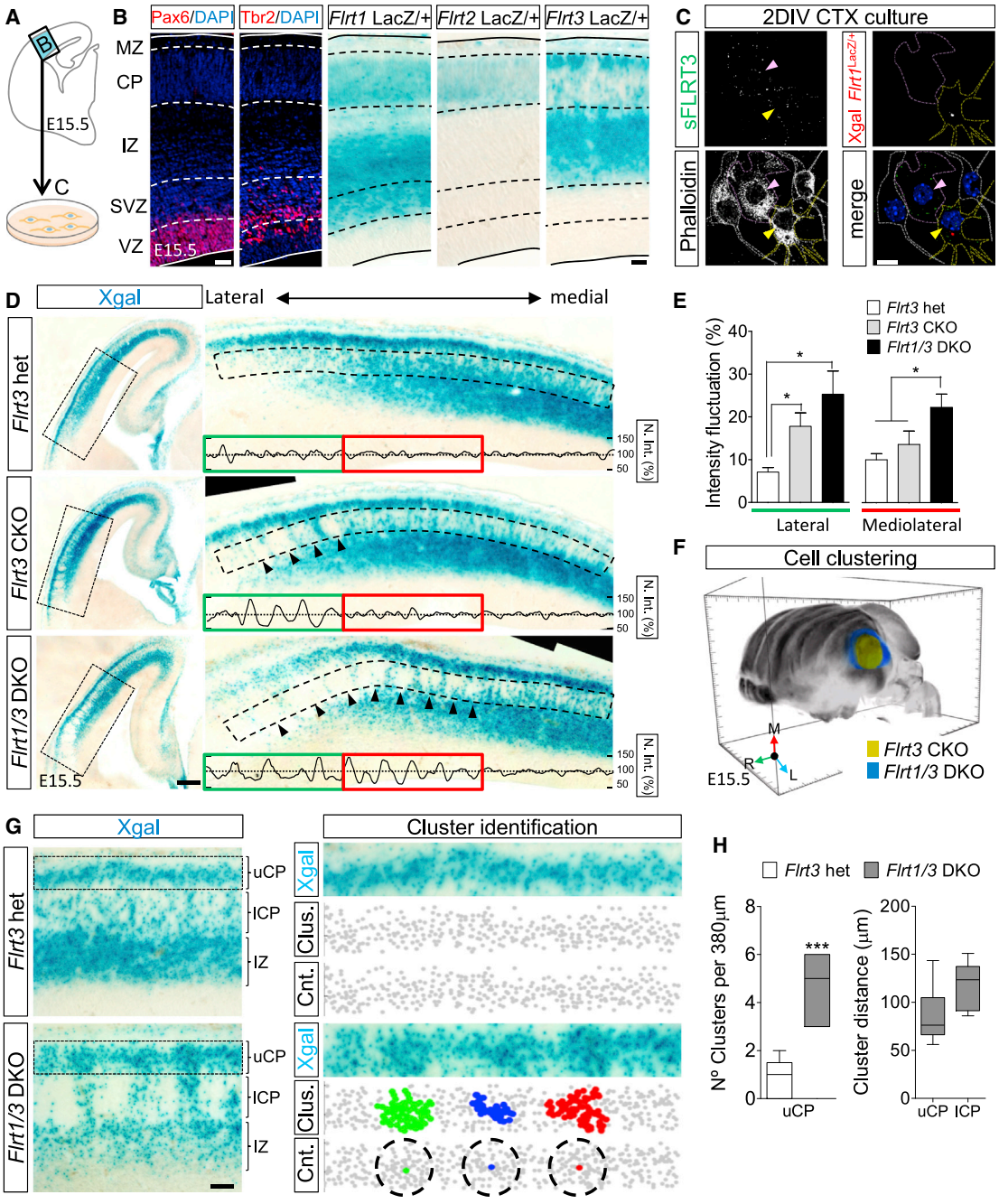

Figure 1. FLRT1 and FLRT3 Control Lateral Migration of Cortical Neurons

(A) Cortical region shown in (B) and source of cortical neurons shown in (C).

(B) X-gal staining of FLRT1-3 expression on coronal sections of E15.5 cortex from *Flrt1-3*$^{lacZ/lx}$ reporter lines. Cortical layers were identified by DAPI and immunostained for Pax6 and Tbr2.

(C) *Flrt1*$^{lacZ/+}$ cortical cultures at E15.5 (2 days in vitro), immunostained for FLRT3 (surface staining, green in merge), X-gal (for labeling Flrt1+ cells, red in merge), and phalloidin. Yellow arrowheads/outlines indicate FLRT1/3 double-positive neurons. Magenta arrowheads/outlines show FLRT3 single-positive neurons. White outlines show FLRT3-negative neurons.

(D) X-gal staining of coronal sections from E15.5 *Flrt3* heterozygous (*Flrt3*$^{lox/lacZ}$), *Flrt3* CKO and *Flrt1/3* DKO embryos. Areas in dashed rectangles are shown with higher magnification on the right. Normalized intensity plots are shown, obtained from the areas delineated with a dashed rectangle. Arrowheads indicate regions containing cell clusters, and green boxes highlight lateral and red boxes mediolateral portions of the cortex at intermediate-caudal levels.

(E) Quantification of the intensity fluctuations in those portions of the neocortex; n = 3–5 mice/group, 2 sections/mouse; *p < 0.05, one-way ANOVA test with Tukey's post hoc analysis.

(legend continued on next page)

Previously, we have established that genetic ablation in mice of FLRT3, a member of the fibronectin leucine rich-repeat transmembrane protein (FLRT) family of cell adhesion molecules, leads to altered distribution of pyramidal neurons during cortical development, forming a repeated pattern of clusters along the tangential axis (Seiradake et al., 2014). FLRTs have the unique property of acting as adhesion molecules by homophilic and heterophilic binding to Latrophilin proteins and as repellents by binding to Unc5/Netrin receptors (Jackson et al., 2015, 2016; Yamagishi et al., 2011). Here we report that genetic ablation of FLRT1 and FLRT3 leads to the development of macroscopic cortical sulci during embryogenesis. Mechanistically, this process happens independent of progenitor cell amplification. Instead, we found that cortical neurons display reduced intercellular adhesion, faster neuronal migration, and clustering along the tangential axis, thereby leading to sulcus formation in the normally smooth mouse neocortex. Our results suggest that intercellular adhesion of migrating cortical neurons is a key factor underpinning folding of the cerebral cortex.

RESULTS

FLRT1 and FLRT3 Control the Lateral Dispersion of Pyramidal Neurons

Expression analysis of FLRTs in the developing cortex from embryonic day 13.5 (E13.5) to E17.5 (Figures 1A and 1B and Figures S1A–S1C and S1F) revealed a partial overlap between FLRT1 and FLRT3 in both the intermediate zone (IZ) and cortical plate (CP), whereas FLRT2 was confined to the CP. In cultures of dissociated cortical neurons from E15.5 embryos, approximately 30% were FLRT3-positive, and, among those, 35% co-expressed FLRT1 (Figure 1C). This finding was consistent with a molecular identity analysis from the E15.5 mouse cortex that also revealed strong enrichment of both FLRT1 and FLRT3 in migrating upper cortical neurons among other cell types (Figures S1D and S1G). To investigate whether FLRT1 plays a role in pyramidal neuron migration, possibly in a functionally redundant fashion with FLRT3, we generated double knockout mice lacking FLRT3 in developing neurons and progenitors and FLRT1 in all cells (*Flrt1*$^{-/-}$;*Flrt3*$^{lox/lacZ}$;*Nestin-Cre* mice; in short, *Flrt1/3* double knockout [DKO]) and compared them to the respective single mutants (*Flrt3*$^{lox/lacZ}$;*Nestin-Cre*; in short, *Flrt3* conditional knockout [CKO], and *Flrt1* knockout [KO] mice). In agreement with our previous work (Seiradake et al., 2014), we found that FLRT3-deficient (β-galactosidase [β-gal]+) neurons in *Flrt3* CKOs showed abnormal cell clustering in the lateral portion of the neocortex within the lower CP (Figures 1D and 1E; Figure S1I). Interestingly, this cell clustering effect was enhanced in *Flrt1/3* DKO compared with *Flrt3* CKO mice, extending into medial and caudal regions of the cortex (Figures 1D–1F; Figure S1J; data not shown). To analyze the distribution of β-gal+ neurons, we calculated the normalized intensity profile of the X-gal staining in the lower half of the cortical plate (dashed region, Figure 1D), which revealed extended fluctuations in the density of *Flrt1/3* DKO neurons compared with *Flrt3* CKO and *Flrt3* heterozygous neurons (Figure 1E). To test whether the repeated pattern of cell clusters extended to the upper CP, we performed a distance-based clustering analysis, using as input the coordinates of X-gal-positive neurons populating the upper CP. We observed clustering of neurons in the upper CP of *Flrt1/3* DKO following a pattern of approximately 75- to 120-μm intervals, in line with the pattern present in the lower CP (Figures 1G and 1H). This suggests that the altered localization and clustering of cells in the *Flrt1/3* DKO extended into the upper CP, where cells normally spread laterally to form cortical layers. Taken together, these results indicate partially redundant roles of FLRT1 and FLRT3 in controlling the tangential distribution of pyramidal neurons during cortical development.

Flrt1/3 CKO Mice Develop Cortical Sulci

Upon further inspection of *Flrt1/3* DKO embryos, we found that, in 33% of the cases, the clustering of upper CP neurons at E15.5 correlated with the formation of an incipient sulcus in the otherwise smooth mouse neocortex (Figure 2A; Figures S2A and S2B). These cortical sulci developed on the lateral side of the cortex from intermediate to caudal levels where the repeated pattern of neuronal clusters was present in mutant embryos (Figures 2B and 2C), suggesting that these processes were causally linked. At later stages of cortical development (E17.5), cortical sulci were found in *Flrt1/3* DKO embryos, with a similar penetrance of 31% (Figure S2C). They showed considerable phenotypic variability between embryos, ranging from shallow to deep sulci that were easily visible in intact brains after removal of the meninges (Figures 2D and 2E).

Because cortical folding is not a random process but, rather, forms stereotyped patterns in gyrencephalic species (Borrell and Reillo, 2012), we determined the spatial distribution of sulci at E17.5. We used a kernel density estimator based on the location of sulci in coronal sections and plotted it onto a 3D mouse brain template. This analysis revealed that the left hemisphere had a higher probability of developing sulci and that they were mostly located between the perirhinal and postrhinal cortices of the mouse, close to the rhinal fissure (Beaudin et al., 2013; Figure 2F; Movie S1). In contrast, the right hemisphere developed sulci in rostro-medial cortical regions where clusters were not visible, suggesting that other mechanisms might also participate

(F) 3D mouse brain (template from the Allen Mouse Brain Atlas) with cortical areas displaying cell clustering in *Flrt3* CKO (green area) and *Flrt1/3* DKO (blue area) at E15.5.

(G) X-gal staining of coronal sections from E15.5 *Flrt3* heterozygous and *Flrt1/3* DKO embryos. Cell clusters in the upper CP were identified based on the position of individual X-gal+ neurons (areas in dashed rectangles are shown with higher magnification on the right) using a distance-based clustering method (a cluster was defined as a minimum of 25 cells spaced less than 20 μm). Cluster identification is as follows. Neuron clusters in *Flrt1/3* DKO embryos are marked with different colors (red, green, and blue; "Clus"), and centroids of each cluster (cnt) are shown in the same color. Neurons that are not clustered are colored in gray.

(H) Quantification of the number of clusters and the distance between them from the data shown in (G); n = 3–5 mice/group; ***$p < 0.001$, unpaired Student's t test. Whiskers in the box plot represent minimum and maximum. The data are presented as mean ± SEM. Scale bars represent 150 μm (B), 14 μm (C), 300 μm (D), and 50 μm (G).

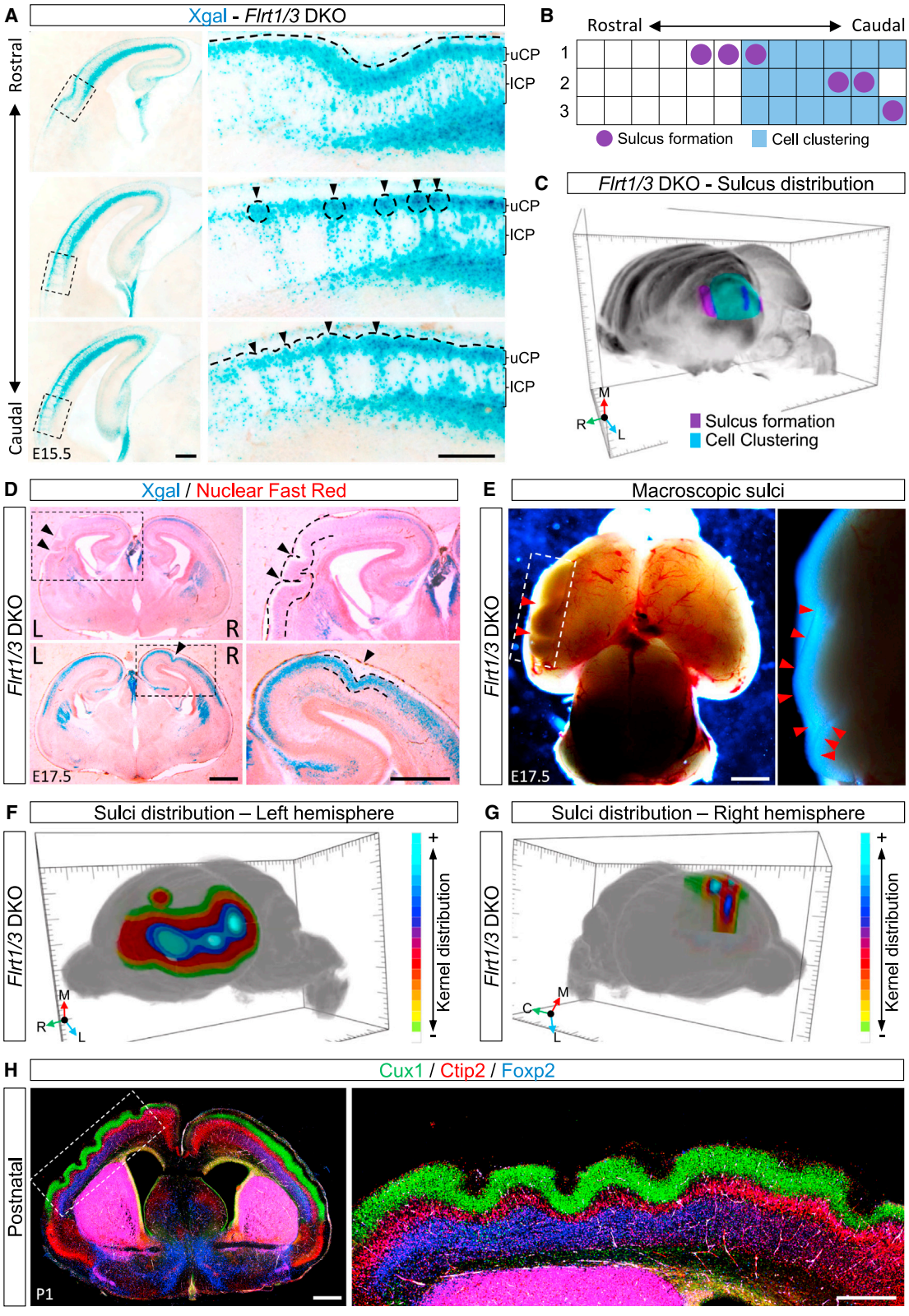

(legend on next page)

in this process (Figure 2G; Movie S1). The variability in sulcus location may have to do with the absence of gene expression microdomains. These structures play an important role in the generation of gyri/sulci at specific locations and are present in the developing cortex of gyrencephalic species such as the ferret but not in the lissencephalic mouse (de Juan Romero et al., 2015). Sulci were also found in postnatal stages of *Flrt1/3* DKO mice (penetrance, 24%) (Figure 2H; Figures S2D and S2E), indicating that these were not transient embryonic structures. The examination of single mutant brains revealed that *Flrt1* KO, but not *Flrt2* or *Flrt3* CKO, brains showed sulcus formation, albeit with lower penetrance (12%–16%; Figures S2C and S2D). In addition, *Flrt2/3* DKO brains rarely showed sulcus formation (1 in 13), suggesting that *Flrt1* plays a major role in the phenotype (Figures S2C and S2F). The morphologies of the sulci in *Flrt1* KO brains were comparable with those observed in *Flrt1/3* DKO brains (Figure S2G), suggesting that the underlying mechanisms were similar. These results indicate that FLRT1 and FLRT3 have partially redundant functions in the formation of a smooth neocortex.

Cortical Sulci Develop Independent of Cell Proliferation

As a first step toward understanding the mechanism involved in sulcus formation in *Flrt1/3* DKO brains, we analyzed cell proliferation in brain sections at different stages of cortical development by quantifying the numbers of apical (Pax6+) and basal (Tbr2+) progenitors (Englund et al., 2005). We also stained for the phosphorylated forms of vimentin (Pvim) and histone H3 (PH3) that label dividing radial glial (RG) and mitotic cells, respectively (Pilz et al., 2013). We did not find significant increases in mitotic and dividing RG cells in mutant embryos at different developmental stages and in different rostro-caudal regions, except for a small increase in intermediate cortical regions at E13.5 (Figures 3A–3C; Figures S3A–S3L). Moreover, the proportion of mitotic cells in basal versus apical germinal layers was unchanged in *Flrt1/3* mutant brains (Figure 3D; Figures S3D, S3H, and S3L), and the numbers of dividing basal RG cells were less than 5% in all experimental groups (data not shown). Quantification of total cell nuclei (stained with DAPI), Pax6+ and Tbr2+ progenitor cells, and short pulses of BrdU did not reveal significant increases in *Flrt1/3* mutant brains (Figure 3C; Figures S3C, S3G, S3K, and S3M–S3Q), suggesting that cortical sulci develop independent of changes in cell proliferation.

Next we explored alternative mechanisms underlying sulcus formation, such as alterations in the RG fiber scaffold, basement membrane formation, and Cajal-Retzius (CR) cell development. Tracing of individual RG fibers in *Flrt1/3* DKOs based on brain lipid-binding protein (BLBP) staining showed that RG processes located in sulcus areas reached the marginal zone (MZ), similar to control regions, even when sulci were very deep (Figure 3E; Figure S4A). The overall densities and lengths of RG processes in sulcus areas did not differ from adjacent regions (Figure S4B). The curvature index of RG processes was significantly higher in sulcus areas because of the convergence of fibers at sulcal pits (Figures 3E and 3F), similar to those reported in classic descriptions of gyrencephalic species such as ferrets and monkeys (Rakic, 1972; Smart and McSherry, 1986). Remarkably, the basal membrane was intact in seven of eight mutant brains (Figures S4C and S4D), suggesting that these sulci were not the result of neuronal ectopias as observed in cobblestone lissencephaly (Devisme et al., 2012). Because CR cells originating from the cortical hem (CH) express both FLRT1 and FLRT3 (Figures S4E–S4G), we also explored whether loss of FLRT1/3 affected CH-derived CR cell migration. We found that the distribution and density of CR cells in the MZ of sulcus areas in mutant brains appeared normal (Figure 3E), even in dramatic cases where the MZ followed the depth of the sulcus (Figure S4A). These results suggest that cortical sulci in *Flrt1/3* DKOs are not the result of alterations in RG scaffold, basal membrane formation, or CR cell development.

FLRT1/3-Deficient Pyramidal Neurons Reach Upper Cortical Layers Faster

Given the lack of strong alterations in progenitors and glial cells, we next asked whether sulcus formation correlated with changes in the migration and distribution of pyramidal neurons. Cortical layering seemed well preserved in sulcus areas of *Flrt1/3* DKO compared with controls (Figure 3G), but layer thickness was reduced, particularly in the lower CP (Figures S4H and S4I), similar to those reported in gyrencephalic species such as the ferret (Smart and McSherry, 1986). Notably, the proportion of Cux1+ neurons (Nieto et al., 2004) in the upper versus lower CP was significantly higher in sulci with respect to adjacent areas (Figures 3H and 3I). Similar results were obtained after bromodeoxyuridine (BrdU) pulse labeling of newborn pyramidal neurons at E14.5 and analyzing their distribution in the CP at E17.5

Figure 2. *Flrt1/3* CKO Mice Develop Cortical Sulci

(A) X-gal-stained serial coronal sections from the cortex of an E15.5 *Flrt1/3* DKO embryo. Areas in dashed rectangles are shown with higher magnification on the right. Dashed circles and arrowheads indicate prominent clustering of neurons in the upper CP, and horizontal dashed lines highlight incipient sulcus formation (top) and a wavy surface of the upper CP (bottom).

(B) Twelve sections, rostral to caudal, of three *Flrt1/3* DKO brains (rows 1–3) at E15.5 were analyzed for the presence of sulci (circles) or cell clustering (blue squares).

(C) 3D representation of the data shown in (B).

(D) Coronal sections from two E17.5 *Flrt1/3* DKO brains with different degrees of sulcus formation in the cortical plate (arrowheads). Sections were stained with X-gal and nuclear fast red. Areas in dashed rectangles are shown with higher magnification on the right.

(E) Macroscopic sulci in an E17.5 *Flrt1/3* DKO embryo. The area in the dashed rectangle is shown with higher magnification on the right, and sulci are indicated by arrowheads.

(F and G) Sulcus distribution in the left (F) and right (G) hemispheres of all E17.5 *Flrt1/3* DKO embryos. The color bar indicates a higher (blue colors) or lower (green-white) density of sulci.

(H) P1 FLRT1 KO brain section stained with Cux1, Ctip2, and Foxp2. Areas in dashed rectangles are shown with higher magnification on the right.

Scale bars represent 300 μm (A), 500 μm (D), 1 mm (E), and 2.4 mm and 0.4 mm (H).

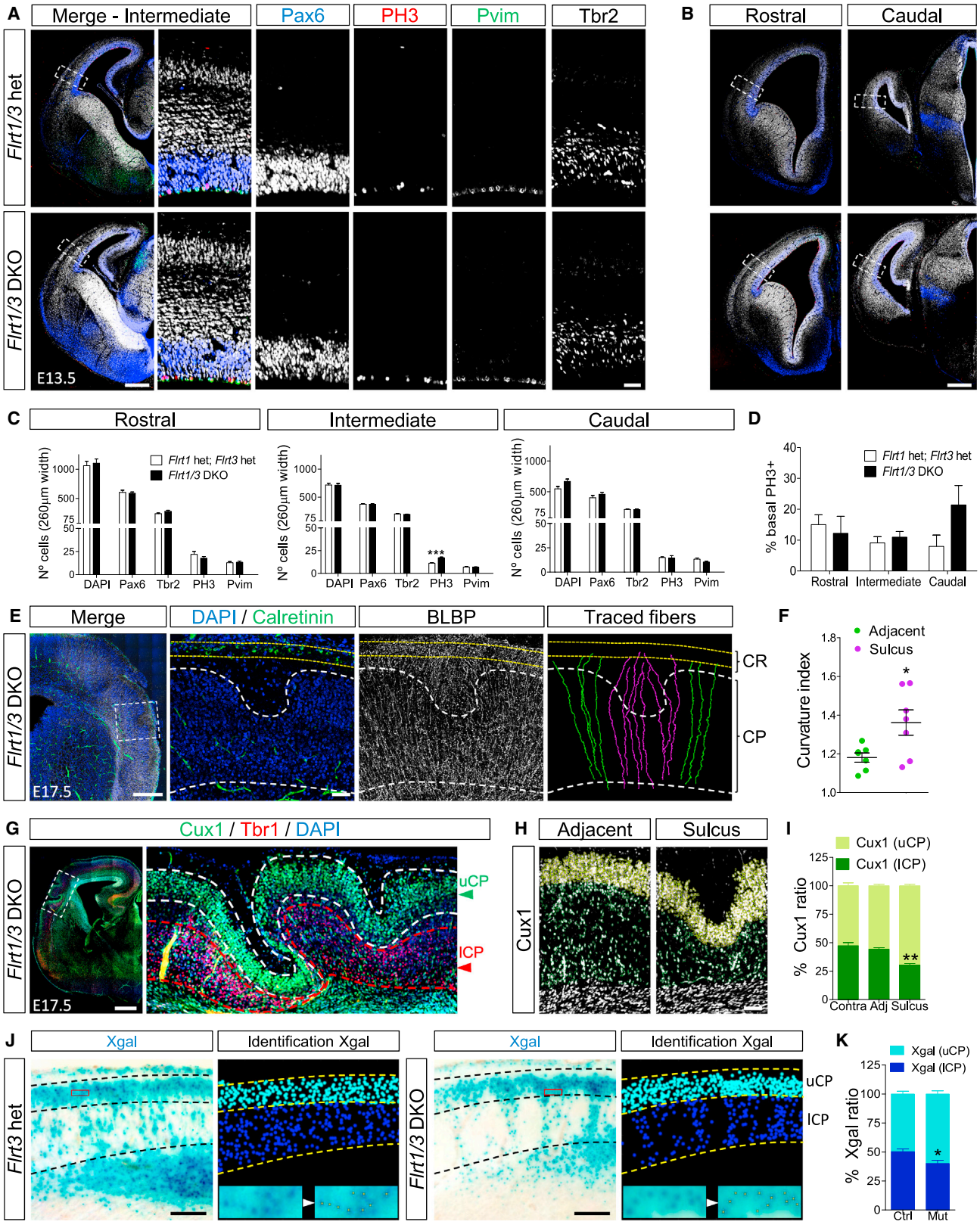

(legend on next page)

(Figures S4J and S4K). These results suggested that either FLRT1/3-deficient pyramidal neurons migrated faster through the cortical plate, thereby causing sulcification, or that sulcification provided a shorter migration distance compared with non-sulcus areas, resulting in a higher proportion of cells in the upper CP. Given that only a portion of migrating neurons expressed FLRT proteins, we next analyzed the distribution of FLRT3-deficient (β-gal+) neurons and compared non-sulcus areas of *Flrt1/3* DKOs with controls. We found that the proportion of cells in the upper CP was higher in *Flrt1/3* DKOs (Figures 3J and 3K). These results suggest that FLRT1/3-deficient pyramidal neurons migrate faster through the cortical plate than FLRT1/3-expressing neurons.

Lack of FLRT1/3 Increases Migration Speed

To obtain direct evidence for changes in the migration speed of cortical neurons, we performed live imaging of embryonic cortices ex vivo. Control and *Flrt1/3* DKO brains were sliced and imaged 48 hr after electroporation with pCAG-CRE and the Cre reporter pCALNL-DsRed to visualize migrating cells. This approach (Cre electroporation into *Flrt1/3* DKO embryos) was chosen over Cre electroporation into *Flrt1*$^{-/-}$*Flrt3*$^{lox/lox}$ brains because the latter approach did not reliably induce sulci compared with control brains, presumably because of the low abundance of electroporated cells (data not shown). A caveat of the former approach was that only a subset of Cre reporter-positive cells expressed FLRT proteins because these brains also contain many non-FLRT-expressing cells (Figure 4A; Figures S5A and S5B). Hence, a large proportion of Cre reporter-positive cells in *Flrt1/3* DKO brains were not directly affected by the *Flrt1/3* mutations, thereby potentially masking subtle defects. Individual Cre reporter-positive neurons entering the CP from the IZ were tracked and processed using a custom Python algorithm that allowed us to quantify migration parameters and to color-code portions of each track based on migration speed (Figure 4B). Overall, Cre+ cells in *Flrt1/3* DKO neurons displayed parallel and straight paths (Figure S5C), except in rare cases when migrating through a forming sulcus, where they displayed convergent paths (Figure S5D; Movie S2). Similar to controls, Cre+ neurons exhibited the stereotypic RG-based locomotor pattern with high speeds (>32 μm/h) in the middle of the CP and decreasing speeds toward the upper CP (Kawauchi, 2015; Tabata and Nagata, 2016; Figure 4C). Given that Cre+ cells in *Flrt1/3* DKO neurons showed trends toward higher maximum speed and acceleration, we analyzed their speed profiles. These results revealed an increased proportion of high-speed segments (>58 μm/h) in *Flrt1/3* DKO compared with control brains (Figure 4D; Figures S4E and S4F). Plotting the relative frequencies of the maximum migration speeds revealed that the fraction of cells reaching >70 μm/h was significantly increased in *Flrt1/3* DKO brains compared with controls (19% versus 12%) (Figure 4E). These results suggest that *Flrt1/3* mutant neurons reached higher speeds more often than control neurons.

To assess the morphologies of individual *Flrt1/3* mutant neurons, we sparsely labeled *Flrt1/3* DKO neurons in an otherwise control background by introducing Cre and a Cre reporter into *Flrt1*$^{-/-}$*Flrt3*$^{lox/lox}$ brains using the Supernova system, which makes use of a leaky Tet promoter driving Cre expression in few cells (Mizuno et al., 2014; Figure 4F). The general complexity of mutant neurons populating the lower CP appeared similar to those observed in control sections, as assessed by Sholl analysis (data not shown). When categorizing the neurons according to increasing maturity into multipolar, unipolar and bipolar neurons, and "bipolar branched" morphologies (Figure 4F), we observed a significant shift toward immature morphologies in the upper CP of Cre-induced *Flrt1/3* mutant neurons compared with controls (Figure 4G). Thus, ablation of FLRT1/3 increases the abundance of immature neurons in the upper cortical plate.

Modeling Clustering and Speed Profiles of *Flrt1/3* DKO Neurons

So far our analysis suggested a model in which increased migration speeds of *Flrt1/3* mutant neurons and/or the formation of cell clusters in the CP could be causal to sulcus formation (Figure 5A). To test this hypothesis, we performed data-driven computational modeling of neurons migrating through the CP. We took the following points into consideration. Both FLRT3 gain- and loss-of-function experiments in vivo revealed a repeated pattern

Figure 3. Pyramidal Neuron Distribution, but Not Cell Proliferation, Is Changed in Sulcus Areas

(A and B) E13.5 cortices from intermediate (A) and rostral, caudal regions (B) of control and Flrt1/3 DKO embryos were labeled for the neuronal progenitors Pax6 (blue) and Tbr2 (white), mitotic cells (PH3, red), and dividing RG cells (Pvim, green). Areas in dashed rectangles in (A) are shown with higher magnification on the right.

(C) Quantification of the data shown in (A) and (B) (n = 3–4 mice/group). ***p < 0.001, unpaired Student's t test.

(D) Proportion of basal mitotic cells (PH3) (n = 3–4 mice/group; no significant changes between groups, unpaired Student's t test).

(E) *Flrt1/3* DKO section immunostained for BLBP (white), calretinin (green), and DAPI (blue). The area in the dashed rectangle is shown with higher magnification on the right. White dashed lines delineate sulci, and yellow dashed lines show the margins of the MZ where calretinin+ CR cells are located. Single traced RG processes are colored in magenta (in the sulcus region) or green (adjacent areas).

(F) Quantification of the curvature index of traced fibers shown in (E). n = 7 adjacent fibers, n = 8 sulcus fibers. *p < 0.05, unpaired Student's t test .

(G) E17.5 *Flrt1/3* DKO cortex immunostained for upper (Cux1, green) and deeper-layer (Tbr1, red) neurons and DAPI (blue).

(H) Sulcus and adjacent region from an E17.5 *Flrt1/3* DKO section immunostained with Cux1 (white). Cux1+ cells in the upper CP are highlighted in light green, and Cux1+ cells still migrating in the lower CP are highlighted in dark green.

(I) Quantification of the data shown in (H) (n = 12 sections from a total of 5 mutant brains). **p < 0.01, one-way ANOVA test with Tukey's post hoc analysis.

(J) X-gal staining of coronal sections from E15.5 *Flrt3* heterozygous and *Flrt1/3* DKO embryos. The CP was subdivided into upper and lower CP (Figure S1I). The coordinates of X-gal precipitates (the red rectangle is shown with higher magnification on the right) were plotted as circles colored cyan (upper CP) and blue (lower CP).

(K) Quantification of the data shown in (J).

ICP, lower cortical plate (lCP). The data are represented as mean ± SEM. Scale bars represent 400 and 150 μm (A), 400 μm (B), 600 and 100 μm (E), 500 μm (G), 90 μm (H), and 120 μm (J).

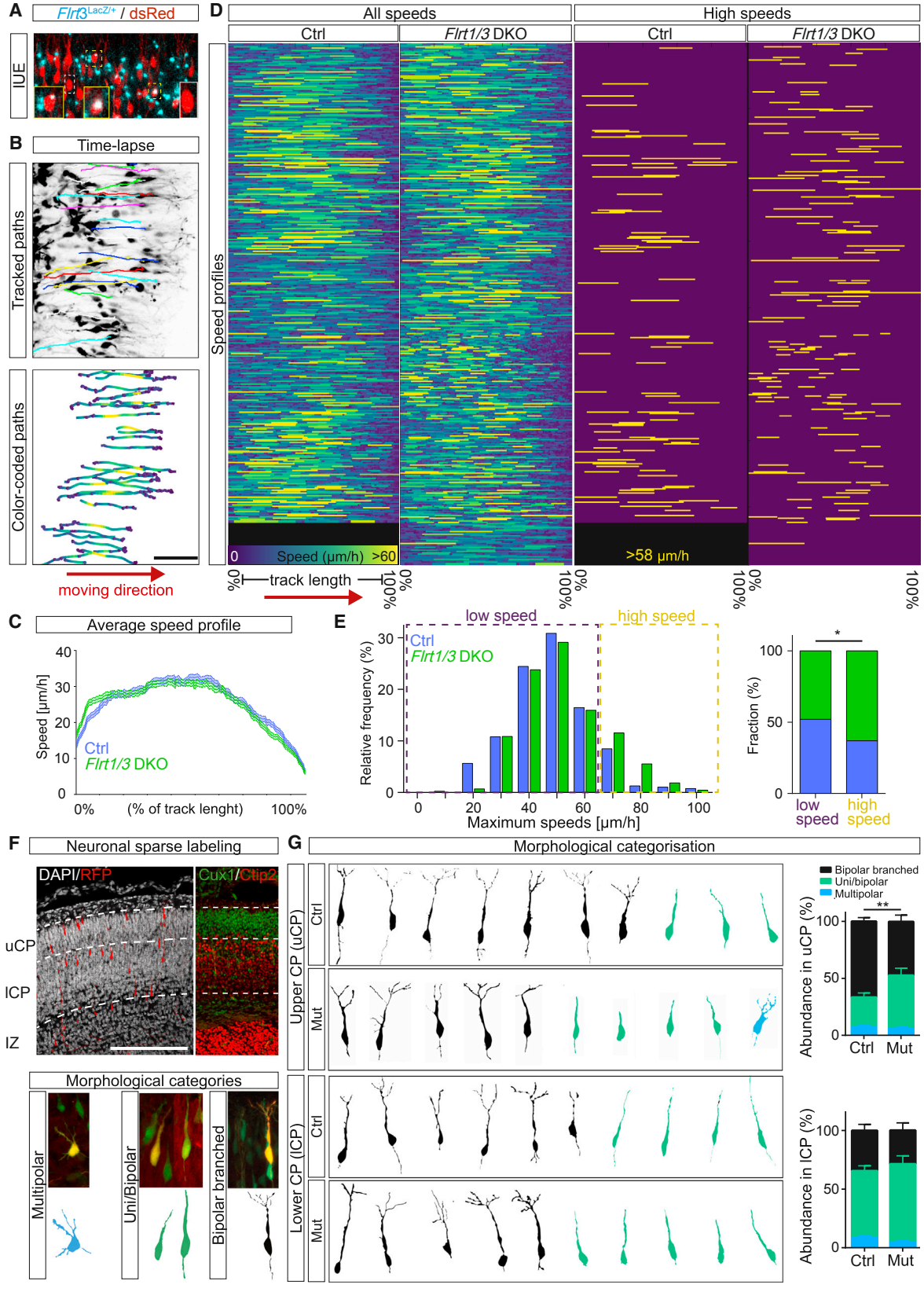

(legend on next page)

of cell clusters (Seiradake et al., 2014; Figure 1), which can be modeled as sine equations (Figure 5B). FLRTs act as cell adhesion molecules. This was shown for FLRT3 overexpression on cell clustering in vivo (Seiradake et al., 2014) and for FLRT-mediated cell aggregation in vitro (Figures S6A and S6B). The effects of *Flrt1/3* ablation on cell clustering in vivo are likely non-cell autonomous and may be the result of repulsive interactions with surrounding cells. Based on these considerations, we established two rules for the computational model: the sine equation modeled from gain-of-function experiments reflected the attraction forces of FLRT1/3+ neurons, and the sine equation from loss-of-function experiments represented the repulsion forces that FLRT1/3+ neurons are exposed to from surrounding cells. We distributed particles representing FLRT1/3-positive and -negative cells in a 2D grid, keeping equal distances and homogeneous distributions as observed in *Flrt1/3* heterozygous control sections. Particles representing FLRT1/3+ neurons showed attraction between them (first rule), whereas surrounding particles elicited repulsion toward them (second rule) (Figure 5C). To analyze the behavior of the particles during movement, particles were set to move along the z axis, and both speed and attraction-repulsion forces were random within a small range (ε) to mimic the fluctuations present in biological systems (Wilkinson, 2009). The attraction force was modulated by changing its amplitude and phase with respect to the repulsive force, which was kept constant under all conditions to reflect FLRT1/3 gain- and loss-of-function experiments (Figure S6C). Kernel distribution and minimum neighbor analysis of particles representing FLRT1/3+ neurons showed homogeneous distribution of particles when attraction and repulsion forces were balanced (Figures 5D and 5E). In contrast, particle clustering was observed when the attraction between particles was either high or low (Figures 5D and 5E; Figure S6D), which was consistent with the formation of neuronal clusters when FLRT1/3 were overexpressed or downregulated in vivo. Interestingly, the distribution of particles in the z axis was also influenced by attraction and repulsion forces. Under both high and balanced attraction conditions, the particles formed a smooth surface after moving along the z axis. Conversely, the low attraction paradigm resulted in a wavy surface because of an increased proportion of particles moving with high speed, reminiscent of the live imaging experiments with *Flrt1/3* DKO sections (Figures 5F and 5G). Taken together, the low attraction paradigm of the computational model matched the experimental observations with *Flrt1/3* DKO mice rather well by generating particle clusters, increasing particle migration speed, and producing a wavy surface area.

FLRT Expression in Gyrencephalic Species

Given that FLRT1/3 ablation promoted sulcus formation in the normally smooth mouse neocortex, we set out to analyze endogenous FLRT1/3 expression in gyrencephalic species such as ferret and human. We hypothesized that FLRT1/3 expression levels may be generally low in gyrencephalic species to permit folding or relatively less abundant in sulcus than in gyrus areas. The ferret cortex is nearly lissencephalic at birth and undergoes complex and stereotyped postnatal folding (Reillo et al., 2011; Smart and McSherry, 1986). We analyzed ferret FLRT1/3 expression prior to morphological distinction of the prospective splenial gyrus and its adjacent lateral sulcus because previous studies have successfully identified genes involved in cortical folding in these regions (de Juan Romero et al., 2015; Figure S6E). In situ hybridization (ISH) for Flrt1/3 revealed that both genes were mainly expressed in the CP, ISVZ, and OSVZ and, to a lesser extent, in the IZ at post-natal day 0 (P0) and P6 (Figures 6A and 6B; Figures S6F and S6G). Quantification of the expression levels revealed that both FLRT1 and FLRT3 were significantly less abundant in the cortical area that will form the lateral sulcus compared with the splenial gyrus (Figures 6C and 6D).

To study FLRT expression in human embryos, we used RNA sequencing (RNA-seq) data from three different sources. We first compared mouse FLRT1 and FLRT3 mRNA expression levels in E14 neocortex (subdivided into medial and lateral portions; (Wang et al., 2016) with RNA-seq data from human embryonic cortex at 12–19 post –conception weeks (pcw) (http://www.brain-map.org) normalized to the housekeeping gene GAPDH (Figures S6H and S6I). There were consistently higher levels in mouse cortex compared with a number of different cortical regions in human samples. Second, we analyzed mouse and human FLRT1 and FLRT3 normalized to GAPDH in different cortical layers (Fietz et al., 2012; Figures 6E and 6G). The abundance of mouse FLRT1 and FLRT3 mRNAs in the SVZ region ranged between 24%–49% of GAPDH, whereas the levels of human FLRT1 and FLRT3 ranged between 1%–3% of GAPDH (the human ISVZ

Figure 4. Faster Speed Profiles of *Flrt1/3* DKO Neurons

(A) *Flrt1/3* DKO embryos were electroporated at E13.5 with pCAG-Cre and the pCALNL-DsRed reporter plasmid (red staining; Figure S5). Yellow and white boxes indicate double dsRed/Flrt3+ and single dsRed+ cells, respectively.

(B) Time-lapse analysis of electroporated neurons migrating into the cortical plate in cultured E15.5 cerebral cortex slices. Migrating neurons were tracked (colored lines, top) and color-coded based on speeds in individual segments (bottom).

(C) Average speed profiles normalized to CP length of *Flrt1/3* DKO and littermate control embryos (from >400 tracked neurons).

(D) Color-coded speed profiles of >400 tracked neurons in controls and *Flrt1/3* DKO embryos normalized to total migration distance. Speeds higher than 58 μm/h are highlighted in yellow on the right.

(E) Maximum speed frequency distribution of all tracked neurons in controls and *Flrt1/3* DKO embryos. Dashed rectangles indicate low (blue) and high (yellow) speed profiles, and their fraction is shown on the right. *$p < 0.05$, chi-square contingency analysis.

(F) Sparse cell labeling via electroporation at E13.5 of the Supernova vector system into either *Flrt1−/−;Flrt3lx/lx* (mutant) or *Flrt1+/−;Flrt3lx/+* (control) littermates. At E16.5, Cre+ neurons were imaged and categorized according to their degree of maturity into multipolar, uni/bipolar, or bipolar branched phenotypes (example images are shown). The upper third portion of the CP was designated as upper CP based on the staining of Cux1 (top, green) and Ctip2 (bottom, red) markers.

(G) Abundance of each category of neurons in the lower and upper CP of mutant and control brains (representative images are shown; >150 neurons/group, *$p < 0.05$, chi-square contingency analysis).

IUE, in utero electroporation. The data bars are represented as mean ± SEM. Scale bars represent 50 μm (B) and 200 μm (F).

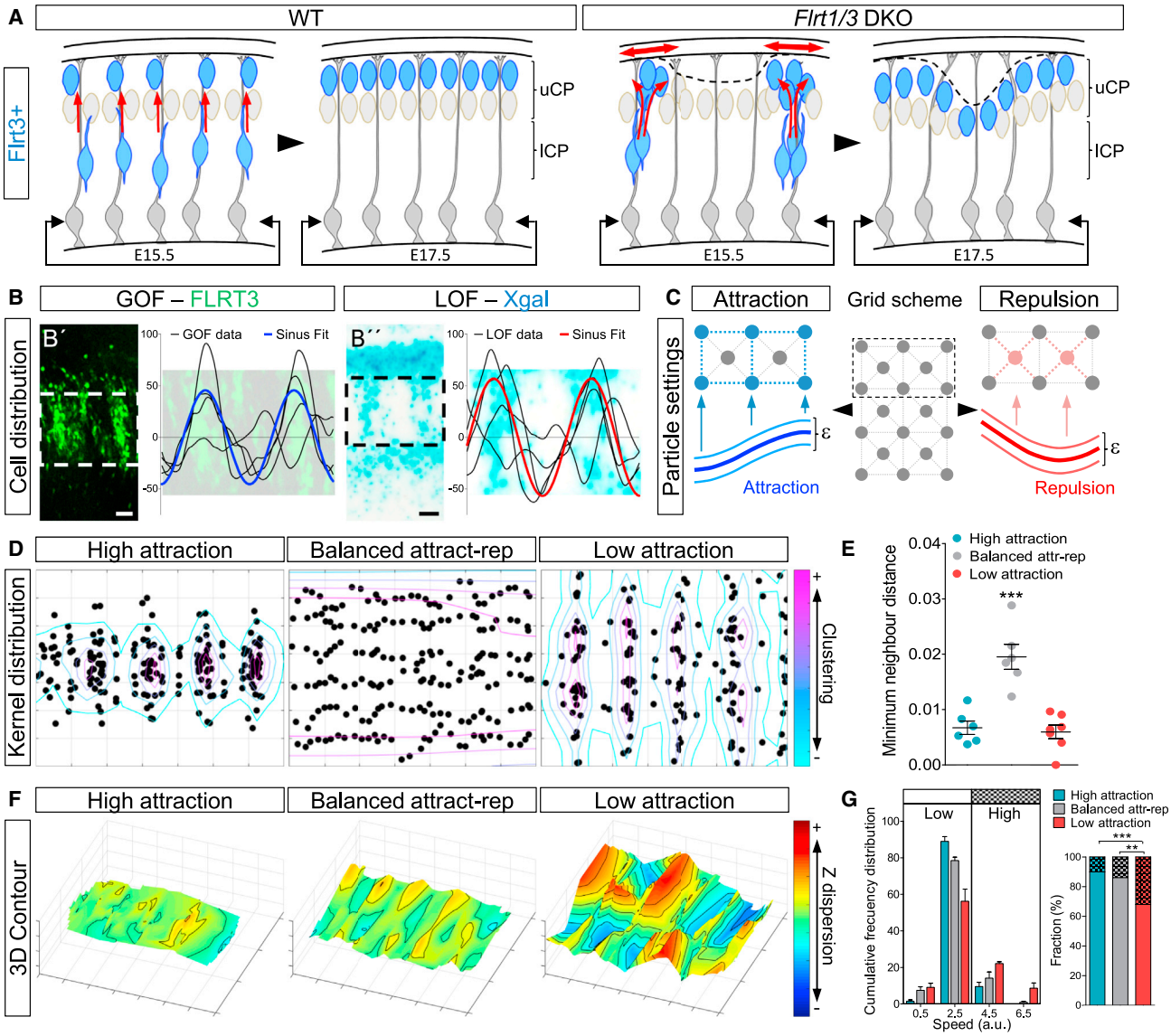

Figure 5. Computer Modeling Matches *Flrt1/3* DKO Experimental Observations

(A) Hypothetical model of sulcus formation in *Flrt1/3* DKO brains. In the wild-type (WT), Flrt1/3+ neurons show homogeneous distribution while migrating through the CP at E15.5 and form a uniform layer in the upper CP at E17.5. Loss of FLRT1/3 induces cell clustering in the lower and upper CP, creating imbalanced tension forces, and loss of adhesion may increase tissue elasticity, ultimately leading to sulcus formation.

(B) FLRT1/3 overexpression (GOF, B') or ablation (LOF, B'') alters the attraction-repulsion balance, resulting in the formation of neuronal cell clusters, which can be modeled as sinus equations. The graphs depict experimental data (black) and sinus fit (colored). The scale bar represents 40 μm.

(C) Scheme illustrating how particles representing FLRT1/3-positive (blue) and -negative neurons (red) are arranged. Blue particles show attraction between them. Red particles repel blue particles. Both attraction and repulsion forces are based on the sinus equation modeled (B). ε represents noise added to the system.

(D) Distribution of particles representing FLRT1/3+ neurons after computer simulations with high, balanced, or low attraction forces. The colored lines indicate a higher (magenta) or lower (cyan) density of particles based on their kernel distribution.

(E) Minimum neighbor distance of particles shown in (D). n = 10 computer simulations comprising 480 particles. ***$p < 0.001$, one-way ANOVA test with Tukey's post hoc analysis.

(F) Distribution of particles on the z axis after computer simulations. Note that both high and balanced attraction conditions result in a uniform surface, whereas low attraction conditions produce a wavy surface after computer simulations.

(G) Frequency distribution of speed profiles of particles shown in (F). Rectangles indicate low (plain) and high (pattern) speed profiles, and their relative fractions are shown on the right. **$p < 0.01$, ***$p < 0.001$, chi-square contingency analysis.

The data are represented as mean ± SEM.

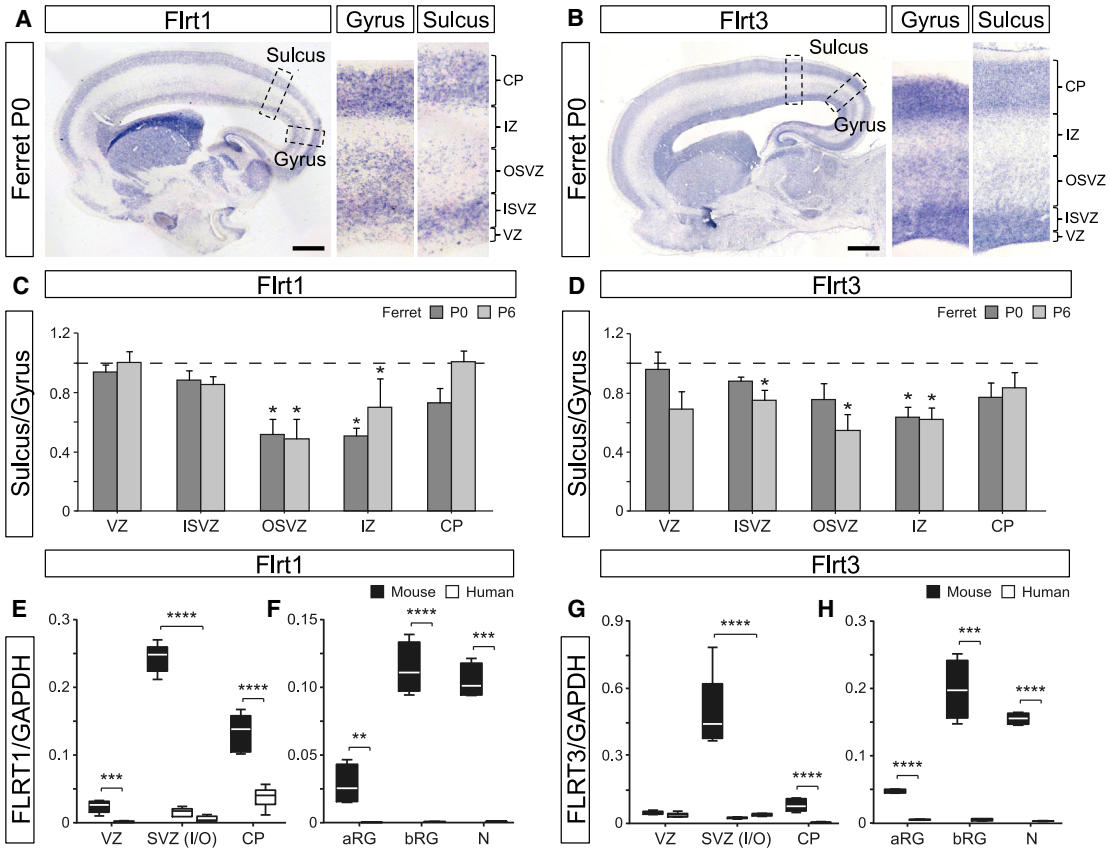

Figure 6. Low Endogenous Levels of FLRT1 and FLRT3 in a Future Sulcus Area of Ferret Cortex and in Specific Layers of Human Cortex

(A and B) ISH for FLRT1 (A) and FLRT3 (B) in sagittal sections of ferret cortex at P0. Regions marked by dashed rectangles delineate a prospective lateral sulcus (Sulcus) and splenial gyrus (Gyrus) and are shown with higher magnification on the right. The scale bars represent 1 mm.

(C and D) Intensity quantification of the images in (A) and (B) and Figures S6F and S6G, expressed as a ratio of sulcus/gyrus in different cortical layers at P0 and P6 (n = 3 separate ISH experiments for each group). *p < 0.05, unpaired Student's t test.

(E–H) Comparison of FLRT1 and FLRT3 expression between mouse and human with sequencing data from Fietz et al. (2012) (GEO: GSE38805) and Florio et al. (2015) (GEO: GSE65000). FLRT1 and FLRT3 mRNAs are more abundant in mouse compared with human when comparing different germinal layers (E and G) and specific cell types, including apical radial glia cells (aRG), basal radial glial cells (bRG), and migrating neurons (F and H).

FLRT sequencing data were normalized to housekeeping genes, including GAPDH (this figure) and PGK1 (Figures S6J–S6M). Whiskers in the boxplot represent minimum and maximum; unpaired Student's t test, **p < 0.01, ***p < 0.001, ****p < 0.0001.

and OSVZ were combined). Relatively higher levels of mouse FLRT1 and FLRT3 were also seen in the CP. Higher levels of mouse FLRT1, but not FLRT3, were seen in the VZ. Normalizing FLRT1 and FLRT3 expression to another housekeeping gene (PGK1) gave similar results (Figures S6J and S6L). Third, we compared FLRT1/3 expression in apical and basal RG and migrating neurons in human and mouse (Florio et al., 2015; Figures 6F and 6H; Figures S6K and S6M). FLRT1 and FLRT3 expression in the mouse was highest in migrating neurons and basal RG cells, which are the mouse homologs of the outer RG cells found in gyrencephalic species (Borrell and Götz, 2014). Notably, FLRT1/3 levels in these cells were much higher in mouse than in human cortex. Given the high levels of FLRT1/3 in basal RG cells, we also asked whether the fraction of pvim-positive cells that display a basal radial glia-like morphology was altered in the FLRT1/3 DKO mice. This was not the case (Figures S6N and S6O), providing more evidence for lack of basal radial glia involvement in the FLRT KO phenotype. Overall, these results revealed an inverse correlation between the presence of cortical folds/sulci and FLRT1/3 levels. Thus, the human neocortex expresses lower levels of FLRT1/3 compared with the mouse neocortex, and, in the ferret cortex, FLRT1/3 expression levels are less abundant in prospective sulcus than in gyrus areas.

DISCUSSION

In this study, we have identified FLRT1 and FLRT3 adhesion molecules as regulators of mammalian cortex folding. Genetic ablation of *Flrt1/3* in mice resulted in the formation of macroscopic cortical sulci that were maintained post-natally. These anatomical changes did not require progenitor cell amplification but, rather, correlated with changes in the behavior of migrating cortical neurons. Lack of FLRT1/3 reduced intercellular

adhesion, enhanced neuron clustering along the tangential axis, and mildly accelerated radial migration, resulting in a larger proportion of immature neurons reaching the upper cortical plate during late embryogenesis. These findings suggest that regulation of intercellular adhesion of migrating neurons is critical for sulcus formation in the cerebral cortex. Moreover, our expression analysis of FLRT1 and FLRT3 in gyrencephalic species revealed an inverse correlation between FLRT1/3 levels and sulcus formation, supporting a model by which increased abundance of FLRT1/3 levels during evolution led to the smoothing of an ancestral folded cortex. Therefore, *Flrt1/3* DKO mice are an interesting genetic model to study the cellular and molecular mechanisms of cortex folding induced by migrating neurons independent of progenitor amplification.

Mechanisms of FLRT1/3 Function

Flrt1/3 DKO mice are a unique genetic mouse model in which the cortex is folded without increases in neurogenic progenitor cells and basal radial glia. The lack of effects on neurogenic progenitor cells in *Flrt1/3* DKO is consistent with the lack of FLRT1/3 expression in apical or BPs (Figure 1; Figure S1; data not shown). Previous work in lissencephalic mice linked the expansion of the BP pool to gyrus formation (Florio et al., 2015; Ju et al., 2016; Rash et al., 2013; Stahl et al., 2013; Wang et al., 2016). In the gyrencephalic ferret, cortical regions with abundant BPs are more likely to develop into a gyrus than regions with fewer BPs (de Juan Romero et al., 2015; Reillo et al., 2011). Ectopic expansion of the BP pool in the ferret generates additional gyri (Masuda et al., 2015; Nonaka-Kinoshita et al., 2013), and its reduction has a stronger effect on cortical layering of gyri than sulci (Toda et al., 2016). The absence of BP pool expansion and of increases in neuron numbers in folded regions of *Flrt1/3* DKO mice suggests that the folds do not represent radial expansions and gyrus-like structures but, rather, furrows and sulcus-like structures.

FLRT1 and FLRT3 regulate the tangential distribution of cortical neurons. Lack of FLRT1/3 leads to transient neuron clustering in the embryonic cortical plate, and this process is spatially correlated with sulcus formation in early embryonic stages, suggesting that the two events are causally linked. Linking cortical folding to cell clustering and lowered intercellular adhesion may not be without precedent. Overexpression of the hominoid-specific gene TBC1D3 in the mouse brain leads to cortical folding and increased generation of basal progenitors (Ju et al., 2016). TBC1D3-expressing cells show decreased levels of the adhesion protein N-cadherin and exhibit a clustered distribution reminiscent of cell clustering in Flrt1/3 DKO brains. Although the authors of that study concentrated mainly on the link between cell proliferation and cortex folding, our computational model suggests that reduced intercellular adhesion and cell clustering may be a salient feature of TBC1D3-induced cortex folding.

The horizontal layers of the mammalian cortex are organized in cortical columns that contain closely related neurons. Clonal studies of cortical migration show that, in rodents, cortical neurons mostly migrate radially along a single parent RG fiber (Noctor et al., 2001); however, in folded brains like those of the ferret or macaque, migrating neurons show increased cellular dynamics and exploratory behavior, including increased lateral dispersion (Kornack and Rakic, 1995; Ware et al., 1999), but the mechanisms controlling this process are largely unknown. Our findings suggest that neuron clustering along the tangential axis in *Flrt1/3* DKO mice resembles the lateral dispersion observed in gyrencephalic species. This raises the interesting possibility that the underlying mechanisms may be similar. Neuron clustering in *Flrt1/3* DKO mice is likely the result of reduced intercellular adhesion, which alters the delicate balance of adhesion/repulsion required for cell migration (Cooper, 2013; Solecki, 2012). This conclusion is supported by our computational model, which shows that changes in the balance of adhesion/repulsion alter the distribution of cells from a uniform salt-and-pepper distribution to a clustered pattern. Hence, the increased lateral dispersion of cortical neurons in gyrencephalic brains may be the result of lowered intercellular adhesion.

The clustering mechanism alone is not likely to cause cortex folding because other mouse models with altered tangential neuron distribution do not show cortex folding (Dimidschstein et al., 2013; Torii et al., 2009). Our findings suggest that *Flrt1/3* DKO mice combine neuron clustering with increased migration speed and that this combination underlies sulcus formation. Similar to neuron clustering, increased migration speed may also be caused by reduced intercellular adhesion. This is suggested by our computational model, by previous mathematical models (DiMilla et al., 1991; Zaman et al., 2005), and by experimental studies (Lauro et al., 2006). A higher migration speed may increase the intercalation of neurons in local areas of the upper cortical plate (uCP), which, according to the radial intercalation hypothesis, increases tension and alters tissue elasticity, leading to sulcus formation (Striedter et al., 2015). We also find that the increased proportion of neurons reaching the upper CP of *Flrt1/3* DKO causes a shift toward more immature morphologies. Indeed, previous studies have shown that improper laminar position affects dendritic arborization of cortical neurons (Morgan-Smith et al., 2014). Whether this also contributes to sulcus formation will have to await further experimental analysis.

Evolutionary Considerations

The finding that lack of FLRT1/3 favors sulcus formation in the normally smooth mouse neocortex raised the question to what extent FLRT1/3 proteins are relevant for regulating cortical folding during evolution. Some studies suggest that the most recent common mammalian ancestor was gyrencephalic (Lewitus et al., 2014; O'Leary et al., 2013), and it was hypothesized that several transitions from gyrencephaly to lissencephaly occurred during mammalian evolution (Kelava et al., 2012; Lewitus et al., 2014). This conclusion is supported by the finding that the marmoset, despite being a lissencephalic species, retains neurogenic features characteristic of gyrencephalic neocortices (Kelava et al., 2012). Although these studies point out that lissencephaly has evolved from gyrencephaly, the mechanisms controlling this process are not known.

Our results suggest that FLRT1/3 expression levels might have participated in the transition from gyrencephaly to lissencephaly. In the wild-type mouse brain, high expression levels of FLRT1/3 promote adhesion between neurons, resulting in coordinated migration and little lateral dispersion, which favors the formation

of homogeneous and smooth cortical layers. Conversely, the absence of FLRT1/3 expression reduces adhesion between neurons, allowing them to acquire wide dynamic migratory profiles and a lateral distribution, which are features characteristic of neurons in the ferret at the onset of cortical folding (Gertz and Kriegstein, 2015). Interestingly, the gyrencephalic human neocortex expresses much lower levels of FLRT1/3 compared with the lissencephalic mouse neocortex, and regions in the ferret neocortex undergoing sulcus formation have lower levels of FLRT1/3 compared with regions developing into a gyrus. Notably, this markedly distinct expression pattern was mainly seen in the OSVZ, which is a key layer involved in cortical folding of gyrencephalic species (Borrell and Götz, 2014; Lui et al., 2011).

Our findings thus unraveled FLRT1/3 as key factors involved in the regulation of cortical migration and sulcus formation. Manipulations of their expression levels have a profound effect on the coordination of cortical migration and lateral dispersion of neurons, which, in turn, influences cortical folding. This scenario provides molecular and cellular insights into the evolution of neuronal migration from gyrencephalic to lissencephalic species.

STAR★METHODS

Detailed methods are provided in the online version of this paper and include the following:

- KEY RESOURCES TABLE
- CONTACT FOR REAGENT AND RESOURCE SHARING
- EXPERIMENTAL MODEL AND SUBJECT DETAILS
  - Mouse lines
  - Ferret
  - Primary cultures
- METHOD DETAILS
  - Immunohistochemistry and enzymatic staining
  - In utero electroporation assays
  - Time-lapse experiments
  - Nissl Staining
  - Cell morphology analysis
  - BrdU analysis
  - Computer modeling
  - in situ hybridization
  - RNaseq analysis
- QUANTIFICATION AND STATISTICAL ANALYSIS

SUPPLEMENTAL INFORMATION

Supplemental Information includes six figures and two movies and can be found with this article online at http://dx.doi.org/10.1016/j.cell.2017.04.012.

AUTHOR CONTRIBUTIONS

D.d.T. characterized the Flrt1/3 DKO phenotype, performed neuronal cultures/explants, and designed the computational model. T.R. characterized the Flrt1 KO and performed IUE and time-lapse and morphology analyses. E.C. performed bioinformatics analysis of RNA-seq data and analysis of the Flrt2/3 DKO. G.S.B. characterized FLRT1-3 expression and assisted with IF assays. A.V. performed ISH on ferret sections. R.K. and V.B. supervised experiments. D.d.T. and R.K. wrote the manuscript with input from all other authors.

ACKNOWLEDGMENTS

We thank M. Götz for her insightful comments during the course of this study, R. Portugués and A. Boehm for help with the computational model, S. Falk for help with setting up time-lapse experiments, R. Kasper for technical help with the time-lapse setup, A. Yeroslaviz and B. Habermann for help with gene expression analysis, T. Gaitanos for help with Cell Profiler, T. Iwasato for the Supernova system, and H. Kucukdereli and A. Kist for help with Python programming. T.R., a member of the graduate program IMPRS-LS, was funded by a Boehringer Ingelheim Ph.D. fellowship. E.C. was supported by a postdoctoral research fellowship from the Alexander von Humboldt Foundation, and A.V. was supported by a predoctoral Severo Ochoa contract with the Spanish Ministry of Economy and Competitiveness (MINECO, SVP-2014-068671). This work was funded by the Max Planck Society and the Deutsche Forschungsgemeinschaft (Synergy) (to R.K.) and by the European Research Council (CORTEXFOLDING, 309633) and MINECO (SAF2015-69168-R to V.B.).

Received: October 6, 2016
Revised: February 9, 2017
Accepted: April 7, 2017
Published: May 4, 2017

REFERENCES

Beaudin, S.A., Singh, T., Agster, K.L., and Burwell, R.D. (2013). Borders and comparative cytoarchitecture of the perirhinal and postrhinal cortices in an F1 hybrid mouse. Cereb. Cortex *23*, 460–476.

Borrell, V., and Götz, M. (2014). Role of radial glial cells in cerebral cortex folding. Curr. Opin. Neurobiol. *27*, 39–46.

Borrell, V., and Reillo, I. (2012). Emerging roles of neural stem cells in cerebral cortex development and evolution. Dev. Neurobiol. *72*, 955–971.

Bribián, A., Nocentini, S., Llorens, F., Gil, V., Mire, E., Reginensi, D., Yoshida, Y., Mann, F., and del Río, J.A. (2014). Sema3E/PlexinD1 regulates the migration of hem-derived Cajal-Retzius cells in developing cerebral cortex. Nat. Commun. *5*, 4265.

Buchholz, J. (2009). MATLAB Particles 2.0.

Cooper, J.A. (2013). Cell biology in neuroscience: mechanisms of cell migration in the nervous system. J. Cell Biol. *202*, 725–734.

de Juan Romero, C., Bruder, C., Tomasello, U., Sanz-Anquela, J.M., and Borrell, V. (2015). Discrete domains of gene expression in germinal layers distinguish the development of gyrencephaly. EMBO J. *34*, 1859–1874.

Devisme, L., Bouchet, C., Gonzalès, M., Alanio, E., Bazin, A., Bessières, B., Bigi, N., Blanchet, P., Bonneau, D., Bonnières, M., et al. (2012). Cobblestone lissencephaly: neuropathological subtypes and correlations with genes of dystroglycanopathies. Brain *135*, 469–482.

Dimidschstein, J., Passante, L., Dufour, A., van den Ameele, J., Tiberi, L., Hrechdakian, T., Adams, R., Klein, R., Lie, D.C., Jossin, Y., and Vanderhaeghen, P. (2013). Ephrin-B1 controls the columnar distribution of cortical pyramidal neurons by restricting their tangential migration. Neuron *79*, 1123–1135.

DiMilla, P.A., Barbee, K., and Lauffenburger, D.A. (1991). Mathematical model for the effects of adhesion and mechanics on cell migration speed. Biophys. J. *60*, 15–37.

Egea, J., Erlacher, C., Montanez, E., Burtscher, I., Yamagishi, S., Hess, M., Hampel, F., Sanchez, R., Rodriguez-Manzaneque, M.T., Bösl, M.R., et al. (2008). Genetic ablation of FLRT3 reveals a novel morphogenetic function for the anterior visceral endoderm in suppressing mesoderm differentiation. Genes Dev. *22*, 3349–3362.

Englund, C., Fink, A., Lau, C., Pham, D., Daza, R.A.M., Bulfone, A., Kowalczyk, T., and Hevner, R.F. (2005). Pax6, Tbr2, and Tbr1 are expressed sequentially by radial glia, intermediate progenitor cells, and postmitotic neurons in developing neocortex. J. Neurosci. *25*, 247–251.

Fernández, V., Llinares-Benadero, C., and Borrell, V. (2016). Cerebral cortex expansion and folding: what have we learned? EMBO J. *35*, 1021–1044.

Fietz, S.A., Lachmann, R., Brandl, H., Kircher, M., Samusik, N., Schröder, R., Lakshmanaperumal, N., Henry, I., Vogt, J., Riehn, A., et al. (2012). Transcriptomes of germinal zones of human and mouse fetal neocortex suggest a role of extracellular matrix in progenitor self-renewal. Proc. Natl. Acad. Sci. USA *109*, 11836–11841.

Finlay, B.L., and Darlington, R.B. (1995). Linked regularities in the development and evolution of mammalian brains. Science *268*, 1578–1584.

Florio, M., Albert, M., Taverna, E., Namba, T., Brandl, H., Lewitus, E., Haffner, C., Sykes, A., Wong, F.K., Peters, J., et al. (2015). Human-specific gene ARHGAP11B promotes basal progenitor amplification and neocortex expansion. Science *347*, 1465–1470.

Gertz, C.C., and Kriegstein, A.R. (2015). Neuronal Migration Dynamics in the Developing Ferret Cortex. J. Neurosci. *35*, 14307–14315.

Geschwind, D.H., and Rakic, P. (2013). Cortical evolution: judge the brain by its cover. Neuron *80*, 633–647.

Gorski, J.A., Talley, T., Qiu, M., Puelles, L., Rubenstein, J.L., and Jones, K.R. (2002). Cortical excitatory neurons and glia, but not GABAergic neurons, are produced in the Emx1-expressing lineage. J. Neurosci. *22*, 6309–6314.

Hansen, D.V., Lui, J.H., Parker, P.R.L., and Kriegstein, A.R. (2010). Neurogenic radial glia in the outer subventricular zone of human neocortex. Nature *464*, 554–561.

Jackson, V.A., del Toro, D., Carrasquero, M., Roversi, P., Harlos, K., Klein, R., and Seiradake, E. (2015). Structural basis of latrophilin-FLRT interaction. Structure *23*, 774–781.

Jackson, V.A., Mehmood, S., Chavent, M., Roversi, P., Carrasquero, M., Del Toro, D., Seyit-Bremer, G., Ranaivoson, F.M., Comoletti, D., Sansom, M.S.P., et al. (2016). Super-complexes of adhesion GPCRs and neural guidance receptors. Nat. Commun. *7*, 11184.

Ju, X.-C., Hou, Q.-Q., Sheng, A.-L.S., Wu, K.-Y., Zhou, Y., Jin, Y., Wen, T., Yang, Z., Wang, X., and Luo, Z.-G. (2016). The hominoid-specific gene TBC1D3 promotes generation of basal neural progenitors and induces cortical folding in mice. eLife *5*, e18197.

Kawauchi, T. (2015). Cellular insights into cerebral cortical development: focusing on the locomotion mode of neuronal migration. Front. Cell. Neurosci. *9*, 394.

Kelava, I., Reillo, I., Murayama, A.Y., Kalinka, A.T., Stenzel, D., Tomancak, P., Matsuzaki, F., Lebrand, C., Sasaki, E., Schwamborn, J.C., et al. (2012). Abundant occurrence of basal radial glia in the subventricular zone of embryonic neocortex of a lissencephalic primate, the common marmoset Callithrix jacchus. Cereb. Cortex *22*, 469–481.

Kornack, D.R., and Rakic, P. (1995). Radial and horizontal deployment of clonally related cells in the primate neocortex: relationship to distinct mitotic lineages. Neuron *15*, 311–321.

Lauro, C., Catalano, M., Trettel, F., Mainiero, F., Ciotti, M.T., Eusebi, F., and Limatola, C. (2006). The chemokine CX3CL1 reduces migration and increases adhesion of neurons with mechanisms dependent on the beta1 integrin subunit. J. Immunol. *177*, 7599–7606.

Lewitus, E., Kelava, I., Kalinka, A.T., Tomancak, P., and Huttner, W.B. (2014). An adaptive threshold in mammalian neocortical evolution. PLoS Biol. *12*, e1002000.

Liao, Y., Smyth, G.K., and Shi, W. (2014). featureCounts: an efficient general purpose program for assigning sequence reads to genomic features. Bioinformatics *30*, 923–930.

Love, M.I., Huber, W., and Anders, S. (2014). Moderated estimation of fold change and dispersion for RNA-seq data with DESeq2. Genome Biol. *15*, 550.

Lui, J.H., Hansen, D.V., and Kriegstein, A.R. (2011). Development and evolution of the human neocortex. Cell *146*, 18–36.

Masuda, K., Toda, T., Shinmyo, Y., Ebisu, H., Hoshiba, Y., Wakimoto, M., Ichikawa, Y., and Kawasaki, H. (2015). Pathophysiological analyses of cortical malformation using gyrencephalic mammals. Sci. Rep. *5*, 15370.

Matsuda, T., and Cepko, C.L. (2007). Controlled expression of transgenes introduced by in vivo electroporation. Proc. Natl. Acad. Sci. USA *104*, 1027–1032.

Mizuno, H., Luo, W., Tarusawa, E., Saito, Y.M., Sato, T., Yoshimura, Y., Itohara, S., and Iwasato, T. (2014). NMDAR-regulated dynamics of layer 4 neuronal dendrites during thalamocortical reorganization in neonates. Neuron *82*, 365–379.

Moon, H.M., and Wynshaw-Boris, A. (2013). Cytoskeleton in action: lissencephaly, a neuronal migration disorder. Wiley Interdiscip. Rev. Dev. Biol. *2*, 229–245.

Morgan-Smith, M., Wu, Y., Zhu, X., Pringle, J., and Snider, W.D. (2014). GSK-3 signaling in developing cortical neurons is essential for radial migration and dendritic orientation. eLife *3*, e02663.

Nieto, M., Monuki, E.S., Tang, H., Imitola, J., Haubst, N., Khoury, S.J., Cunningham, J., Gotz, M., and Walsh, C.A. (2004). Expression of Cux-1 and Cux-2 in the subventricular zone and upper layers II-IV of the cerebral cortex. J. Comp. Neurol. *479*, 168–180.

Noctor, S.C., Flint, A.C., Weissman, T.A., Dammerman, R.S., and Kriegstein, A.R. (2001). Neurons derived from radial glial cells establish radial units in neocortex. Nature *409*, 714–720.

Nonaka-Kinoshita, M., Reillo, I., Artegiani, B., Martínez-Martínez, M.Á., Nelson, M., Borrell, V., and Calegari, F. (2013). Regulation of cerebral cortex size and folding by expansion of basal progenitors. EMBO J. *32*, 1817–1828.

O'Leary, M.A., Bloch, J.I., Flynn, J.J., Gaudin, T.J., Giallombardo, A., Giannini, N.P., Goldberg, S.L., Kraatz, B.P., Luo, Z.-X., Meng, J., et al. (2013). The placental mammal ancestor and the post-K-Pg radiation of placentals. Science *339*, 662–667.

Pilz, G.-A., Shitamukai, A., Reillo, I., Pacary, E., Schwausch, J., Stahl, R., Ninkovic, J., Snippert, H.J., Clevers, H., Godinho, L., et al. (2013). Amplification of progenitors in the mammalian telencephalon includes a new radial glial cell type. Nat. Commun. *4*, 2125.

Rakic, P. (1972). Mode of cell migration to the superficial layers of fetal monkey neocortex. J. Comp. Neurol. *145*, 61–83.

Rash, B.G., Tomasi, S., Lim, H.D., Suh, C.Y., and Vaccarino, F.M. (2013). Cortical gyrification induced by fibroblast growth factor 2 in the mouse brain. J. Neurosci. *33*, 10802–10814.

Reillo, I., de Juan Romero, C., García-Cabezas, M.Á., and Borrell, V. (2011). A role for intermediate radial glia in the tangential expansion of the mammalian cerebral cortex. Cereb. Cortex *21*, 1674–1694.

Schindelin, J., Arganda-Carreras, I., Frise, E., Kaynig, V., Longair, M., Pietzsch, T., Preibisch, S., Rueden, C., Saalfeld, S., Schmid, B., et al. (2012). Fiji: an open-source platform for biological-image analysis. Nat. Methods *9*, 676–682.

Seiradake, E., del Toro, D., Nagel, D., Cop, F., Härtl, R., Ruff, T., Seyit-Bremer, G., Harlos, K., Border, E.C., Acker-Palmer, A., et al. (2014). FLRT structure: balancing repulsion and cell adhesion in cortical and vascular development. Neuron *84*, 370–385.

Smart, I.H., and McSherry, G.M. (1986). Gyrus formation in the cerebral cortex of the ferret. II. Description of the internal histological changes. J. Anat. *147*, 27–43.

Solecki, D.J. (2012). Sticky situations: recent advances in control of cell adhesion during neuronal migration. Curr. Opin. Neurobiol. *22*, 791–798.

Stahl, R., Walcher, T., De Juan Romero, C., Pilz, G.A., Cappello, S., Irmler, M., Sanz-Aquela, J.M., Beckers, J., Blum, R., Borrell, V., and Götz, M. (2013). Trnp1 regulates expansion and folding of the mammalian cerebral cortex by control of radial glial fate. Cell *153*, 535–549.

Striedter, G.F., Srinivasan, S., and Monuki, E.S. (2015). Cortical folding: when, where, how, and why? Annu. Rev. Neurosci. *38*, 291–307.

Tabata, H., and Nagata, K. (2016). Decoding the molecular mechanisms of neuronal migration using in utero electroporation. Med. Mol. Morphol. *49*, 63–75.

Thomson, R.E., Kind, P.C., Graham, N.A., Etherson, M.L., Kennedy, J., Fernandes, A.C., Marques, C.S., Hevner, R.F., and Iwata, T. (2009). Fgf receptor 3 activation promotes selective growth and expansion of occipitotemporal cortex. Neural Dev. *4*, 4.

Toda, T., Shinmyo, Y., Dinh Duong, T.A., Masuda, K., and Kawasaki, H. (2016). An essential role of SVZ progenitors in cortical folding in gyrencephalic mammals. Sci. Rep. *6*, 29578.

Torii, M., Hashimoto-Torii, K., Levitt, P., and Rakic, P. (2009). Integration of neuronal clones in the radial cortical columns by EphA and ephrin-A signalling. Nature *461*, 524–528.

Trapnell, C., Roberts, A., Goff, L., Pertea, G., Kim, D., Kelley, D.R., Pimentel, H., Salzberg, S.L., Rinn, J.L., and Pachter, L. (2012). Differential gene and transcript expression analysis of RNA-seq experiments with TopHat and Cufflinks. Nat. Protoc. *7*, 562–578.

Tronche, F., Kellendonk, C., Kretz, O., Gass, P., Anlag, K., Orban, P.C., Bock, R., Klein, R., and Schütz, G. (1999). Disruption of the glucocorticoid receptor gene in the nervous system results in reduced anxiety. Nat. Genet. *23*, 99–103.

Wagenführ, L., Meyer, A.K., Braunschweig, L., Marrone, L., and Storch, A. (2015). Brain oxygen tension controls the expansion of outer subventricular zone-like basal progenitors in the developing mouse brain. Development *142*, 2904–2915.

Wang, L., Hou, S., and Han, Y.-G. (2016). Corrigendum: Hedgehog signaling promotes basal progenitor expansion and the growth and folding of the neocortex. Nat. Neurosci. *19*, 1115.

Ware, M.L., Tavazoie, S.F., Reid, C.B., and Walsh, C.A. (1999). Coexistence of widespread clones and large radial clones in early embryonic ferret cortex. Cereb. Cortex *9*, 636–645.

Wilkinson, D.J. (2009). Stochastic modelling for quantitative description of heterogeneous biological systems. Nat. Rev. Genet. *10*, 122–133.

Yamagishi, S., Hampel, F., Hata, K., Del Toro, D., Schwark, M., Kvachnina, E., Bastmeyer, M., Yamashita, T., Tarabykin, V., Klein, R., and Egea, J. (2011). FLRT2 and FLRT3 act as repulsive guidance cues for Unc5-positive neurons. EMBO J. *30*, 2920–2933.

Zaman, M.H., Kamm, R.D., Matsudaira, P., and Lauffenburger, D.A. (2005). Computational model for cell migration in three-dimensional matrices. Biophys. J. *89*, 1389–1397.

STAR★METHODS

KEY RESOURCES TABLE

REAGENT or RESOURCE	SOURCE	IDENTIFIER
Antibodies		
Rabbit anti-βIII Tubulin	Sigma-Aldrich	Cat#SAB4300623; RRID:AB_11128202
Rabbit anti-Cux1	Santa Cruz	Cat#SC-13024; RRID:AB_2261231
Rabbit anti-Tbr1	Abcam	Cat#AB31940; RRID:AB_2200219
Rabbit anti-Tbr2	Abcam	Cat#AB23345; RRID:AB_778267
Rabbit anti-laminin	Sigma-Aldrich	Cat#L9393; RRID:AB_477163
Rabbit anti-Pax6	BioLegend	Cat#901301; RRID:AB_2565003
Rabbit anti-BLBP	Millipore	Cat#ABN14; RRID:AB_10000325
Rabbit anti-Calretinin	Swant	Cat#7697; RRID:AB_2619710
Rat anti-Histone H3	Abcam	Cat#AB10543; RRID:AB_2295065
Rat anti-Ctip2	Abcam	Cat#18465; RRID:AB_2064130
Mouse anti-Pvim	Abcam	Cat#AB22651; RRID:AB_447222
Mouse anti-BrdU	Roche	Cat#11170376001; RRID:AB_514483
Mouse anti-Reelin	MBL	Cat#D223-3; RRID:AB_843523
Goat anti-FLRT1	R&D	Cat#AF2794; RRID:AB_2106598
Goat anti-FLRT3	R&D	Cat#AF2795; RRID:AB_2106855
Goat anti-FoxP2	Santa Cruz	Cat#SC-21069; RRID:AB_2107124
Anti-phalloidin-Cy3	Sigma-Aldrich	Cat#P5282
Chemicals, Peptides, and Recombinant Proteins		
BrdU	Sigma-Aldrich	B5002; CAS:59-14-3
Cresyl Violet acetate (for Nissl staining)	Sigma-Aldrich	C5042; CAS:10510-54-0
Deposited Data		
Mouse RNaseq data (lateral and medial cortex)	Wang et al., 2016	GEO: GSE80958
Human and mouse RNaseq data (cortical layers)	Fietz et al., 2012	GEO: GSE38805
Human and mouse RNaseq data (aRG, bRG and migrating neurons)	Florio et al., 2015	GEO: GSE65000
Human RNaseq data (different cortical regions)	Allan Brain Atlas	http://www.brain-map.org
Mouse reference genome, NCBIM37	The Ensembl Project	http://may2012.archive.ensembl.org/Mus_musculus/
Human reference genome, GRCh37	Genome Reference Consortium	https://www.ncbi.nlm.nih.gov/grc/human
Experimental Models: Cell Lines		
Primary cell lines from FLRT1 lacZ mouse	EUCOMM	HEPD0528
Primary cell lines from FLRT3 lacZ mouse	Egea et al., 2008	N/A
Experimental Models: Organisms/Strains		
Mouse: FLRT1 null	Yamagishi et al., 2011	HEPD0528
Mouse: FLRT1 lacZ	EUCOMM	HEPD0528
Mouse: FLRT2 lox	EUCOMM	EPD0347
Mouse: FLRT2 null	Yamagishi et al., 2011	N/A
Mouse: FLRT2 lacZ	EUCOMM	EPD0347
Mouse: FLRT3 lox	Yamagishi et al., 2011	N/A
Mouse: FLRT3 null	Egea et al., 2008	N/A
Mouse: FLRT3 lacZ	Egea et al., 2008	N/A
Mouse: Nestin-Cre	Tronche et al., 1999	N/A

(*Continued on next page*)

Continued

REAGENT or RESOURCE	SOURCE	IDENTIFIER
Mouse: EMX-Cre	Gorski et al., 2002	N/A
Pigmented ferrets (Mustela putorius furo)	Marshall Bioresources and Euroferret	N/A
Oligonucleotides		
ISH: Flrt1-foward TCAGCGTGCAGGTCATCTAC	This paper	N/A
ISH: Flrt1-reverse GCAGCCACAGGAGGTTACAG	This paper	N/A
ISH: Flrt3-foward TCTCCGACTGCTTTTCCTGT	This paper	N/a
ISH: Flrt3-reverse TATTCATTGCGTTCCCCTGT	This paper	N/A
Recombinant DNA		
Plasmid: SUPERNOVA plasmid system	Mizuno et al., 2014	N/A
Plasmid: pCAG-Cre	Anjen Chenn lab	Cat#26647 (Addgene)
Plasmid: pCALNL-DsRed	Matsuda and Cepko, 2007	Cat#13769 (Addgene)
Software and Algorithms		
MATLAB, version R2015a	Mathworks Inc, USA	http://mathworks.com
MATLAB particles, version 2.1	Buchholz, 2009	N/A
Prism, version 5	Graphpad Software, USA	https://www.graphpad.com/
ImageJ (Fiji), version 2.0.0	Schindelin et al., 2012	https://imagej.net/Fiji
RStudio, version 0.98.1091	RStudio, USA	https://www.rstudio.com/
LAS software, version 4.7	Leica Microsystems, Germany	http://www.leica-microsystems.com/products/microscope-software/
Python, version 3.0	Python Software Foundation	https://www.python.org/
CellProfiler, version 2.2.0	CellProfiler, USA	http://cellprofiler.org
FASTX-Toolkit, version 0.0.13	Hannon lab	http://hannonlab.cshl.edu/fastx_toolkit/
TopHat, version 2.0.14	Trapnell et al., 2012	https://ccb.jhu.edu/software/tophat/
featureCounts, version 1.5.1	Liao et al., 2014	http://bioinf.wehi.edu.au/featureCounts/
DESeq2, version 3.4	Love et al., 2014	https://bioconductor.org/packages/release/bioc/html/DESeq2.html

CONTACT FOR REAGENT AND RESOURCE SHARING

Further information and request for resources and reagents should be directed to and will be fulfilled by the Lead Contact, Rüdiger Klein (rklein@neuro.mpg.de).

EXPERIMENTAL MODEL AND SUBJECT DETAILS

Mouse lines

Flrt3$^{lacZ/lx}$ mice (Egea et al., 2008) carrying the floxed allele for *Flrt3* were crossed with Flrt1$^{-/-}$ (Yamagishi et al., 2011) and the nervous system-specific Nestin-Cre (Tronche et al., 1999). Flrt2$^{lacZ/lx}$ mice (line EPD0347 from EUCOMM) carrying the floxed allele for *Flrt2* were crossed with Flrt3$^{-/lx}$ mice (Egea et al., 2008) and the nervous system-specific EMX-Cre (Gorski et al., 2002). More information is available in the key resources table. All mice (C57BL/6 background) were housed with 12:12h light/dark cycle and food/water available ad libitum. All animal experiments were approved by the government of upper Bavaria.

Ferret

Pigmented ferrets (Mustela putorius furo) were obtained from Marshall Boiresources and Euroferret and kept on a 16:8h light:dark cycle at the Animal Facilities of the Universidad Miguel Hernández. Ferret were employed independently of their gender. Healthy animals postnatal day 0 had an average weight of 10 gr and postnatal day 6 animals weighed around 35 gr. Non previous procedures were performed in the animals used for tissue collection. All animals were treated according to Spanish and EU regulations, and experimental protocols were approved by the Universidad Miguel Hernández Institutional Animal Care and Use Committee (IACUC).

Primary cultures

Cortical neurons and hem explants were performed as described previously (Bribián et al., 2014; Seiradake et al., 2014; Yamagishi et al., 2011). Briefly, cortical hem explants from E12.5 Flrt3$^{lacZ/+}$ embryos were dissected out and placed on 13 mm coverslips in

4 well-plate (Thermofisher, catalog 176740) coated with 0.5 μg/ml Poly-D-Lysine (Sigma) and 20 μg/ml laminin (Thermofisher). Neurons were dissociated from cortices of E15.5 Flrt1$^{lacZ/+}$ embryos and cultured on coverslips coated with 0.5 μg/ml Poly-D-Lysine in 24 well-plates (Thermofisher, catalog 140675). Explants and neurons were cultured for 1 day in vitro at 37°C, 5% CO2 in Neurobasal medium supplemented with B27 (Invitrogen). Cultures were fixed with 4% Paraformaldehyde for 10 min and processed for immunostaining.

METHOD DETAILS

Immunohistochemistry and enzymatic staining

To stain for β-galactosidase activity, mouse brains were fixed for 1.5 hr in 0.2% glutaraldehyde and 1% PFA in PBS (containing 5 mM EGTA, 2 mM MgCl2, and 0.02% NP40). Vibratome sections (50 μm) were stained for β-galacatosidase activity by incubating them for 2–3 hr at 37°C in a 1 mg/ml X-gal solution (Invitrogen) containing 5 mM $K_4Fe(CN)_6$ and 5 mM $K_3Fe(CN)_6$. After rinsing, brain sections were counterstained with FastRed (Vector Laboratories).

For immunostaining, cultured cells, explants or embryonic brains were fixed in 4% PFA for ~15 min and over-night, respectively. For BrdU staining, sections were pretreated with 2N HCl for 30 min and subsequently neutralized with sodium-tetraborate ($Na_2B_4O_7$ 0.1M, pH: 8.5) for 2 × 15 min. Cells and explants were incubated with primary antibodies after 10 min or 1 hr of permeabilization with 1% BSA, 0.1% Triton X-100/PBS, respectively. We used rabbit anti-βIII Tubulin 1/1,000 (Sigma), rabbit anti-Cux1 antibody 1/300 (Santa Cruz), rabbit anti-Tbr1 and anti-Tbr2 1/300 (Abcam), rat anti-Ctip2 1/300 (Abcam), mouse anti-BrdU (Roche), goat anti-FLRT3 1/200 (R&D), anti-phalloidin-Cy3 1/100 (Sigma), goat anti-FoxP2 1/300 (Santa Cruz), mouse anti-Reelin 1/500 (MBL), rabbit anti-laminin 1/300 (Sigma), rabbit anti-Pax6 1/300 (BioLegend), rabbit anti-BLBP 1/300 (Millipore), rabbit anti-Histone H3 1/300 (Abcam), mouse anti-Pvim 1/300 (Abcam), rabbit anti-Calretinin 1/300 (Swant), goat anti-FLRT1/3 1/100 (R&D). The secondary antibodies were Alexa Fluor 488-, 555- and 647-conjugated goat or donkey anti-rabbit/mouse/goat (Molecular Probes 1:400). Samples were imaged using a SP8 laser scanning confocal spectral microscope (Leica Microsystems). Images were taken using a 20 × (immunohistochemistry) or 40 × (neuronal cultures, cortical explants) numerical aperture objective with a 1.5 × digital zoom and 2 Airy disk pinhole.

In utero electroporation assays

In utero electroporation was performed at E13.5 as previously described (Seiradake et al., 2014) on Isoflurane anesthetized C57BL/6 control mice. DNA plasmids were used at 1μg/μl and mixed with 1% fast green (Sigma, final concentration 0.2%). 1 μl of plasmid solution were injected into the lateral ventricle with a pump-controlled micropipette (Picospritzer III). After injection, six 50ms (1 s interval) electric (30V) pulses were generated with electrodes confronting the uterus above the ventricle. The abdominal wall and skin were sewed and the mice were kept until the desired embryonic stage.

Time-lapse experiments

Embryos were electroporated at E13.5 using a combination of pCAG-Cre and pCALNL-DsRed plasmids (Matsuda and Cepko, 2007). pCALNL-DsRed was a gift from Connie Cepko (Addgene plasmid # 13769) and pCAG-Cre was a gift from Anjen Chenn (Addgene plasmid # 26647). After 48 hr, embryonic brains were dissected in ice cold sterile filtered and aerated (95% O_2/5% CO_2) dissection medium (15.6g/l DMEM/F12 (Sigma); 1.2g/l $NaHCO_3$; 2.9g/l glucose (Sigma); 1%(v/v) penicillin streptomycin (GIBCO)). Brains were embedded in 4% low melting agarose (Biozym) and cut into 300μm thick sections using a vibratome (Leica, VT1200S). Sections were suspended in a collagen mix (64%(v/v) cell matrix type I-A, Nitta Gelatin; 24%(v/v) 5xDMEM/F12; 12%(v/v) reconstitution buffer (200mM HEPES; 50mM NaOH; 260mM $NaHCO_3$) and transferred onto a cell culture insert (Millicell; PICMORG50). Sections were incubated for 10 min at 37°C to solidify collagen. 1.5 mL slice medium (88%(v/v) dissection medium; 5%(v/v) horse serum; 5%(v/v) fetal calf serum; 2%(v/v) B27 supplement (GIBCO); 1%(v/v) N2 supplement (GIBCO)) was added into the dish surrounding the culture insert and incubated for 30 min at 37°C. Before start of time-lapse experiment, culture medium was added on top of the sections to allow objective immersion. Sections were imaged using a 20 × water immersion objective on a Leica SP8 confocal microscope system equipped with a temperature-controlled carbon dioxide incubation chamber set to 37°C, 95% humidity and 5% CO^2. Sequential images were acquired every 20 min for 14-60 hr. After imaging slices were genotyped to identify Flrt1/3 DKOs. Single cell movement was tracked using the Fiji plugin "Manual Tracking." Only neurons entering the cortical plate were tracked. Single cell track analysis and plotting was carried out using homemade python scripts. All cells moving less than 4μm/h were considered as not moving.

Nissl Staining

Postnatal brains were fixed in 4% PFA over-night. Vibratome sections (50 μm) were dried on superfrost slides (Thermo Science) over-night at 42°C. Sections were incubated in 1:1 ethanol/chloroform for 2 hr and then rehydrated through 100%, 90%, 75%, 50% and 0% ethanol/distilled water (5min each step). Sections were stained in 0.1% cresyl violet solution for 5 min at 37°C and rinsed quickly in distilled water. Then sections were dehydrated from 0 to 100% ethanol/water (same steps as rehydration) and cleared in histo-clear (National diagnostics) before mounting with DPX mounting medium (Sigma-Aldrich). Images were acquired with Leica M205 FA stereomicroscope and processed with LAS software (version 4.7, Leica).

Cell morphology analysis

Flrt1−/−;Flrt3lx/lx (mutant) or Flrt1+/−;Flrt3lx/+ (control) embryos were electroporated at E13.5. For neuronal sparse labeling we used the SUPERNOVA plasmid system (1μg/μl, pCAG-loxP-STOP-loxP-RFP-ires-tTA-WRPE; 300ng/μl, pTRE-Cre (Mizuno et al., 2014). After 3 days, embryonic brains were collected, fixed in 4% PFA over-night and vibratome cut into 100μm sections. For single cell morphology analysis in the lateral cortex only posterior sections were used. Single cell morphology was reconstructed and analyzed using ImageJ (version 1.49) and RStudio (version 0.98.1091, RStudio).

BrdU analysis

Pregnant females were injected intraperitoneally with 0.15-0.2ml of 10mg/ml 5-bromo-2′-deoxyuridine (BrdU, Sigma-Aldrich) dissolved in PBS. This thymidine analog is incorporated during S-phase of the cell cycle. Pregnant females received a single injection of BrdU (final concentration 50 μg per g of mouse weight) at E14.5 and were sacrificed at E17.5, or at E12.5 (1.5 hr prior to sacrifice, short BrdU pulse analysis). Brains from the offspring were removed, fixed overnight with 4% PFA, and processed for immunohistochemistry.

Computer modeling

A sine curve was fitted to the normalized intensity profiles of GFP expression (GOF experiments overexpressing FLRT3 (Seiradake et al., 2014)) and Xgal staining (LOF experiments) after subtracting average intensity value (bs, basal subtraction) to center curves along the y axis at 0 position using the curve fitting tool from MATLAB (Mathworks, Inc). The sine equation contained one term as follows: Curve = Asin(λx+ϕ), where A is the amplitude, λ the frequency and ϕ the phase. Sine fitting revealed no statistically significance in the frequency (λ) between GOF and LOF fitted curves ((λ, 0.55-0.12 range value) but a difference in their amplitude (A, GOF: 41.41, LOF: 56.74) from 4-6 independent experiments. The strength of both curves was adjusted with the term κ,which was 1/3 for the repulsion curve (LOF experiments) and from 1 to 1/5 for the attraction curve (GOF experiments) in order to mimic high attraction (1 and 1/2), balanced (1/3 equal to repulsion curve) and low attraction (1/4 and 1/5) conditions. The basal subtraction value (bs) used for fitting both curves was added to the equations together with the noise factor ε, which ranged randomly from −10 to 10. The complete equation for both curves used for particle simulation was:

$$\text{curve} = \kappa[A \sin(\lambda x + \phi)] + \text{bs} + \varepsilon.$$

Particle distribution and analysis was carried out in MATLAB using the particle system toolbox, MATLAB particles version 2.1 (Buchholz, 2009). Particles representing FLRT1/3+ cells were arranged in a matrix of 6 rows and 36 columns spaced by 0.2 units and were given an attraction toward neighboring particles in both axes based on their x axis position using the fitted attraction (GOF) curve. Particles representing FLRT1/3 negative cells where arranged in a matrix of 5 rows and 35 columns that were shifted 0.1 units in both X/y axis with respect to the previous matrix to keep the same distances between particles of both matrices. These particles were set to repel neighboring particles from the previous matrix (which represents FLRT1/3+ cells). Their repulsion force was set based on their x axis position using the fitted repulsion (LOF) curve and multiplying the result by −1 (negative force). All particles received random speed (ranging from 6 to 12 arbitrary units) for moving along the Z axis and were simulated during 100 frames (0.001 units step time). After simulation, the position of every particle representing FLRT1/3+ cells (first matrix) was retrieved and analyzed based on minimum neighbor distance and 2D kernel distribution which determines density of particles based on total counts per region (total area was divided in 4x4 regions). Particle speed was calculated based on number of frames and final position of each particle, which was also represented in 3D by using surface plot (MATLAB).

in situ hybridization

For ISH, new ferret probes were designed and cloned based on Flrt1/3 DNA sequences from Ensembl.org data. The designed primers to perform the PCR from ferret cDNA were the following: Flrt1-foward TCAGCGTGCAGGTCATCTAC, Flrt1-reverse GCAGC CACAGGAGGTTACAG, Flrt3-foward TCTCCGACTGCTTTTCCTGT and Flrt3-reverse TATTCATTGCGTTCCCCTGT. Sense and antisense cRNA probes were synthesized and labeled with digoxigenin (DIG; Roche Diagnostics) according to the manufacturer's instructions. Briefly, 50 micron-thick frozen ferret brain sections were hybridized with DIG-labeled cRNA probes overnight in hybridization solution [50% formamide (Ambion), 10% dextran sulfate, 0.2% tRNA (Invitrogen), 1 × Denhardt's solution (from a 50 × stock; SIGMA), 1 × salt solution (containing 0.2 M NaCl, 0.01 M Tris, 5 mM NaH2PO4, 5 mM Na2HPO4, 5 mM EDTA, pH 7.5)]. After sections were washed, alkaline phosphatase-coupled anti-digoxigenin Fab fragments were applied. For visualization of the labeled cRNAs, sections were incubated in nitroblue tetrazolium (NBT)/5-bromo-4-chloro-3-indolyl phosphate (BCIP) solution [3.4 μl/ml from NBT stock and 3.5 μl/ml from BCIP stock in reaction buffer (100 mg/ml NBT stock in 70% dimethylformamide; 50 mg/ml BCIP stock in 100% dimethylformamide; Roche)]. Brain sections were processed for the detection of Flrt1 and Flrt3 mRNA using aforementioned probes, and developed in parallel and for an identical length of time. Digital images were obtained from equivalent rostro-caudal levels and latero-medial positions and with identical exposure settings. Color information was eliminated from images, and the brightness of signal above background noise was measured using ImageJ software. For each gene, 2 measurements per section, 3 sections per embryo were analyzed.

RNaseq analysis

RNaseq data were accessed from the NCBI Gene Expression Omnibus with accession numbers GEO: GSE80958 (Wang et al., 2016), GEO: GSE38805 (Fietz et al., 2012), GEO: GSE65000 (Florio et al., 2015) and the Allan Brain Atlas (http://www.brain-map.org) (Figure 6; Figure S6). Raw reads were processed with FASTX-Toolkit (http://hannonlab.cshl.edu/fastx_toolkit/) for initial quality control, where reads with a quality score > 20 and a nucleotide length > 20 were excluded. The processed reads were then mapped to Ensembl annotation files for human (GRCh37) and mouse (NCBIM37) genomes with TopHat (version 2.0.14) (Trapnell et al., 2012). Reads assigned to annotated genes were quantified with featureCounts (Liao et al., 2014) and used as input for DESeq2 (Love et al., 2014). The normalized output data were used to compare between orthologous genes of different length. Sequencing data of FLRTs relative to housekeeping genes is presented for cross-species comparisons (GAPDH in Figure 6 and PGK1 in Figure S6). For the regional cortical comparisons in Figure S6H,I, the same parameters described in Wang et al., 2016 were used. Briefly, RNA-seq data from early mid-trimester human fetuses at 12-19 pcw from the Allan Brain Atlas was compared to E14 mouse embryonic cortices. Values were log-transformed and expressed relative to GAPDH.

QUANTIFICATION AND STATISTICAL ANALYSIS

Statistical significance was determined using one-way ANOVA Tukey's post hoc test or unpaired Student's t test (for comparison between mutant and control mice) with the Prism version 5 (Graphpad Software). Statistical significance was defined as $p < 0.05$. All values in the text and in the figure legends indicate mean + SEM.

Supplemental Figures

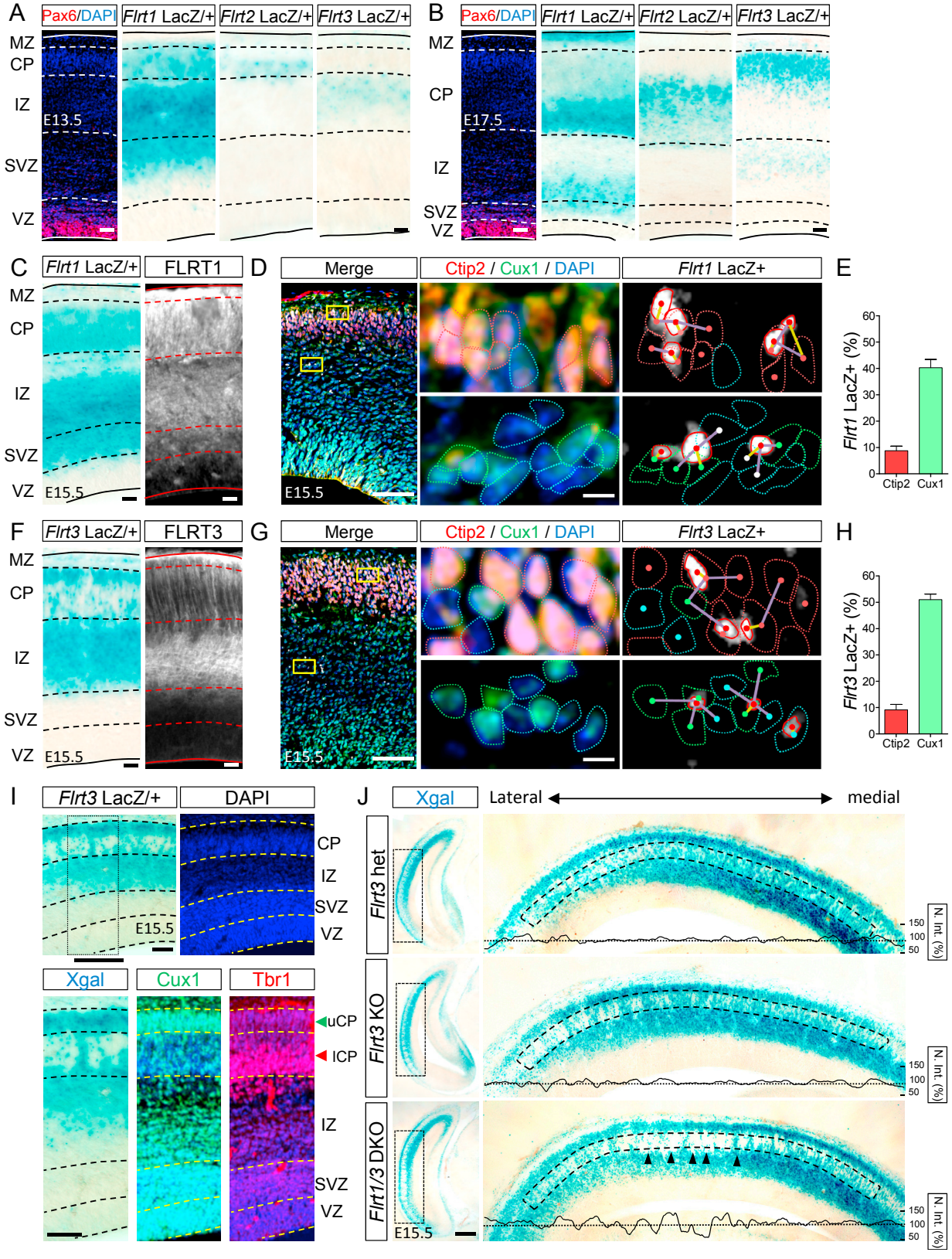

(legend on next page)

Figure S1. Expression of FLRTs in the Developing Mouse Cortex and Cell Clustering Phenotype in *Flrt1/3* DKO Mice, Related to Figure 1

(A and B) Xgal staining showing FLRT1-3 expression on coronal sections of E13.5 (A) and E17.5 (B) cortex from individual *Flrt1-3*$^{lacZ/lx}$ reporter lines. Cortical layers were identified by DAPI, and immunostaining for Pax6.

(C) Pattern of Xgal staining of FLRT1 at E15.5 (left image) in comparison to FLRT1 immunostaining (right image).

(D) Xgal staining of FLRT1 (white) on E15.5 coronal sections immunostained for upper layer (Cux1, green in merge) and lower layer (Ctip2, red) neuronal markers. Areas in yellow rectangles are shown with higher magnification on the right. Xgal precipitates were assigned to a particular cell based on the shortest distance between centers of mass. Centers of mass were calculated from the outlines of Xgal precipitates (red) and cells (dashed lines colored in pink for Ctip2, green for Cux1 or blue for remaining cells). Lines connecting the centers of mass are colored in magenta or yellow for the shortest one.

(E) Quantification of data shown in (D).

(F) Pattern of Xgal staining of FLRT3 at E15.5 (left image) in comparison to FLRT3 immunostaining (right image).

(G) Similar experiment as described in (D) except for FLRT3 expression.

(H) Quantification of data shown in (G).

(I) Xgal staining of FLRT3 on E15.5 coronal sections (left image) and DAPI staining (right image) to delineate cortical layers. Area in dashed rectangle is shown with higher magnification in lower panels. CP was subdivided into upper and lower CP based on Cux1 (upper) and Tbr1 (lower) staining of adjacent sections. Both regions were used to quantify F*lrt3* Xgal distribution (Figures 1D, 1G, and S1J).

(J) Xgal staining of caudal coronal sections from E15.5 *Flrt3* heterozygous *Flrt3*$^{lox/lacZ}$ (het), *Flrt3* conditional KO and *Flrt1/3* double KO embryos. Areas in dashed rectangles are shown with higher magnification on the right. Normalized intensity plots (N. int.) are shown, obtained from the areas delineated with a dashed rectangle. Abbreviations: Marginal zone (MZ), cortical plate (CP), intermediate zone (IZ), subventricular zone (SVZ) and ventricular zone (VZ).

The data are represented as mean ± SEM. Scale bars represent 150 μm (A, B, C), 200, 15 μm (D), 150 μm (F), 200, 15 μm (G), 140 μm (I) and 300 μm (E).

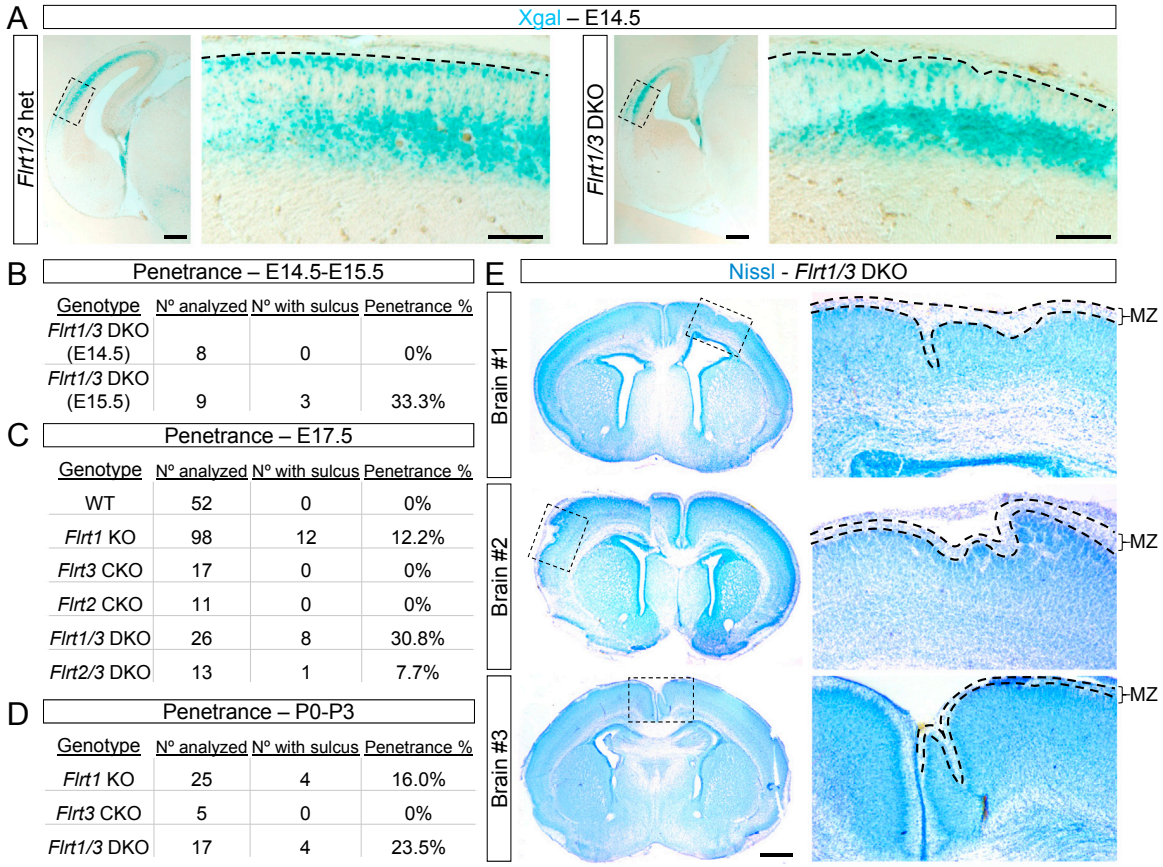

Genotype	Nº analyzed	Nº with sulcus	Penetrance %
Flrt1/3 DKO (E14.5)	8	0	0%
Flrt1/3 DKO (E15.5)	9	3	33.3%

Genotype	Nº analyzed	Nº with sulcus	Penetrance %
WT	52	0	0%
Flrt1 KO	98	12	12.2%
Flrt3 CKO	17	0	0%
Flrt2 CKO	11	0	0%
Flrt1/3 DKO	26	8	30.8%
Flrt2/3 DKO	13	1	7.7%

Genotype	Nº analyzed	Nº with sulcus	Penetrance %
Flrt1 KO	25	4	16.0%
Flrt3 CKO	5	0	0%
Flrt1/3 DKO	17	4	23.5%

(legend on next page)

Figure S2. *Flrt1/3* CKO Mice Develop Cortical Sulci, Related to Figure 2

(A) Xgal staining of caudal coronal sections from E14.5 *Flrt1/3* heterozygous and *Flrt1/3* double KO embryos. Dashed line delineates the surface of the upper CP.

(B–D) Cortical folding penetrance at embryonic and postnatal stages of the indicated genotypes. Brains were analyzed for the presence of one or more sulci as shown in Figure 2 and Figures S2 and S3.

(E) Nissl-stained postnatal brain sections from *Flrt1/3* DKO brains. Dashed rectangles are shown with higher magnification on the right and sulci are delineated by dashed lines.

(F) Coronal brain sections of *Flrt2/3* DKO brains at E17.5.

(G) Coronal brain sections of *Flrt1* single KO brains at E17.5. To distinguish upper and lower cortical plate, sections from panels F and G were immunostained with anti-Cux1 (upper, green) and anti-Ctip2 (lower, red) antibodies. Scale bars represent 150 μm (A), 800 μm (E) and 600 μm (F, G).

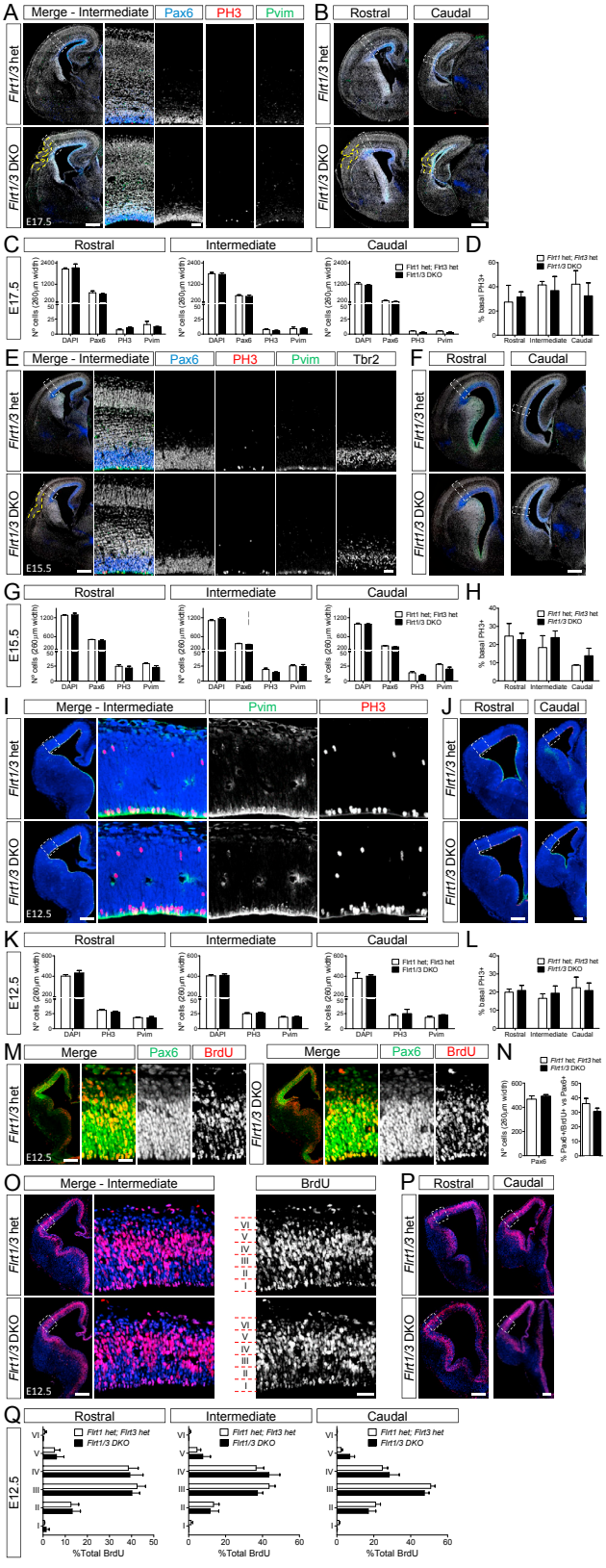

(legend on next page)

Figure S3. Cell Proliferation Is Unchanged in *Flrt1/3* DKO Brains, Related to Figure 3

(A and B) E17.5 cortices from rostral to caudal regions were labeled for neuronal progenitors Pax6 (blue), mitotic cells (PH3, red), dividing RG cells (Pvim, green) and DAPI (white). Areas in dashed rectangles in (A) are shown with higher magnification on the right. Yellow stippled line delineates a sulcus in the E17.5 *Flrt1/3* DKO section.

(C) Quantification of data shown in panels A,B (n = 3-6 mice per group. No significant changes between groups, unpaired Student's t test).

(D) Proportion of basal mitotic cells (PH3) from rostral to caudal regions (n = 3-6 mice per group. No significant changes between groups, unpaired Student's t test).

(E and F) Similar experiment as shown in panels A,B except for E15.5 cortices and including Tbr2 staining (white) .

(G) Quantification of data shown in panels E,F (n = 3-5 mice per group. No significant changes between groups, unpaired Student's t test).

(H) Proportion of basal mitotic cells (PH3) from rostral to caudal regions (n = 3-5 mice per group. No significant changes between groups, unpaired Student's t test).

(I and J) E12.5 cortices from rostral to caudal regions were labeled for mitotic cells (PH3, red) and dividing RG cells (Pvim, green). Areas in dashed rectangles in (I) are shown with higher magnification on the right.

(K) Quantification of data shown in (I) and (J) (n = 3-4 mice per group. No significant changes between groups, unpaired Student's t test).

(L) Proportion of basal mitotic cells (PH3) from rostral to caudal regions (n = 3-4 mice per group. No significant changes between groups, unpaired Student's t test).

(M) Control and mutant E12.5 cortices previously labeled with a short pulse (1.5h) of BrdU (red) were immunostained for neuronal progenitors (Pax6, green in the merge).

(N) Quantification of data shown in (M) (n = 3-4 mice per group. No significant changes between groups, unpaired Student's t test).

(O and P) Same experiment as in M except that BrdU-labeled brains (red) were counterstained with Dapi (blue).

(Q) Distribution of BrdU+ cells was quantified using a grid of 6 equal horizontal bins (I-VI) of data shown in (O) and (P) (n = 3-4 mice per group. No significant changes between groups, unpaired Student's t test).

The data are represented as mean ± SEM. Scale bars represent 400, 150 μm (A and B), 400, 150 μm (E and F), 300, 100 μm (I and J), 300, 100 μm (M) and 300,100 μm (O).

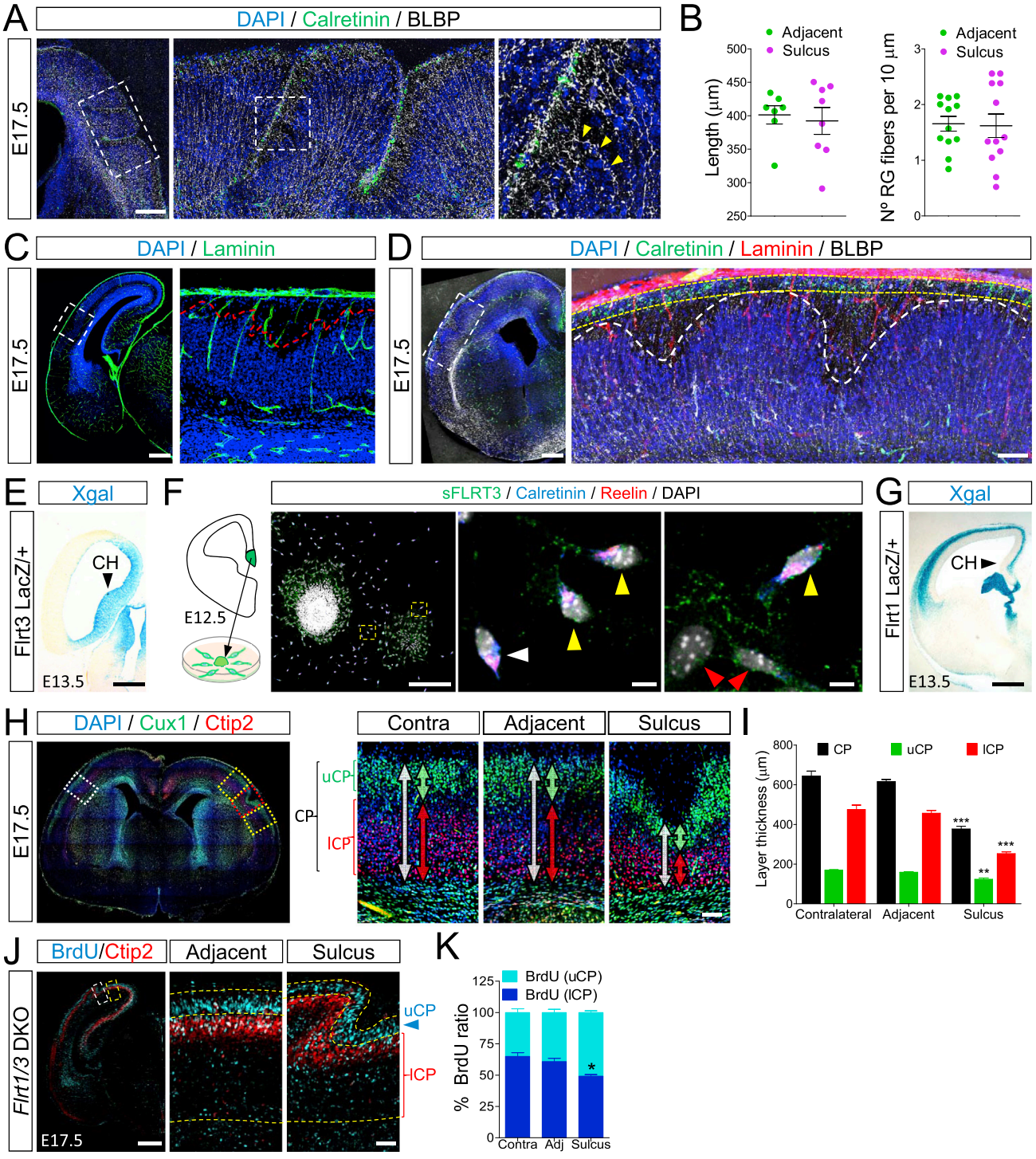

Figure S4. Radial Glia Fibers and the Basal Membrane Are Unchanged in *Flrt1/3* DKO Brains, Related to Figure 3

(A) E17.5 *Flrt1/3* DKO cortex immunostained for BLBP (white) to visualize radial glia (RG) and for calretinin (green) a marker for Cajal-Retzius cells (CR). Nuclei are stained with DAPI (blue). Yellow arrows indicate RG fibers that converge to the sulcal pit. Note that CR cells follow the MZ into the sulcal pit.

(B) Quantification of the length of traced RG fibers (see example image in Figure 3D) and of the density of fibers, n = 7 adjacent fibers, n = 8 sulcus fibers (left graph) and n = 12 sections (right graph) from 5 *Flrt1/3* DKO brains.

(C) E17.5 *Flrt1/3* DKO cortex immunostained for laminin (green), a marker for basal membrane, and DAPI (blue). Dashed rectangle is shown with higher magnification on the right and the emerging sulcus is delineated by a red dashed line.

(legend continued on next page)

(D) E17.5 *Flrt1/3* DKO cortex immunostained for laminin (red), calretinin (green), BLBP (white) and DAPI (blue). Dashed rectangle is shown with higher magnification on the right and sulci are delineated by a white dashed line. The MZ is outlined with a yellow dashed line. CR cells are within the MZ.
(E) Xgal staining showing FLRT3 expression on sagittal sections of E13.5 cortex from *Flrt3*$^{lacZ/lx}$ reporter line. Cortical hem (CH) position is indicated by black arrowhead.
(F) Schematic representation of experimental design. E12.5 CH explants were cultured for 1 day and immunostained for FLRT3 (surface staining, green), calretinin (blue), reelin (red) and DAPI (white). Yellow arrowheads indicate CR cells expressing FLRT3, white arrowhead shows CR cell negative for FLRT3 and red arrowheads show FLRT3-positive cells which are not CR.
(G) Xgal staining showing FLRT1 expression on coronal sections of E13.5 cortex from *Flrt1*$^{lacZ/lx}$ reporter line. CH position is indicated by black arrowhead.
(H) Coronal brain sections of *Flrt1/3* DKO brain at E17.5. To distinguish upper and lower cortical plate, sections were immunostained with anti-Cux1 (upper, green) and anti-Ctip2 (lower, red) antibodies. Dashed rectangles are shown with higher magnification on the right. Arrows indicate the thickness of CP (white), upper (green) and lower (red) CP.
(I) Quantification of cortical thickness as shown in (H) (n = 12 sections from a total of 5 mutant brains). $^{**}p < 0.01$, $^{***}p < 0.001$ one-way ANOVA test with Tukey's post hoc analysis.
(J) E17.5 *Flrt1/3* DKO cortex labeled for BrdU (blue, E14.5 injection) and deeper layer neurons (Ctip2, red). Areas in dashed rectangles are shown with higher magnification on the right. Yellow dashed lines delineate the margins of upper and lower CP.
(K) Quantification of data shown in (L). $^{*}p < 0.05$, one-way ANOVA test with Tukey's post hoc analysis.
The data are represented as mean ± SEM. Scale bars represent 400 μm (A), 300,100 μm (C,D), 300 μm (E, G), 120, 15 μm (F), 300 μm (H) and 500 μm and 90 μm (J). 150 μm (J) and 120 μm (L).

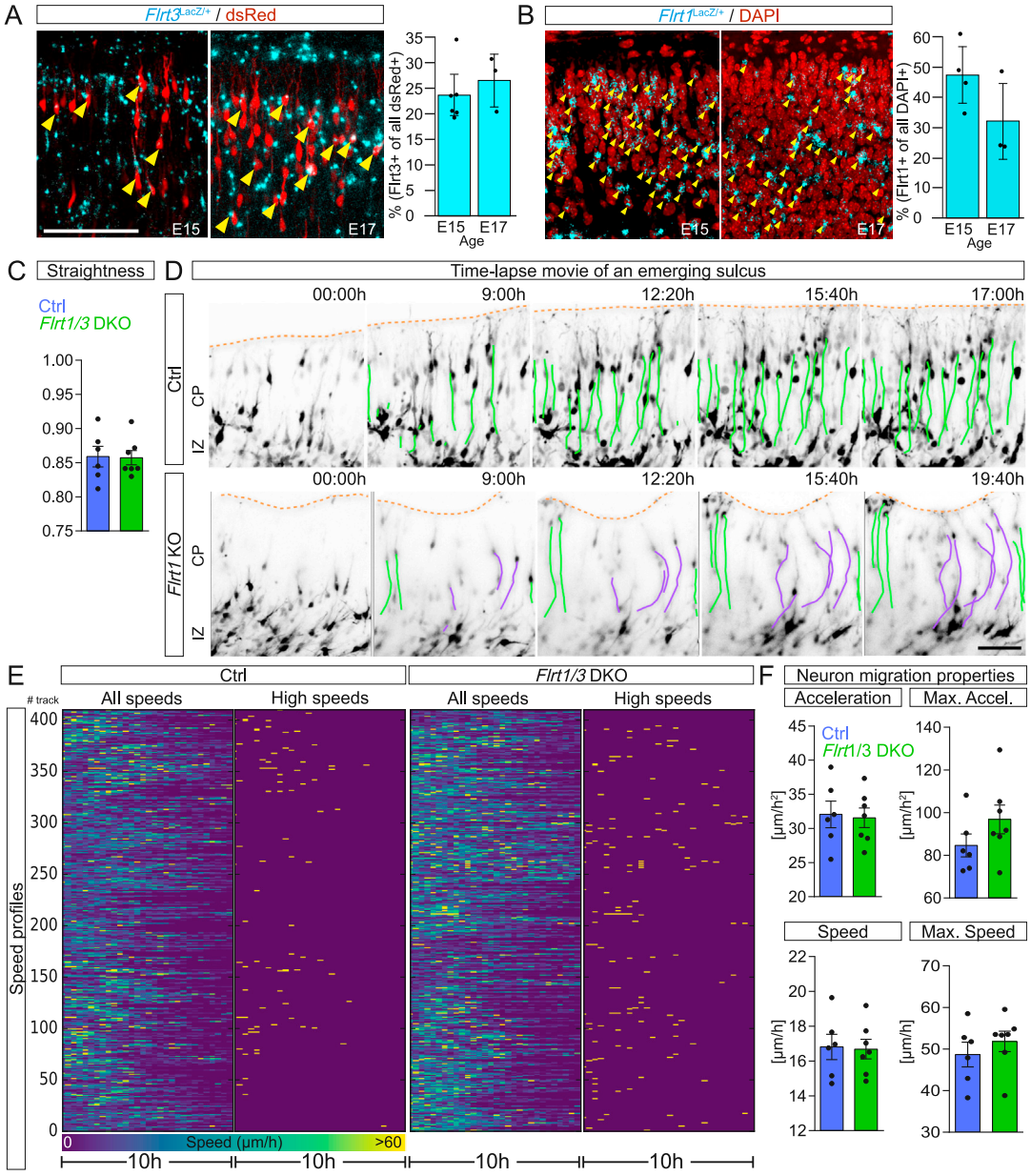

Figure S5. Faster Speed Profiles of *Flrt1/3* DKO Neurons, Related to Figure 4

(A) *Flrt3*$^{lacZ/+}$ embryos were electroporated in utero at E13.5 using a combination of pCAG-Cre and the pCALNL-DsRed reporter plasmid (Red staining). Xgal staining (blue) performed at E15.5 or E17.5 revealed that approximately 25% of all electroporated neurons expressed FLRT3 (right graph, n = 3-6 brains).

(B) Individual *Flrt1*$^{lacZ/+}$ reporter line embryos stained for beta-galactosidase (blue) at E15.5 or E17.5 revealed that 32%–48% of all CP neurons expressed FLRT1 (right graph, n = 3-4 brains).

(C) Quantification of the average straightness of the paths of electroporated neurons migrating into the cortical plate in cultured E15.5 cerebral cortex slices from data shown in Figure 4.

(D) Still pictures of time-lapse movies of an emerging sulcus in a *Flrt1*$^{-/-}$*Flrt3*$^{lox/lox}$ background electroporated with a combination of pCAG-Cre and pCALNL-DsRed plasmid (Flrt1 KO, bottom) compared to electroporated controls. Live imaging shows that in the region of the sulcus neurons follow a curved track (purple) compared to straight tracks in adjacent regions (green) or control sections. Acquisition interval, 20min. Scale bar, 50µm.

(E) Color-coded speed profiles of > 400 tracked neurons from data shown in Figure 4 during time acquisition interval (10 h). Each speed segment represents 20min. High speeds, > 58µm/h.

(F) Quantification of average speed, acceleration and their maximum values from data shown in (C). n ≥ 6 experiments per condition comprising 8-10 brains. The data are represented as mean ± SEM. Scale bars represent 200 µm (A), 60 µm (D).

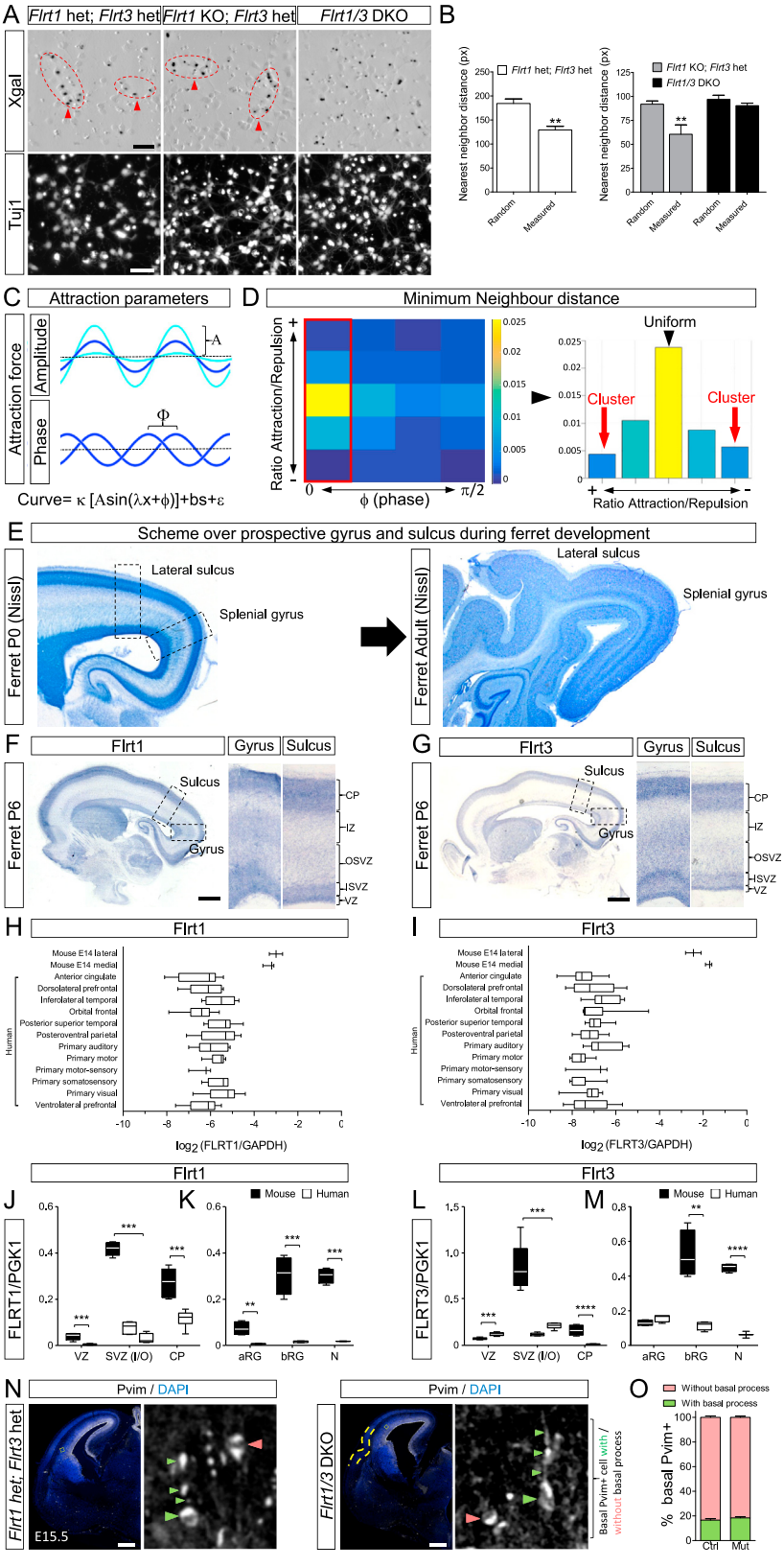

(legend on next page)

Figure S6. Clustering of Flrt1/3-Positive Neurons In Vitro and FLRT Expression in Gyrencephalic Species, Related to Figures 5 and 6

(A) Brightfield images of cortical neurons from heterozygous, *FLRT1* KO and *Flrt1/3* DKO embryos at E15.5 cultured for 2 days. FLRT3-expressing neurons are identified by Xgal staining (black dots). Neurons are identified by Tuj1 immunostaining.

(B) Quantification of the nearest neighbor distance between Xgal+ cells shown in A. n = 3-5 animals/cultures per group. **p < 0.01, unpaired Student's t test.

(C) Parameters modulating the attraction force between particles representing FLRT1/3+ neurons. Amplitude (A) modulates the strength while phase (ϕ) reflects its position with respect to the repulsive force. κ and bs (basal subtraction) are parameters used to modulate and fit both curves respectively, while ε represents the noise added to the system (see material and STAR Methods).

(D) Quantification of minimum neighbor distance between particles with different attraction amplitude and phase (as shown in [C]). Every square represents the average of 10 simulations comprising 480 particles with specific amplitude and phase. Red rectangle indicates the condition where particles clustered when attraction was high or low but showed uniform distribution when both forces were balanced. This condition requires similar phase for both attraction and repulsion. Quantification of this particular condition is shown on the right.

(E) Sagittal sections of ferret cortex at P0 and adult stained with Nissl. Dashed boxes indicate prospective lateral sulcus and splenial gyrus which are fully developed in the adult section on the right. Note the absence of cortical folding at P0.

(F and G) In situ hybridization for FLRT1 and FLRT3 in sagittal sections of ferret at P6. Dashed rectangles delineate prospective lateral sulcus (Sulcus) and splenial gyrus (Gyrus). Quantification is shown in Figure 6.

(H–M) Comparison of FLRT1 and FLRT3 expression between mouse and human with sequencing data from Wang et al. (2016) (GEO: GSE80958), Fietz et al. (2012) (GEO: GSE38805), Florio et al. (2015) (GEO: GSE65000) and the Allan Brain Atlas (http://www.brain-map.org). Expression normalized to housekeeping gene GAPDH (H and I) and PGK1 (J–M). Whiskers in boxplot represents min and max. Unpaired Student's t test where **p < 0.01, ***p < 0.001, ****p < 0.0001.

(N) E15.5 control and *Flrt1/3* DKO sections immunostained for Pvim (white) and DAPI (blue). Dashed rectangle is shown with higher magnification on the right and sulci is delineated by a yellow dashed line. Basal Pvim-positive cells with and without a basal process are indicated with green and pink arrowhead respectively. Basal process is indicated with small green arrowheads.

(O) Quantification of the proportion of basal Pvim-positive cells with/without basal process as shown in (J) (n = 4-5 sections from each 4-5 mice per group. No significant changes between groups, unpaired Student's t test).

The data are represented as mean ± SEM. Scale bars represent 50μm (A), 1mm (F and G) and 300 μm (N).

3.2 Second publication

3.2.1 FLRT structure: Balancing repulsion and adhesion in cortical and vascular development

CellPress

Neuron
Article

FLRT Structure: Balancing Repulsion and Cell Adhesion in Cortical and Vascular Development

Elena Seiradake,[1,7] Daniel del Toro,[2,7] Daniel Nagel,[2,5] Florian Cop,[3,4] Ricarda Härtl,[3,4] Tobias Ruff,[2] Gönül Seyit-Bremer,[2] Karl Harlos,[1] Ellen Clare Border,[1] Amparo Acker-Palmer,[3,4] E. Yvonne Jones,[1,*] and Rüdiger Klein[2,6,*]

[1]Division of Structural Biology, Wellcome Trust Centre for Human Genetics, University of Oxford, Roosevelt Drive, OX3 7BN Oxford, UK
[2]Max Planck Institute of Neurobiology, Am Klopferspitz 18, 82152 Martinsried, Germany
[3]Institute of Cell Biology and Neuroscience and Buchmann Institute for Molecular Life Sciences, Goethe University Frankfurt, Max-von-Laue-Str. 15, 60438 Frankfurt am Main, Germany
[4]Focus Program Translational Neurosciences, Johannes Gutenberg University Mainz, Saarstr. 21, 55122 Mainz, Germany
[5]Graduate School of Systemic Neurosciences, Ludwig-Maximilians-University Munich, Großhaderner Str. 2, 82152 Planegg-Martinsried, Germany
[6]Munich Cluster for Systems Neurology (SyNergy), 80336 Munich, Germany
[7]Co-first author
*Correspondence: yvonne@strubi.ox.ac.uk (E.Y.J.), rklein@neuro.mpg.de (R.K.)
http://dx.doi.org/10.1016/j.neuron.2014.10.008

SUMMARY

FLRTs are broadly expressed proteins with the unique property of acting as homophilic cell adhesion molecules and as heterophilic repulsive ligands of Unc5/Netrin receptors. How these functions direct cell behavior and the molecular mechanisms involved remain largely unclear. Here we use X-ray crystallography to reveal the distinct structural bases for FLRT-mediated cell adhesion and repulsion in neurons. We apply this knowledge to elucidate FLRT functions during cortical development. We show that FLRTs regulate both the radial migration of pyramidal neurons, as well as their tangential spread. Mechanistically, radial migration is controlled by repulsive FLRT2-Unc5D interactions, while spatial organization in the tangential axis involves adhesive FLRT-FLRT interactions. Further, we show that the fundamental mechanisms of FLRT adhesion and repulsion are conserved between neurons and vascular endothelial cells. Our results reveal FLRTs as powerful guidance factors with structurally encoded repulsive and adhesive surfaces.

INTRODUCTION

The development of complex tissues depends on a balance of intercellular adhesive and repulsive signaling. Cell adhesion provides spatial stability to nonmoving cells and traction for migrating cells (Solecki, 2012). Cell repulsion is the dominant mechanism for cell and axon segregation, tissue boundary formation, and topographic map formation (Dahmann et al., 2011; Klein and Kania, 2014). Several families of cell surface receptors, termed cell adhesion molecules (CAMs), provide homophilic (e.g., cadherins; Brasch et al., 2012; Cavallaro and Dejana, 2011) or heterophilic (e.g., integrins; Luo et al., 2007) cell-cell adhesive interactions. Members of the Netrin, semaphorin, slit, and ephrin families of cell guidance molecules act as cell-attached or secreted ligands, mediating repulsive or attractive/adhesive signaling via heterophilic interactions with cognate cell surface receptors (Bashaw and Klein, 2010; Kolodkin and Tessier-Lavigne, 2011). The fibronectin leucine-rich transmembrane proteins (FLRTs) are distinctive in sharing the characteristics of both functional groupings; they function as homophilic CAMs (Karaulanov et al., 2006; Maretto et al., 2008; Müller et al., 2011) and as heterophilic chemorepellents interacting with uncoordinated-5 (Unc5) receptors (Karaulanov et al., 2009; Yamagishi et al., 2011). Molecular-level insights into the mechanisms underlying these diverse modes of action are lacking, as is clarity on the contributions of adhesive versus repulsive activities to FLRT function in vivo.

The FLRTs (FLRT1–3) are regulators of early embryonic, vascular, and neural development (Egea et al., 2008; Leyva-Díaz et al., 2014; Maretto et al., 2008; Müller et al., 2011; O'Sullivan et al., 2012; Yamagishi et al., 2011). The homophilic and Unc5 interactions both involve the FLRT N-terminal leucine-rich repeat domain (LRR) (Karaulanov et al., 2006, 2009). This domain is followed by a linker region, a type 3 fibronectin domain (FN) and a juxtamembrane linker, which contains a metalloprotease cleavage site (Figure 1A). Proteolytic shedding of the FLRT2 ectodomain controls the migration of Unc5D-expressing neurons in the developing cortex (Yamagishi et al., 2011).

Like FLRTs, Unc5 receptors (Unc5A–D) are type 1 transmembrane proteins. The extracellular region contains two immunoglobulin-type domains (Ig1 and Ig2) and two thrombospondin-like domains (TSP1 and TSP2) (Figure 1A). Unc5 receptors act as classical dependence and repulsive signaling receptors for secreted Netrin ligands in the neural system (Lai Wing Sun et al., 2011). Netrin/Unc5B signaling also directs vascular development by controlling blood vessel sprouting (Larrivée et al., 2007). However, Netrin is not present in many Unc5-expressing tissues, for example, in the developing cortex, suggesting a dependence on other ligands.

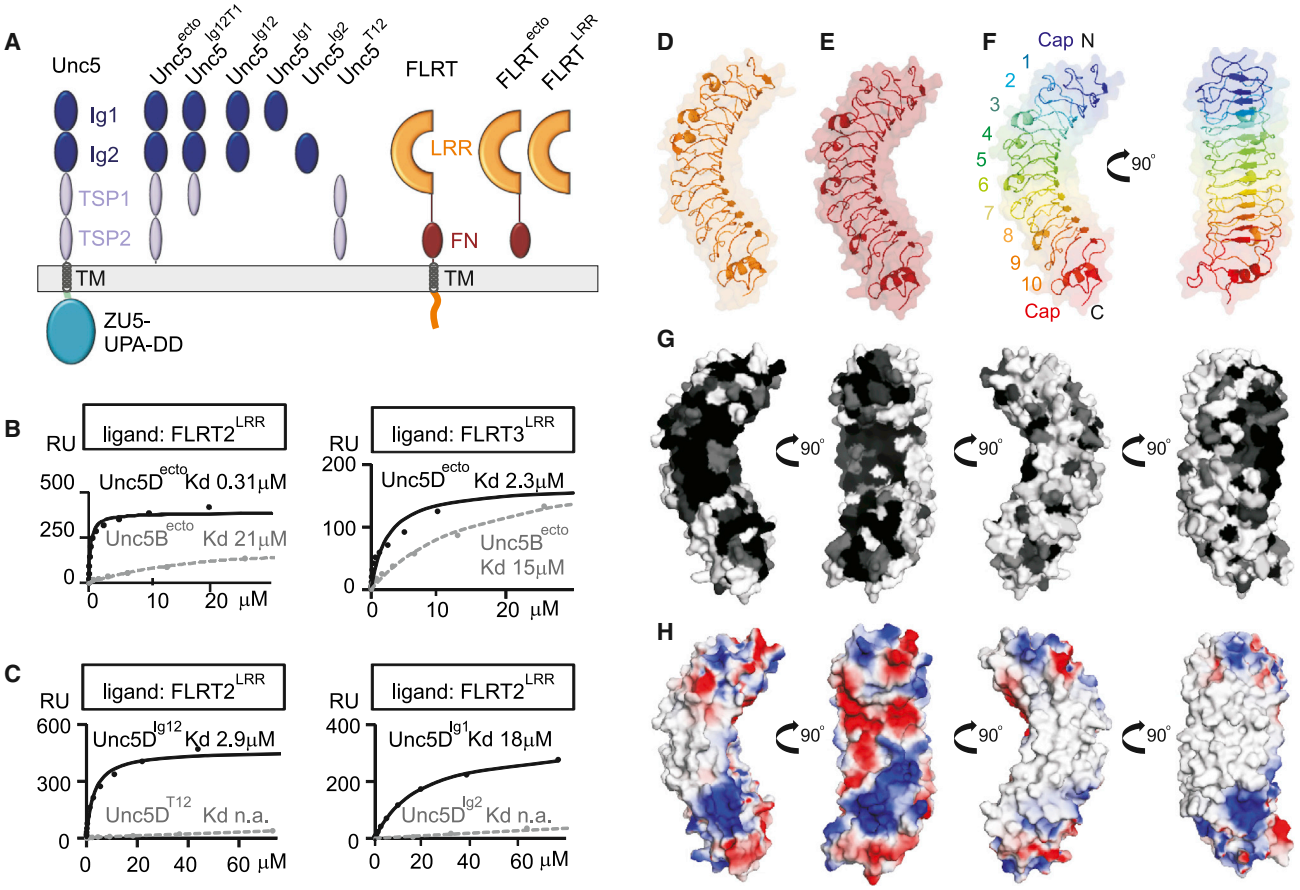

Figure 1. SPR Experiments and Crystal Structures of FLRT^{LRR} Proteins

(A) Overview of *Flrt* and *Unc5* constructs used in SPR experiments. The intracellular region of Unc5 is composed of three domains: ZU5, UPA, and a death domain (DD) (Wang et al., 2009).

(B) We amine-coupled FLRT2^{LRR} (left) or FLRT3^{LRR} (right) on a CM5 chip and measured the binding of Unc5D^{ecto} (black, solid lines) and Unc5B^{ecto} (gray, dashed lines). Plotted are equilibrium response units (RU) at different analyte concentrations (μM). Curves were fitted and Kds calculated with a 1:1 binding model.

(C) As in (B), but measuring the binding of different Unc5D fragments to immobilized FLRT2^{LRR}.

(D) The crystal structure of FLRT2^{LRR} is shown as a surface and ribbon diagram.

(E) FLRT3^{LRR} is shown.

(F) FLRT3^{LRR} colored according to the rainbow. Blue, N terminus; red, C terminus. The *lrr* motifs are numbered 1–10, and the positions of the cap structures are indicated.

(G) Surface views of FLRT3^{LRR}, colored according to sequence conservation within FLRT2/FLRT3 from mouse, fish, frog, and bird. Black, highest conservation; white, lowest conservation.

(H) Views of FLRT3^{LRR} oriented as in (D), colored according to surface electrostatic surface potential (red, −69 kT/e; white, 0 kT/e; blue, +69 kT/e). k, Boltzmann's constant; T, temperature (310 K); e, $-1.6021766 \times 10^{-19}$ coulombs.

The dual functionality of FLRTs as CAMs that also elicit repulsion (as one of several possible Unc5 ligands) renders the analysis of their contributions in vivo challenging. Can cells integrate FLRT adhesive and repulsive signaling activities, and what are the contributions of these contradictory functionalities in different cellular contexts? To address the complexities of FLRT function we first sought to identify the structural determinants of the homophilic and heterophilic interactions.

Here we report crystal structures of FLRT2, FLRT3, Unc5A, Unc5D, and a FLRT2-Unc5D complex. Based on these data we assign homophilic adhesion and heterophilic repulsion to distinct molecular surfaces of FLRT. We show that by using these surfaces, FLRT can trigger both adhesive and repulsive signals in the same receiving cell, leading to an integrative response. Besides confirming that FLRT2/Unc5D repulsion regulates the radial migration of cortical neurons, we show here that FLRT3 also acts as a CAM in cortical development and modulates the tangential spread of pyramidal neurons. We further identify FLRT3 as a controlling factor in retinal vascularization. We demonstrate that FLRT controls the migration of human umbilical artery endothelial cells (HUAECs) through a similar mechanism to that which we found in the neuronal system. Taken together, our results reveal FLRT functions in cortical patterning and vascular development, and establish the FLRTs

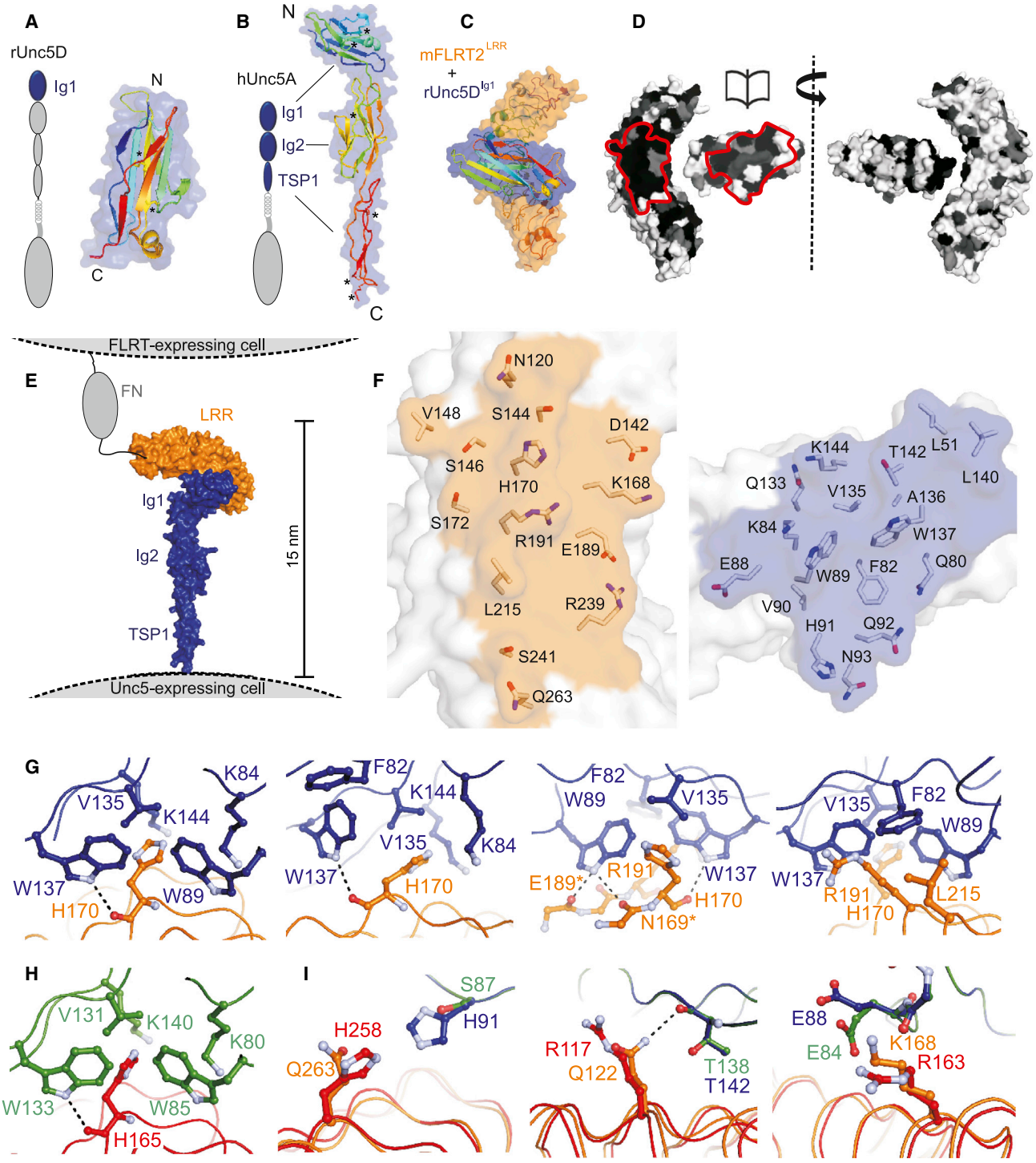

Figure 2. Crystal Structures of Unc5 and a FLRT2-Unc5D Complex

(A) The structure of Unc5D^{Ig1} is shown as surface and rainbow ribbons (N terminus, blue; C terminus, red). Asterisks mark disulphide bridges.

(B) Structure of the complete human Unc5A ectodomain. Note that human Unc5A contains only one TSP domain. Asterisks mark disulphide bridges.

(C) Structure of FLRT2^{LRR} (orange with rainbow ribbons) in complex with Unc5D^{Ig1} (blue with rainbow ribbons).

(D) Left: view of FLRT2^{LRR} and Unc5D^{Ig1} as found in complex structure ("open book view"). Interacting surfaces are encircled in red. Surface colors represent sequence conservation within FLRT2/FLRT3 or Unc5B/Unc5D, respectively, from mouse, fish, frog, and bird. Black, highest conservation; white, lowest conservation. Right: FLRT2^{LRR} and Unc5D^{Ig1} rotated by 180° to reveal their less-conserved faces.

(legend continued on next page)

as a bimodal guidance system that combines homophilic adhesion with heterophilic repulsion.

RESULTS

Characterization of a High-Affinity Minimal FLRT-Unc5 Complex

We performed surface plasmon resonance (SPR) measurements using purified ectodomains of Unc5A, Unc5B, and Unc5D ($Unc5A^{ecto}$, $Unc5B^{ecto}$, $Unc5D^{ecto}$) and the LRR domains of their ligands FLRT2 and FLRT3 ($FLRT2^{LRR}$, $FLRT3^{LRR}$). These revealed a hierarchy of equilibrium dissociation constants (Kds), with the affinity of FLRT2 and Unc5D being the highest (Figure 1B; Table S1 available online). The relative affinities are consistent with those from previous cell-based binding assays (Karaulanov et al., 2009; Yamagishi et al., 2011), although the absolute values are lower, presumably due to differences in the techniques applied.

We also used SPR to test the binding of $FLRT2^{LRR}$ to Unc5D fragments encompassing different regions of the ectodomain ($Unc5D^{ecto}$, $Unc5D^{Ig12}$, $Unc5D^{Ig1}$, $Unc5D^{Ig2}$, and $Unc5D^{T12}$; depicted in Figure 1A). The results showed that the N-terminal Unc5D Ig domain ($Unc5D^{Ig1}$) harbors the major $FLRT2^{LRR}$-binding site (Figure 1C).

Crystal Structures of $FLRT^{LRR}$ Reveal Conserved Surface Patches

We determined the crystal structures of mouse $FLRT2^{LRR}$ and $FLRT3^{LRR}$. Crystallographic details are provided in Table S2. Both structures consist of ten *lrr* repeats plus flanking cap structures, together forming a horseshoe-shaped solenoid (Figures 1D–1F, S1A, and S1B). Superposition underscores the similarity of the two structures with a root-mean-square deviation (rmsd) (Krissinel and Henrick, 2004) of 1.17 Å for 320 (out of 321) corresponding Cα atoms. We generated sequence conservation scores (Glaser et al., 2003) using alignments of FLRT2 and FLRT3 from mouse, chicken, frog, and fish and mapped these onto the $FLRT^{LRR}$ structures. A sequence-conserved patch extends from the concave to a lateral side surface of both $FLRT^{LRR}$ structures (Figures 1G and S1B). Comparison of $FLRT2^{LRR}$ with structures in the Dali database (Holm and Rosenström, 2010) shows strongest similarity (rmsd for 264 aligned Cα atoms = 1.8) with the cell adhesion protein decorin, which is known to dimerize via the concave surface of its LRR domain (Scott et al., 2004). The predominantly charged concave surfaces of $FLRT2^{LRR}$ and $FLRT3^{LRR}$ (Figures 1H and S1B) provide lattice contacts in all of our crystal structures (Figure S1), suggesting that these regions could mediate functional FLRT-FLRT interactions.

A $FLRT2^{LRR}$-$Unc5D^{Ig1}$ Complex Reveals a Conserved Binding Interface

We determined the crystal structure of rat $Unc5D^{Ig1}$ (Table S2). The domain conforms to the Ig subtype 1 topology (Chothia and Jones, 1997) (Figure 2A). The structure is most similar to that of the N-terminal Ig domain of receptor protein tyrosine phosphatase delta (RPTPδ, rmsd for 86 aligned Cα atoms = 1.9 Å), although Unc5D lacks the positively charged surface patch that mediates the RPTPδ-glycosaminoglycan interaction (Coles et al., 2011).

We also solved a crystal structure for $Unc5A^{Ig12T2}$ (Table S2), thereby revealing the fold of the second Ig domain, also subtype 1, and the TSP domain (Figure 2B). The crystallized construct corresponds to the complete human Unc5A isoform 1 ectodomain. The overall structure is elongated and lacks extended interdomain linkers. All human Unc5A isoforms and mouse Unc5A isoform 2 lack the first of the two TSP domains that are present in other Unc5 homologs. Otherwise, the sequences of Unc5A–D are 44%–63% conserved between the human Unc5 homologs.

We solved the crystal structure of $FLRT2^{LRR}$ in complex with $Unc5D^{Ig1}$ (Table S2). Crystals diffracted to 4 Å only; however, the higher-resolution models of unliganded $FLRT2^{LRR}$ and $Unc5D^{Ig1}$ provide detailed information on the location of residues within each chain. $Unc5^{Ig1}$ binds to $FLRT2^{LRR}$ burying a total of ~1,280 $Å^2$ protein surface, which is highly sequence conserved on both sides (Figures 2C and 2D).

Superposition of $Unc5A^{Ig12T}$ with $Unc5D^{Ig1}$ as found in complex with $FLRT2^{LRR}$ generates a model in which the domains downstream of Unc5 Ig1 extend away from the interface with $FLRT^{LRR}$, suggesting that the Ig1 domain is the only interacting domain (Figure 2E). Based on this model alone, we cannot rule out that the extracellular FLRT regions downstream of the LRR domain also interact with Unc5. However, in SPR experiments we measured similar Unc5-binding affinities for $FLRT^{ecto}$ and $FLRT^{LRR}$ constructs (data not shown), suggesting that there is no major second Unc5-binding site on FLRT. We provide further support for this conclusion using a mutagenesis approach (see next section).

The core of the FLRT2-Unc5D-binding interface contains predominantly hydrophobic and positively charged residues (Figures 2F and 2G). The conserved FLRT2 histidine H170 forms a central anchor point that reaches deep into a hydrophobic pocket formed by Unc5D F82, K84, W89, V135, W137, and K144 and likely provides a hydrogen bond to Unc5D W137 (Figure 2G). FLRT2 R191 and L215 may stabilize this arrangement by providing additional contacts to Unc5D F82 and W137. The main residues forming the hydrophobic FLRT2-binding surface of Unc5D are fully conserved in Unc5B (Figure 2H), with the exception of F82, which is replaced by a tyrosine (Y78).

(E) The model of a FLRT-Unc5 complex between the surfaces of opposing cells was created by superposing Unc5A ectodomain (blue) on $Unc5D^{Ig1}$ as found in complex with $FLRT2^{LRR}$ (orange). Cell surfaces and FLRT2 regions that were not crystallized are depicted in gray.
(F) Residues within the interacting surfaces of FLRT2 (orange) and Unc5D (blue) are shown.
(G) Views of the interface between FLRT2 (orange) and Unc5D (blue). Selected residues are shown as sticks. Main chain stick atoms are not shown for all residues. Residues of which the main chain, but not the side chain, atoms are shown are marked with an asterisk. Putative hydrogen bonds are shown as dotted lines.
(H) View of FLRT-Unc5 interface residues as in (F), but showing the $FLRT3^{LRR}$ structure (red) and a homology model of $Unc5B^{Ig1}$ (green), in an arrangement based on the $FLRT2^{LRR}$-$Unc5D^{Ig1}$ structure.
(I) Views of interface residues that are not conserved between Unc5D/Unc5B (green/blue) and FLRT2/ FLRT3 (orange/red).

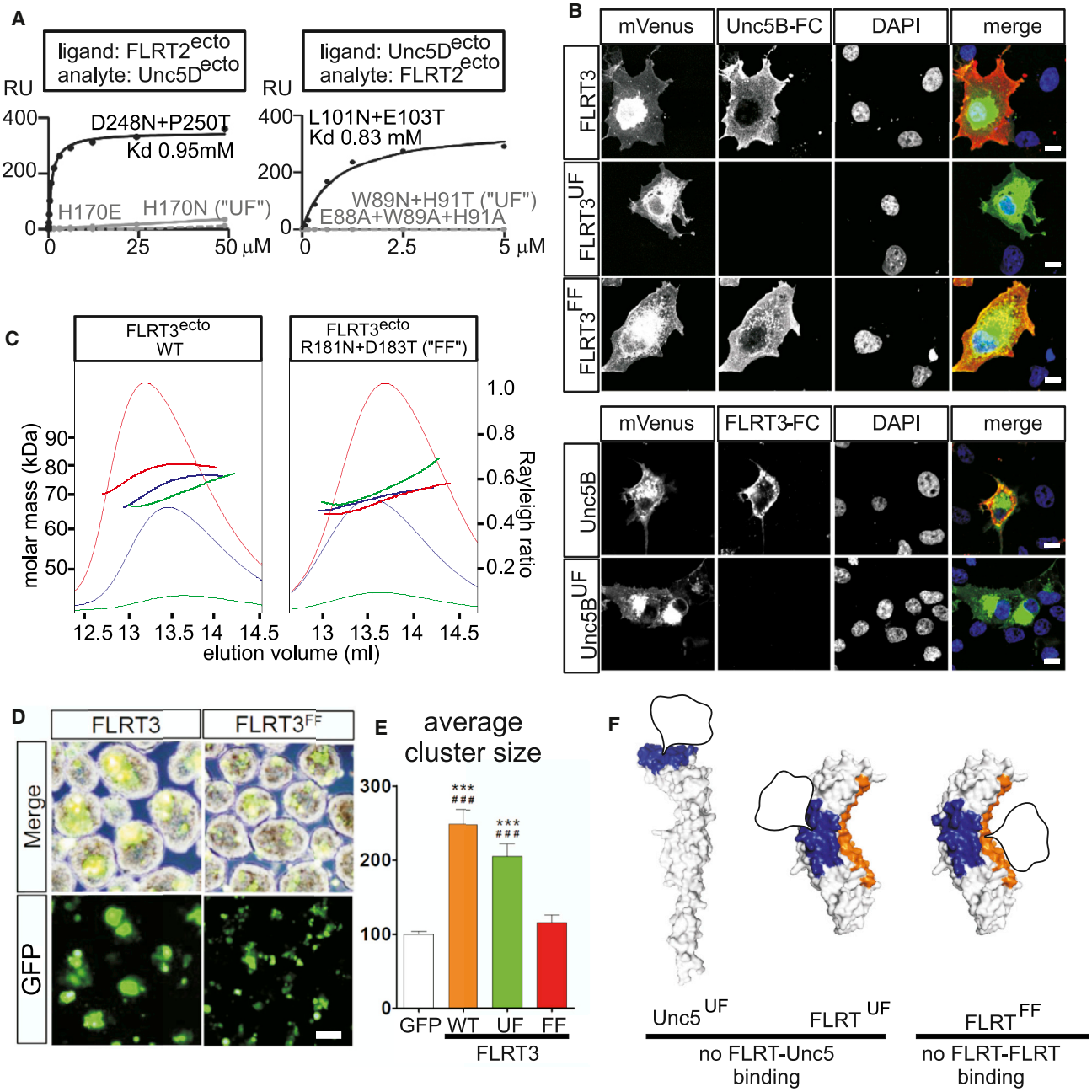

Figure 3. Distinct Mutations Abolish FLRT-Unc5 and FLRT-FLRT Binding

(A) SPR data showing that FLRT2 H170E or H170N and Unc5D W89N+H91T or E88A+W89A+H91A disrupt FLRT2-Unc5D binding. FLRT2 D248N+P250T and Unc5D L101N+E103T do not disrupt binding. The nonbinding mutants FLRT2 H170E and Unc5D W89N+H91T are henceforth denoted as "UF."

(B) We used an immunofluorescence-based binding assay (Yamagishi et al., 2011) to confirm mVenus-tagged FLRT3^{UF} and Unc5B^{UF} at the surface of cells do not bind Unc5B and FLRT3 ectodomains, respectively. Scale bars, 10 μm. Results for FLRT2 and Unc5D mutants are shown in Figure S2B.

(C) SEC-MALS experiments using wild-type FLRT3^{ecto} and mutant proteins. Rayleigh ratios are depicted as thin lines (right axis). Protein concentrations at the peak maxima are ~0.1 mg/ml (green curves), ~0.5 mg/ml (blue curves), and ~1 mg/ml (red curves). Calculated masses are shown as thick lines (left axis). Multimerization leads to an increase in apparent molecular mass of wild-type FLRT3^{ecto} at high concentrations, but not of the mutant FLRT3^{ectoFF}. Note that FLRT3^{ectoUF} also multimerizes at high concentrations (Figure S2D).

(D) HEK cells transfected with control or *Flrt3* constructs (pCAGIG) were cultured in suspension. The average cluster size of transfected cells was measured and the results normalized to the GFP control. Scale bars, 40 μm. Data for FLRT2 are shown in Figures S2E and S2F.

(legend continued on next page)

The high degree of sequence conservation at the FLRT-Unc5-binding interface is in agreement with the observed binding promiscuity. Subtle differences in binding affinities for different homologs are likely due to sequence variations at the periphery of the binding interface (Figure 2I).

Histidine residues have a side chain $pKa_{(His)}$ of ~6, below which they are protonated. We predicted that the protonated FLRT2 H170 would be incompatible with binding to the hydrophobic binding pocket on Unc5D. Indeed, at pH ~5.7, $Unc5D^{ecto}$ does not interact with $FLRT2^{ecto}$ (Figure S2A).

Mutations in the FLRT-Unc5 Interface Inhibit the Interaction

Based on the crystal structures, we designed mutations in the FLRT2-Unc5D interface to disrupt binding. In FLRT2 H170E and H170N, we replaced the central histidine with a negative-charged residue or an N-linked glycosylation site, respectively. Neither of these mutants binds Unc5D in our assays, confirming the binding site we describe is essential for the interaction (Figure 3A). Also, the Unc5D mutants E88A+W89A+H91A and W89N+H91T show poor binding to FLRT2 (Figure 3A). Binding was unaffected by FLRT2 and Unc5D mutations at sites involved in minor interactions in the crystal (FLRT2 D248N+P250T, Unc5D L101N+E103T), suggesting that these sites are not physiologically relevant (Figure 3A). For subsequent functional analysis we chose the non-Unc5-binding FLRT2 mutant H170N and the non-FLRT2-binding Unc5D mutant W89N+H91T. We henceforth refer to these Unc5-FLRT noninteracting mutants as $FLRT2^{UF}$ and $Unc5D^{UF}$, respectively. We confirmed our SPR results using a cell-based assay, in which we visualized the binding of soluble FC-tagged ectodomain proteins to mVenus-tagged receptors expressed on the surface of COS7 (Figure S2B).

The high degree of conservation in the Unc5-FLRT-binding sites allowed us to design binding-impaired mutants also for FLRT3 and Unc5B. We selected $FLRT2^{UF}$ and $Unc5D^{UF}$ as templates to design FLRT3 H165N ($FLRT3^{UF}$) and Unc5B W85N+S87T ($Unc5B^{UF}$) (Figure 3B). Additionally, we produced Unc5C W99N+H101T ($Unc5C^{UF}$), to test whether our mutants are valid also beyond the functionally well-characterized ligand/receptor pairs FLRT2-Unc5D and FLRT3-Unc5B. We showed that wild-type Unc5C, but not the UF mutant, is able to bind FLRT (Figure S2B). We confirmed that wild-type and mutant FLRT and Unc5 constructs are expressed at the cell surface (Figure S2C).

FLRT-FLRT and Unc5-FLRT Interactions Are Mediated via Distinct Surfaces

Previous studies showed that FLRT-FLRT binding between cells is mediated via the LRR domain (Karaulanov et al., 2006). We were unable to detect $FLRT^{LRR}$-$FLRT^{LRR}$ binding using purified proteins in SPR experiments, possibly due to the low-affinity nature of the interaction. However, using size-exclusion chromatography coupled to multiangle light scattering (SEC-MALS), we could show that both $FLRT3^{ecto}$ and $FLRT3^{LRR}$ oligomerize in a concentration-dependent manner (Figures 3C and S2D). An increased population of FLRT dimers or oligomers at higher concentrations is detected as an apparent increase in molecular mass. We found that the calculated mass of $FLRT3^{ecto}$ and $FLRT3^{LRR}$ correlates with the protein concentration across the elution peak; the resulting "upside-down smiley" mass profile is typical for proteins undergoing concentration-dependent oligomerization.

Our crystal structures revealed that $FLRT^{LRR}$-$FLRT^{LRR}$ lattice contacts depend on the concave surface of the proteins, a region that mediates homophilic dimerization in other LRR proteins (Kajander et al., 2011; Scott et al., 2004, 2006; Seiradake et al., 2009). To probe this region, we produced the FLRT3 mutant R181N+D183T, which contains an N-linked glycosylation site in the concave surface. In contrast to wild-type $FLRT3^{ecto}$, the mutant does not undergo concentration-dependent oligomerization; i.e., the apparent mass does not increase in correlation with the protein concentration. These data show that the homophilic interaction depends on the concave surface of the FLRT3 LRR domain (Figure 3C). We henceforth call this FLRT-FLRT noninteracting mutation $FLRT^{FF}$, and the mutant ectodomain $FLRT3^{ectoFF}$. In contrast to $FLRT3^{ectoFF}$, the non-Unc5-binding mutant $FLRT3^{ectoUF}$ still oligomerizes in a concentration-dependent manner (Figure S2D).

We and others have shown that the expression of transmembrane FLRT in suspended HEK cells leads to the formation of separate cell aggregates (Egea et al., 2008; Karaulanov et al., 2006). Using this assay, we revealed that mutations in the concave surface of the FLRT3 LRR domain ($FLRT3^{FF}$), which disrupt FLRT3-FLRT3 ectodomain oligomerization in solution, also disrupt full-length FLRT3-based cell adhesion (Figure 3D). In contrast, FLRT3 with mutations in the convex surface of the LRR domain (S192N+P193G) and the Unc5-binding mutant $FLRT3^{UF}$ were still able to mediate cell adhesion (Figure 3E; data not shown). Based on our FLRT3 results, we designed an equivalent $FLRT2^{FF}$ mutant (R186N+D188T). The expression of FLRT2 and $FLRT2^{UF}$, but not $FLRT2^{FF}$, induced cell aggregation (Figures S2E and S2F). Thus, the FLRT-FLRT interaction surface we identified is conserved between the two homologs. We observed a small decrease in aggregation between cells expressing the UF mutants compared to wild-type FLRTs; however, the difference is not statistically significant. Western blot analysis confirmed similar expression levels of wild-type and mutant (Figure S2G). Finally, we demonstrated that $FLRT3^{FF}$ and $FLRT2^{FF}$ bind Unc5 ectodomains (Figures 3B and S2B). We conclude that FLRT-FLRT and FLRT-Unc5 interactions are mediated via distinct FLRT surfaces and can be controlled using specific mutations (Figure 3F).

FLRTs Act as Chemo and Contact Repellents through Interaction with Unc5 in *trans*

We previously showed that shed ectodomains of FLRTs act as repulsive guidance cues and cause axonal growth cone collapse

(E) Quantification of the data shown in (D). $n \geq 3$ experiments per condition. $^{***}p < 0.001$ (versus GFP), $^{###}p < 0.001$ (versus FF), one-way ANOVA test with Tukey's post hoc analysis. The data are presented as mean ± SEM.
(F) The structures of $Unc5A^{ecto}$ (shades of blue) and $FLRT3^{LRR}$ (orange) are shown. To generate non-Unc5-FLRT-binding mutants $Unc5^{UF}$ and $FLRT^{UF}$ and the non-FLRT-FLRT-binding mutant $FLRT^{FF}$, we introduced N-linked glycosylation sites (schematized) in the respective binding sites.

of cortical neurons (Yamagishi et al., 2011). Here we use our specific FLRT mutant proteins to test whether this activity is solely dependent on FLRT-Unc5 interaction. We chose intermediate thalamic explants (iTh) expressing Unc5B (Figure 4A), the functional receptor of FLRT3. Using an automatic image analysis program (Figures S3A–S3C), we found that iTh growth cones collapse upon incubation with FLRT3^{ecto} or FLRT3^{ectoFF}, compared to FC control protein. FLRT3^{ectoUF} did not induce growth cone collapse, indicating that the collapse effect is dependent on FLRT3^{ecto}-Unc5 interaction (Figures 4B–4D). Similar results were obtained with a mixed culture of Unc5B/Unc5D-expressing cortical neurons stimulated with mutant or wild-type mixtures of FLRT2+FLRT3 (Figures S3D–S3G). We also performed stripe assays (Vielmetter et al., 1990) to test the responses of iTh axons toward different FLRT proteins. We found that iTh axons were repelled by stripes containing FLRT3^{ecto} and FLRT3^{ectoFF} (Figures 4E and 4F). iTh axons were also repelled by stripes presenting the non-Unc5-binding mutant FLRT3^{ectoUF}, but the effect was significantly less compared to the wild-type and FF mutant (Figures 4G and 4H). To investigate this further, we arranged alternating stripes presenting wild-type FLRT3^{ecto} and the mutant FLRT3^{ectoUF}. iTh prefer to grow and extend axons on FLRT3^{ectoUF}, suggesting that the repulsive effect of FLRT3^{ecto} is dependent, at least in part, on interaction with Unc5. Conversely, when asked to choose between the Unc5-binding competent FLRT3^{ecto} and FLRT3^{ectoFF} proteins, iTh axons do not show significant preference for either surface (Figures 4I–4K).

The stripe assay data raise the possibility that FLRT could also act as a surface-bound contact repellent. We confronted growing iTh axons with HeLa cells expressing a cleavage-resistant FLRT3 mutant, whose ectodomain is not shed (Yamagishi et al., 2011). Cells transfected with the noncleavable FLRT3 construct repelled ~80% of the extending axons, while non-transfected control cells repelled only ~20% of the axons (Figures 4L and 4M; Movies S1 and S2). Thus, FLRTs act as chemo and contact repellents, and this activity is largely mediated by Unc5 receptors.

FLRT-FLRT Interaction Attenuates Unc5 Repulsion

During brain development, FLRTs and Unc5s are also expressed in overlapping regions. While iTh axons do not express detectable levels of FLRT3, rostral thalamic (rTh) axons express both Unc5B and FLRT3 (Figures 5A and 5B; Leyva-Díaz et al., 2014). We found that in stripe assays, rTh axons are repelled by FLRT3^{ecto}, but the effect is less pronounced compared to iTh axons. We also found that rTh axons from a *Flrt3* conditional mutant are repelled more strongly by FLRT3^{ecto} stripes comparable to iTh axons lacking endogenous FLRT3 (Figures 5C–5E; see also Figure 4F). These data suggest that endogenous FLRT3 expressed on the axons modulates the response to FLRT3 presented (in *trans*) on stripes. Two scenarios could underlie this phenomenon: (a) FLRT3-FLRT3-mediated adhesion could counteract FLRT3-Unc5-mediated repulsion, or (b) FLRT3 could bind Unc5B in *cis*, thus reducing the number of Unc5B receptors that are able to respond to exogenous FLRT3 ("*cis* inhibition"). We performed stripe assays to explore this further. We found that rTh axons prefer to grow on wild-type FLRT3^{ecto} rather than mutant FLRT3^{ectoFF}. rTh axons from a *Flrt3* conditional mutant do not distinguish between FLRT3^{ecto} and FLRT3^{ectoFF}, thus behaving similar to iTh axons that naturally do not express FLRT3 (Figures 5F–5H; see also Figure 4K). These data suggest that the attenuation of repulsion observed for FLRT3-expressing neurons is due, at least in part, to adhesive FLRT3-FLRT3 interaction in *trans*. In stripe experiments where rTh axons choose between an inactive FLRT3 double mutant, containing both the FF and UF mutations (FLRT3$^{ectoFF-UF}$; Figure 5I) and FLRT3^{ectoFF}, rTh axons are repelled at least equally well by FLRT3^{ectoFF} compared to iTh axons (Figures 5J–5L). These results argue that most, if not all, Unc5 receptors must be unmasked, despite the presence of endogenous FLRT3. Therefore, we conclude that in rTh axons FLRT3 and Unc5B function in parallel, such that adhesive FLRT interaction reduces the repulsive response triggered by FLRT-Unc5 interaction in a combinatorial way (Figure 5M).

FLRTs Control Cell Migration in the Developing Cortex by Distinct Mechanisms

Having established how the adhesive and repulsive functions of FLRTs are mediated, we are now able to dissect these functionalities in vivo, using cortical development as a model system. During development, pyramidal neurons are born in the proliferative zone and radially migrate to settle in one of six cortical layers (Rakic, 1988). We previously showed that Unc5D-expressing neurons display a delayed migration to the FLRT2-enriched cortical plate consistent with FLRT2 acting as a repulsive cue for Unc5D+ cells (Yamagishi et al., 2011). Therefore, we wanted to investigate how much of the observed migration delay is due to FLRT-Unc5 signaling. In agreement with our previous work, we found that Unc5D overexpression by in utero electroporation (IUE) in E13.5-born neocortical cells delayed their migration. This delay was partially rescued when overexpressing Unc5D^{UF} (Figures 6A–6C), confirming that the migration delay observed in Unc5D-overexpressing cells is at least partially due to interaction with FLRT2.

The pattern of FLRT3/Unc5B expression in E15.5 cortex is complementary to FLRT2/Unc5D, with FLRT3 expressed in migrating neurons and Unc5B in cortical plate (Figure 6D). To investigate whether FLRT3 plays a role in neuronal migration, we analyzed the positioning of neurons expressing FLRT3 in the developing cortex using brain sections from a *Nestin-Cre; Flrt3*$^{lox/lacZ}$ conditional mutant and β-galactosidase staining. We found that the distribution of FLRT3-deficient (β-gal+) neurons is affected in mutant cortex, leading to abnormal neuronal clustering in the cortical plate, which contrasts with the homogeneous distribution in control littermates (Figures 6E and 6F). To analyze the distribution of the β-galactosidase-positive neurons, we calculated the normalized intensity profile of the Xgal staining in the lower half of the cortical plate (dashed rectangle, Figures 6E and 6F), which revealed substantial fluctuations in the density of mutant neurons (Figure 6G). We also measured the Voronoi nearest neighbor distance to assess cellular distribution independently of cell density (Villar-Cerviño et al., 2013). Mutant neurons showed increased minimum distance between cells, which indicates that FLRT3 deletion affects the regular distribution present in control tissue (Figures S4A and S4B). This

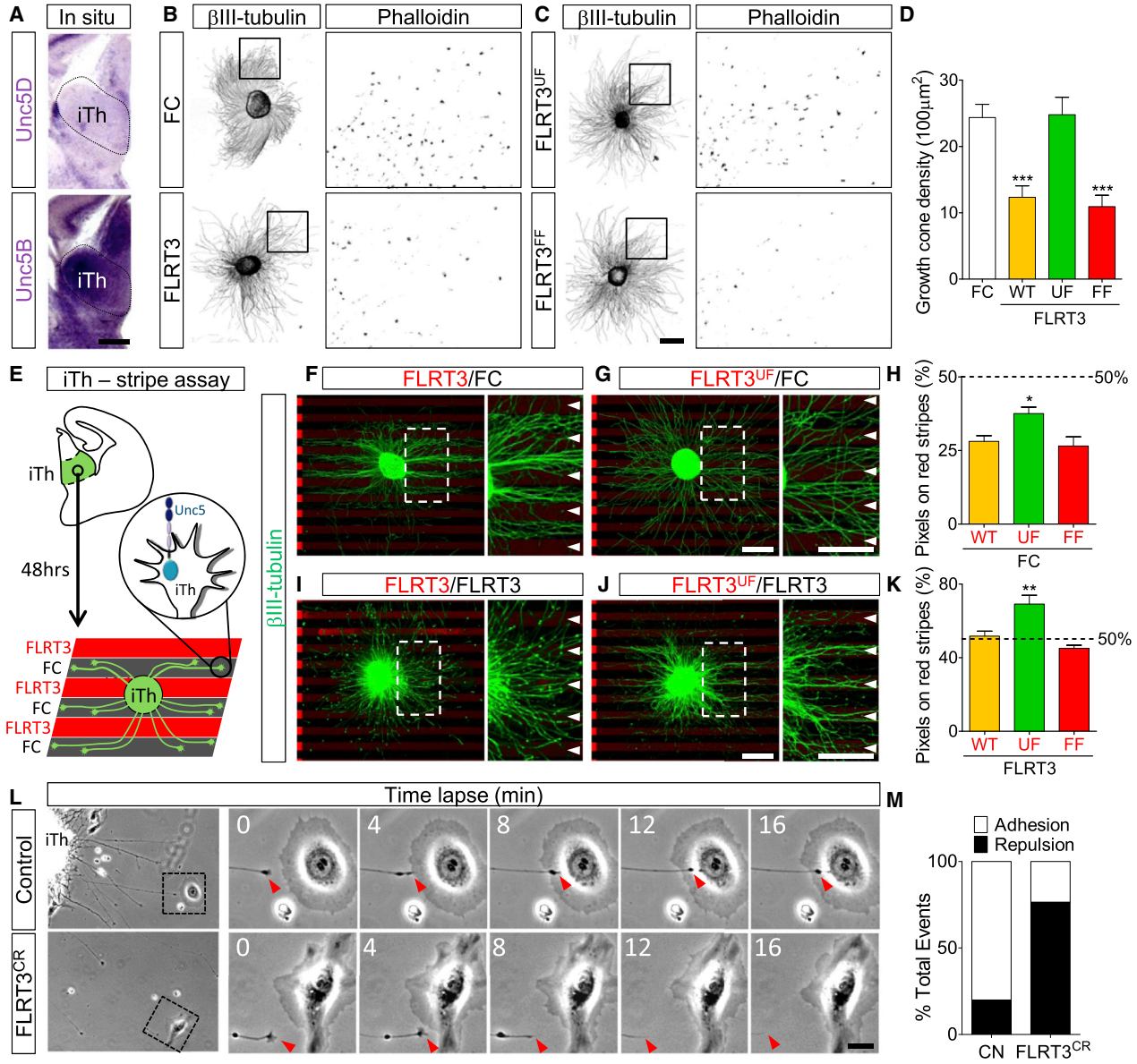

Figure 4. FLRT-Unc5 Interaction in *trans* Induces Repulsion

(A) In situ hybridization reveals *Unc5B* expression in the intermediate thalamus (iTh) of coronal sections through the telencephalon of E15.5 mouse embryos.

(B and C) iTh explants were treated with FLRT3^{ecto}, FLRT3^{ectoFF}, or FLRT3^{ectoUF} fixed and stained with beta-III-tubulin and phalloidin.

(D) The density of growth cones in experiments shown in (B) and (C) was quantified as a measure to assess FLRT3-induced growth cone collapse. n ≥ 30 iTh explants per condition; ***p < 0.001, one-way ANOVA test with Tukey's post hoc analysis.

(E) Diagram depicting the stripe assay we used to probe the responses of iTh axons expressing Unc5B to surface-bound FLRT3 and FC control proteins.

(F and G) E15.5 iTh explants were grown on alternate stripes containing FC control protein or FLRT3^{ecto} protein (wild-type or mutant). Explants were stained with anti-beta-III-tubulin to visualize the axons (green). FLRT3-containing stripes are marked in red on the left side of each image. After imaging, the percentage of beta-III-tubulin+ pixels on red stripes was quantified.

(H) Quantification of the data shown in (F) and (G). n ≥ 20 iTh explants per condition; *p < 0.05 (UF versus WT and FF), one-way ANOVA test with Tukey's post hoc analysis.

(I and J) Stripe assays were performed as described in (F) and (G), but using alternating stripes of wild-type and mutant FLRT3^{ecto}.

(K) Quantification of the data shown in (I) and (J). n ≥ 15 iTh explants per condition. **p < 0.01 (UF versus WT and FF), one-way ANOVA test with Tukey's post hoc analysis.

(L) Cell-bound FLRT3 repels iTh axons in time-lapse experiments. iTh explants were confronted with HeLa cells (control or expressing noncleavable FLRT3). Frames were acquired every 4 min. A repulsive event was defined as a contact between an extending axon and a HeLa cell lasting less than eight frames.

(M) Quantification of the data shown in (L); n ≥ 30 contacts per condition. The data are presented as mean ± SEM. Scale bars, 200 μm (A), 350 μm (B and C), 300 μm (F, G, I, and J), 13 μm (L).

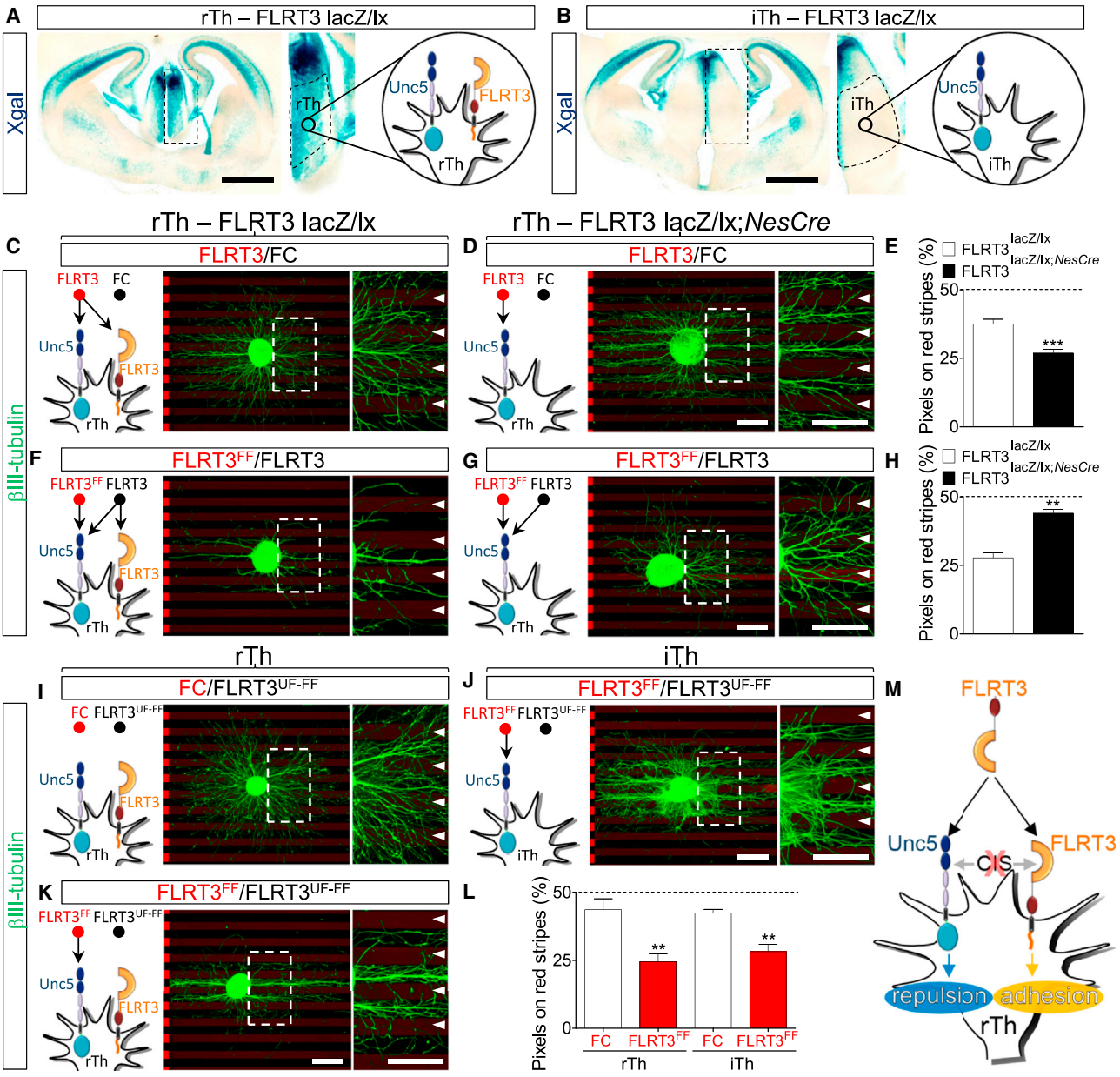

Figure 5. FLRTs Act in *cis* as Attenuators of Unc5 Repulsion

(A and B) Serial coronal sections through the telencephalon of E15.5 embryos from a *Flrt3*$^{lacZ/lx}$ reporter line showing high expression of *Flrt3* in rostral thalamus (rTh), but not intermediate thalamus (iTh).

(C and D) E15.5 wild-type or *Flrt3* conditional knockout rTh explants were grown on alternate stripes containing FC and FLRT3^{ecto}. Explants were stained with anti-beta-III-tubulin to visualize the axons (green). FLRT3-containing stripes are marked in red on the left side of each image. After imaging, the percentage of beta-III-tubulin+ pixels on red stripes was quantified.

(E) Quantification of the data shown in (C) and (D). n = 77 wild-type rTh from five embryos, n = 52 knockout rTh from six embryos. ***p < 0.001, two-tailed Student's t test.

(F and G) Stripe assays were performed as in (C) and (D), but using alternate stripes of FLRT3^{ecto} and FLRT3^{ectoFF}.

(H) Quantification of the data shown in (F) and (G). n = 20 wild-type rTh from two embryos, n = 23 knockout rTh from three embryos. **p < 0.01, two-tailed Student's t test.

(I–K) rTh and iTh explants were grown on alternate stripes containing FC and FLRT3$^{ectoUF-FF}$, or FLRT3^{ectoFF} and FLRT3$^{ectoUF-FF}$.

(L) Quantification of the data shown in (I) and (J). n ≥ 10 rTh and iTh explants per condition. **p < 0.01, two-tailed Student's t test.

(M) A model showing that FLRT-FLRT adhesion in *trans*, rather than FLRT-Unc5 interaction in *cis*, modulates FLRT-Unc5 repulsion in rTh axons. The data are presented as mean ± SEM. Scale bars, 850 μm (A and B), 300 μm (C, D, F, G, I, J, and K).

phenotype suggests that the normal tangential dispersion of cortical neurons is impaired in FLRT3 mutant mice. The radial positioning of pyramidal neurons seems unaffected; Cux1, a marker for upper-layer (Nieto et al., 2004), and TBR1, a marker of lower-layer, postmitotic neurons (Hevner et al., 2003), are expressed normally in FLRT3 mutant mice (Figures S4C–S4E). These results suggest that FLRT3 is required for the spatial arrangement of pyramidal neurons in the tangential axis. Mechanistically, this function of FLRT3 does not seem to involve interaction with Unc5B, since GFP-transfected migrating neurons show no preference between Unc5B^{ecto}-FC- and control FC-containing stripes (Figures 6H–6J). To obtain more insight into the mechanism of FLRT3 activity, we overexpressed the different mutants of FLRT3 in embryonic cortex using IUE. We analyzed transfected brains in cleared whole-mount preparations in both coronal and horizontal brain sections (Figure 6K). We found that FLRT3-overexpressing neurons migrate slower (Figures 6L and 6M) and distribute abnormally in the tangential axis, forming a repeating pattern of aggregates (Figures 6N, 6O, S4F, and S4G; Movies S3 and S4). Whereas the altered radial migration is not observed in the FLRT3 conditional mutants and may therefore be unphysiological, the altered tangential distribution is also seen when FLRT3 expression is ablated. FLRT3^{UF} behaves similarly to wild-type FLRT3 and disrupts cell migration, and more importantly, tangential distribution of migrating neurons, suggesting that Unc5B does not affect the migration of FLRT3-expressing neurons (Figures 6L–6O, S4F, and S4G). Conversely, the mutation in FLRT3^{FF} largely preserves the regular distribution of neurons in the tangential axis, indicating that FLRT-FLRT interaction is responsible for the observed effect (Figures 6L–6O, S4F, and S4G). FLRT3-overexpressing cells contain the differentiation marker Cux1, implying that FLRT3 affects the migration, but not differentiation, of the cells (Figures 6P and 6Q). Our results show that FLRTs have distinct functions in cortical development, mediating repulsion to control radial migration and homophilic adhesion to direct tangential distribution (Figures 6R and 6S).

FLRT3 Controls Retinal Vascularization

FLRT and Unc5 proteins are expressed broadly during development, not just in the nervous system. FLRTs have been previously implicated in heart and vascular development (Müller et al., 2011), and artery endothelial cells are known to express Unc5B (Larrivée et al., 2007; Lu et al., 2004; Navankasattusas et al., 2008). We tested whether FLRT-Unc5 interaction plays a role in directing vascular cells. We found that primary HUAECs express both FLRT3 and Unc5B (Figure 7A). Stripe assays reveal that HUAECs are repelled strongly by FLRT3^{ecto} compared to the FLRT3^{ectoUF} mutant (Figures 7B and 7C). Conversely, the mutant FLRT3^{ectoFF}, which is unable to provide FLRT-FLRT adhesion, but still binds Unc5, is more repulsive than wild-type FLRT3 (Figures 7B–7E). As shown above for rTh neuronal axons (Figure 5), the data suggest that the response of HUAECs to FLRT3-presenting stripes is a product of adhesive FLRT-FLRT and repulsive FLRT-Unc5 interaction.

Next, we tested whether FLRT-Unc5 interaction plays a role in the developing vascular system. The mouse retina is an established model tissue for vascularization and, from birth until P8/P9, contains high levels of Unc5B in retinal arteries, capillaries, and endothelial tip cells (Larrivée et al., 2007). We found that FLRT3 is expressed in the inner plexiform layer of the retina during the stages when Unc5-expressing blood vessels develop (Figure 7F). To study the role of FLRT-FLRT and FLRT-Unc5 interactions in tip cell filopodia extension, we used live-mounted retinal explants (age P5). After incubation with FLRT3^{ecto} or FLRT3^{ectoFF}, we measured significantly fewer tip cell filopodia at the vascular front compared to control and FLRT3^{ectoUF} retinas (Figures 7G and 7H). Consistent with FLRT3-Unc5B repulsive interaction having a function during vascularization in vivo, we observed increased vascular branching in the retinas of *Sox2-Cre;Flrt3*$^{lox/lacZ}$ conditional mutants (Figures 7I and 7J). These data indicate that FLRT3 acts as a controlling factor of retinal vascular development and suggests that the action of FLRT3 depends on its interaction with Unc5B.

DISCUSSION

The structural data presented here indicate that distinct FLRT LRR surfaces mediate homophilic adhesion and Unc5-dependent repulsion. By using these surfaces, FLRTs can affect both adhesive and repulsive functions in the same receiving cell, e.g., neurons or vascular cells that coexpress FLRT and Unc5. We show that coexpressed FLRT and Unc5 act in parallel, and that cells must integrate these adhesive and repulsive effects. This separation of adhesive and repulsive functionalities allows FLRTs to regulate the behavior of migrating pyramidal neurons in distinct ways; FLRT2 repels Unc5D+ neurons and thereby controls their radial migration, while FLRT3-FLRT3 homophilic interactions regulate their tangential distribution. FLRT3 also controls retinal vascularization, possibly involving combinatorial signaling via FLRT and Unc5. To distinguish FLRTs from adhesion-only CAMs, we propose to define a new subgroup, here designated as repelling CAMs (reCAMs). reCAMs provide a guidance system that combines the finely tunable cell adhesion of classical homophilic CAMs with repulsive functions through the addition of a heterophilic receptor.

FLRT-FLRT and Unc5-FLRT Interaction Surfaces Are Distinct

We show here that FLRT-mediated adhesion involves the conserved concave surface on the LRR domain. This mode of homophilic binding resembles that of other LRR-type CAMs, for example, decorin (Scott et al., 2004). The FLRT-FLRT binding affinity is weak (below the sensitivity of our SPR assay ~100 μM), and FLRT oligomerization correlates with local concentration. Thus, FLRTs are ideal candidates for providing the finely tuned adhesive cell-cell traction required for cell migration.

In contrast to the low-affinity adhesive binding, repulsive FLRT-Unc5 interaction is of nanomolar affinity and mediated through a distinct binding surface on the FLRT LRR domain. The high degree of conservation within the binding surfaces of Unc5 and FLRT homologs suggests the interaction evolved before homolog diversification. The mode of interaction is atypical for LRR-type proteins, which mostly bind ligands via the concave surface of the domain, although some examples of ligand-binding surfaces other than the concave side exist (Bella et al., 2008).

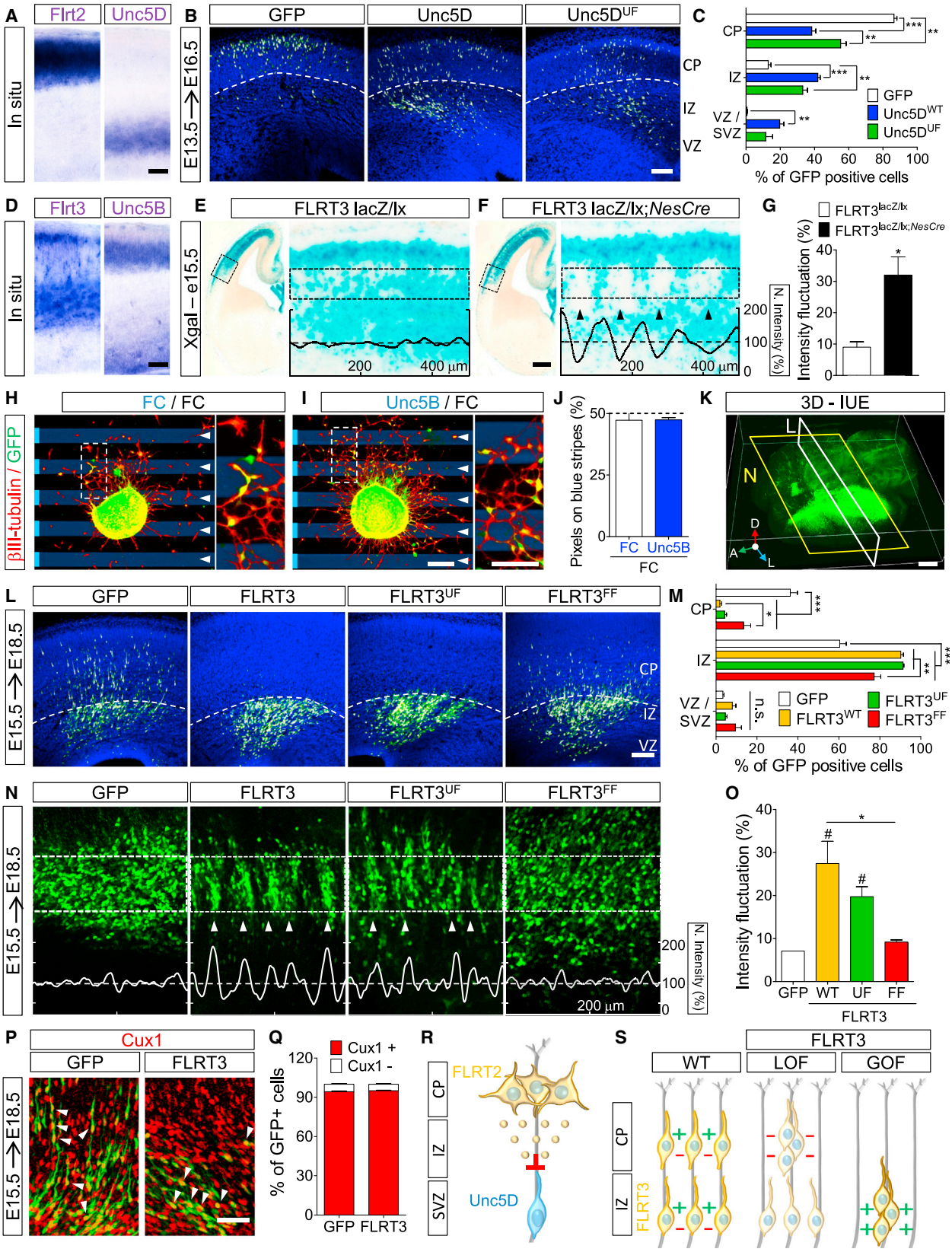

(legend on next page)

Our results with thalamic neurons and vascular cells indicate that coexpressed FLRTs act as attenuators of Unc5 repulsion. Stripe assays with FLRT3-positive, compared to FLRT3-negative, thalamic axons provide strong evidence that the attenuation results from FLRT-FLRT interaction in *trans*, rather than in *cis*, masking. Further work will be necessary to elucidate the functional consequences of this parallel signaling and the relative importance of membrane-associated versus soluble FLRT ectodomains in vivo.

FLRTs Control Cortical Neuron Migration by Distinct Mechanisms

The mammalian cerebral cortex is organized in horizontal layers and intersecting columns. During development, cortical progenitors and their neuronal progeny settle in different layers in an inside-out fashion. The layered structure of the cortex helps to organize cortical inputs and outputs. Cortical progenitors and their neuronal progeny also form vertical ontogenic columns of sister neurons. Subpopulations of clonally related neurons undergo limited tangential dispersion to neighboring columns (Rakic, 1988). The molecular mechanisms and significance of this behavior are poorly understood. We have previously shown that FLRT2/Unc5D signaling is implicated in the radial migration of cortical neurons (Yamagishi et al., 2011). The FLRT2 ectodomain produced and shed by cells in the cortical plate prevents Unc5D+ cells from prematurely migrating from the subventricular zone to the cortical plate. In support of this model, Unc5D overexpression in E13.5-born neocortical cells further delayed their migration (this study and Yamagishi et al., 2011). Using the non-FLRT-binding mutant Unc5D^{UF}, we now confirm that this effect is at least partially due to FLRT/Unc5D interactions.

Our present results suggest that the related FLRT3 protein is implicated in the tangential dispersion of cortical neurons in a manner that involves FLRT3-FLRT3 homophilic interactions. The irregular distribution of cortical neurons in *Flrt3* mutant mice resembles the phenotype seen in *ephrinA* triple-knockout mice (Torii et al., 2009). Likewise, the tangential clustering of neurons after FLRT3 overexpression resembles the phenotype seen after EphA7 or ephrinB1 overexpression (Dimidschstein et al., 2013; Torii et al., 2009). The function of Eph/ephrin signaling appears to modulate cell morphology and mobility during the multipolar phase of migration (Dimidschstein et al., 2013). Based on its molecular functions, we hypothesize that FLRT3 affects the adhesive properties of migrating cells and thereby disrupts the delicate balance of adhesion/repulsion necessary for cell migration (Cooper, 2013; Marquardt et al., 2005; Solecki, 2012). This conclusion is supported by the fact that the non-FLRT-interacting mutant FLRT3^{FF} is not able to disrupt the tangential dispersion. Interestingly, this function of FLRT3 may be shared by the related FLRT1 that is coexpressed with FLRT3 in the developing cortex and displays similar characteristics in terms of homophilic and Unc5 binding (Yamagishi et al., 2011; data not shown). A preliminary characterization of *Flrt1;Flrt3* double-knockout mutants revealed a stronger spatial disruption in the tangential axis of the cortex than single *Flrt3* mutants (data not shown). Together, these findings shed light on the cell-cell communication mechanisms operating during radial and tangential patterns of migration of pyramidal neurons.

FLRT3 Controls Vascularization

Unc5B is a negative regulator of developmental vascularization (Bouvrée et al., 2008; Koch et al., 2011; Larrivée et al., 2007;

Figure 6. FLRT Controls Radial and Lateral Migration of Cortical Neurons via Distinct Mechanisms

(A) In situ hybridization shows *Flrt2* and *Unc5D* expression in coronal sections of E15.5 cortex.

(B) Coronal sections of E16.5 cortex after IUE at E13.5 with *GFP*, *Unc5D-IRES-GFP*, or *Unc5D*^{UF}*-IRES-GFP*. GFP+ cells located in the cortical plate (CP), intermediate zone (IZ), and subventricular zone (SVZ) were quantified.

(C) Quantification of the data shown in (B). n ≥ 5 electroporated embryos per condition. **p < 0.01, ***p < 0.001, one-way ANOVA test with Bonferroni post hoc analysis.

(D) In situ hybridization shows *Flrt3* and *Unc5B* expression in coronal sections of E15.5 cortex.

(E and F) Xgal staining of E15.5 coronal sections from control (*Flrt3*$^{lacZ/lx}$) or conditional (*Flrt3*$^{lacZ/lx;NesCre}$) mutant. Normalized intensity plots are shown, obtained from the areas delineated with a dashed rectangle.

(G) Quantification of the intensity fluctuations by measuring the distances between minima and maxima and the normalized intensity values (dashed line). n = 3 controls, n = 4 conditional mutants. *p < 0.05, two-tailed Student's t test.

(H and I) GFP-electroporated cortical explants (from E13.5 to E15.5) were plated on alternating stripes coated with FC control protein or Unc5B^{ecto}-FC fusion. Explants were stained with anti-beta-III-tubulin to visualize neurons exiting the explant (red). After imaging, the percentage of GFP+ pixels on blue stripes was quantified.

(J) Quantification of the data shown in (H) and (I). n ≥ 7 cortical explants per condition.

(K) Cleared whole-mount electroporated brain (E15.5–E18.5) showing the orientation of sections presented in (L) (coronal) and (N) (horizontal).

(L) Coronal sections of E18.5 cortex after IUE at E15.5 with *GFP*, *Flrt3-IRES-GFP*, *Flrt3*^{UF}*-IRES-GFP*, and *Flrt3*^{FF}*-IRES-GFP*. GFP+ cells located in the CP, IZ, and SVZ were quantified.

(M) Quantification of the data shown in (L). n ≥ 5 electroporated embryos per condition. *p < 0.05, **p < 0.01, ***p < 0.001, statistical analysis as in (C).

(N) As in (L), but showing horizontal optical sections from a cleared whole-mounted electroporated brain.

(O) Quantification as described for (G), but for data shown in (N). n ≥ 3 electroporated embryos per condition. *p < 0.05, one-way ANOVA test with Tukey's post hoc analysis and #p < 0.05 (WT and UF versus FF), two-tailed Student's t test.

(P) Staining of electroporated slices (*GFP* or *Flrt3-IRES-GFP*) with the laminar marker Cux1 (red).

(Q) Quantification of the data shown in (P). n ≥ 3 electroporated embryos per condition.

(R) Cartoon depicting how FLRT2, expressed and shed in the cortical plate, delays the migration of Unc5D+ neurons located in the SVZ.

(S) Cartoon depicting how FLRT3 directs cortical neuron migration. In the WT, the lateral distribution of neurons is controlled by a correct balance of adhesive and repulsive interactions. FLRT3 knockdown (LOF) or overexpression (GOF) alters this balance, resulting in the formation of neuronal cell clusters. The data are presented as mean ± SEM. Scale bars, 400 μm (A and D), 250 μm (E and F), 150 μm (B and L), 300 μm (H and I), 1 mm (K), 100 μm (P).

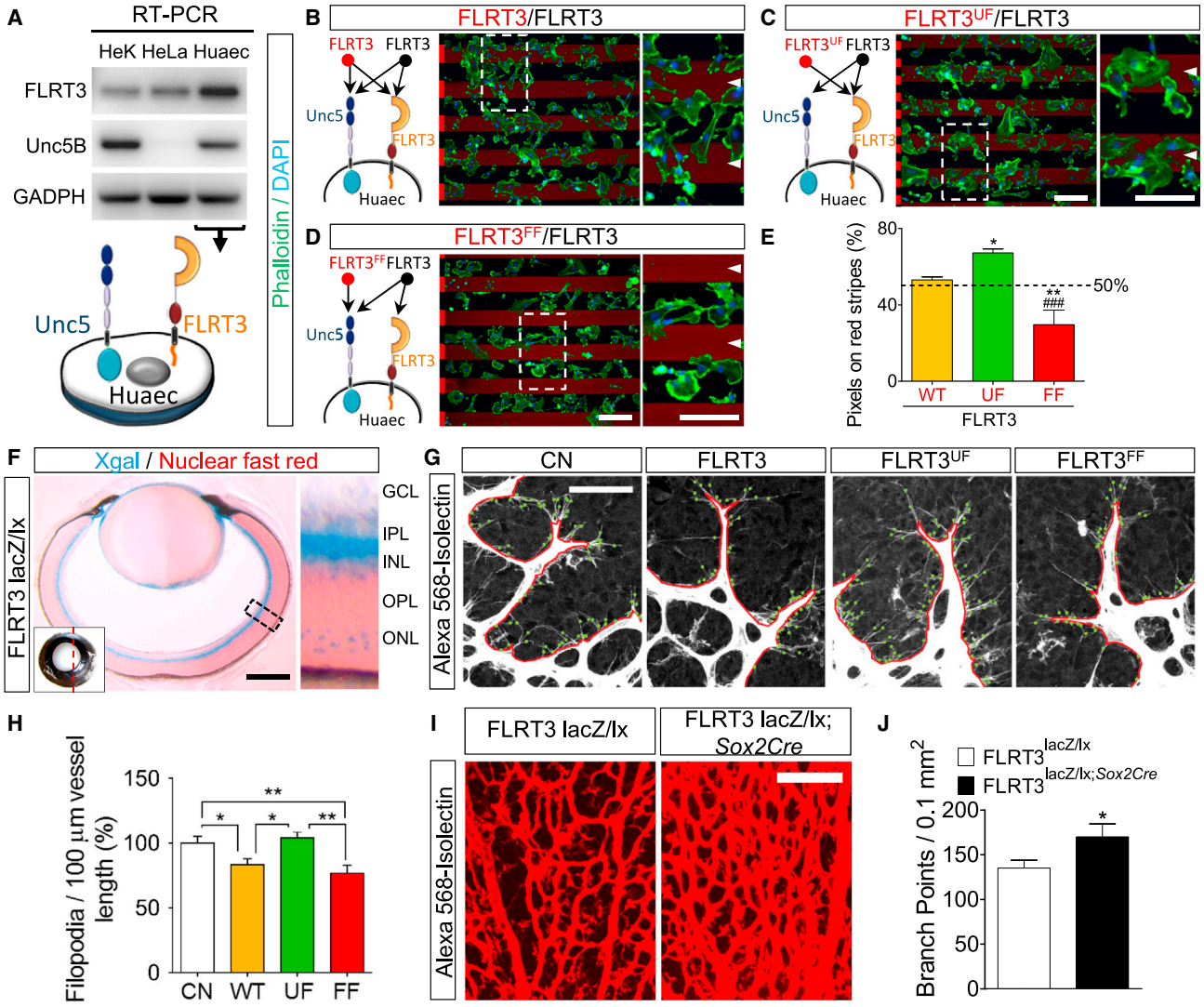

Figure 7. FLRT Controls Vascular Development via Conserved Mechanisms

(A) RT-PCR data showing that HUAECs express *Flrt3* and *Unc5B*.

(B–D) HUAECs were grown on alternate stripes containing wild-type and mutant FLRT3^{ecto}. Cells were stained with phalloidin (green) and DAPI (blue). The location of the faintly stained red stripes is indicated on the left side of each image.

(E) After imaging, the percentage of DAPI+ pixels on red stripes was quantified. HUAECs are attracted to FLRT3^{ectoUF} stripes and repelled by FLRT3^{ectoFF} stripes, when FLRT3^{ecto} is present on the control stripes (black). n ≥ 2 cultures made in duplicate. *p < 0.05, **p < 0.01 (versus WT), and ###p < 0.001 (versus UF), one-way ANOVA test with Tukey's post hoc analysis.

(F) Longitudinal section through the eye of a P2 mouse from an *Flrt3*$^{lacZ/lx}$ reporter line showing expression of *Flrt3* in the inner plexiform layer and outer nuclear layer, counterstained with FastRed. GCL, ganglion cell layer; IPL, inner plexiform layer; INL, inner nuclear layer; OPL, outer plexiform layer; ONL, outer nuclear layer.

(G) P5 retinal explants were incubated with wild-type FLRT3, mutant FLRT3^{UF}, or FLRT3^{FF} protein for 4 hr. The number of tip cell filopodia at the vascular front was quantified.

(H) Quantification of data shown in (G). n = 3–9. *p < 0.05, **p < 0.01, one-way ANOVA test with Tukey's post hoc analysis.

(I) The branch points in the retinal vasculature from control (*Flrt3*$^{lacZ/lx}$) or conditional (*Flrt3*$^{lacZ/lx;Sox2Cre}$) mutant (P3) were quantified.

(J) Quantification of data shown in (I). n = 4–8. *p < 0.05, two-tailed Student's t test. The data are presented as mean ± SEM. Scale bars, 90 µm (A), 300 µm (F), 50 µm (G), 100 µm (I).

Lu et al., 2004), and Unc5B knockdown leads to increased vascular branching in the mouse retina (Koch et al., 2011). Netrin-1 and Robo-4 have been shown to interact with Unc5B in the vasculature (Koch et al., 2011; Lu et al., 2004); however, neither *Netrin1*$^{-/-}$ nor *Robo4*$^{-/-}$ mice display the hypervascularization effects observed in *Unc5B*$^{-/-}$ retinas, indicating that

other factors may play a role. Here we demonstrate that *Flrt3*$^{-/-}$ mice present with a vascularization phenotype that strongly resembles that reported for Unc5B$^{-/-}$. Using our tip cell collapse experiments, we show that soluble FLRT3 controls the extension of endothelial tip cell filopodia through its specific Unc5B-binding site, providing functional evidence for a direct interaction of FLRT3 and Unc5. These results suggest that FLRT3 is a major player in controlling vascularization via Unc5B, and may therefore explain the puzzling lack of effects in retinal vascularization after removing other Unc5B ligands. Our stripe assays showed that surface-tethered FLRT3 also repels endothelial cells through interaction with Unc5B. Further work is required to understand whether FLRT3 acts in its soluble or cell-bound form in vivo.

Further questions remain; how do FLRTs signal adhesion/attraction in response to homotypic interaction with other FLRTs? Are the downstream pathways activated by the FLRT intracellular domain similar to classical CAMs? Are small GTPases such as Rnd proteins (Chen et al., 2009; Karaulanov et al., 2009) and cytoskeletal proteins involved? FLRTs have also been reported to bind other proteins, for example, latrophilin (O'Sullivan et al., 2012). It will be important to understand the molecular determinants of these interactions and how they influence FLRT functions. The crosstalk of FLRT3-Unc5B interactions to other key vascular players, such as VEGF/VEGFR2, also remains to be investigated.

In summary, we integrated information generated by a broad range of biological methods to understand the functions of FLRT and Unc5 receptors in cortical and vascular development. Our results reveal how FLRTs act as bimodal guidance molecules directing essential developmental processes through structurally distinct, combinatorial mechanisms. As FLRT and Unc5 are expressed in a wide range of tissues (Engelkamp, 2002; Haines et al., 2006), the conserved functional mechanisms we report are likely to control cell adhesion and repulsion in tissues beyond those described here.

EXPERIMENTAL PROCEDURES

Vectors and Cloning

We cloned constructs of mouse *Flrt2* (UniProt Q8BLU) and *Flrt3* (UniProt Q8BGT1), human *Unc5A* (UniProt Q6ZN44), mouse or human *Unc5B* (UniProt Q8K1S3 and Q8IZJ1), and rat *Unc5D* (UniProt F1LW30) into the Age1-Kpn1 or EcoR1-Kpn1 cloning site of vectors from the pHLSec family (Aricescu et al., 2006), depending on whether the construct includes a native secretion signal sequence. For crystallization or functional analysis, we cloned *Flrt2*^{LRR} (residues 35–362), *Flrt3*^{LRR} (residues 29–359), *Flrt2*^{ecto} (residues 35–540), *Flrt3*^{ecto} (residues 29–526), *Unc5A*^{Ig12T1} (residues 1–303), human *Unc5B*^{ecto} (residues 1–375), *Unc5D*^{Ig1} (residues 1–161), *Unc5D*^{Ig12} (residues 1–244), *Unc5D*^{T12} (residues 249–382), and *Unc5D*^{ecto} (residues 1–382) into pHLSec vectors containing short C-terminal tags (poly-His or poly-His+avitag; see Aricescu et al., 2006). For visualization in cells, we cloned full-length *Flrt2* (residues 35–660), *Flrt3* (residues 29–649), *Unc5B* (residues 27–934), *Unc5C* (residues 41–931), and *Unc5D* (residues 46–953) into a pHLSec vector that codes for a C-terminal mVenus and a polyhistidine tag (Seiradake et al., 2010). Hemagglutinin epitope (HA) tags are included at the N terminus of transmembrane constructs, following the vector secretion signal sequence. For expression in vivo, we subcloned *Flrt* and *Unc5* constructs with the pHLSec vector signal sequence and HA tag into a pCAGIG vector coding for a C-terminal internal ribosome entry site (IRES) and GFP. We generated point mutants using standard PCR techniques. We verified the correct cell surface expression of all transmembrane plasmids by immunostaining (Figure S2C; data not shown).

Protein Purification, Crystallization, and Data Collection

We expressed FLRT and Unc5 ectodomain proteins destined for crystallization or functional analysis transiently in GnTI-deficient HEK293S cells or HEK293T cells (Aricescu et al., 2006), respectively, and purified the proteins using Ni-affinity and size-exclusion chromatography. Prior to crystallization, we added recombinant endoglycosidase F1 (Chang et al., 2007) at a concentration of 0.01 mg/ml to all samples. Crystals were grown by the vapor diffusion method at 20°C by mixing protein and crystallization solutions in a 1:1 (v/v) ratio. See Supplemental Experimental Procedures for crystallization solutions. We collected X-ray diffraction images at the Diamond Light Source beamlines I03, I04, and I24 and processed data using XDS (Kabsch, 1993), xia2 (Winter et al., 2013), and programs from the Collaborative Computational Project 4. In brief, the structure of Unc5D^{Ig1} was solved by the single anomalous diffraction method. All other structures were solved by molecular replacement. See the Supplemental Experimental Procedures.

SPR

We performed equilibrium experiments using a Biacore T200 machine (GE Healthcare) at 25°C. The experiments were carried out at pH 7.5 (PBS, 0.005% [v/v] polysorbate 20), unless indicated otherwise. Experiments at pH 5.7 were run in 150 mM NaCl and 50 mM citric acid. The regeneration buffer was 2 cM $MgCl_2$. To mimic the native membrane insertion topology, we biotinylated proteins enzymatically at the C-terminal avidity tag and attached the resulting biotin label to streptavidin-coated Biacore chip surfaces. Data were analyzed with Scrubber2 (BioLogic). K_d and maximum analyte binding (B_{max}) values were obtained by nonlinear curve fitting of a 1:1 Langmuir interaction model (bound = $B_{max}/(K_d c+cC)$, where C is analyte concentration calculated as monomer).

Multiangle Light Scattering

We purified protein samples by size-exclusion chromatography and concentrated to 1–10 mg/ml. Separation for MALS was achieved using an analytical Superdex S200 10/30 column (GE Heathcare), and the eluate was passed through online static light scattering (DAWN HELEOS II, Wyatt Technology), differential refractive index (Optilab rEX, Wyatt Technology), and Agilent 1200 UV detectors (Agilent Technologies). We analyzed data using the ASTRA software package (Wyatt Technology).

Stripe Assay, Growth Cone Collapse, Cell Aggregation, Cell-Binding Assay, IUE, Cleared Whole-Mount Brains, Retinal Explants Culture, and Immunostaining

These assays were performed as described previously (Calegari et al., 2004; Chung and Deisseroth, 2013; Sawamiphak et al., 2010; Yamagishi et al., 2011). See also the Supplemental Experimental Procedures.

Mouse Lines

Flrt3$^{lacZ/lx}$ mice (Egea et al., 2008) carrying the floxed allele for *Flrt3* were crossed with the nervous system-specific *Nestin-Cre* (Tronche et al., 1999) or *Sox2-Cre* line (Hayashi et al., 2002). All animal experiments were approved by the government of upper Bavaria.

ACCESSION NUMBERS

The wwPDB accession numbers for the crystal structures reported in this paper are 4v2a (hUnc5A ectodomain), 4v2b (rUnc5D Ig1 domain), 4v2c (complex of rUnc5D Ig1 and mFLRT2 LRR domains), 4v2d (mFLRT2 LRR domain), and 4v2e (mFLRT3 LRR domain).

SUPPLEMENTAL INFORMATION

Supplemental Information includes four figures, two tables, four movies, and Supplemental Experimental Procedures and can be found with this article online at http://dx.doi.org/10.1016/j.neuron.2014.10.008.

AUTHOR CONTRIBUTIONS

E.S. led crystallography, mutagenesis, SPR, and MALS and assisted stripe/collapse assays. D.d.T. led assays with HUAECs, neuronal cultures/explants, mutant brain sections, and IUE. D.N. led cell-based binding assays and analyzed IUE experiments, T.R. cleared and analyzed IUE brains, and G.S.-B. led HEK aggregation assays. F.C. and R.H. lead tip cell collapse assays and mutant retina analysis. T.R. performed whole-mounted cleared brain studies. K.H. assisted crystal freezing. E.C.B. produced FLRT3^{LRR} for MALS assays. The above and A.A.P., E.Y.J., and R.K. contributed to discussions and manuscript preparation.

ACKNOWLEDGMENTS

We thank E. Robertson, E. Bikoff, M. Harkiolaki, and A.R. Aricescu for *Flrt* constructs and discussion; Y. Zhao and W. Lu for protein expression; M. Jones and T.S. Walter for technical support; the Diamond Light Source for beamtime (proposal mx8423); and the staff of beamlines I03, I04, and I24. This work was funded by the Max Planck Society, Cancer Research UK (CRUK) (C375/A10976), the UK Medical Research Council (G9900061), and the Deutsche Forschungsgemeinschaft SFB 834 and EXC 115. D.d.T. was funded by a Marie Curie IEF fellowship (ID 274541). E.S. was supported by a CRUK travel grant (ref. C33663/A17200). E.C.B. was supported by a Wellcome Trust Doctoral Award, code RPSJ0. The Wellcome Trust Centre for Human Genetics (WTCHG) is supported by the Wellcome Trust (090532/Z/09/Z).

Accepted: October 2, 2014
Published: October 22, 2014

REFERENCES

Aricescu, A.R., Lu, W., and Jones, E.Y. (2006). A time- and cost-efficient system for high-level protein production in mammalian cells. Acta Crystallogr. D Biol. Crystallogr. *62*, 1243–1250.

Bashaw, G.J., and Klein, R. (2010). Signaling from axon guidance receptors. Cold Spring Harb. Perspect. Biol. *2*, a001941.

Bella, J., Hindle, K.L., McEwan, P.A., and Lovell, S.C. (2008). The leucine-rich repeat structure. Cell. Mol. Life Sci. *65*, 2307–2333.

Bouvrée, K., Larrivée, B., Lv, X., Yuan, L., DeLafarge, B., Freitas, C., Mathivet, T., Bréant, C., Tessier-Lavigne, M., Bikfalvi, A., et al. (2008). Netrin-1 inhibits sprouting angiogenesis in developing avian embryos. Dev. Biol. *318*, 172–183.

Brasch, J., Harrison, O.J., Honig, B., and Shapiro, L. (2012). Thinking outside the cell: how cadherins drive adhesion. Trends Cell Biol. *22*, 299–310.

Calegari, F., Marzesco, A.-M., Kittler, R., Buchholz, F., and Huttner, W.B. (2004). Tissue-specific RNA interference in post-implantation mouse embryos using directional electroporation and whole embryo culture. Differentiation *72*, 92–102.

Cavallaro, U., and Dejana, E. (2011). Adhesion molecule signalling: not always a sticky business. Nat. Rev. Mol. Cell Biol. *12*, 189–197.

Chang, V.T., Crispin, M., Aricescu, A.R., Harvey, D.J., Nettleship, J.E., Fennelly, J.A., Yu, C., Boles, K.S., Evans, E.J., Stuart, D.I., et al. (2007). Glycoprotein structural genomics: solving the glycosylation problem. Structure *15*, 267–273.

Chen, X., Koh, E., Yoder, M., and Gumbiner, B.M. (2009). A protocadherin-cadherin-FLRT3 complex controls cell adhesion and morphogenesis. PLoS ONE *4*, e8411.

Chothia, C., and Jones, E.Y. (1997). The molecular structure of cell adhesion molecules. Annu. Rev. Biochem. *66*, 823–862.

Chung, K., and Deisseroth, K. (2013). CLARITY for mapping the nervous system. Nat. Methods *10*, 508–513.

Coles, C.H., Shen, Y., Tenney, A.P., Siebold, C., Sutton, G.C., Lu, W., Gallagher, J.T., Jones, E.Y., Flanagan, J.G., and Aricescu, A.R. (2011). Proteoglycan-specific molecular switch for RPTPσ clustering and neuronal extension. Science *332*, 484–488.

Cooper, J.A. (2013). Cell biology in neuroscience: mechanisms of cell migration in the nervous system. J. Cell Biol. *202*, 725–734.

Dahmann, C., Oates, A.C., and Brand, M. (2011). Boundary formation and maintenance in tissue development. Nat. Rev. Genet. *12*, 43–55.

Dimidschstein, J., Passante, L., Dufour, A., van den Ameele, J., Tiberi, L., Hrechdakian, T., Adams, R., Klein, R., Lie, D.C., Jossin, Y., and Vanderhaeghen, P. (2013). Ephrin-B1 controls the columnar distribution of cortical pyramidal neurons by restricting their tangential migration. Neuron *79*, 1123–1135.

Egea, J., Erlacher, C., Montanez, E., Burtscher, I., Yamagishi, S., Hess, M., Hampel, F., Sanchez, R., Rodriguez-Manzaneque, M.T., Bösl, M.R., et al. (2008). Genetic ablation of FLRT3 reveals a novel morphogenetic function for the anterior visceral endoderm in suppressing mesoderm differentiation. Genes Dev. *22*, 3349–3362.

Engelkamp, D. (2002). Cloning of three mouse Unc5 genes and their expression patterns at mid-gestation. Mech. Dev. *118*, 191–197.

Glaser, F., Pupko, T., Paz, I., Bell, R.E., Bechor-Shental, D., Martz, E., and Ben-Tal, N. (2003). ConSurf: identification of functional regions in proteins by surface-mapping of phylogenetic information. Bioinformatics *19*, 163–164.

Haines, B.P., Wheldon, L.M., Summerbell, D., Heath, J.K., and Rigby, P.W.J. (2006). Regulated expression of FLRT genes implies a functional role in the regulation of FGF signalling during mouse development. Dev. Biol. *297*, 14–25.

Hayashi, S., Lewis, P., Pevny, L., and McMahon, A.P. (2002). Efficient gene modulation in mouse epiblast using a Sox2Cre transgenic mouse strain. Mech. Dev. *119* (*Suppl 1*), S97–S101.

Hevner, R.F., Daza, R.A.M., Rubenstein, J.L.R., Stunnenberg, H., Olavarria, J.F., and Englund, C. (2003). Beyond laminar fate: toward a molecular classification of cortical projection/pyramidal neurons. Dev. Neurosci. *25*, 139–151.

Holm, L., and Rosenström, P. (2010). Dali server: conservation mapping in 3D. Nucleic Acids Res. *38*, W545–W549.

Kabsch, W. (1993). Automatic processing of rotation diffraction data from crystals of initially unknown symmetry and cell constants. J. Appl. Crystallogr. *26*, 795–800.

Kajander, T., Kuja-Panula, J., Rauvala, H., and Goldman, A. (2011). Crystal structure and role of glycans and dimerization in folding of neuronal leucine-rich repeat protein AMIGO-1. J. Mol. Biol. *413*, 1001–1015.

Karaulanov, E.E., Böttcher, R.T., and Niehrs, C. (2006). A role for fibronectin-leucine-rich transmembrane cell-surface proteins in homotypic cell adhesion. EMBO Rep. *7*, 283–290.

Karaulanov, E., Böttcher, R.T., Stannek, P., Wu, W., Rau, M., Ogata, S., Cho, K.W.Y., and Niehrs, C. (2009). Unc5B interacts with FLRT3 and Rnd1 to modulate cell adhesion in *Xenopus* embryos. PLoS ONE *4*, e5742.

Klein, R., and Kania, A. (2014). Ephrin signalling in the developing nervous system. Curr. Opin. Neurobiol. *27*, 16–24.

Koch, A.W., Mathivet, T., Larrivée, B., Tong, R.K., Kowalski, J., Pibouin-Fragner, L., Bouvrée, K., Stawicki, S., Nicholes, K., Rathore, N., et al. (2011). Robo4 maintains vessel integrity and inhibits angiogenesis by interacting with UNC5B. Dev. Cell *20*, 33–46.

Kolodkin, A.L., and Tessier-Lavigne, M. (2011). Mechanisms and molecules of neuronal wiring: a primer. Cold Spring Harb. Perspect. Biol. *3*, a001727.

Krissinel, E., and Henrick, K. (2004). Secondary-structure matching (SSM), a new tool for fast protein structure alignment in three dimensions. Acta Crystallogr. D Biol. Crystallogr. *60*, 2256–2268.

Lai Wing Sun, K., Correia, J.P., and Kennedy, T.E. (2011). Netrins: versatile extracellular cues with diverse functions. Development *138*, 2153–2169.

Larrivée, B., Freitas, C., Trombe, M., Lv, X., Delafarge, B., Yuan, L., Bouvrée, K., Bréant, C., Del Toro, R., Bréchot, N., et al. (2007). Activation of the UNC5B receptor by Netrin-1 inhibits sprouting angiogenesis. Genes Dev. *21*, 2433–2447.

Leyva-Díaz, E., del Toro, D., Menal, M.J., Cambray, S., Susín, R., Tessier-Lavigne, M., Klein, R., Egea, J., and López-Bendito, G. (2014). FLRT3 is a

Robo1-interacting protein that determines Netrin-1 attraction in developing axons. Curr. Biol. *24*, 494–508.

Lu, X., Le Noble, F., Yuan, L., Jiang, Q., De Lafarge, B., Sugiyama, D., Bréant, C., Claes, F., De Smet, F., Thomas, J.-L., et al. (2004). The netrin receptor UNC5B mediates guidance events controlling morphogenesis of the vascular system. Nature *432*, 179–186.

Luo, B.-H., Carman, C.V., and Springer, T.A. (2007). Structural basis of integrin regulation and signaling. Annu. Rev. Immunol. *25*, 619–647.

Maretto, S., Müller, P.-S., Aricescu, A.R., Cho, K.W.Y., Bikoff, E.K., and Robertson, E.J. (2008). Ventral closure, headfold fusion and definitive endoderm migration defects in mouse embryos lacking the fibronectin leucine-rich transmembrane protein FLRT3. Dev. Biol. *318*, 184–193.

Marquardt, T., Shirasaki, R., Ghosh, S., Andrews, S.E., Carter, N., Hunter, T., and Pfaff, S.L. (2005). Coexpressed EphA receptors and ephrin-A ligands mediate opposing actions on growth cone navigation from distinct membrane domains. Cell *121*, 127–139.

Müller, P.-S., Schulz, R., Maretto, S., Costello, I., Srinivas, S., Bikoff, E., and Robertson, E. (2011). The fibronectin leucine-rich repeat transmembrane protein Flrt2 is required in the epicardium to promote heart morphogenesis. Development *138*, 1297–1308.

Navankasattusas, S., Whitehead, K.J., Suli, A., Sorensen, L.K., Lim, A.H., Zhao, J., Park, K.W., Wythe, J.D., Thomas, K.R., Chien, C.-B., and Li, D.Y. (2008). The netrin receptor UNC5B promotes angiogenesis in specific vascular beds. Development *135*, 659–667.

Nieto, M., Monuki, E.S., Tang, H., Imitola, J., Haubst, N., Khoury, S.J., Cunningham, J., Gotz, M., and Walsh, C.A. (2004). Expression of Cux-1 and Cux-2 in the subventricular zone and upper layers II–IV of the cerebral cortex. J. Comp. Neurol. *479*, 168–180.

O'Sullivan, M.L., de Wit, J., Savas, J.N., Comoletti, D., Otto-Hitt, S., Yates, J.R., III, and Ghosh, A. (2012). FLRT proteins are endogenous latrophilin ligands and regulate excitatory synapse development. Neuron *73*, 903–910.

Rakic, P. (1988). Specification of cerebral cortical areas. Science *241*, 170–176.

Sawamiphak, S., Ritter, M., and Acker-Palmer, A. (2010). Preparation of retinal explant cultures to study ex vivo tip endothelial cell responses. Nat. Protoc. *5*, 1659–1665.

Scott, P.G., McEwan, P.A., Dodd, C.M., Bergmann, E.M., Bishop, P.N., and Bella, J. (2004). Crystal structure of the dimeric protein core of decorin, the archetypal small leucine-rich repeat proteoglycan. Proc. Natl. Acad. Sci. USA *101*, 15633–15638.

Scott, P.G., Dodd, C.M., Bergmann, E.M., Sheehan, J.K., and Bishop, P.N. (2006). Crystal structure of the biglycan dimer and evidence that dimerization is essential for folding and stability of class I small leucine-rich repeat proteoglycans. J. Biol. Chem. *281*, 13324–13332.

Seiradake, E., von Philipsborn, A.C., Henry, M., Fritz, M., Lortat-Jacob, H., Jamin, M., Hemrika, W., Bastmeyer, M., Cusack, S., and McCarthy, A.A. (2009). Structure and functional relevance of the Slit2 homodimerization domain. EMBO Rep. *10*, 736–741.

Seiradake, E., Harlos, K., Sutton, G., Aricescu, A.R., and Jones, E.Y. (2010). An extracellular steric seeding mechanism for Eph-ephrin signaling platform assembly. Nat. Struct. Mol. Biol. *17*, 398–402.

Solecki, D.J. (2012). Sticky situations: recent advances in control of cell adhesion during neuronal migration. Curr. Opin. Neurobiol. *22*, 791–798.

Torii, M., Hashimoto-Torii, K., Levitt, P., and Rakic, P. (2009). Integration of neuronal clones in the radial cortical columns by EphA and ephrin-A signalling. Nature *461*, 524–528.

Tronche, F., Kellendonk, C., Kretz, O., Gass, P., Anlag, K., Orban, P.C., Bock, R., Klein, R., and Schütz, G. (1999). Disruption of the glucocorticoid receptor gene in the nervous system results in reduced anxiety. Nat. Genet. *23*, 99–103.

Vielmetter, J., Stolze, B., Bonhoeffer, F., and Stuermer, C.A. (1990). In vitro assay to test differential substrate affinities of growing axons and migratory cells. Exp. Brain Res. *81*, 283–287.

Villar-Cerviño, V., Molano-Mazón, M., Catchpole, T., Valdeolmillos, M., Henkemeyer, M., Martínez, L.M., Borrell, V., and Marín, O. (2013). Contact repulsion controls the dispersion and final distribution of Cajal-Retzius cells. Neuron *77*, 457–471.

Wang, R., Wei, Z., Jin, H., Wu, H., Yu, C., Wen, W., Chan, L.-N., Wen, Z., and Zhang, M. (2009). Autoinhibition of UNC5b revealed by the cytoplasmic domain structure of the receptor. Mol. Cell *33*, 692–703.

Winter, G., Lobley, C.M.C., and Prince, S.M. (2013). Decision making in xia2. Acta Crystallogr. D Biol. Crystallogr. *69*, 1260–1273.

Yamagishi, S., Hampel, F., Hata, K., Del Toro, D., Schwark, M., Kvachnina, E., Bastmeyer, M., Yamashita, T., Tarabykin, V., Klein, R., and Egea, J. (2011). FLRT2 and FLRT3 act as repulsive guidance cues for Unc5-positive neurons. EMBO J. *30*, 2920–2933.

Chapter 4

Results - FLRT3 as a potential RGC marker in the mouse retina

The aim of this project was to study the functions of FLRTs in the retina. I evaluated their expression pattern by the use of LacZ reporter lines during development and adult stages. Among all FLRTs, I focused on FLRT3 both during development where I studied the effects of its depletion in the retina, and in the adult where I have explored its potential use as a marker for a specific RGC subpopulation.

4.1 The role of FLRTs in retina development

During development, members of the FLRT protein family, FLRT1 and FLRT3, show high expression in the retina. At mid-neurogenesis (E15.5), the *Flrt1-LacZ* reporter line showed that *Flrt1* expression forms a gradient across the whole mouse retina (Figure 4.1 A). Moreover, *Flrt1* expressing cells form a ring around the exit of the optic nerve (Figure 4.1 A and B) suggesting a possible role in axonal pathfinding.

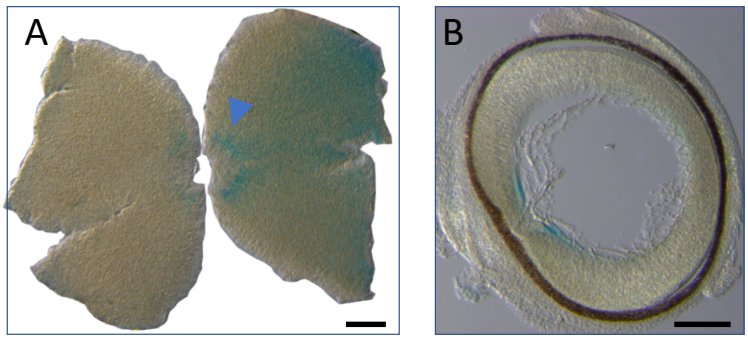

Figure 4.1: Embryonic *Flrt1* expression in the retina. A: Retina whole mount *Flrt1-LacZ* staining of an embryonic E15.5 mouse. B: *Flrt1-LacZ* retinal section showing *Flrt1* expression around the optic nerve exit. Scale, 200 µm

Similar to *Flrt1*, *Flrt3-LacZ* also shows expression and the formation of a gradient in the retina (high close to the lens and low close to the optic nerve). Interestingly, it shows also expression in the epithelium that covers the lens. Later during retina development, *Flrt3* is expressed in GCL and INL from P2 to P60, while its expression in the ONL is found at P2, P7 but not P60 (Figure 4.2).

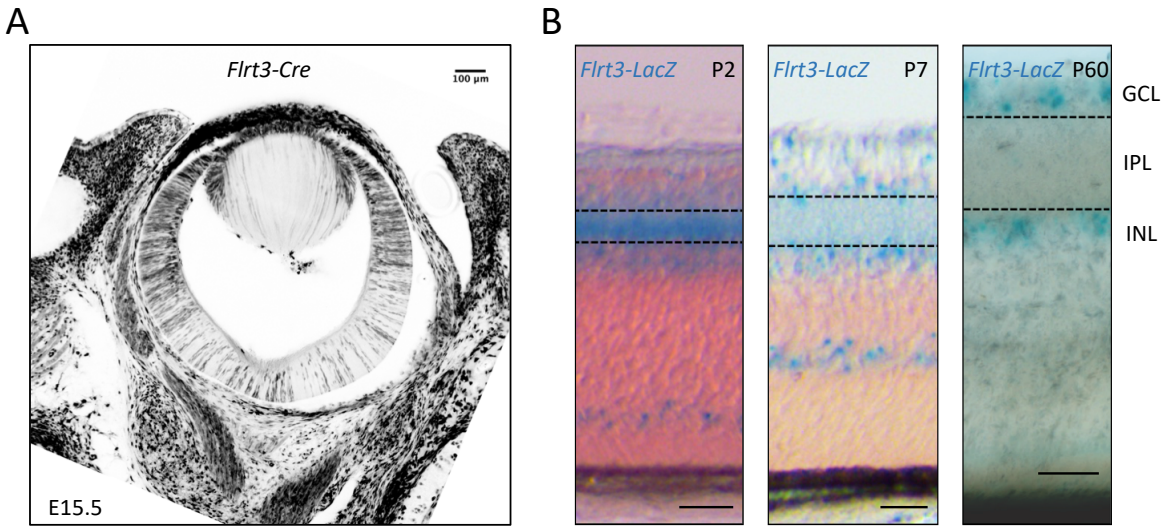

Figure 4.2: *Flrt3* expression pattern during embryonic and early postnatal development. A: *Flrt3* expression pattern at E15.5. B: *Flrt3* expression pattern during early postnatal stages (P2 and P7) until adulthood. GCL: ganglion cell layer, IPL: inner plexiform layer, INL: inner nuclear layer. Scale: A: 100 µm, B: 50 µm

4.1.1 Early embryonic Flrt3 removal leads to eye malformations

Previous work from the lab and others has shown that FLRT3 has a role in both the neuronal and vascular systems [296, 67]. Given that *Flrt3* is expressed in neurons and some endothelial cells in the retina, I was interested in using a specific genetic-loss-of-function approach in mice to find neuronal and vascular-specific *Flrt3* functions. Since *Flrt3* is expressed from E13.5 on (and possibly earlier) I crossed the *Flrt3 lox/lox* line with the *SOX2-Cre* line which removes *Flrt3* during early embryonic stages. The removal of *Flrt3* during development led to blindness, cataract formation and eye malformations in most of the adult *Flrt3 SOX2* KO mice. In one extreme case almost all RGCs were missing and the cell density within the RGC dropped by half (Figure 4.3 A and B). Interestingly the displaced amacrine cell population was not affected. Other *FLRT3 SOX2* KO mice however retained their RGCs (data not shown). Overall the *Flrt3 SOX2* KO showed high phenotype variability. In collaboration with the lab of Amparo Acker-Palmer, we showed that removal of FLRT3 led to hypervascularization in the retina. This suggests that the observed phenotype in *Flrt3 SOX2* KO might be the result of vascularization problems during development. To constrict FLRT3 removal to RGCs, I crossed the *Brn3b-Cre* line from Eloisa Herera's lab to our *Flrt3 lox/lox* mice. The Brn3b-Cre mice however showed no developmental eye abnormalities (data not shown) further strengthening the link between vascularization and the previous observed phenotype. Since I was not interested in the vascular system I stopped further analysis of the phenotype.

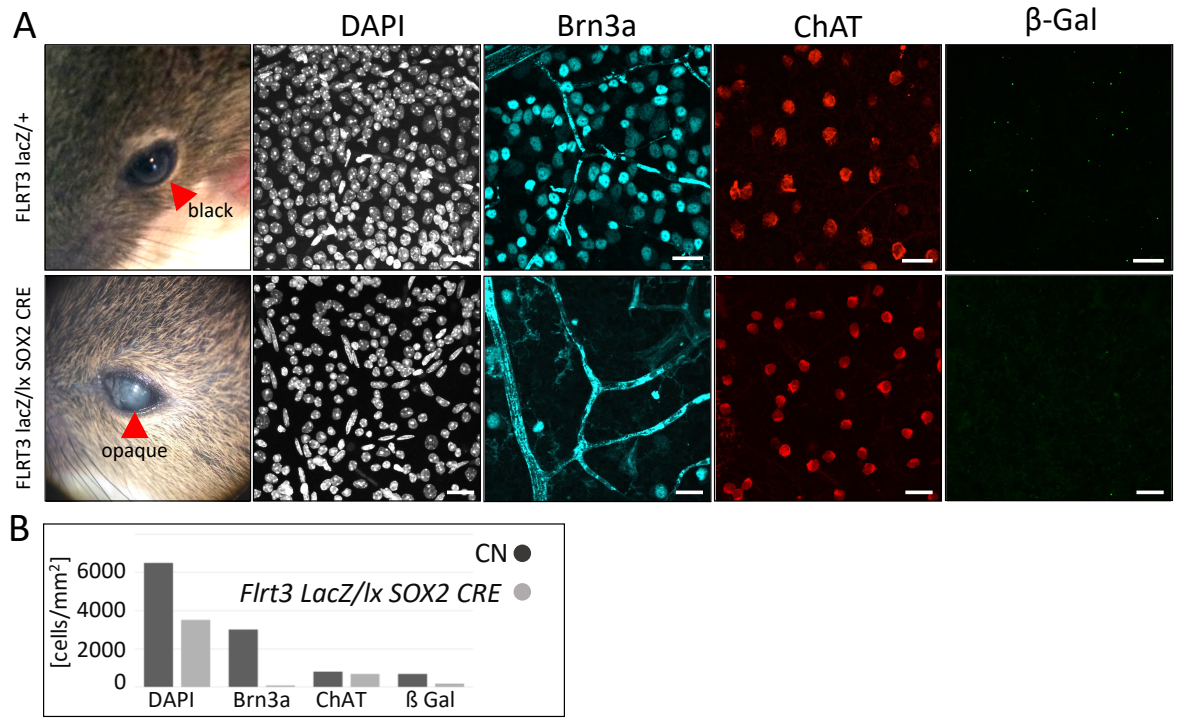

Figure 4.3: *Flrt3 SOX2* KO leads to frequent eye malformations. A: Often the eyes in *Flrt3* KO look opaque. In one extreme case almost all RGCs (Brn3a+) were absent and only amacrine cells survived. B: Quantification of images shown in A. Scale: 40 µm.

4.2 Flrt1,2,3 expression pattern in the mouse retina

To determine if *Flrts* are expressed in the adult mouse retina, I performed X-Gal staining in *Flrt* 1,2 and 3 LacZ knock-in mice. Results showed that all three *Flrts* are expressed in the retina (Figure 4.4 B). *Flrt1* and *Flrt2* are mainly expressed in the GCL while *Flrt3* is expressed in both the GCL and INL (Figure 4.4 B).

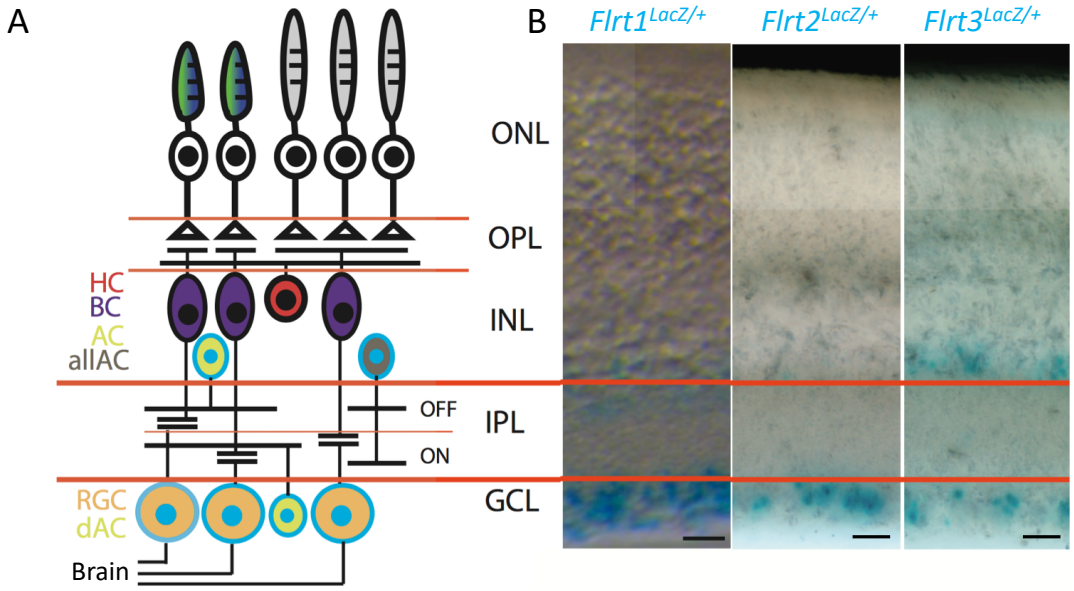

Figure 4.4: *Flrt*1, 2 and 3 expression pattern in retinal cross sections. A: Illustration of the retinal layers and cell types. B: *Flrt1* and *Flrt2* are mainly expressed in the GCL. *Flrt3* is expressed in the GCL and INL. GCL, ganglion cell layer; INL, inner nuclear layer; OPL, outer plexiform layer; ONL, outer nuclear layer; IPL, inner plexiform layer; HC, horizontal cell; BC, bipolar cell; AC, amacrine cell; dAC, displaced amacrine cell. Scale: 40 µm.

Figure 4.5 A/C shows that *Flrt2* and *Flrt3* are expressed across the whole adult mouse retina. To identify which cell types express *Flrt2* and *Flrt3* we stained against the pan RGC marker RBPMS and LacZ. Since only 2 neuronal cell types exist in the GCL, all RBPMS negative cells were considered to be amacrine cells. The quantification of *Flrt-LacZ* and RBPMS colocalization was very challenging since the LacZ+ cells showed only small fluorescent punctae that required a very clean staining. Since *Flrt1* LacZ staining showed strong expression in almost all cells in the GCL, only the *Flrt2* and *Flrt3-LacZ* retinas were quantified. The results showed that 87% of the *Flrt3-LacZ* and 92% of the *Flrt2-LacZ* cells co-label with the RGC marker RBPMS suggesting that a majority of FLRT2+ and FLRT3+ cells in the GCL are RGCs (Figure 4.5 B/D). FLRT2+ RGCs represent about 48% and FLRT3+ RGCs stain 23% of the whole RGC population (Figure 4.5 B/D).

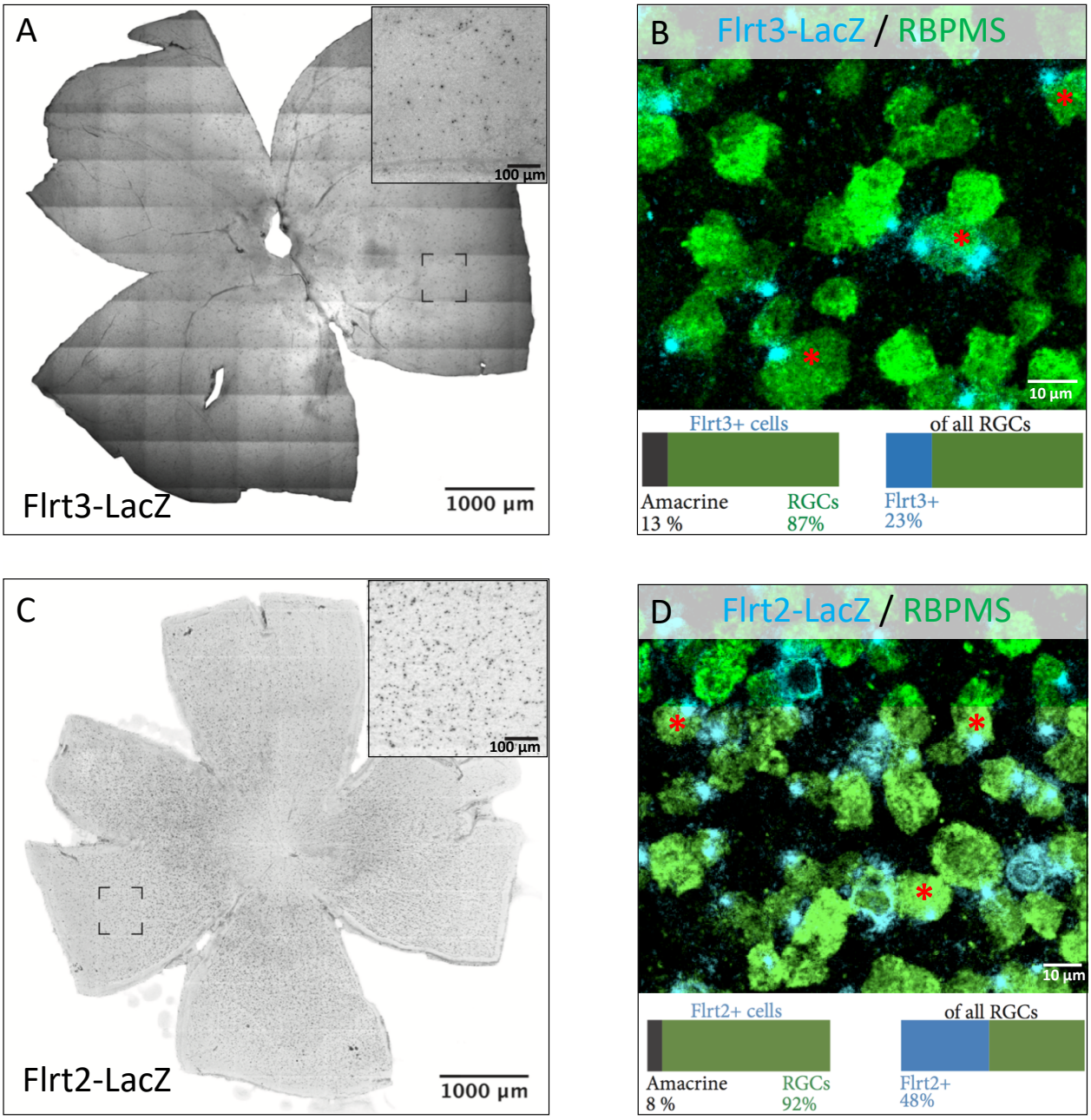

Figure 4.5: A: Retina whole mount FLRT3-LacZ staining of an adult P60 mouse. B: Quantification of FLRT3+ RGCs. C: Retina whole mount FLRT2-LacZ staining of and adult P60 mouse. D: Quantification of FLRT2+ RGCs. Red asterix label examples of FLRT+ RGCs.

Next I asked if FLRT2 and FLRT3+ cells represent separate cell populations. Thus I crossed our *Flrt2-LacZ* mice with the *Flrt3-LacZ* line to generate a *Flrt2-LacZ/Flrt3-LacZ* mouse line. Quantifications of X-Gal stainings from that line compared to the *Flrt2-LacZ* and *Flrt3-LacZ* showed that there is co-expression in only 13% of all cells, suggesting that FLRT2 and FLRT3+ cells are two separate cell populations (Figure 4.6).

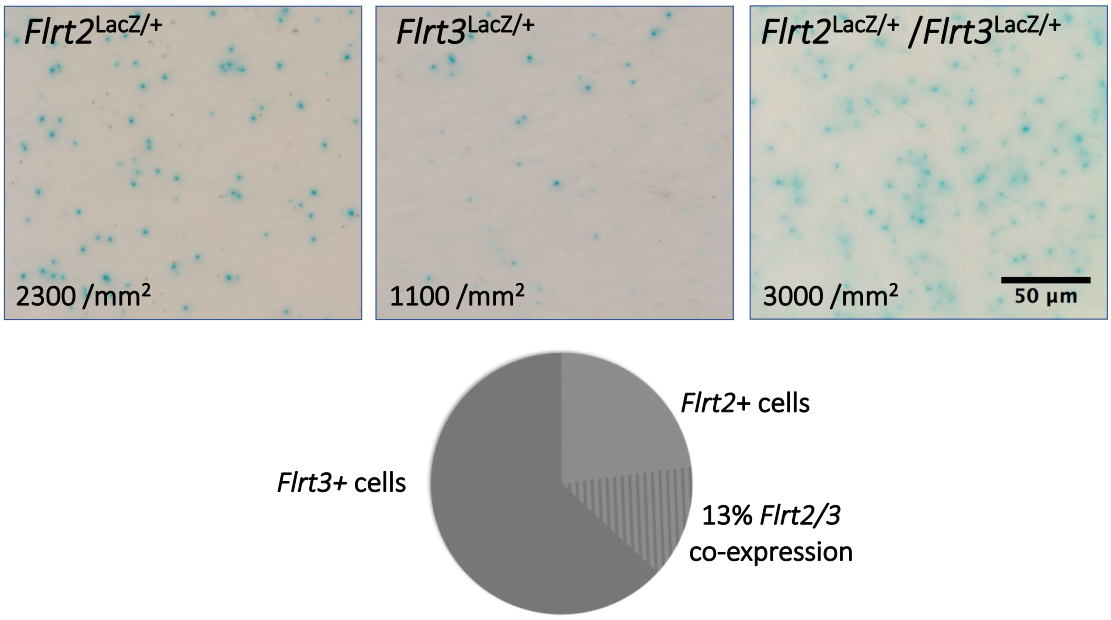

Figure 4.6: *Flrt2* and *Flrt3* cells in the GCL are mostly separate population with only 13% *Flrt2/3* coexpressing cells.

So far, W3 cells in mice are the largest known cell population with a common functional property and represent about 13 % of all RGCs. Since the *Flrt3-LacZ*/RBPMS quantification suggested that FLRT3+ RGCs represent about 23% of all RGCs we concluded that the chance of labelling a single cell population is higher for FLRT3 and thus focused on generating a *Flrt3-Cre* mouse instead of the *Flrt2-Cre*. Moreover we decided to make the Tamoxifen line inducible for three reasons. First, in a normal *Flrt3-Cre* line, each cell that once expressed *Flrt3* would be labelled when crossed to a reporter making it difficult to study a particular cell type. Second, my results using the *Flrt3 SOX2-Cre* line showed strong phenotypes probably due to vascular defects (see Figure 4.3). Third, early embryonic *Flrt3* removal is lethal [67]. By combining the FLRT3-Cre protein with an estrogen receptor domain, we can inhibit Cre from entering into the nucleus until we inject Tamoxifen and may thus control the timepoint of *Flrt3-Cre* induction. Important to note is that this system represents an On or Off system where the intensity of the reporter expression does not correlate with *Flrt3*-expression. In theory only one Cre molecule would be sufficient to intensively label a FLRT3+ cell by recombining a reporter gene.

4.3 Generation of a Flrt3-CreERT2 knock-in mouse

The *Flrt3-Cre* knock-in mouse was generated by homologous recombination of Exon 2 in the *Flrt3* locus with a CreERT2 replacement-type targeting vector in embryonic stem cells (Figure 4.7). Correct insertion of the CreERT2 targeting vector was confirmed using specific probes. To further characterize the expression pattern, the *Flrt3-CreERT2* line was crossed to a Tomato-reporter line that labelled all Cre+ cells in red. To induce Cre expression, adult mice were injected with a maximum dose of 60 µg/g 4-Hydroxy-Tamoxifen. I analysed the expression pattern of three *Flrt3-CreERT2* founder lines in the adult brain and retina. As expected from a knock-in mouse, all three lines showed a

very similar expression pattern in the brain and retina (Figure 4.8). In the retina all three lines showed a similar distribution of FLRT3+ cells in the GCL (data not shown). We chose the 1D5 line for further experiments and cryoconserved the 2G10 line as a backup.

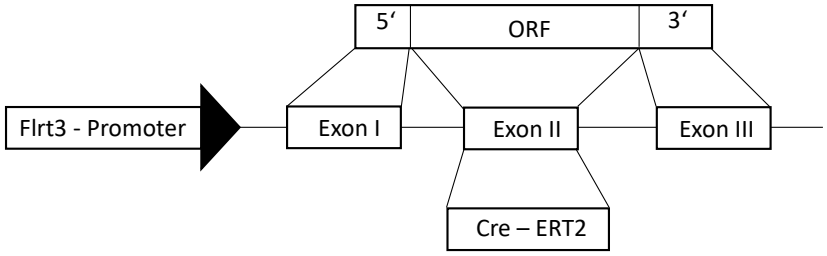

Figure 4.7: *Flrt3-CreERT2* knock-in strategy. Exon II of the *Flrt3* locus was replaced with a CreERT2 targeting vector via homologous recombination

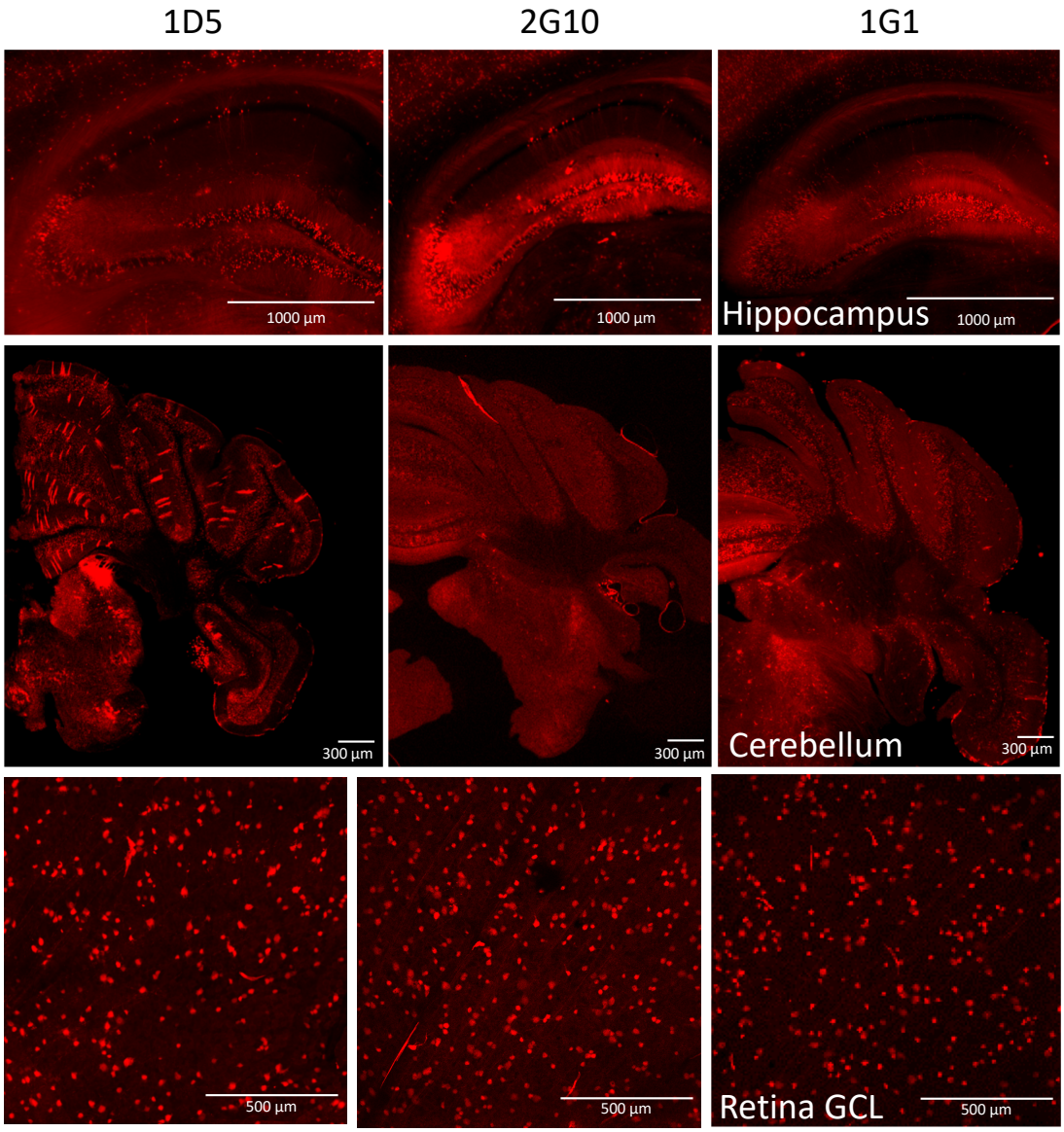

Figure 4.8: Adult *Flrt3-CreERT2* founder lines 1D5, 2G10 and 1G1 crossed to a Tomato reporter line after injection with 60 µg/g 4-Hydroxy-Tamoxifen. All three lines showed a very similar expression pattern in the retina and brain. In the cerebellum the 1D5 line sparsely labelled Purkinje cells which were not labelled in the 2G10 and 1G1 line.

4.4 Characterization of the FLRT3-CreERT2 mouse

To obtain a 4-Hydroxy-Tamoxifen concentration that yields in optimal Cre expression, we tested concentrations of 0 µg/g, 2 µg/g, 10 µg/g and 60 µg/g. At 0 µg/g we obtained labelling of a few cells suggesting that our *Flrt3-CreERT2* line is leaky. 2 µg/g and 10 µg/g only marginally increased the number of Tomato positive labelled cells while a maximum concentration of 60 µg/g showed a plateau of induced expression (Figure 4.9).

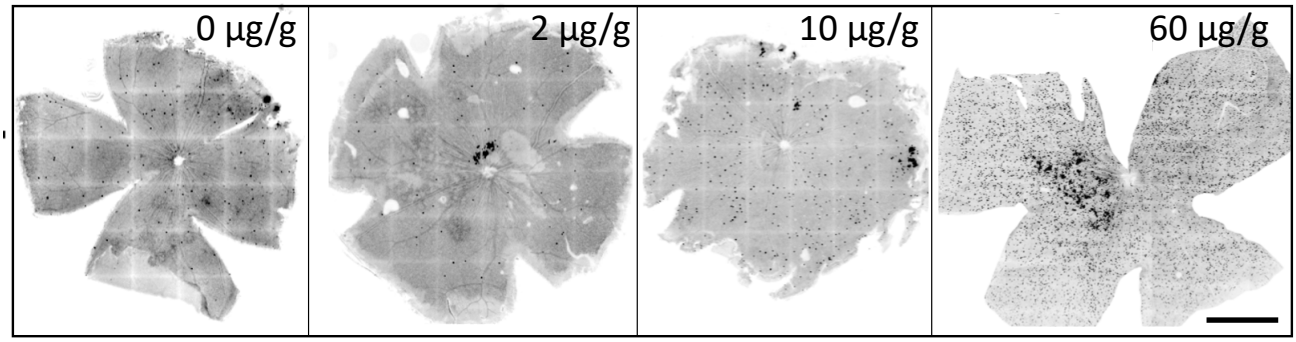

Figure 4.9: Retina whole mount of adult *Flrt3-CreERT2:tdTomato* mice injected with different 4-Hydroxy-Tamoxifen doses. Scale, 1000 µm.

4.4.1 Flrt3-Cre expression pattern in the brain is similar to Flrt3 LacZ expression

To confirm correct insertion of the *Flrt3-CreERT2* construct into the mouse genome we compared our *Flrt3-CreERT2* to the already existing *Flrt3-LacZ* line [296]. Figure 4.10 shows several coronal sections from regions that have a defined *Flrt3* expression. Overall the expression pattern of the *Flrt3-Cre* line matches that of the *Flrt3-LacZ*. For example, in the hippocampus *Flrt3* is only expressed in the CA3 and dentate gyrus (DG) but not in the CA1 (Figure 4.10). Within the cortex the *Flrt3-LacZ* line shows a more intense staining compared to the *Flrt3-CreERT2* line. Slight differences in expression intensity can be explained by the different labelling mechanism. Assuming that both alleles are expressed similarly, the beta Galactosidase expression and thus the X-Gal staining intensity in the *Flrt3-LacZ* line correlates with *Flrt3* expression levels. In the *Flrt3-CreERT2* line however, staining intensity is only dependent on the Tomato driver and does not correlate with the degree of *Flrt3* expression.

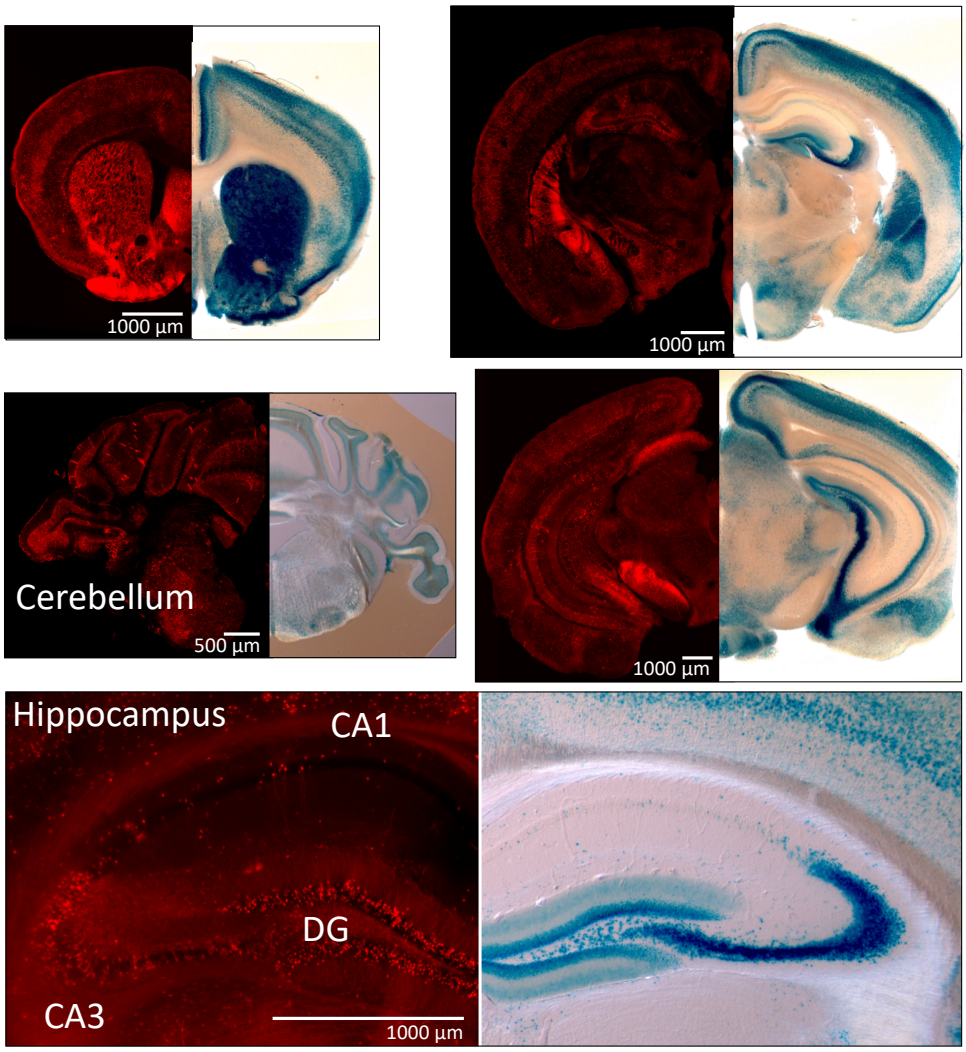

Figure 4.10: *Flrt3-CreERT2* Tomato expression compared to the *Flrt3-LacZ* line. Both lines are knock-in mice and were generated by replacing Exon II of the *Flrt3* locus. DG, dentate gyrus.

4.4.2 Flrt3 is expressed by amacrine and retinal ganglion cells within the ganglion cell layer of the adult mouse retina

To analyse *Flrt3* expression within the retina, P30 *Flrt3-CreERT2:tdTomato* mice were injected with 60 µg/g 4-Hydroxy-tamoxifen one week before collecting the retinas. Similar to the *Flrt3-LacZ* mouse, cross section of *Flrt3-Cre* mouse retinas shows FLRT3+ cells labelled in the ganglion cell layer and inner nuclear layer (Figure 4.11). In the inner nuclear layer four different cell types exist that can potentially be labelled by FLRT3: horizontal cells, amacrine cells, displaced RGCs and bipolar cells. Since we were mainly interested in specifying a new RGC subpopulation I did not molecularly characterize the cells in the INL. To ascertain if the ratio of FLRT3+ RGCs and amacrines in the GCL of the *Flrt3-CreERT2:tdTomato* matches with the *Flrt3-LacZ* stainings, I again stained against the RGC marker RBPMS. Since only displaced amacrines and RGCs populate the ganglion cell layer, all RBPMS negative FLRT3-cells were considered amacrines.

Some retinas occasionally showed clusters of Mueller glia cells labelled (Figure 4.11 A). These however are easily distinguishable by morphology only. In contrast to the *Flrt3-LacZ* quantifications where most FLRT3+ cells were amacrines, here I found 67% of all FLRT3+ cells in the GCL to be amacrine cells and only 23% were RGCs. Overall the FLRT3+ RGC population represents only 6% of all RGCs (Figure 4.11 B). Compared to other known functional RGC subgroups, the FLRT3-RGC population is very small.

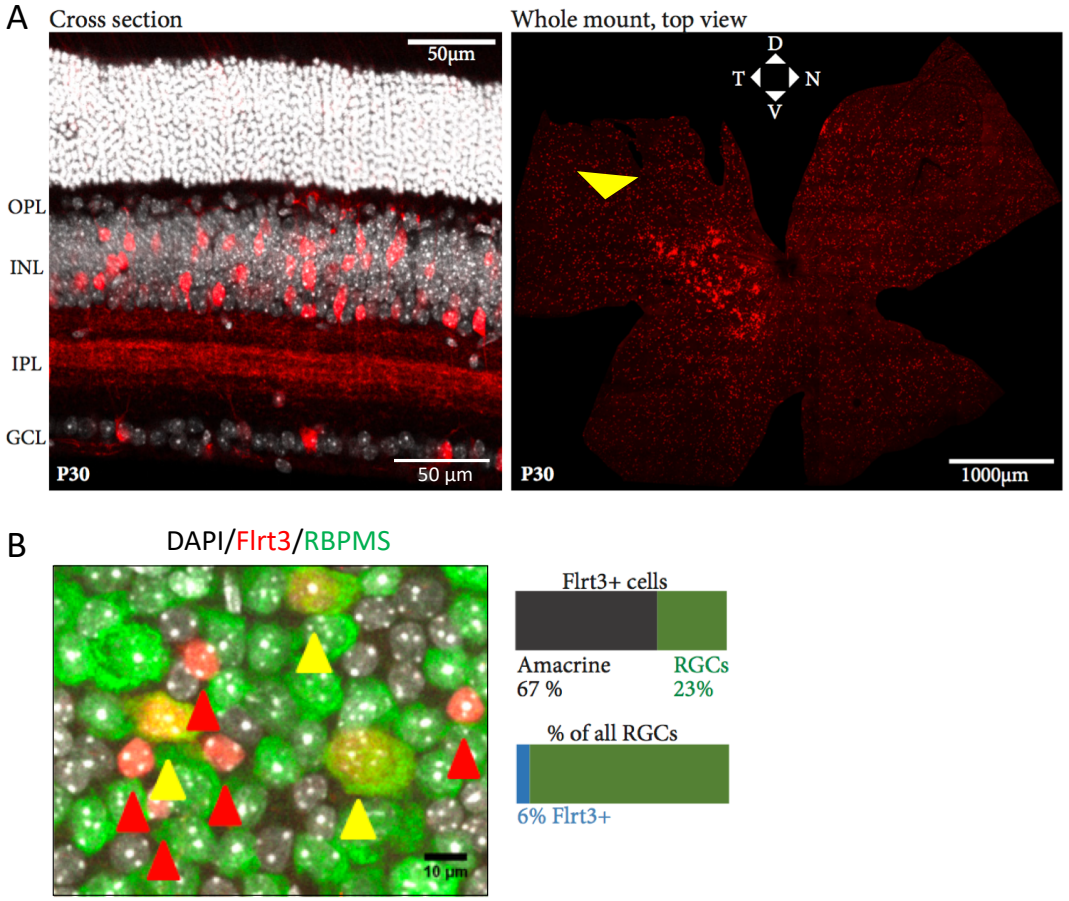

Figure 4.11: *Flrt3-CreERT2:tdTomato* expression in the mouse retina at P30. A: The cross section shows sparse labelling in the ganglion cell layer and inner nuclear layer. The whole mount view shows a z-projection of the ganglion cell layer only. FLRT3+ cells distribute across the whole retinal surface. Occasionally also Mueller cells are labelled (yellow arrow). B: RBPMS staining against RGCs showed that 23% of all FLRT3+ cells are RGCs. In total FLRT3+ RGCs represent about 6% of all RGCs.

4.5 Regular distribution analysis of FLRT3-RGCs

A general hallmark of all functional RGC and amacrine subpopulations found so far is that they cover the whole visual space by evenly distributing across the retina. The probability of finding another cell of the same subgroup within a certain radius is lower compared to random distribution. This drop in density, also called exclusion zone, can be quantified by the density recovery profile (DRP) (Figure 4.12). To calculate the DRP I wrote a Python algorithm that projects the 2D coordinates (Figure 4.12 A) of each cell to the center (x=0,y=0) and moves all surrounding cells within 150 µm radius by the same x and y values. Repeating that process over all cells results in an autocorrelogram

(Figure 4.12 B). Next, the algorithm calculates the density of cells within 10 µm radii steps (=annulus) and normalises that value by the total amount of cells resulting in a density recovery profile (Figure 4.12 C). If a cell distributes regularly, like the ChAT+ amacrine cells in Figure 4.12 A, a drop in density should be apparent within the first few annuli. Randomly distributed cells show the same density. To evaluate if my FLRT3+ RGCs are a homogeneous cell population, I determined the density recovery profile of RBPMS+ RGCs and RBPMS- amacrines. Neither FLRT3+ amacrines (Figure 4.12 B) or FLRT3+ RGCs (Figure 4.12 C) show a regular distribution, raising the possibility that both populations consist of further functionally defined subpopulations.

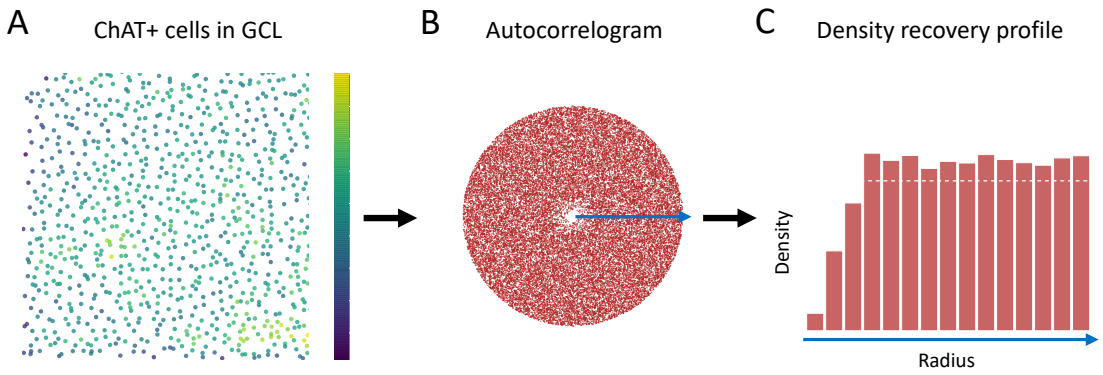

Figure 4.12: Example of a density recovery profile from mosaic-like distributing ChAT+ amacrine cells. A: Displaced amacrine cells in the GCL. B: Autocorrelogram shows the correlation of each cell to all other cells. C: Measuring the density within certain annuli from the center of the autocorrelogram results in the density recovery profile.

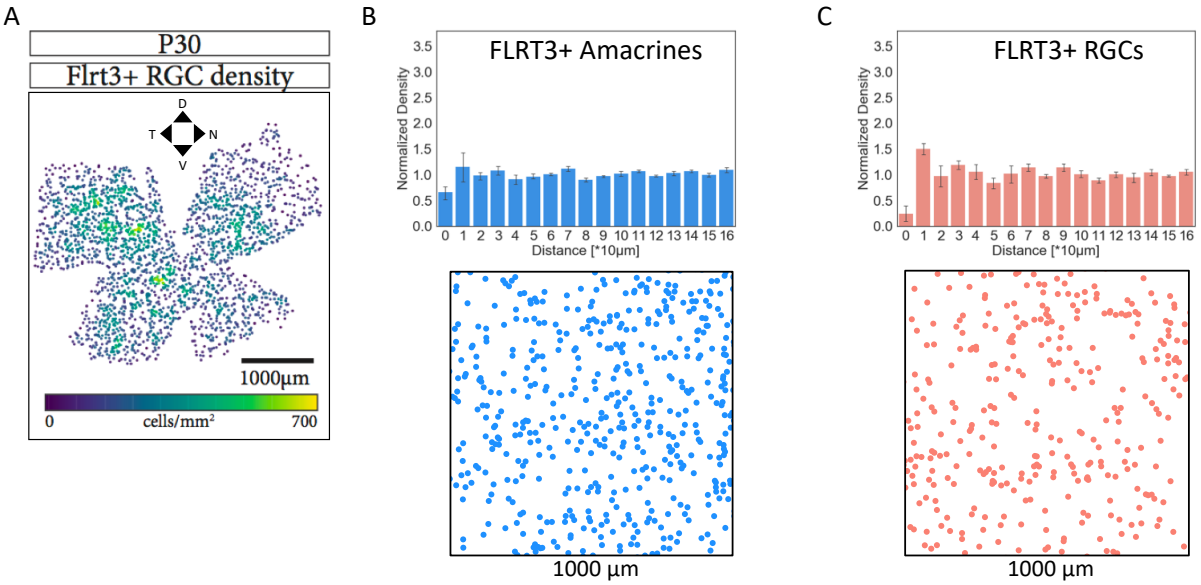

Figure 4.13: Density recovery profiles to analyse FLRT3+ cell distribution. A: Color coded FLRT3+ RGC density across the whole retina shows a slight increase in the dorsotemporal region of the retina. B: FLRT3+ amacrines show no regular distribution. C: FLRT3+ RGCs show no regular distribution.

4.6 Molecular definition of the FLRT3 RGC subpopulation

Since the cell distribution analysis of FLRT3+ RGCs suggested that FLRT3+ RGCs are a heterogeneous population, I immunostained FLRT3+ RGCs with other known RGC markers. Results showed that 23% of FLRT3+ RGCs co-label with CART, a marker that labels ON-OFF directionally selective RGCs (Figure 4.14). GAD67, an inhibitory marker that labels amacrine cells labelled 37% of all FLRT3+ amacrines (Figure 4.14). No co-staining was found for ChAT concluding that FLRT3+ amacrine cells do not contain any starburst amacrine cells (Figure 4.14).

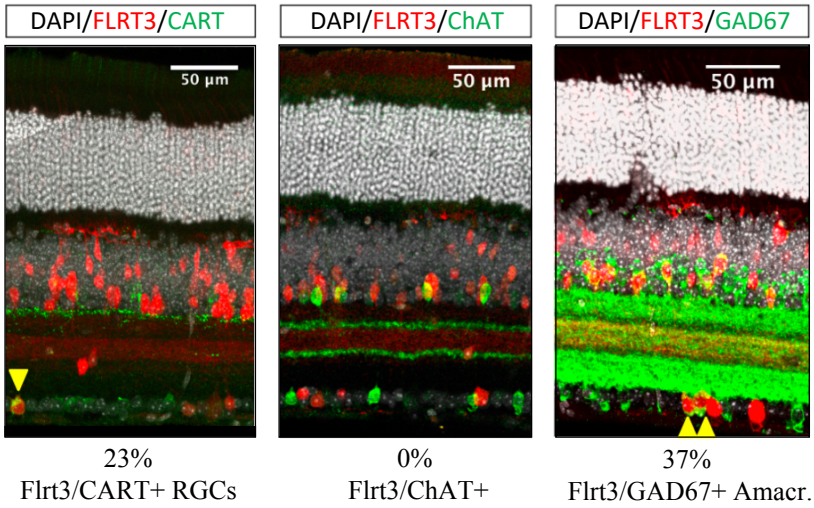

Figure 4.14: Fraction of FLRT3+ RGCs that coexpress other known ganglion cell layer markers. 23% of all FLRT3+ RGCs express CART, a marker for ooDSGCs. 37% of all the inhibitory amacrine cell marker GAD67.

Further analysis of known RGC markers showed that Calbindin labelled about 20% of all FLRT3-RGCs. Notably, morphological reconstruction of Calbindin positive RGCs showed that there are about 10 morphologically different subpopulations that still lack a molecular marker [89]. About 17% of all RGCs stained for Parvalbumin, which is a known RGC marker that labels about 8 morphologically distinct RGCs without known function (Figure 4.15) [131]. Brn3c is expressed by about 3 morphologically distinct RGCs, and it is expressed by 10% of the FLRT3+ RGCs[8]. Finally, smaller FLRT3-RGC subpopulations express the alpha RGC marker SMI32 (7%) and Satb1 (3%) (Figure 4.15).

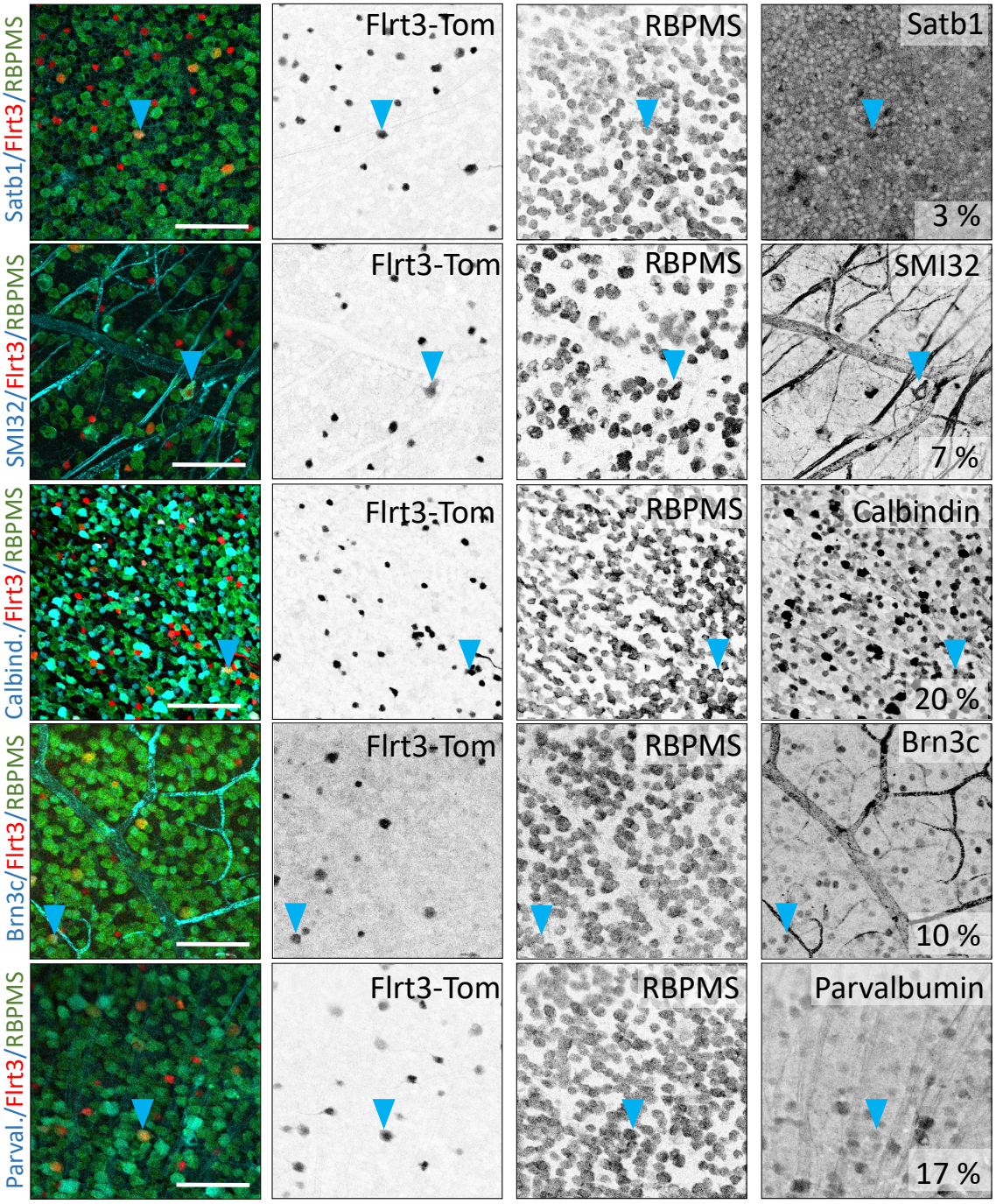

Figure 4.15: The biggest FLRT3+ RGC subpopulations are Parvalbumin (17%) and Calbindin (20%). Other markers such as Satb1, SMI32 and Brn3c are expressed by only a small fraction of FLRT3+ RGCs.

Next, I analyzed whether the largest identified FLRT3-RGC subpopulations labelled with CART (23%) and Calbindin (20%) represent homogeneous populations based on their density recovery profile. Neither CART+/FLRT3+ nor CART-/FLRT3+ distribute in a mosaic like fashion (Figure 4.14 A and B). Also, the density recovery profile did not show any sign of regular distribution in Calbindin + or - FLRT3-RGCs (Figure 4.15). Moreover, the Calbindin - and + amacrine cell populations do not show any regular distribution pattern (Figure 4.17).

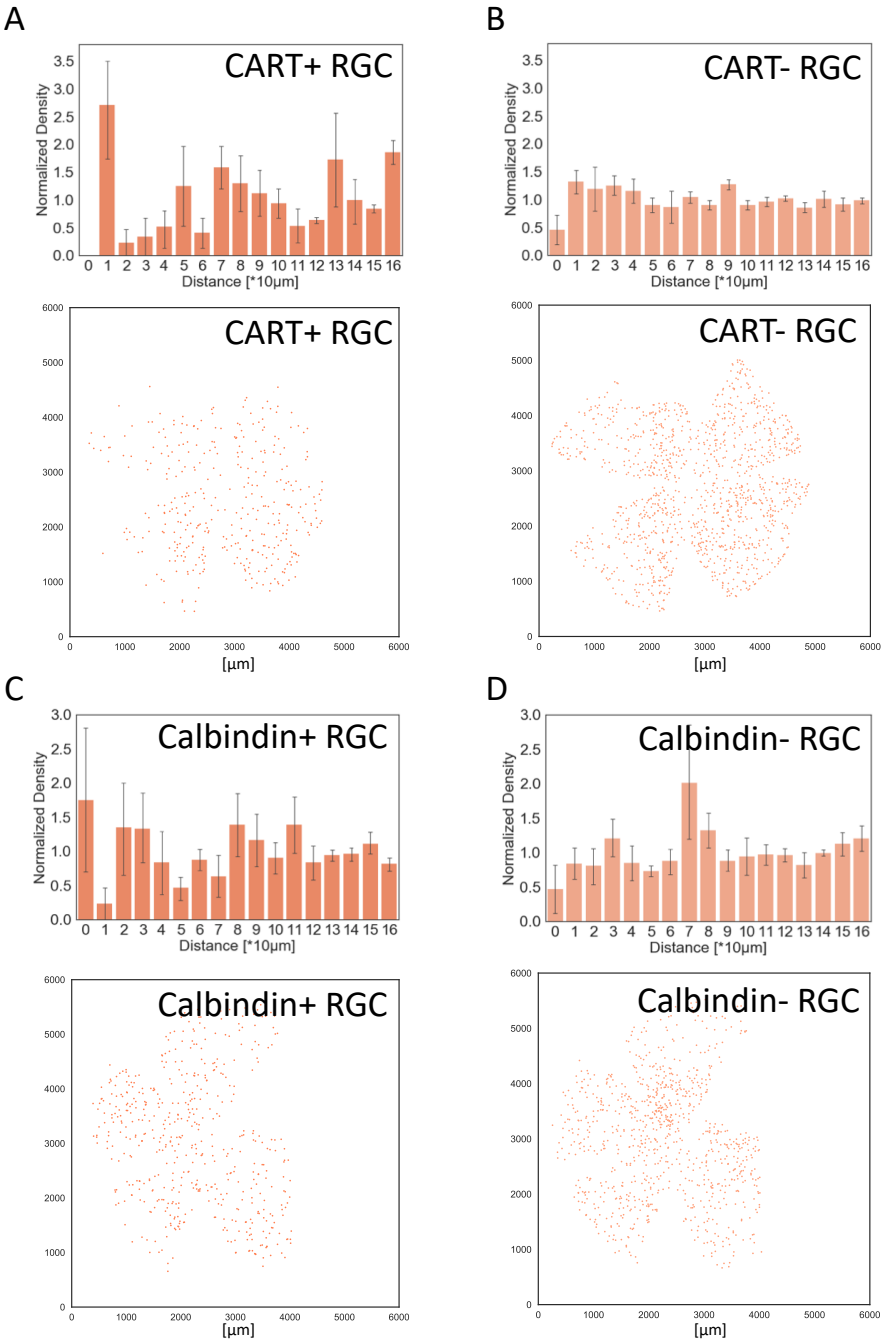

Figure 4.16: A: Distribution of CART+ FLRT3+ RGCs. B: Distribution of CART- FLRT3+ RGCs. C: Distribution of Calbindin+ FLRT3+ RGCs. D: Distribution of Calbindin- FLRT3+ RGCs. Error bar: SEM.

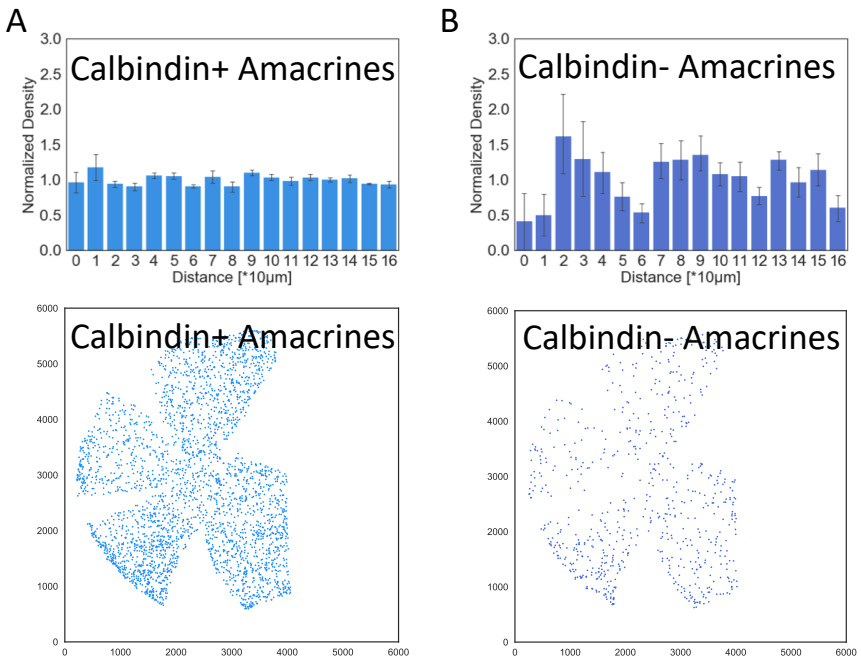

Figure 4.17: A: Distribution of Calbindin+ FLRT3 amacrines. B: Distribution of Calbindin- FLRT3 amacrines. Error bar: SEM.

Altogether, the known RGC markers used in this study suggest that *Flrt3* labels a heterogeneous population of RGCs. Therefore, a combination of several markers would be required to define specific populations. It is also possible that other molecular markers that were not tested here might subdivide the FLRT3+ RGCs into defined subpopulations.

4.7 Morphological reconstruction of FLRT3+ cells in the GCL

4.7.1 Soma size of FLRT3+ RGCs is larger than most FLRT3- RGCs

The soma size varies between 50 and 500 mm for RGCs and may give an indication of their average activity. The SMI-32 positive alpha RGCs for example can have very large soma sizes (Figure 4.18). The soma size of FLRT3+ RGCs varies between 50 and 350 mm with most of the cells being around 150 mm large (Figure 4.18). Thus FLRT3+ RGCs are larger than the majority of other RGCs (Figure 4.18).

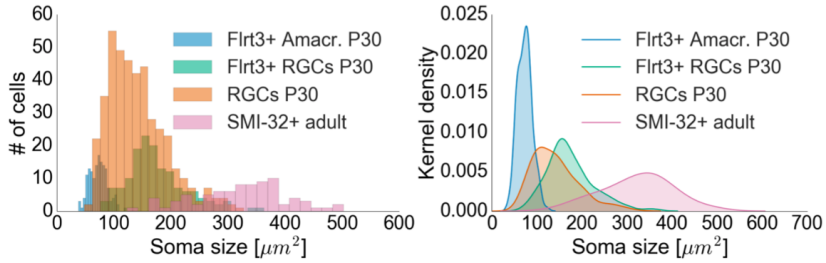

Figure 4.18: Frequency distribution and Kernel density of the FLRT3+ RGC soma sizes. The data shows that FLRT3+ RGCs have larger somas than the average RGC but are still smaller than the big SMI-32+ alpha-RGCs.

4.7.2 FLRT3+ neurons from the GCL and INL mainly stratify between layer 4 and 6

Since the functional properties of the different RGC subpopulations depend largely on their stratification it is important to determine the stratification depth of a new cell population. Overall most FLRT3+ cells from the ganglion cell and inner nuclear layers stratify between layer 3 and 7, between the two ON and OFF bands formed by ChAT+ starburst amacrine cells (Figure 4.19). Since most of the cells labelled by FLRT3 are amacrine cells or cells from the inner nuclear layer, this pattern should not represent the average stratification pattern of FLRT3+ RGCs. To determine the exact stratification pattern of FLRT3+ RGCs, I decided to inject fluorescent dyes in single FLRT3+ RGCs within the ganglion cell layer to visualize their morphology.

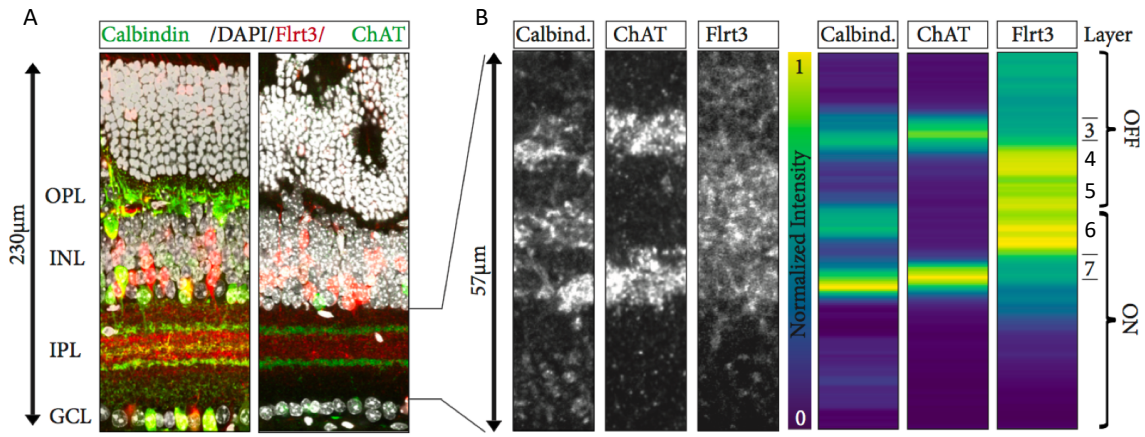

Figure 4.19: Overall FLRT3+ cells from the ganglion cell and inner nuclear layer stratify between the ON and OFF ChAT bands at layer 4-6.

4.7.3 Morphological reconstruction of dye injected FLRT3+ neurons in the GCL

To reconstruct single cell morphologies I mildly fixed the retinas for 15 min in 4% PFA and injected more than 139 cells with Lucifer yellow or Alexa488 dye. I had to discard 39 cells due to poor dye penetration resulting in 107 cells for reconstruction. After semiautomatic morphological reconstruction of the dentritic tree, I resliced the image

and manually cropped out the IPL of all neurons. Next, I used a custom-written Python code to determine the stratification depth, perform sholl analysis and determine the total neurite length and number of branching points of each neuron (Figure 4.20). I used the RBPMS RGC marker to distinguish RGCs from amacrines.

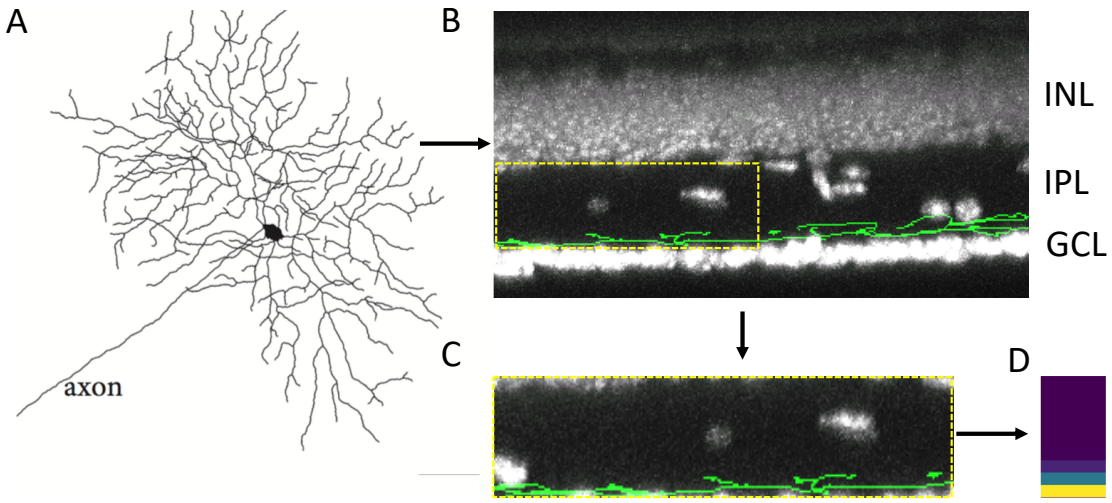

Figure 4.20: Morphological reconstruction of an Alexa488 injected RGC. A: Manually reconstructed RGC. B: Reslicing the image stack allows analysis of stratification within the IPL. C: Manual selection of the IPL to allow automatic analysis of stratification using a python script. D: Stratification density. All images were binned into 10 layers, summed up and normalized across overall intensity.

For clustering morphologically similar cell types I used the hierarchical clustering method. When I included all morphological features, such as stratification depth, bifurcation points, total neurite length, soma size and sholl analysis, the hierarchical clustering approach resulted in about 13 different clusters (Figure 4.21). The threshold for different clusters was set so that cells with different stratification depths should not be within the same cluster. Except for four amacrine cells, the hierarchical clustering method successfully separated RGCs from amacrines without the marker information resulting in seven RGC only, four amacrine only and two mixed clusters (Figure 4.21). The largest four RGC clusters mainly have most of their dendrites stratify in the ON layer 7-10 suggesting that most FLRT3+ RGCs react to increasing light stimuli. The FLRT3+ amacrine cells in contrast seem to prefer layer 5-6 suggesting that most of the FLRT3+ stratification between layer 3 and 7 in Figure 4.19 comes from amacrine cells. Overall the dendritic trees of FLRT3+ amacrine cells are less branched but bigger compared to the FLRT3+ RGCs.

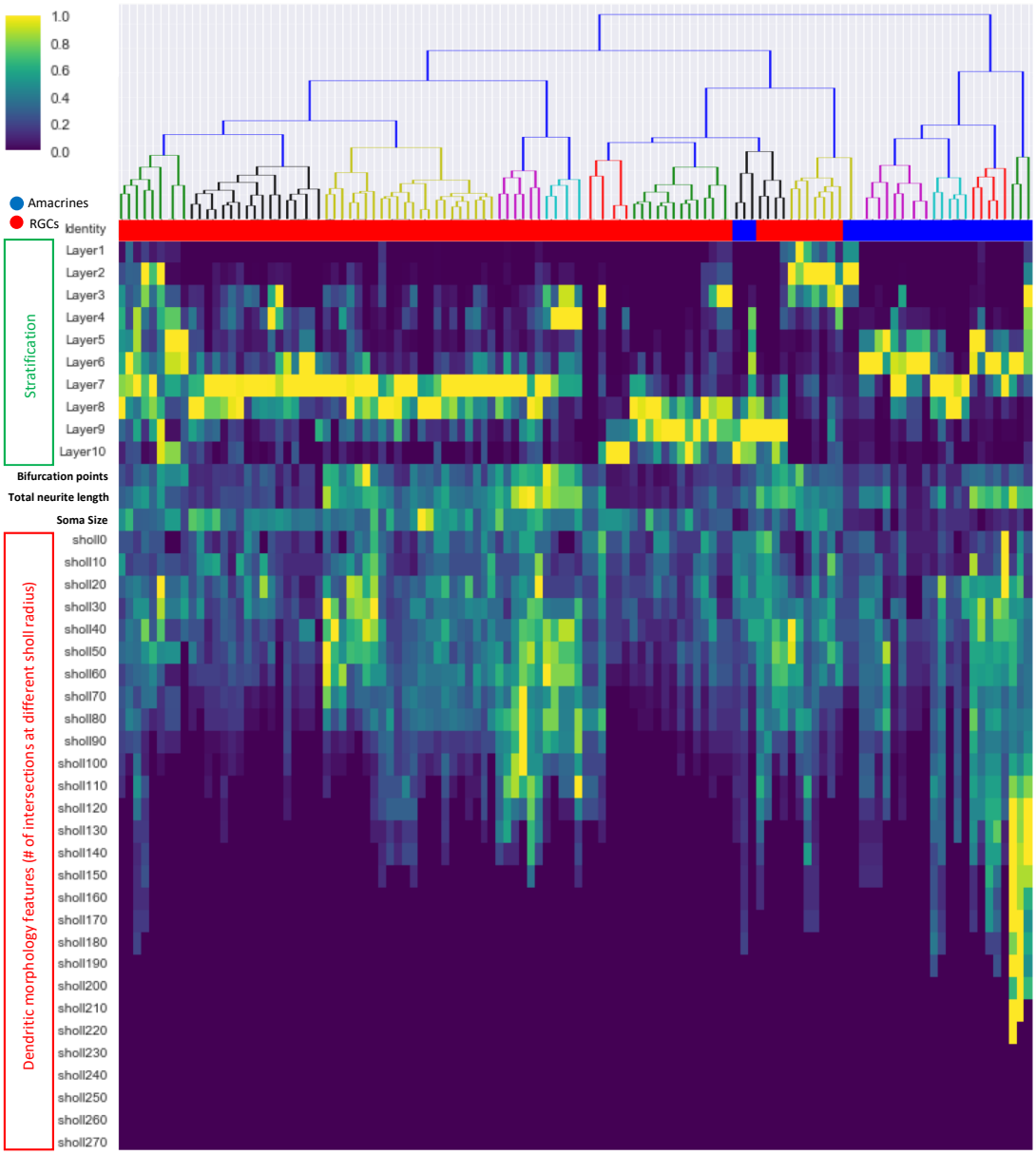

Figure 4.21: Hierarchical clustering of cell morphology features to extract FLRT3+ cell subpopulations. The data used for clustering includes stratification pattern, sholl analysis, soma size, total neurite length and bifurcation points. All data is normalized to values between 0 and 1. RGC and amacrine clusters are indicated in red and blue respectively.

Although dendritic morphology such as complexity and size influence the function of an RGC, our data shows great variation of dendritic tree complexity even within cells of the same layer (Figure 4.21 and Supplemental Figure 7.1). Supporting this notion, the work of Sumbul et al. [252] suggests that general morphology is a poor feature to classify RGCs and that best results may be obtained by focusing on the stratification depth only. Thus, I again performed hierarchical clustering including only the stratification features. RGCs clustered into six different clusters (Figure 4.22). The biggest two clusters (F3-Cluster1 mono and F3-Cluster2 mono) (Figure 4.22) contained only monostratified cells, that bifurcate mainly in the ON Layer 7,8,9 and 10 and represent 49% of all injected cells. A small group (14%) of cells bistratified in the ON and OFF layers (F3-Cluster3 bi and F3-Cluster5 bi) and a small cluster of nine cells showed a rather diffuse stratification

pattern between layer 2 and 8 (Figure 4.22). Six cells monostratified within layer 1 and 2 (F3-Cluster4-mono) (Figure 4.22).

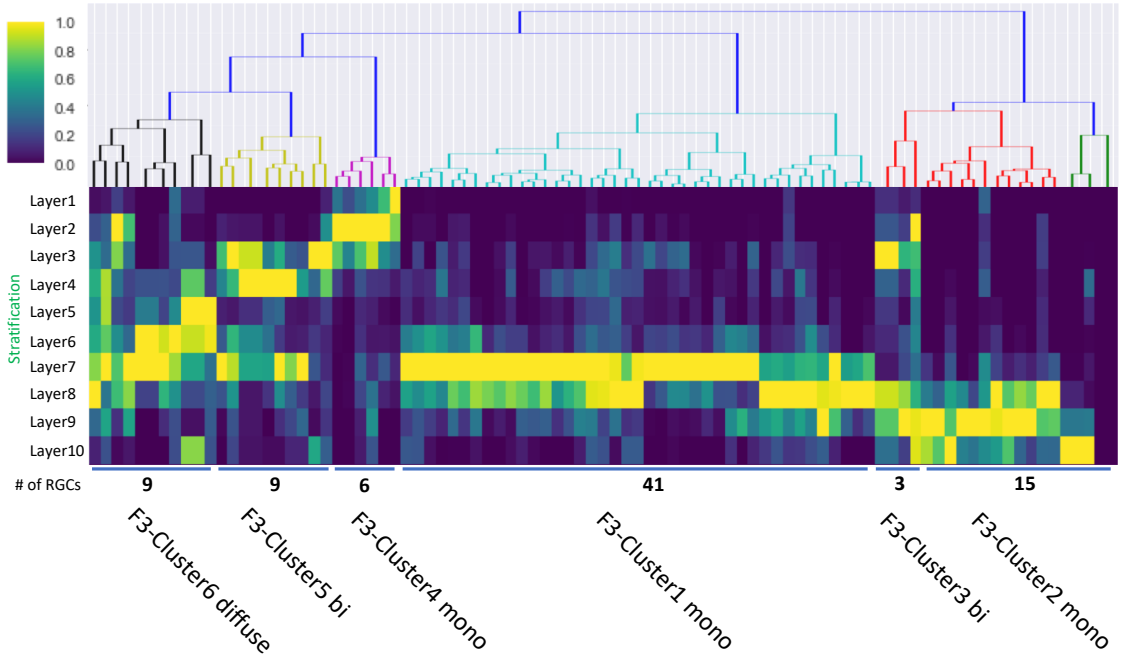

Figure 4.22: Hierarchical clustering of FLRT3+ RGCs based on stratification features only reveals six FLRT3+ RGC subpopulations. Most RGCs (Cluster1 and 2) mono-stratify in layer 7-10. 2 clusters bistratify in the ON and OFF layers (Cluster 3 and 5). Cluster 4 monostratifies in the OFF layer 1-2 and cluster 6 cells show a very diffuse stratification pattern. All data is normalized to values between 0 and 1.

Since I was selecting for RGCs based on cell soma size during the injections, I only injected 24 displaced amacrine cells. Based on stratification features, displaced amacrine cells cluster into two monostratified populations that stratify either in layer 4-5 (Cluster1) or layer 6-7 (Cluster2) (Figure 4.23). The remaining cells were too sparse to be considered a whole population.

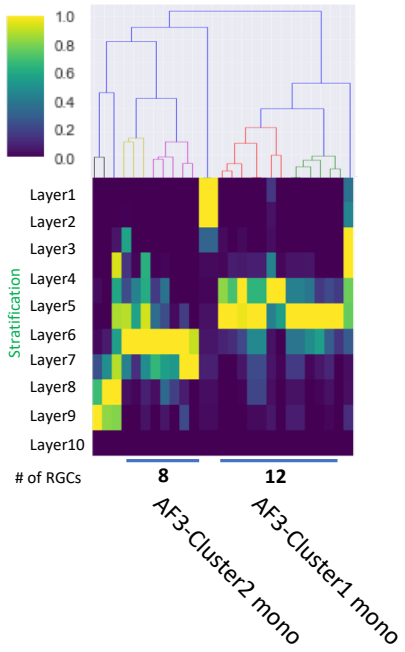

Figure 4.23: Hierarchical clustering of FLRT3+ amacrines in the GCL based on stratification features only reveals mainly 2 different subpopulations. Cluster 1 stratifies in layer 4-5 and cluster 2 in layer 6-7. All data is normalized to values between 0 and 1.

4.8 Retinofugal projection pattern of FLRT3+ RGCs

Since the retinofugal projection pattern may provide a hint as to the function of the FLRT3+ RGC population, I injected 1 µl of a Cre-dependent AAV2-GFP into one eye of an adult *Flrt3-CreERT2* mouse. 4-Hydroxytamoxifen was injected directly after and 24 hours after the AAV injection. To label all RGCs, I injected 4 µg CTB647 4 days before fixation of the retina. Figure 4.24 A/B shows homogeneous CTB647 and GFP labelling across the whole retina. As expected the Cre-dependent AAV2 labels less RGCs (FLRT3-Cre+) compared to the CTB647 (all RGCs) (Figure 4.24 A and B).

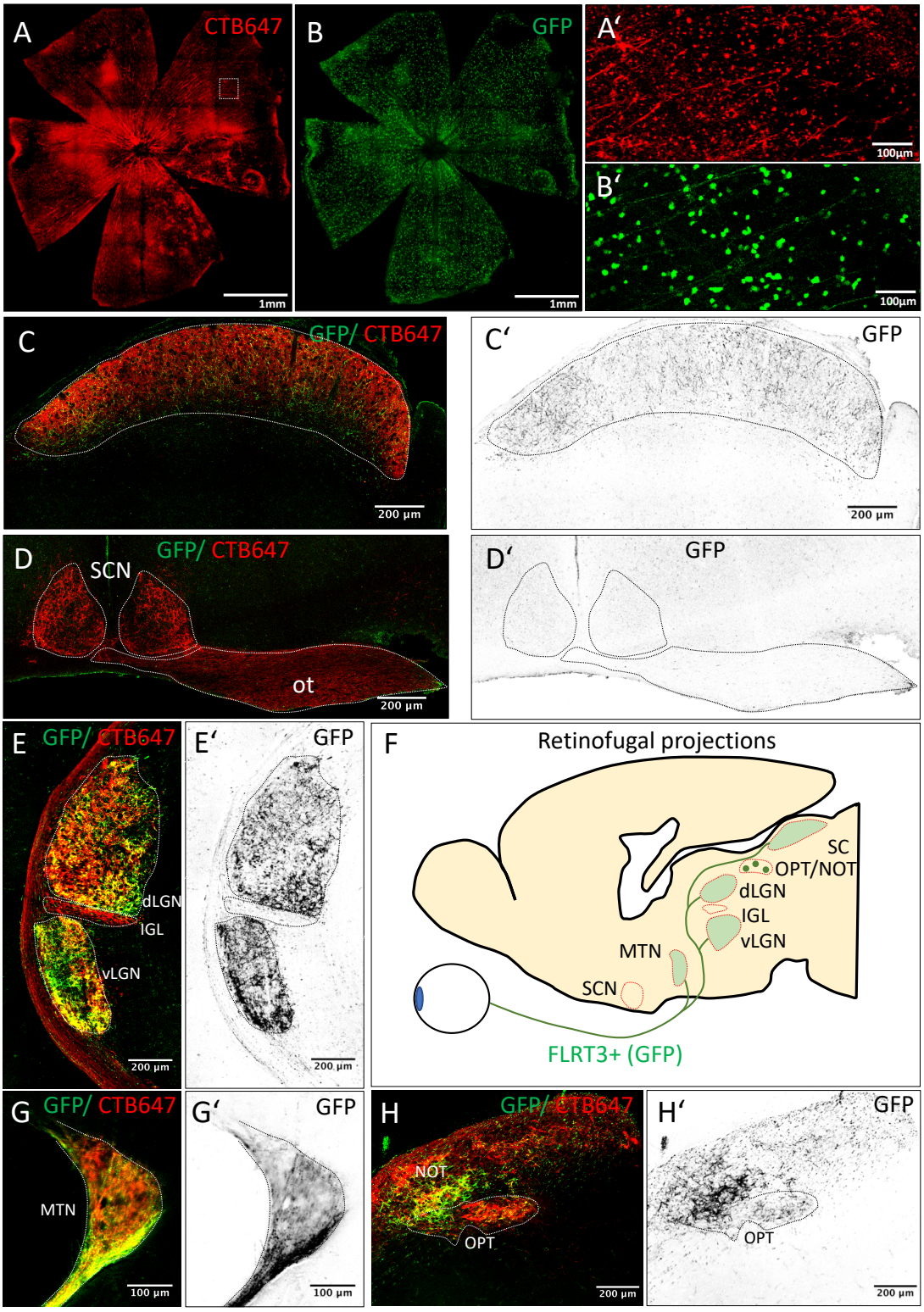

Figure 4.24: Retinofugal projections of FLRT3+ RGCs labelled by intravitreal injection of Cre-dependant AAV2-GFP (GFP) and fluorophore-conjugated CTB. A/B: Whole mount retina after intravitreal CTB647 (A) and Cre-dependant AAV2-GFP (B) injection. A'/B': Magnifications of A and B. C/C': No layer specific projection pattern in the superior colliculus. D/D': FLRT3+ RGCs do not project to the suprachiasmatic nucleus. E/E': FLRT3+ RGCs project to the dLGN and vLGN but avoid the IGL. F: Schema of all analysed retinofugal projections in the brain (adapted from [226]). G/G': FLRT3+ RGCs project to the non-image forming MTN. H/H': Projections to the OPT and NOT. CTB, cholera toxin subunit B; SC, superior colliculus; SCN, suprachiasmatic nucleus; ot, optic tract; dLGN, dorsal lateral geniculate nucleus; vLGN, ventral lateral geniculate nucleus; IGL, intergeniculate leaflet; OPT, olivary pretectal nucleus; MTN, Medial terminal nucleus; NOT, nucleus of the optic tract. Representative images of data from n=2 animals.

Results show that FLRT3+ RGCs project to image and non-image forming regions in the brain. These regions include the dorsal and ventral lateral geniculate nucleus (dLGN, vLGN) (Figure 4.24 E/E'), the superior colliculus (SC) (Figure 4.24 C/C'), the medial terminal nucleus (MTN) (Figure 4.24 G/G'), the olivary pretectal nucleus (OPT) and the nucleus of the optic tract (NOT) (Figure 4.24 H/H'). FLRT3+ RGCs avoided the non-image forming suprachiasmatic nucleus (SCN) and the intermediate geniculate leaf, which are targets of ipRGCs (Figure 4.24 E/E', D/D') [66]. Closer analysis of a series of sections through the whole LGN shows that FLRT3+ RGCs show no region specificity within the dLGN or vLGN (Representative Figure 4.24 E/E'). Despite the fewer axons travelling along the outer shell of the LGN, FLRT3-RGC axon projection is indistinguishable from the overall projection pattern of all RGC. The second largest projection target of the retina is the SC. Different types of RGCs have been shown to preferentially project to different layers within the superior colliculus [59]. Figure 4.24 C and C' show the retinofugal projections in the SC. Here again no obvious difference in stratification depth or projection preference was visible. In addition, closer analysis of consecutive sections through the SC showed no difference in the projection pattern (data not shown).

Chapter 5

Discussion - Role of FLRT1/3 in cerebral cortex folding

5.1 A unifying model of folding: Migration and cell proliferation

All papers providing experimental evidence so far suggested an increase in the number of neural progenitors and neurons as the main mechanism driving cortical folding [247, 76, 122, 279]. However, our work showed that cortical folding can be induced without the need for increased cell proliferation. Assuming a constant brain volume, folding a mouse brain would not necessarily require more neurons but a redistribution of existing neurons into a thinner but larger cortex [179]. Since the volume of the skull remains constant the increased cortical surface would have to fold in order to fit into the skull. We hypothesize that during evolution an increased number of neural progenitors combined with altered neuronal migration and/or a change in tissue stiffness led to the gyrification of the smooth cortex. Increases in cell proliferation alone cannot mechanistically explain why those neurons did not just stack on top of each other to induce radial growth instead of expanding laterally [187]. According to the radial unit hypothesis, a defined group of neural progenitor cells in the ventricular and subventricular zones contributes to a specified number of cortical columns above them [213]. Since the ventricular surface is much smaller than total cortical surface area, the same number of progenitors would have to build more cortical columns. To compensate, humans and other gyrencephalic animals added additional progenitor cells above the ventricular surface to generate more cortical units. To avoid radial cortical expansion by adding more layers, gyrencephalic brains enforced the lateral dispersion instead of strict radial migration along one fiber, to enable cortical surface expansion. This explains why cortical neurons from gyrencephalic species tend to disperse laterally in contrast to lissencephalic species like the mouse [6, 219, 277, 282, 259]. Thus, controlling the ratio between horizontal and radial dispersion appears critical for cortical expansion and its folding.

Interestingly, we showed that removal or overexpression of *Flrt3* induces FLRT3 neurons to cluster suggesting that the right dose of *Flrt3* expression is essential to maintain the balance of adhesive/repulsive forces between neurons and therefore their lateral distribution. Notably, the clustering of FLRT3-depleted neurons is enhanced when FLRT1 is also depleted, suggesting that there are redundant functions between FLRT3 and FLRT1.

In control conditions, FLRT3-expressing neurons show a random, salt and pepper, distribution in the mouse cortex. However, the same neurons tend to aggregate in vitro when present in dissociated cultures and therefore are out of their context. These results suggest that *in vivo* there is another adhesive/repulsive factor Y that contributes to the homogeneous mixing with other non-FLRT expressing neurons. EphrinA7 or EphrinB1 overexpression has also been shown to induce neuronal clusters similar to the FLRT3 overexpression suggesting that homotypic cell distribution depends on a tightly regulated balance between adhesion and repulsion [65, 266].

In addition, we hypothesize that cortical deformation into folds requires the tissue to be more flexible [14]. The radial intercalation hypothesis proposes that the folding forces are generated by the intercalation of newly born neurons between existing neurons within the same layer [250]. Taking into account the limitations of the live imaging experiments where both FLRT positive and negative neurons where labelled from mutant sections (which can dilute the phenotype), we observed that the removal of FLRT1/3 increases the chance of high speed migration sequences which causes neurons to arrive too early at the upper cortical plate. In line with this result, above each FLRT3 cluster the density of FLRT3+ neurons was increased, which caused a less smooth and wavy surface. Our simulations of cortical migration confirmed that reducing intercellular adhesion forces during migration causes more chaotic and clustered but less concerted neuronal migration. Some neurons arrive earlier than others which again causes a wavy cortical surface. The increased number of FLRT3+ neurons arriving too early at the upper CP could thus increase the lateral expansion forces as proposed by the radial intercalation hypothesis [250]. Moreover, we have shown that FLRTs are important for intercellular adhesion, suggesting a general role in tissue stability. The removal of FLRT1/3 might increase tissue flexibility and therefore facilitate folding. Moreover the FLRT3 cell clusters in the lateral posterior regions of the cortex show high correlation temporally and spaciously with the occurrence of folds suggesting a causal link between both phenotypes. The combination of increased tissue flexibility and the disorganised cortical migration that leads to the wavy cortical plate might provide the initial seed for eventual fold formations. This hypothesis is supported by the observation that human cortex and future sulci regions in ferrets have reduced FLRT levels. On the other hand, our simulations showed that increasing FLRT mediated adhesion increases concerted cortical migration resulting in a more smooth cortical surface. To further confirm the role of FLRT1/3 mediated adhesion in cortex folding future work will need to confirm that overexpression of *Flrts* in gyrencephalic species like ferrets reduces the number of cortical folds.

Many different molecular and cellular mechanisms have the potential to induce folding of a smooth cortex. Specific changes in cell proliferation, migration or lateral distribution are all valid mechanisms to induce folds and evolution could adopted any of them in isolation or concert. One problem with all experimental evidence provided so far is that peak cell proliferation, radial migration and also dendritic arbor differentiation do not temporally coincide with the exponential increase in folding, suggesting that those events are not the direct inducers of cortical folds but provide the framework for later force generating events[21, 29, 142]. The folding events in ferret or human occur at the onset of gliogenesis suggesting that the intercalation of glial cells, which are mostly responsible for early postnatal brain growth, could be the "force generating" cells that induce folds. However, no studies so far have shown a link between gliogenesis and folding. Thus, the fact that Flrt1/3 DKOs were able to induce occasional folds in the embryonic smooth mouse brain and the finding that they are downregulated in humans and ferrets

supports the notion that the evolution of cortical migration has an important role in cortex folding. In that sense, FLRT-induced folding represents just one out of many mechanistic possibilities by which today's neuroengineers could fold a brain. Evolution had a pool of many thousand protein-coding genes, each of which can be up-, downregulated or modified individually leaving us with nearly endless possibilities of how to convert a lissencephalic into a gyrencephalic brain and visa versa. Despite endless possibilities evolution usually does not invent the same thing twice and tries to develop upon the existing. Based on that evolutionary assumption, future experiments should focus on comparing the time resolved proteome of as many gyrencephalic and lissencephalic species as possible in order to find meaningful differences that explain folding. To show a link between FLRTs and evolutionary folding it is thus necessary to examine the *Flrt1/3* expression levels in as many gyrencephalic and lissencephalic species as possible to see a consistent upregulation in lissencephalic and downregulation in gyrencephalic species. Even if future work concludes that a downregulation of FLRTs are not the underlying mechanism that lead to the evolution of cortical folding, this work shows that little changes in cell-cell interactions can have huge effects on tissue morphology.

5.2 Why are cortical folds asymmetrically distributed?

Our data shows that while the cell clusters appear bilaterally in the *Flrt3 KO* and the *Flrt1/3 DKOs*, the cortical folds almost exclusively formed unilaterally. Removing both *Flrt1* and *Flrt3* increased the chance of unilateral folds. Moreover, it is more likely to observe folds on the left hemisphere of the *Flrt1/3 DKOs*. For the *Flrt1* single KOs the laterality was not tracked. How can this asymmetry be explained? So far, the differences in neuronal cell organization or the molecular pathways regulating those differences are unknown. Three different hypotheses might explain the left-right asymmetry of cortical folding in *Flrt1/3 DKO*:

The first hypothesis suggests that symmetric *Flrt* expression levels would require the asymmetric expression of another functionally relevant FLRT interaction partner. Known proteins that bind FLRTs are latrophilins(1-3) or Unc5s(a-d) and both are important for keeping the balance between cell adhesion and repulsion [155]. However, it is unknown if there is a left-right gradient of latrophilin or Unc5s.

The second explanation for a left shifted folding phenotype assumes asymmetric *Flrt1/3* expression. In that model FLRT1/3 mainly stabilise the left cortical hemisphere while another factor X might assure right hemisphere stability. Indeed, preliminary results (data not shown) suggest higher expression levels of FLRT1 in the left hemisphere. This would require asymmetric induction of *Flrt* expression by other factors. Serial analysis of gene expression and subsequent verification of candidate genes via in-situ hybridization identified about 27 differentially expressed genes between left and right cortical sides [254]. Most of the identified genes are involved in cell signalling and gene expression regulation, one of which could also be important for *Flrt* induction or be responsible for stabilizing the right hemisphere.

The third hypothesis assumes equal left-right expression of *Flrt1/3* and an underlying structural difference between the left and right hemisphere that makes the left side more susceptible to a loss of intercellular FLRT-FLRT adhesion. Many structural and functional properties were already shown to be lateralized. In humans the language-related areas of the left hemisphere contain more layer 3 pyramidal cells compared to the right

[113]. Additionally, brain disorders like polymicrogyria were reported to appear unilaterally and may be inherited as a Mendelian trait (e.g. right-sided polymicrogyria) [36]. Moreover, across almost all cultures most humans (90%) preferentially use the right hand (controlled by the left hemisphere) which is reflected in a deeper left central sulcus [2]. Asymmetry is already present during early developmental stages since human embryos prefer to suck their right thumb, which later correlates with right handedness [99, 100]. This suggests that handedness and thus also brain asymmetry is genetically encoded and not random or influenced by external stimulations [133, 48]. The right biased hand use is not limited to humans but can be found in other mammals and non-human primates as well. Furthermore, mice show a preference for using either left or right paws [45]. MRI scans of adult male mouse brains showed that the motor, sensorimotor ,visual cortex and other brain regions are larger on the left side compared to the right side [244]. Since it is believed that the ratio between cortical surface area and thickness correlates with folding, this left sided enlargement could result in a higher sensitivity to folding [179]. The bilateral removal of FLRT-FLRT adhesion combined with a pre-existing structural asymmetry might therefore favour left folded brains.

How initial asymmetry of those regulatory genes is established in the first place is still under debate. Most studies so far have analysed asymmetric organisation of other organs like the heart, lung, liver and stomach. More importantly animals are not only asymmetric, but asymmetric to the same direction (e.g the stomach is always on the left side, language processing always in left side). This shows that the left-right axis is not the result of a random process where initial small but random variations in left-right gene expression determines the future orientation. Instead, left-right asymmetry is inherited by the next generation. The prevailing idea that morphogen gradients in the mother's uterus determines the embryo's orientation was challenged by the observation that embryos continue to develop the proper left-right axis even when cultured separately from the mother. This means that the left-right axis must develop independent of external controls. A hint at the mechanism was the observation that 50% of patients with immotile cilia also show an inverted left-right axis (situs inversus) [124]. Indeed, studies showed that a cilia-induced leftward flow of extracellular fluid around the node is essential to establish the proper left-right asymmetry. It is hypothesized that the initial symmetry break is induced by posterior-tilted cilia that rotate in a clockwise direction only [52]. This tilt rotation causes a unidirectional flow of extracellular fluid to the left side of the embryo [7]. How that unidirectional fluid flow initiates asymmetric expression of morphogens (e.g. Nodal, Lefty, Pitx2) is still under debate. Fluid flow could either itself establish a morphogen gradient or be sensed by immotile cilia that get bent in one direction [171, 306]. Although it is accepted that asymmetric cilia play an important role in establishing left-right asymmetry it is still not known if it is the initial cellular cause of asymmetry break. In animals like chicken, pigs and frogs, proper left-right asymmetry develops without the need for cilia movement [87, 248, 272, 11, 17, 299]. Moreover, people with ciliary dyskenesia still retain an asymmetric brain suggesting there could be another mechanism upstream for generating asymmetry [128]. Whatever the initial cellular mechanism is, it is very likely based on the chirality of some functional molecule that itself builds an asymmetric biomolecule which has some asymmetric function. Overall one of these symmetry breaks built the foundation for later brain asymmetry and might explain the asymmetric effect of the loss of FLRT1 and FLRT3 on each cortical hemisphere.

5.3 Outlook: Would a gyrificated cortex make the mouse smarter?

The main aim of this project was to elucidate the mechanism by which FLRT mediated cell adhesion can induce folds. By removing *Flrt1* and *Flrt3* we succeeded in generating folded mouse brains. The obvious question that arises is: will a folded mouse cortex lead to a "smarter" mouse? Will the mouse smell, see, hear or move better if the corresponding cortical areas are folded? I hypothesize that a folded mouse brain would perform worse compared to a non-folded brain. This hypothesis is based on two assumptions: The cortex is organized in functional columns where each column represents a computational unit and each computational unit needs a minimum number of neurons for optimal signal processing. During development each neural progenitor of the VZ and SVZ contributes to a specified number of cortical columns above them (Radial unit hypothesis) [213]. Moreover, neurons from the same progenitor cell preferentially connect to those originating from the same progenitor cell and thereby provide the circuitry for columnar signal processing [305]. Within each column each layer has a specific function. Layer IV where sensory information comes in, layer II and III for associational signal processing and layer V and VI for generating the motor output [63, 30]. Interestingly the human cortex is only about 10 times thicker compared to the mouse cortex but expanded 1000 times laterally. Inducing folds is not a mechanism to fit in more neurons into the same brain volume. Indeed, simply stacking neurons on top of each other would be an efficient way to get more neurons into a limited brain volume. Instead folding allows more cortical columns to coexist within a limited volume. These evolutionary developments suggest that each cortical column already contains an optimal number of neurons for most efficient signal processing. Attempting to artificially fold a mouse brain would require each cortical column to reduce the number of neurons. Indeed, in our *Flrt1/3 DKO* the regions of a sulcus showed a dramatic reduction in neuron number, especially in the deeper cortical layers, which most likely negatively affects cortical processing in that region. In human sulci regions the deeper cortical layers are also thinner and resemble what we saw in our *Flrt1/3 DKO*. However, in humans the sulci are deep enough so that more normal sized cortical columns are gained at the expense of a few regions with reduced cortical thickness. In our folded mouse model the sulci were just not deep enough to give the mouse more normal sized cortical columns for cortical computations. Instead folding actually reduces the amount of normal sized cortical columns. Thus, for increasing cortical computation power we would first need to expand the mouse brain volume and then fold the cortex to fit enough cortical units into the same brain volume. This hypothesis however completely depends on the idea mentioned before, that each species requires an optimal thickness of the cortex for efficient signal processing. To confirm the hypothesis, it will thus be necessary to evaluate the behavioural effects that cortical folding has in the adult mouse. To date, we have observed folds in up to 3 days old animals and even in embryonic brains the probability of getting a fold is only 31%. For behavioural tests we need to increase the probability of folds which then remain until adulthood. To improve folding penetrance, we could induce a local increase in cell proliferation by in utero injections/electroporation of proliferative genes into our *Flrt1/3 DKO* mice. Candidate genes that were shown to increase cell proliferation are sonic hedgehog, ARGHAP11B, Trnp1 or TBC1D3 and will all be tested [279, 247, 76, 119]. In case one of those genes successfully increases the folding penetrance and survival into adulthood in our model, it would allow us to investigate the effect those foldings have on vision, hearing and motor performance.

Our model might also help to mechanistically understand the symptoms like seizures and mental retardation that are associated with polymicrogyria. Use of linear multielectrodes would allow analysis of how information flows between the different cortical layers and neighbouring areas within a sulcus is changed compared to the non-folded regions [229]. Finally despite the possibility that FLRT1/3-induced cortical folding might not be determinant of the evolutionary mechanism of cortical folding, I believe that the generation of a mouse model in which one can modulate the organization of the cortex (total thickness, lamina specific variations, surface area, total neuron number and number of folds) will serve as a valuable tool to answer questions on the optimal parameters for the most efficient cortical signal processing for vision, hearing and motor function.

Chapter 6

Discussion - Role of FLRTs in the retina

6.1 Expression and function of Flrts during retina development

Our results show that FLRT proteins are present in the retina during development. Both Flrt1 and Flrt3 are expressed at early stages and form gradients suggesting a potential role for these proteins in axon guidance and/or neuronal migration as has been shown for other guidance families such as Eph/ephrins [134]. Among all Flrts, I focused on Flrt3 during retina development because of its high expression compared with Flrt1 and Flrt2 (data not shown). Given that Flrt3 is expressed in both neuronal and endothelial cells in the retina during development, I aimed to compare the effects of depleting Flrt3 from all cells (using SOX2-Cre line) or only in RGCs (using Brn3b-Cre) to distinguish possible phenotypes which could be attributable to vascular or neuronal functions. Indeed, previous work from our lab and others have shown that FLRT proteins are widely expressed in both neuronal and vascular systems during development where they exert important functions [296, 150, 180].

Complete depletion of FLRT3 using the *Sox2-Cre* line produced a series of strong phenotypes ranging from blindness, cataract and eye malformation and even the absence of majority of RGCs. Interestingly, these phenotypes were not observed when *Flrt3* was specifically removed from RGCs, suggesting that they were mainly produced because of vascular and not neuronal defects. In agreement with these results, in collaboration with the lab of Amparo Acker-Palmer, we could show that retinas from *Flrt3 SOX2* mutant mice display hypervascularization [236] which reinforces the hypothesis that complete removal of *Flrt3* has strong effects on the vascular system. Endothelial cells were shown to express Unc5 receptors and respond with strong repulsion when challenged with FLRT proteins. Therefore, our work shows that the fundamental mechanisms of FLRT adhesion and repulsion events are conserved between neurons and vascular endothelial cells. Although, I did not observe major defects in the number and distribution of *Flrt3*-depleted RGCs (based on X-gal staining using *Flrt3-LacZ* reporter line), we cannot exclude morphological defects or dendritic layering misrouting. Indeed, previous work suggests that FLRTs together with Unc5s proteins could be important for correct layering of the RGC dendrites [275]. Future work should test this hypothesis by, for example, crossing the newly generated *Flrt3-CreER* line with Thy1-reporter lines (only expressed in RGCs).

This approach not only will show whether morphology or layering is affected in RGCs upon *Flrt3* removal, but also whether the axonal targeting of upstream brain visual areas such as as dLGN and SC could be affected.

6.2 Flrt3 as a candidate marker for subtype specific RGC labelling

All FLRT proteins are also expressed in the retina at later stages of development and in the adult mouse. X-gal staining using LacZ reporter lines showed that *Flrt1* and *Flrt2* are mainly expressed in the ganglion cell layer (GCL), while *Flrt3* was also expressed in the inner nuclear layer. Given that all FLRT proteins showed expression in the GCL where RGCs are located in the adult mouse retina, we asked whether we could use *Flrts* as a novel marker to identify subsets of RGCs. Despite the fact that more than 30 functionally different RGCs have been identified in the retina, about 50% of those subgroups still lack a genetic marker to fully characterize each individual population [9, 231, 226]. Since *Flrt1* was heavily expressed in the GCL we excluded it as a possible marker of a specific subpopulation. Initially FLRT2 seemed to be the best candidate because of its exclusive expression in the GCL. However, quantifications in *Flrt2-LacZ* mice showed that *Flrt2* was about twice as abundantly expressed (48% of all RGCs) compared to *Flrt3* (23% of all RGCs). Additionally, the overall expression of FLRT3+ cells was lower compared to FLRT2. The abundance of other known functional RGC subpopulations is in the range of 1-16% of all RGCs and is more similar to the 23% for the FLRT3+ RGCs [231]. To exclude that FLRT3 cells are a subpopulation of the larger FLRT2 population both LacZ lines were crossed resulting in a mouse labelling both FLRT2 and FLRT3 cells. Cell density comparison showed that both populations show very little overlap of only 13%. Thus, we concluded that FLRT3 labels a subset of RGCs that are in relatively low abundance and therefore has the highest chance of labelling a specific RGC subpopulation compared to all other FLRTs [231]. Therefore, all further efforts to characterize a functional RGC subpopulation were focused on FLRT3.

6.3 Flrt3-CreERT2 line labels amacrine and RGCs in the GCL

After we decided that FLRT3 was the most likely candidate for a functional RGC subpopulation, we generated an inducible *Flrt3-CreERT2* mouse line by the same strategy as the *Flrt3-LacZ* line. The combination of the Cre-recombinase with a mutated form of the estrogen receptor allowed us to determine the time point when cells express *Flrt3*. Moreover, immunostaining showed that *Flrt3* is expressed in the vasculature during embryonic development which would give us a lot of background staining when crossed to a reporter line. Interestingly, when I quantified the proportion of FLRT3+ amacrines and RGCs again, I found 67% of FLRT3+ cells in the ganglion cell layer to be amacrines and only 23% to be RGCs vs. 87% RGCs and 13% amacrines in the *Flrt3-LacZ* line. Consequently the fraction of FLRT3+ RGCs to the total number of RGCs reduces from 23% in the *Flrt3-LacZ* quantifications to about 6% in the *Flrt3-Cre* line. An explanation for that discrepancy is that the LacZ staining used for quantification was not labelling the whole cell body but showing only small punctae (Figure 4.5). Often those punctae

were at the boarder of two cells making it difficult to assign them to RBPMS positive or negative cells. However, the expression pattern between the *Flrt3-LacZ* mouse and the *Flrt3-CreERT2:tdTomato* line in the brain was very similar indicating that difficult quantification conditions in the *Flrt3-LacZ* line lead to the diverging numbers. Moreover, the counting was based on the assumption that each cell contains a maximum of one *Flrt3-LacZ* puncta (based on stainings in the developing cortex), but it could be that is not the case in the retina, possibly exaggerating the number of FLRT3+ cells. The overall stratification pattern within the inner plexiform layer matches previous work that used a FLRT3 antibody staining to identify lamination within the IPL, suggesting that our *Flrt3-Cre* line labels *Flrt3* expressing neurons in the retina [275].

6.4 FLRT3+ RGCs do not distribute in a mosaic like fashion

Functional RGC subpopulations usually distribute in a mosaic-like fashion. I could, however, show that the FLRT3+ RGCs do not show a mosaic-like pattern, already suggesting that FLRT3+ RGCs consist of more than two subpopulations. Previous work on F-RGCs for example showed that the combination of FoxP2 with three other markers could subdivide the population into four distinct subgroups that distribute in a mosaic like fashion. I however was not able to generate a mosaic pattern combining Flrt3 with other well-known RGC markers such as FLRT3+/CART+ or FLRT3+/Calbindin+ RGCs. In case of the FLRT3+CART+ cells this suggests that they represent a mix of two or more of the four different CART+ ooDSGC subpopulations [223]. Since also CART-negative and Calbindin-negative subpopulations did not distribute homogeneously one can conclude that FLRT3+ RGCs consist of at least four different subpopulations. Another possibility is that the FLRT3+ RGC population is polluted by Cre expression even in the absence of Tamoxifen. This "leakyness" is a known phenomenon [141]. The ratio between FLRT3+ RGCs and amacrines however was not changed in the Tamoxifen free retinas, suggesting that true FLRT3+ cells were labelled.

6.5 Stratification based clustering suggests 6 FLRT3+ RGC cluster

The initial attempt to cluster all neurons based on stratification and general morphology lead to more than eight RGC clusters. However, the method of fixed cell injections has some limitations in reconstructing full cell morphology. In comparison to living retina injections, the injected dye does not reach all fine branches leading to incomplete morphological reconstructions [131]. The advantage of fixed cell injections however was that it was possible to inject more neurons in one retina and allowed for RBPMS immunostaining to distinguish FLRT3+ RGCs from FLRT3+ amacrines. In living retina injections it is often not possible to stain after dye injection [131]. The complexity of my morphology reconstructions was quite variable and always less complex compared to other published reconstructions [252]. Since previous classification attempts of randomly injected RGCs showed that stratification is a good way to classify neurons and that dendritic morphology varies a lot within RGCs of the same group, I reclustered my reconstructed FLRT3+ neurons based on stratification pattern only. This approach resulted in six clusters of mono

and bistratified RGCs that stratify in the ON and OFF layers (Figure 6.1). This however does not mean that RGCs stratifying within the same layer have exactly the same functional properties. Recent work that combined Calcium imaging with electron mircoscopy morphology reconstructions showed that even slight changes in dendritic stratification depths leads to changes in the functional response properties [10].

Most FLRT3+ RGCs however monostratified in the ON layer 4 or 5 suggesting that they respond to increases in light intensity only. Fractions of our FLRT3+ RGCs population express Calbindin and Parvalbumin which are both markers that each contain various types of morphologically distinct subpopulations [131, 89]. Based on their stratification in layer S4, our F3-1 ON RGCs could fit to the CB9 and CB10 Calbindin RGCs that were previously described (Figure 6.1) [89]. The Parvalbumin types PV8, 7, 2 and 6 match the stratification depth of our F3-1 ON population (Figure 6.1). The bistratified ON-OFF PV3 RGCs would match our F3-5 and F3-3 RGCs (Figure 6.1).

The very small cluster 4 cells that stratify within the OFF layer 1 could possibly belong to the alpha OFF sustained type or the J-RGCs that responds to upwards movement (Figure 6.1). Both types stratify within the same layer.

The FLRT3 clusters 2 and 5 bistratified in the ON 4 and OFF 2 layers. Also CART+ ooDSGC bistratify in layer 2 and 4 to gain their ON-OFF properties. Since about 23% of the FLRT3+ RGCs were positive for CART, I hypothesize that at least one of those clusters represent ooDSGCs [126].

Two recent publications combined functional Calcium imaging with subsequent morphological reconstructions of RGCs. [10, 9]. The RGCs 1ni, 1no, 1ws from Bae et al. could potentially be represented by the F3-2 ON cluster [10]. Interestingly the 1ni and 1no types are potentially new types that differ from others by a small but consistent difference in the stratification depth. This resolution was made possible by the detailed electron microscopy reconstructions [10]. The Local orientation sensitive and Alpha RGCs from the work of Baden et. al 2016 matched the stratification profile of our F3-6 diffuse cluster(Figure 6.1) [9]. The Step and Slow and the trans large match our F3-4 OFF cluster and the Local transient orientation sensitive and alpha math the F3-1 ON population [9].

Since FLRT3 labels amacrines and RGCs in the GCL, I was mainly injecting FLRT3+ cells with a bigger soma to increase the chance of injecting an RGC. Therefore, the relative proportions of FLRT3+ RGCs might not represent that of the whole FLRT3- RGC population but might be biased towards RGCs with larger cell soma.

Because of the limitations mentioned previously, stratification and marker staining are so far the only two properties to give an indication as to the cell types that FLRT3+ RGCs label. To include dendritic morphology also, it will be better to dye inject in living retinas. The stratification match given in Figure 6.1 is limited by the fact that each group performs their stratification analysis differently. While some works take the ON and OFF ChAT bands as reference, others including me used the two nuclear layers as limitation reference of the inner plexiform layer. Thus, small variations in the data could lead to incorrect matches.

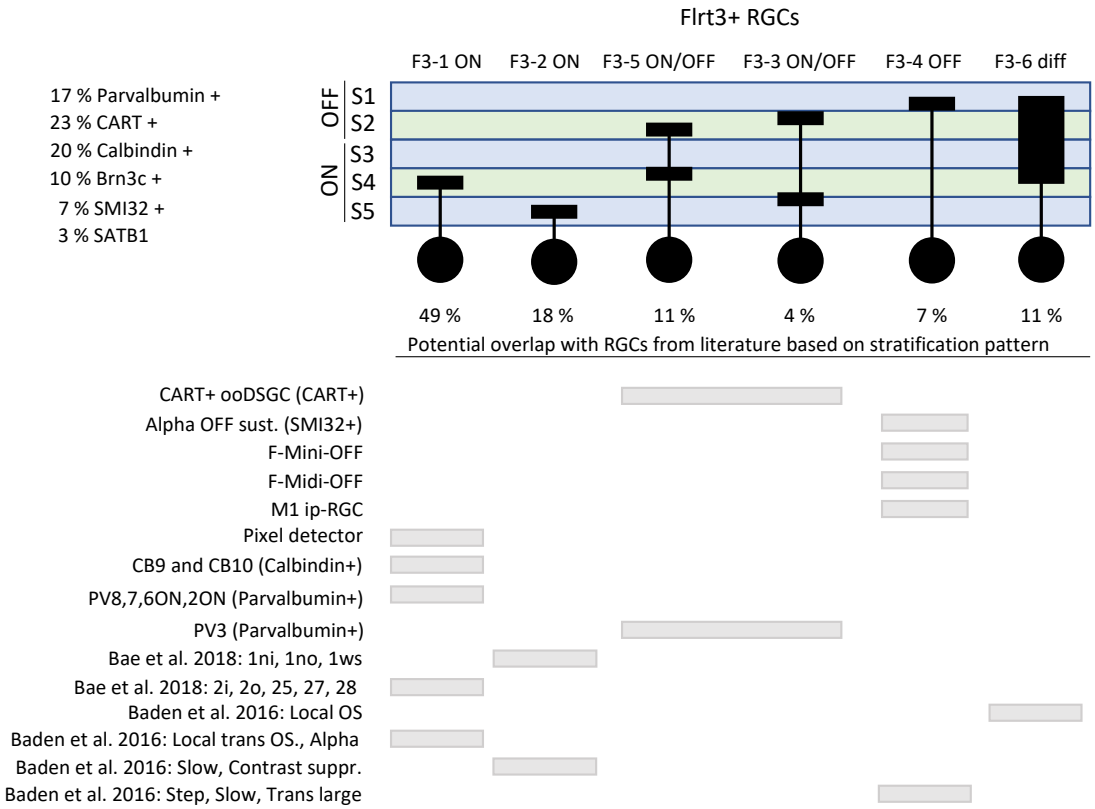

Figure 6.1: FLRT3+ RGCs can be classified into six groups based on their stratification pattern.

6.6 FLRT3+ RGCs project to image and non-image forming regions

Data on the retinofugal projection pattern after Cre-dependent AAV2 injection shows that FLRT3+ RGCs project to the SC, dLGN, vLGN and to targets of the accessory optic system (AOS) (MTN, OPT, NOT). Interestingly, the MTN, which is a target of FLRT3+ RGCs, was shown to receive input mainly from ON-DSGCs, suggesting that at least a fraction of FLRT3+ RGCs are ON-DSGCs [58]. Also the FLRT projections to the NOT resembles those of the ON-DSGCs. Moreover the ON-DSGCs stratification pattern matches with the pattern observed for the most numerous (49%) F3-Cluster1 (Figure 4.22) of the FLRT3+ RGCs. Overall this data supports the idea that about half of all FLRT3-RGCs are ON-DSGCs, which encode for horizontal and vertical image slip compensation [242].

In addition to the projections to the AOS, FLRT3+ RGCs also project to the dLGN, vLGN and the SC. My data shows that about 23% of all FLRT3+ RGCs represent CART+ ooDSGCs. Contrary to the uniform FLRT3+ projection pattern within the dLGN, vLGN and SC, ooDSGCs restrict their projections to the lateral parts of the dLGN, vLGN and to the superficial layers of the SC [126]. This discrepancy suggests that an additional subpopulation is labelled by FLRT3. tOFF-alpha RGCs represent a subclass of alpha RGCs that project to deeper layers of the SC and dLGN and according to immunostainings (SMI32) represent about 7% of FLRT3+ RGCs [109]. Thus tOFF-alpha RGCs could represent a fraction of FLRT3+ RGCs.

The observation that FLRT3+ RGCs avoid the SCN and IGL, suggests that FLRT3+ RGCs are not involved in circadian entrainment and matches with the finding that all FLRT3+ RGCs are negative for the ipRGC marker Melanopsin (data not shown) [41].

Overall the diverse projection patterns support the notion that FLRT3+ RGCs are a heterogeneous cell population.

6.7 Conclusion and Outlook

To conclude, FLRT3+ RGCs are not a structurally homogeneous cell population. The finding that different FLRT3+ RGC subgroups stratify within different layers of the IPL, suggests that they are also a functionally heterogeneous population with a preference for ON signals. It remains unsolved what functional property FLRT3+ RGCs have in common. However the overall projection pattern combined with the stratification depths, suggests that FLRT3 labels a mixture of CART+ ooDSGCs, CART- ON DSGCs and a subpopulation of alpha RGCs. Further functional characterization will be needed to determine the unifying "Flrt3-property". Thus the following work will focus on patch-clamp recording of FLRT3+ RGCs in response to a set of different visual stimuli projected directly onto the retina.

Chapter 7

Materials and Methods

7.1 Oligonucleotides and plasmids

Genotypings were performed according to the following program (Table 7.1) and oligonucleotides (Table 7.2) were bought from Eurofins.

PCR Program	Denat.	Denat.	Annealing	Extension	# cycles	Extension
Cre	92 °C 10 min	92 °C 0:10 min	58 °C 0:15 min	68 °C 1:00 min	50x	68 °C 5:00 min
FLRT1 WT	94 °C 3 min	94 °C 1:00 min	60 °C 1:00 min	72 °C 1:00 min	29x	72 °C 5:00 min
FLRT1 KO	95 °C 3:00 min	94 °C 1:00 min	65 °C 1:00 min	72 °C 1:00 min	29x	72 °C 2:00 min
Tomato	95 °C 3:00 min	95 °C 0:20 min	61 °C 0:30 min	68 °C 0:30 min	39x	68 °C 2:00 min
LacZ	95 °C 5:00 min	95 °C 0:30 min	58 °C 0:30 min	72 °C 0:30 min	34x	72 °C 5:00 min
FLRT2 lx	95 °C 3:00 min	95 °C 0:30 min	55 °C 0:30 min	72 °C 0:30 min	34x	72 °C 3:00 min
FLRT	94 °C 3:00 min	94 °C 1:00 min	62 °C 1:00 min	72 °C 1:00 min	34x	72 °C 20 min

Table 7.1: PCR programs used for genotyping

Name	Sequence
Cre forward	GCC TGC ATT ACC GGT CGA TGC AAC GA
Cre reverse	GTG GCA GAT GGC GCG GCA ACA CCA TT
FLRT3 lox forward	GAT ATT TGC CAA AGG AGA CAG AAA ATA
FLRT3 lox reverse	CTG GGT TCA TTG CTG TCT ACC AAC AAG CAC
LacZ forward	CCA GCT GGC GTA ATA GCG AA
LacZ reverse	CGC CCG TTG CAC CAC AGA TG
FLRT1 null forward	TAG AGG ATC AGC TTG GGC TGC AGG TCG AGG
FLRT1 null reverse	TGA GAT CCA CAG CGA ACA GCA GGC ATT AGC
Tomato WT forward	AAG GGA GCT GCA GTG GAG TA
Tomato WT reverse	CCG AAA ATC TGT GGG AAG TC
Tomato Mut forward	CTG TTC CTG TAC GGC ATG G
Tomato Mut reverse	GGC ATT AAA GCA GCG TAT CC

Table 7.2: Oligonucleotides used for genotyping

7.2 Antibodies

Antibody	Species	Dilution	Source	Cat. Number
RBPMS	Guinea Pig	1:100	Phospho Solutions	1823
RBPMS	Rabbit	1:100	Phospho Solutions	1830
Brn3a	Mouse	1:200	Santa Cruz Biotechnology	Sc-8429
ChAT	Goat	1:100	Millipore	AB144P
CART	Rabbit	1:100	abcam	ab192364
Melanopsin	Rabbit	1:1000	ATS	AB-N38
Calbindin-D-28k	Rabbit	1:400	Swant	300
Calretinin	Rabbit	1:400	abcam	AB-N38
GAD-67	Mouse	1:200	Millipore	MAB5406
SMI-32	Mouse	1:100	Bio Legend	801701
Brn3c	Rabbit	1:400	Santa Cruz Biotechnology	Sc-81980
Parvalbumin	Rabbit	1:400	Swant	PV27
Satb1	Rabbit	1:100	abcam	ab70004

Table 7.3: Primary antibodies used in IHC

Antibody	Species	Dilution	Source
Cy2/3/5	mouse / rabbit / guinea-pig / goat	1:300	Jackson Immuno Research

Table 7.4: Secondary antibodies used in IHC

7.3 Media

Solution	Compounds	Amount
Luria-Bertani (LB) medium 1 L, ph 7.5	Bacto-Tryptone	10 g
	Bacto-Yeast extract	5 g
	NaCl	5 g
	H_2O	0
Artificial cerebrospinal fluid (ACSF)	NaCl	125 mM
	KCl	2.5 mM
	NaH_2PO_4	1.25 mM
	$NaHCO_3$	26 mM
	$MgCl_2$	1 mM
	$CaCl_2$	2 mM
	D-Glucose	20 mM
	L-glutamine	0.5 mM

Table 7.5: Media used for single cell injections and plasmid amplification

7.4 Mouse lines

The *Flrt3-Cre* line was generated by homologous recombination in embryonic stem (ES) cells using a targeting vector. ES cell cultures, electroporation and final clone selection were done by Louise Gaitanos and Jana Lindner according to standard protocols. Southern blots to identify positive clones were done by myself. The probes for confirming correct insertion of the *Flrt3-Cre* construct into the *Flrt3* locus was done by Pilar Alcala Morales. The pronuclear injections to generate the *Flrt3-Cre* mouse were conducted by the transgenic service. PCR against *Flrt3-Cre* resulted in 3 positive clones named C1G1, C1D5 and 2G10. All clones showed a very similar expression pattern. All further experiments were done using the C1D5 clone. All mice were backcrossed onto a C57BL/6N background.

Mouselines	Source
FLRT3^{lx}	Yamagishi et al., 2011
FLRT2^{lx}	EUCOMM
FLRT1^{-}	Yamagishi et al., 2011
FLRT3^{LacZ}	Yamagishi et al., 2011
FLRT2^{LacZ}	EUCOMM
FLRT1^{LacZ}	EUCOMM
R26-tdTomato (Ai9)	Madisen et al., 2012
Brn3b^{Cre}	Eloisa Herera lab
Sox2^{Cre}	Hayashi et al., 2002
FLRT3^{Cre}	unpublished

Table 7.6: Mouse lines used

7.5 Agarose gel electrophoresis

Agarose was dissolved in TAE buffer to a final concentration of 1% by boiling in the microwave. After cooling down to about 40-50°C Ethidium bromide (Roth) was added (0.5 µm final conc.) and the mix was transferred into a plastic tray allowing it to solidify. The pockets were loaded with about 10 µl of the PCR mix and separated by size using gel electrophoresis at a voltage of 100-230 Volts. DNA gels were imaged using a Gel Doc XR+ machine (Biorad).

Solution	Compounds	Amount
Phosphate buffered saline (PBS) pH 7.3	NaCl	137 mM
	KCl	2.7 mM
	Na_2HPO_4*7H_2O	4.3 mM
	Single cell injection	1.4 mM
Master mix genotyping, 48 µl	H_2O	41.6 µl
	2 x Primer (50 pmol)	2x 0.5 µl
	Thermo Pol Reaction buffer 10x (NEB)	5 µl
	dNTPs-mix (25 mM each, Fermentas)	0.4 µl
	Taq Polymerase (NEB)	0.5 µl
50x TRIS-acetate buffer (TAE)	Tris acetate	2 M
	EDTA	50 mM
Gel loading buffer, 50ml	H_2O	24 ml
	Glycerol	25 ml
	TAE 50x	1 ml
	Orange G	0.1 g

Table 7.7: Buffers used for genotyping

7.6 Mouse work and histology

For all brain and retina dissections mice were killed by cervical dislocation.

7.6.1 4-Hydroxy-Tamoxifen administration

4-Hydroxytamoxifen (Sigma, ref: H-7904) powder was re suspended in 100 % ethanol at a final concentration of 40 mg/ml. For complete suspension the 4-Hydroxytamoxifen was vortexed for 10 min, incubated at 60°C for 10 min and vortexed again until complete dissolution. Next the solution was diluted 1:1 in Kolliphor EL (Sigma, ref: C-5135) and stored in 100 µl aliquots at -20°C. Since 4-Hydroxytamoxifen is light sensitive, all solutions were kept in the dark during all procedures. For injection, one aliquot was rapidly thawed, diluted in PBS 1x to the desired concentration and injected intraperitoneally (1 µg/g, 5 µg/g, 15 µg/g, 60 µg/g).

7.6.2 Retina preparation

For retinal whole mount preparation, eyes were enucleated and placed into a dish containing 1x PBS. First the cornea was removed by cutting along the ora serrata using a small scissor. Next the lens was taken out using forceps followed by removal of the vitreous. Finally the retina was detached from the eyecup and transferred onto a cell culture insert (Millipore, Cat.no. PICMORG50). To allow flat mount of the retina, 4 incisions at 0, 90, 180 and 270° were made using a small scissor. Finally the retina was fixed on the membrane for 30 min in 4% PFA.

7.6.3 Transcardial perfusion and brain preparation

For the analysis of retinofugal projections, the animals were deeply anaesthetized with a Ketamine (medistar)/Xylazine(Bernburg) (1.6%/ 0.08%) overdose. As soon as the mice stopped reacting to pain stimuli, it was transcardially perfused for 10 min at a speed of 1 ml/min with ice cold PBS followed by another 10 min ice cold 4% PFA. After brain dissection they were post-fixed in 4 % PFA for another 24-48 h. Brains were stored in PBS (0.02% Sodium azide) until further sectioning.

7.6.4 Retinal single cell injections

For fixed retina injections, retinas were dissected in PBS, mounted on 45 µm cell culture inserts (Millipore, Cat.no. PICMORG50) and fixed for 15 min in 4 % PFA prior to single cell injections. RGCs and amacrine cells of the FLRT3-Cre Tom+/- retinas were identified based on red fluorescence and injected with 4 % neurobiotin (SIGMA L0259) dissolved in ACSF. For injection sharp electrodes were pulled from borosilicate glass capillaries to a final resistance of 200 Ohm (Science Products GP150F-8P) and mounted on a motorized patch-clamp manipulator. The dye was expelled by a positive current of 1-2 nA at 100 msec pulses for about 2 min (90% duty cycle).

7.6.5 Intravitreal virus injections

For adult intravitreal virus injections (Table 7.8), mice were anaesthetized using 5% isofluorane and eyes were treated with 0.5% lidocaine hydrochloride to avoid pain. Next the eye was slightly protruded from the eye socket and punctured at the ora serrata using a 30 gauge needle. Next 2 µl of vitreous liquid was withdrawn from the eye using a 7000 series Neuros Hamilton syringe. Finally the same syringe was used to inject 1 µl of virus or CTB647. To avoid eye irritations Bepanthen eye ointment was applied to each eye.

Virus	Source
rAAV8/CAG-tdTomato	Penn Vector Core
rAAV2/ CAG-GFP	Penn Vector Core
rAAV2/Flex-GFP	Penn Vector Core
rAAV2/Flex-tdTomato	Penn Vector Core

Table 7.8: Used virus for neuronal sparse labeling and retinofugal projection analysis

7.6.6 Immunofluorescent stainings

For immunostainings PFA fixed retinas were permeabilised and blocked with donkey serum and BSA (Table 7.9) for 24h. Next the retina was washed 3 times 5 min in PBS and incubated with the primary antibody solution (Table 7.9) for 24-72h. After 3 washes in PBS for 30 min each, the retina was incubated with the secondary antibody solution (Table 7.9) for 24h. After the final washes the retina was mounted photoreceptor side down onto a slide using Dako mounting medium. To avoid compression plastic spacers were used between the coverslip and slide.

Solution	Compounds	Amount
Blocking solution (Immunohistochemistry, IHC)	PBS	
	Donkey serum	5.0 %
	Bovine serum albumin	0.2 %
	Lysine	0.2 %
	Glycine	0.2 %
Primary antibody solution, IHC	PBS	
	Triton X-100 detergent	0.3 %
	Bovine serum albumin	0.5 %
	Sodium azide	0.02 %
Secondary antibody solution, IHC	PBS	
	Triton X-100	0.3 %
	Donkey serum	3.0 %

Table 7.9: Immunofluorescence histochemistry staining antibody and blocking solutions

7.6.7 XGal-staining

For XGal staining the retina was dissected from the eye and fixed for 30 min in the XGal fixative solution (Table 7.10). Next the retina was washed 2 x in the X-Gal Wash buffer (Table 7.10) and incubated for 2-12h in the X-Gal staining solution (Table 7.10). After 2 quick washes in PBS the retinas were fixed in 4% PFA for 10 min and mounted on a slide for subsequent imaging using Dako fluorescence mounting medium.

Solution	Compounds	Amount
X-Gal fixative	PBS	
	PFA	1 %
	$MgCl_2$	2 mM
	EGTA	5 mM
	NP40 detergent	0.02 %
	Glutaraldehyde (optional)	0.2 %
X-Gal Wash buffer, 1L	0.1 M Na-phosphate buffer pH 7.3	
	$MgCl_2$ (1M)	2 ml
	DOC	0.1 g
	NP-40	0.2 ml
X-Gal staining solution, 50 ml	X-Gal Wash buffer	
	X-Gal, 100 mg/ml	0.5 ml
	(dissolved in N-N-dimethylformamide)	
	$K_4[Fe(CN)_6]$	0.106 g
	$K_3[Fe(CN)_6]$	0.082 g

Table 7.10: XGal staining solutions

7.6.8 Confocal microscopy and image analysis

All fluorescence images were taken using a Leica SP8 confocal microscope with either a 10x (air), 25x (oil), 40x (oil) or 63x (oil) objective. Most images were taken at 400Hz bidirectional scanning and 1024x1024 pixels image size.

7.7 Data analysis

7.7.1 Cell distribution analysis

For cell distribution analysis, all cells of interest were manually labelled using the Fiji plugin cell counter. To analyze distribution regularity a custom made python script was used to calculate the density recovery profile. To calculate the density recovery profile the amount of cells N within different radii r of each cell was counted and divided by the area A covered between radius r and r+ delta r. The DRP is then calculated as density p(r) = N(r + delta r)/A(r + delta r).

7.7.2 Cell morphology analysis and classification

For cell morphology analysis, each cell was traced semi-automatic using the Fiji plugin SimpleNeurite tracer. To extract morphology features like stratification, number of branching points and total neurite lenght a custom made python script was used based on the NeuroM toolkit from the BlueBrain project. To classify neurons based on morphology features, I used a hierarchical clustering algorithm in python where I manually set the clustering threshold.

7.7.3 Statistical analysis

All statistical analysis were done using Python 3 scripts.

Bibliography

[1] M. B. Amar and A. Bordner. Mimicking cortex convolutions through the wrinkling of growing soft bilayers. *Journal of Elasticity*, pages 1–26, 2017.

[2] K. Amunts, G. Schlaug, A. Schleicher, H. Steinmetz, A. Dabringhaus, P. E. Roland, and K. Zilles. Asymmetry in the human motor cortex and handedness. *Neuroimage*, 4(3):216–222, 1996.

[3] D. J. Anderson. The neural crest cell lineage problem: neuropoiesis? *Neuron*, 3(1):1–12, 1989.

[4] S. A. Anderson, C. E. Kaznowski, C. Horn, J. L. Rubenstein, and S. K. McConnell. Distinct origins of neocortical projection neurons and interneurons in vivo. *Cerebral cortex*, 12(7):702–709, 2002.

[5] J. Angevine and R. L. Sidman. Autoradiographic study of cell migration during histogenesis of cerebral cortex in the mouse. *Nature*, 192(4804):766–768, 1961.

[6] C. P. Austin and C. L. Cepko. Cellular migration patterns in the developing mouse cerebral cortex. *Development*, 110(3):713–732, 1990.

[7] D. Babu and S. Roy. Left–right asymmetry: cilia stir up new surprises in the node. *Open biology*, 3(5):130052, 2013.

[8] T. C. Badea and J. Nathans. Morphologies of mouse retinal ganglion cells expressing transcription factors brn3a, brn3b, and brn3c: analysis of wild type and mutant cells using genetically-directed sparse labeling. *Vision research*, 51(2):269–279, 2011.

[9] T. Baden, P. Berens, K. Franke, M. R. Rosón, M. Bethge, and T. Euler. The functional diversity of retinal ganglion cells in the mouse. *Nature*, 529(7586):345, 2016.

[10] J. A. Bae, S. Mu, J. S. Kim, N. L. Turner, I. Tartavull, N. Kemnitz, C. S. Jordan, A. D. Norton, W. M. Silversmith, R. Prentki, et al. Digital museum of retinal ganglion cells with dense anatomy and physiology. *bioRxiv*, page 182758, 2018.

[11] F. Bangs, N. Antonio, P. Thongnuek, M. Welten, M. G. Davey, J. Briscoe, and C. Tickle. Generation of mice with functional inactivation of talpid3, a gene first identified in chicken. *Development*, 138(15):3261–3272, 2011.

[12] H. Barlow and W. R. Levick. The mechanism of directionally selective units in rabbit's retina. *The Journal of physiology*, 178(3):477–504, 1965.

[13] S. B. Baver, G. E. Pickard, P. J. Sollars, and G. E. Pickard. Two types of melanopsin retinal ganglion cell differentially innervate the hypothalamic suprachiasmatic nucleus and the olivary pretectal nucleus. *European Journal of Neuroscience*, 27(7):1763–1770, 2008.

[14] P. Bayly, R. Okamoto, G. Xu, Y. Shi, and L. Taber. A cortical folding model incorporating stress-dependent growth explains gyral wavelengths and stress patterns in the developing brain. *Physical biology*, 10(1):016005, 2013.

[15] C. Behrens, T. Schubert, S. Haverkamp, T. Euler, and P. Berens. Connectivity map of bipolar cells and photoreceptors in the mouse retina. *Elife*, 5, 2016.

[16] Å. K. Björklund, D. Ekman, and A. Elofsson. Expansion of protein domain repeats. *PLoS computational biology*, 2(8):e114, 2006.

[17] M. Blum, A. Schweickert, P. Vick, C. V. Wright, and M. V. Danilchik. Symmetry breakage in the vertebrate embryo: when does it happen and how does it work? *Developmental biology*, 393(1):109–123, 2014.

[18] H. Boije, S. Rulands, S. Dudczig, B. D. Simons, and W. A. Harris. The independent probabilistic firing of transcription factors: A paradigm for clonal variability in the zebrafish retina. *Developmental Cell*, 34(5):532–543, 2015.

[19] D. Bonneau, A. Toutain, A. Laquerriere, S. Marret, P. Saugier-Veber, M.-A. Barthez, S. Radi, V. Biran-Mucignat, D. Rodriguez, and A. Gélot. X-linked lissencephaly with absent corpus callosum and ambiguous genitalia (xlag): clinical, magnetic resonance imaging, and neuropathological findings. *Annals of neurology*, 51(3):340–349, 2002.

[20] V. Borrell. How cells fold the cerebral cortex. *Journal of Neuroscience*, 38(4):776–783, 2018.

[21] V. Borrell and E. M. Callaway. Reorganization of exuberant axonal arbors contributes to the development of laminar specificity in ferret visual cortex. *Journal of Neuroscience*, 22(15):6682–6695, 2002.

[22] V. Borrell and I. Reillo. Emerging roles of neural stem cells in cerebral cortex development and evolution. *Developmental neurobiology*, 72(7):955–971, 2012.

[23] R. T. Böttcher, N. Pollet, H. Delius, and C. Niehrs. The transmembrane protein xflrt3 forms a complex with fgf receptors and promotes fgf signalling. *Nature cell biology*, 6(1):38, 2004.

[24] K. Brose, K. S. Bland, K. H. Wang, D. Arnott, W. Henzel, C. S. Goodman, M. Tessier-Lavigne, and T. Kidd. Slit proteins bind robo receptors and have an evolutionarily conserved role in repulsive axon guidance. *Cell*, 96(6):795–806, 1999.

[25] S. P. Brown and S. Hestrin. Intracortical circuits of pyramidal neurons reflect their long-range axonal targets. *Nature*, 457(7233):1133, 2009.

[26] S. G. S. C. Buchanan and N. J. Gay. Structural and functional diversity in the leucine-rich repeat family of proteins. *Progress in biophysics and molecular biology*, 65(1-2):1–44, 1996.

[27] T. J. Burbridge, H.-P. Xu, J. B. Ackman, X. Ge, Y. Zhang, M.-J. Ye, Z. J. Zhou, J. Xu, A. Contractor, and M. C. Crair. Visual circuit development requires patterned activity mediated by retinal acetylcholine receptors. *Neuron*, 84(5):1049–1064, 2014.

[28] J. Caldwell and N. Daw. New properties of rabbit retinal ganglion cells. *The Journal of Physiology*, 276(1):257–276, 1978.

[29] E. M. Callaway and V. Borrell. Developmental sculpting of dendritic morphology of layer 4 neurons in visual cortex: influence of retinal input. *Journal of Neuroscience*, 31(20):7456–7470, 2011.

[30] W. Calvin. Competing for consciousness: how subconscious thoughts cook on the back burner, 1998.

[31] R. H. Caraballo, R. O. Cersósimo, E. Mazza, and N. Fejerman. Focal polymicrogyria in mother and son. *Brain and Development*, 22(5):336–339, 2000.

[32] V. S. Caviness and T. Takahashi. Proliferative events in the cerebral ventricular zone. *Brain and Development*, 17(3):159–163, 1995.

[33] V. S. Caviness Jr. Neocortical histogenesis in normal and reeler mice: a developmental study based upon [3h] thymidine autoradiography. *Developmental Brain Research*, 4(3):293–302, 1982.

[34] S. Chan and R. Guillery. Changes in fiber order in the optic nerve and tract of rat embryos. *Journal of Comparative Neurology*, 344(1):20–32, 1994.

[35] A. R. Chandrasekaran, R. D. Shah, and M. C. Crair. Developmental homeostasis of mouse retinocollicular synapses. *Journal of Neuroscience*, 27(7):1746–1755, 2007.

[36] B. Chang, K. Apse, R. Caraballo, J. Cross, A. Mclellan, R. Jacobson, K. Valente, A. Barkovich, and C. Walsh. A familial syndrome of unilateral polymicrogyria affecting the right hemisphere. *Neurology*, 66(1):133–135, 2006.

[37] L. Chang, T. Breuninger, and T. Euler. Chromatic coding from cone-type unselective circuits in the mouse retina. *Neuron*, 77(3):559–571, 2013.

[38] B. Chapman. Necessity for afferent activity to maintain eye-specific segregation in ferret lateral geniculate nucleus. *Science*, 287(5462):2479–2482, 2000.

[39] G. Chen, J. Sima, M. Jin, K.-y. Wang, X.-j. Xue, W. Zheng, Y.-q. Ding, and X.-b. Yuan. Semaphorin-3a guides radial migration of cortical neurons during development. *Nature neuroscience*, 11(1):nn2018, 2007.

[40] H. Chen, X. Liu, and N. Tian. Subtype-dependent postnatal development of direction-and orientation-selective retinal ganglion cells in mice. *Journal of neurophysiology*, 112(9):2092–2101, 2014.

[41] S.-K. Chen, T. Badea, and S. Hattar. Photoentrainment and pupillary light reflex are mediated by distinct populations of iprgcs. *Nature*, 476(7358):92, 2011.

[42] S.-K. Chen, K. S. Chew, D. S. McNeill, P. W. Keeley, J. L. Ecker, B. Q. Mao, J. Pahlberg, B. Kim, S. C. Lee, M. A. Fox, et al. Apoptosis regulates iprgc spacing necessary for rods and cones to drive circadian photoentrainment. *Neuron*, 77(3):503–515, 2013.

[43] A. Chenn and C. A. Walsh. Regulation of cerebral cortical size by control of cell cycle exit in neural precursors. *Science*, 297(5580):365–369, 2002.

[44] J. Chu and S. A. Anderson. Development of cortical interneurons. *Neuropsychopharmacology*, 40(1):16–23, 2015.

[45] R. L. Collins. Reimpressed selective breeding for lateralization of handedness in mice. *Brain research*, 564(2):194–202, 1991.

[46] E. Colombo, P. Collombat, G. Colasante, M. Bianchi, J. Long, A. Mansouri, J. L. Rubenstein, and V. Broccoli. Inactivation of arx, the murine ortholog of the x-linked lissencephaly with ambiguous genitalia gene, leads to severe disorganization of the ventral telencephalon with impaired neuronal migration and differentiation. *Journal of Neuroscience*, 27(17):4786–4798, 2007.

[47] J. A. Cooper. Mechanisms of cell migration in the nervous system. *J Cell Biol*, 202(5):725–734, 2013.

[48] M. C. Corballis. The genetics and evolution of handedness. *Psychological review*, 104(4):714, 1997.

[49] B. Cormand, K. Avela, H. Pihko, P. Santavuori, B. Talim, H. Topaloglu, A. de la Chapelle, and A.-E. Lehesjoki. Assignment of the muscle-eye-brain disease gene to 1p32-p34 by linkage analysis and homozygosity mapping. *The American Journal of Human Genetics*, 64(1):126–135, 1999.

[50] J. G. Csernansky, S. K. Gillespie, D. L. Dierker, A. Anticevic, L. Wang, D. M. Barch, and D. C. Van Essen. Symmetric abnormalities in sulcal patterning in schizophrenia. *Neuroimage*, 43(3):440–446, 2008.

[51] M. V. Danilchik and J. C. Gerhart. Differention of the animal-vegetal axis in xenopus laevis oocytes: I. polarized intracellular translocation of platelets establishes the yolk gradient. *Developmental biology*, 122(1):101–112, 1987.

[52] A. Dasgupta and J. D. Amack. Cilia in vertebrate left–right patterning. *Phil. Trans. R. Soc. B*, 371(1710):20150410, 2016.

[53] C. de Juan Romero, C. Bruder, U. Tomasello, J. M. Sanz-Anquela, and V. Borrell. Discrete domains of gene expression in germinal layers distinguish the development of gyrencephaly. *The EMBO journal*, page e201591176, 2015.

[54] J. De Wit, W. Hong, L. Luo, and A. Ghosh. Role of leucine-rich repeat proteins in the development and function of neural circuits. *Annual review of cell and developmental biology*, 27:697–729, 2011.

[55] M. S. Deiner, T. E. Kennedy, A. Fazeli, T. Serafini, M. Tessier-Lavigne, and D. W. Sretavan. Netrin-1 and dcc mediate axon guidance locally at the optic disc: loss of function leads to optic nerve hypoplasia. *Neuron*, 19(3):575–589, 1997.

[56] J. Demas, B. T. Sagdullaev, E. Green, L. Jaubert-Miazza, M. A. McCall, R. G. Gregg, R. O. Wong, and W. Guido. Failure to maintain eye-specific segregation in nob, a mutant with abnormally patterned retinal activity. *Neuron*, 50(2):247–259, 2006.

[57] E. S. Deneris and O. Hobert. Maintenance of postmitotic neuronal cell identity. *Nature neuroscience*, 17(7):899–907, 2014.

[58] O. S. Dhande, M. E. Estevez, L. E. Quattrochi, R. N. El-Danaf, P. L. Nguyen, D. M. Berson, and A. D. Huberman. Genetic dissection of retinal inputs to brainstem nuclei controlling image stabilization. *Journal of Neuroscience*, 33(45):17797–17813, 2013.

[59] O. S. Dhande and A. D. Huberman. Retinal ganglion cell maps in the brain: implications for visual processing. *Current opinion in neurobiology*, 24:133–142, 2014.

[60] O. S. Dhande and A. D. Huberman. Visual circuits: mouse retina no longer a level playing field. *Current Biology*, 24(4):R155–R156, 2014.

[61] O. S. Dhande, B. K. Stafford, J.-H. A. Lim, and A. D. Huberman. Contributions of retinal ganglion cells to subcortical visual processing and behaviors. *Annual Review of Vision Science*, 1:291–328, 2015.

[62] N. Dharmaratne, K. A. Glendining, T. R. Young, H. Tran, A. Sawatari, and C. A. Leamey. Ten-m3 is required for the development of topography in the ipsilateral retinocollicular pathway. *PLoS One*, 7(9):e43083, 2012.

[63] I. Diamond. The subdivisions of neocortex: a proposal to revise the traditional view of sensory, motor, and association areas. *Progress in psychobiology and physiological psychology*, 8:1–43, 1979.

[64] O. Dick, S. tom Dieck, W. D. Altrock, J. Ammermüller, R. Weiler, C. C. Garner, E. D. Gundelfinger, and J. H. Brandstätter. The presynaptic active zone protein bassoon is essential for photoreceptor ribbon synapse formation in the retina. *Neuron*, 37(5):775–786, 2003.

[65] J. Dimidschstein, L. Passante, A. Dufour, J. Van Den Ameele, L. Tiberi, T. Hrechdakian, R. Adams, R. Klein, D. C. Lie, Y. Jossin, et al. Ephrin-b1 controls the columnar distribution of cortical pyramidal neurons by restricting their tangential migration. *Neuron*, 79(6):1123–1135, 2013.

[66] M. T. H. Do and K.-W. Yau. Intrinsically photosensitive retinal ganglion cells. *Physiological reviews*, 90(4):1547–1581, 2010.

[67] J. Egea, C. Erlacher, E. Montanez, I. Burtscher, S. Yamagishi, M. Heß, F. Hampel, R. Sanchez, M. T. Rodriguez-Manzaneque, M. R. Bösl, et al. Genetic ablation of flrt3 reveals a novel morphogenetic function for the anterior visceral endoderm in suppressing mesoderm differentiation. *Genes & development*, 22(23):3349–3362, 2008.

[68] B. Ekesten and P. Gouras. Cone and rod inputs to murine retinal ganglion cells: evidence of cone opsin specific channels. *Visual neuroscience*, 22(6):893–903, 2005.

[69] L. A. Elias, D. D. Wang, and A. R. Kriegstein. Gap junction adhesion is necessary for radial migration in the neocortex. *Nature*, 448(7156):901–907, 2007.

[70] J. Elstrott, A. Anishchenko, M. Greschner, A. Sher, A. M. Litke, E. Chichilnisky, and M. B. Feller. Direction selectivity in the retina is established independent of visual experience and cholinergic retinal waves. *Neuron*, 58(4):499–506, 2008.

[71] L. Erskine and E. Herrera. The retinal ganglion cell axon's journey: insights into molecular mechanisms of axon guidance. *Developmental biology*, 308(1):1–14, 2007.

[72] N. E. Faulkner, D. L. Dujardin, C.-Y. Tai, K. T. Vaughan, C. B. O'Connell, Y.-l. Wang, and R. B. Vallee. A role for the lissencephaly gene lis1 in mitosis and cytoplasmic dynein function. *Nature cell biology*, 2(11):784, 2000.

[73] V. Fernández, C. Llinares-Benadero, and V. Borrell. Cerebral cortex expansion and folding: what have we learned? *The EMBO journal*, page e201593701, 2016.

[74] R. Fernandez-Alonso, L. Davidson, J. Hukelmann, M. Zengerle, A. R. Prescott, A. Lamond, A. Ciulli, G. P. Sapkota, and G. M. Findlay. Brd4-brd2 isoform switching coordinates pluripotent exit and smad2-dependent lineage specification. *EMBO reports*, page e201643534, 2017.

[75] K. Flintoff, Y. Arudchelvan, and S.-G. Gong. Flrt2 interacts with fibronectin in the atdc5 chondroprogenitor cells. *Journal of cellular physiology*, 229(10):1538–1547, 2014.

[76] M. Florio, M. Albert, E. Taverna, T. Namba, H. Brandl, E. Lewitus, C. Haffner, A. Sykes, F. K. Wong, J. Peters, et al. Human-specific gene arhgap11b promotes basal progenitor amplification and neocortex expansion. *Science*, 347(6229):1465–1470, 2015.

[77] G. D. Frantz and S. K. McConnell. Restriction of late cerebral cortical progenitors to an upper-layer fate. *Neuron*, 17(1):55–61, 1996.

[78] M. S. Freedman, R. J. Lucas, B. Soni, M. von Schantz, M. Muñoz, Z. David-Gray, and R. Foster. Regulation of mammalian circadian behavior by non-rod, non-cone, ocular photoreceptors. *Science*, 284(5413):502–504, 1999.

[79] A. E. Fry, K. A. Fawcett, N. Zelnik, H. Yuan, B. A. Thompson, L. Shemer-Meiri, T. D. Cushion, H. Mugalaasi, D. Sims, N. Stoodley, et al. De novo mutations in grin1 cause extensive bilateral polymicrogyria. *Brain*, 2018.

[80] Y. Fukata, H. Adesnik, T. Iwanaga, D. S. Bredt, R. A. Nicoll, and M. Fukata. Epilepsy-related ligand/receptor complex lgi1 and adam22 regulate synaptic transmission. *Science*, 313(5794):1792–1795, 2006.

[81] Y. Fukata, K. L. Lovero, T. Iwanaga, A. Watanabe, N. Yokoi, K. Tabuchi, R. Shigemoto, R. A. Nicoll, and M. Fukata. Disruption of lgi1–linked synaptic complex causes abnormal synaptic transmission and epilepsy. *Proceedings of the National Academy of Sciences*, 107(8):3799–3804, 2010.

[82] L. Galli-Resta, G. Resta, S.-S. Tan, and B. E. Reese. Mosaics of islet-1-expressing amacrine cells assembled by short-range cellular interactions. *Journal of Neuroscience*, 17(20):7831–7838, 1997.

[83] E. Georges-Labouesse, M. Mark, N. Messaddeq, and A. Gansmüller. Essential role of α6 integrins in cortical and retinal lamination. *Current Biology*, 8(17):983–S1, 1998.

[84] J. G. Gleeson, K. M. Allen, J. W. Fox, E. D. Lamperti, S. Berkovic, I. Scheffer, E. C. Cooper, W. B. Dobyns, S. R. Minnerath, M. E. Ross, et al. Doublecortin, a brain-specific gene mutated in human x-linked lissencephaly and double cortex syndrome, encodes a putative signaling protein. *Cell*, 92(1):63–72, 1998.

[85] L. Godinho, J. S. Mumm, P. R. Williams, E. H. Schroeter, A. Koerber, S. W. Park, S. D. Leach, and R. O. Wong. Targeting of amacrine cell neurites to appropriate synaptic laminae in the developing zebrafish retina. *Development*, 132(22):5069–5079, 2005.

[86] D. Göz, K. Studholme, D. A. Lappi, M. D. Rollag, I. Provencio, and L. P. Morin. Targeted destruction of photosensitive retinal ganglion cells with a saporin conjugate alters the effects of light on mouse circadian rhythms. *PloS one*, 3(9):e3153, 2008.

[87] J. Gros, K. Feistel, C. Viebahn, M. Blum, and C. J. Tabin. Cell movements at hensen's node establish left/right asymmetric gene expression in the chick. *Science*, 324(5929):941–944, 2009.

[88] M. S. Grubb and I. D. Thompson. Quantitative characterization of visual response properties in the mouse dorsal lateral geniculate nucleus. *Journal of neurophysiology*, 90(6):3594–3607, 2003.

[89] Y.-N. Gu, E.-S. Lee, and C.-J. Jeon. Types and density of calbindin d28k-immunoreactive ganglion cells in mouse retina. *Experimental eye research*, 145:327–336, 2016.

[90] A. D. Güler, J. L. Ecker, G. S. Lall, S. Haq, C. M. Altimus, H.-W. Liao, A. R. Barnard, H. Cahill, T. C. Badea, H. Zhao, et al. Melanopsin cells are the principal conduits for rod–cone input to non-image-forming vision. *Nature*, 453(7191):102, 2008.

[91] B. P. Haines, L. M. Wheldon, D. Summerbell, J. K. Heath, and P. W. Rigby. Regulated expression of flrt genes implies a functional role in the regulation of fgf signalling during mouse development. *Developmental biology*, 297(1):14–25, 2006.

[92] D. V. Hansen, J. H. Lui, P. R. Parker, and A. R. Kriegstein. Neurogenic radial glia in the outer subventricular zone of human neocortex. *Nature*, 464(7288):554, 2010.

[93] A. Y. Hardan, R. J. Jou, M. S. Keshavan, R. Varma, and N. J. Minshew. Increased frontal cortical folding in autism: a preliminary mri study. *Psychiatry Research: Neuroimaging*, 131(3):263–268, 2004.

[94] J. M. Harris, H. Whalley, S. Yates, P. Miller, E. C. Johnstone, and S. M. Lawrie. Abnormal cortical folding in high-risk individuals: a predictor of the development of schizophrenia? *Biological psychiatry*, 56(3):182–189, 2004.

[95] D. Hartmann, B. De Strooper, and P. Saftig. Presenilin-1 deficiency leads to loss of cajal–retzius neurons and cortical dysplasia similar to human type 2 lissencephaly. *Current biology*, 9(14):719–727, 1999.

[96] S. Hattar, M. Kumar, A. Park, P. Tong, J. Tung, K.-W. Yau, and D. M. Berson. Central projections of melanopsin-expressing retinal ganglion cells in the mouse. *Journal of Comparative Neurology*, 497(3):326–349, 2006.

[97] W. Haubensak, A. Attardo, W. Denk, and W. B. Huttner. Neurons arise in the basal neuroepithelium of the early mammalian telencephalon: a major site of neurogenesis. *Proceedings of the National Academy of Sciences of the United States of America*, 101(9):3196–3201, 2004.

[98] S. Haverkamp, H. Wässle, J. Duebel, T. Kuner, G. J. Augustine, G. Feng, and T. Euler. The primordial, blue-cone color system of the mouse retina. *Journal of Neuroscience*, 25(22):5438–5445, 2005.

[99] P. G. Hepper, S. Shahidullah, and R. White. Handedness in the human fetus. *Neuropsychologia*, 29(11):1107–1111, 1991.

[100] P. G. Hepper, D. L. Wells, and C. Lynch. Prenatal thumb sucking is related to postnatal handedness. *Neuropsychologia*, 43(3):313–315, 2005.

[101] S. Herculano-Houzel, B. Mota, and R. Lent. Cellular scaling rules for rodent brains. *Proceedings of the National Academy of Sciences*, 103(32):12138–12143, 2006.

[102] S. Herculano-Houzel, C. Watson, and G. Paxinos. Distribution of neurons in functional areas of the mouse cerebral cortex reveals quantitatively different cortical zones. *Frontiers in neuroanatomy*, 7, 2013.

[103] L. J. Hogstrom, L. T. Westlye, K. B. Walhovd, and A. M. Fjell. The structure of the cerebral cortex across adult life: age-related patterns of surface area, thickness, and gyrification. *Cerebral cortex*, 23(11):2521–2530, 2012.

[104] Y. K. Hong and C. Chen. Wiring and rewiring of the retinogeniculate synapse. *Current opinion in neurobiology*, 21(2):228–237, 2011.

[105] M. Hoon, H. Okawa, L. Della Santina, and R. O. Wong. Functional architecture of the retina: development and disease. *Progress in retinal and eye research*, 42:44–84, 2014.

[106] D. Horesh, T. Sapir, F. Francis, S. Grayer Wolf, M. Caspi, M. Elbaum, J. Chelly, and O. Reiner. Doublecortin, a stabilizer of microtubules. *Human molecular genetics*, 8(9):1599–1610, 1999.

[107] C. Hu, D. D. Hill, and K. Y. Wong. Intrinsic physiological properties of the five types of mouse ganglion-cell photoreceptors. *Journal of neurophysiology*, 109(7):1876–1889, 2013.

[108] D. H. Hubel and T. N. Wiesel. Receptive fields, binocular interaction and functional architecture in the cat's visual cortex. *The Journal of physiology*, 160(1):106–154, 1962.

[109] A. D. Huberman, M. Manu, S. M. Koch, M. W. Susman, A. B. Lutz, E. M. Ullian, S. A. Baccus, and B. A. Barres. Architecture and activity-mediated refinement of axonal projections from a mosaic of genetically identified retinal ganglion cells. *Neuron*, 59(3):425–438, 2008.

[110] A. D. Huberman, W. Wei, J. Elstrott, B. K. Stafford, M. B. Feller, and B. A. Barres. Genetic identification of an on-off direction-selective retinal ganglion cell subtype reveals a layer-specific subcortical map of posterior motion. *Neuron*, 62(3):327–334, 2009.

[111] R. M. Huckfeldt, T. Schubert, J. L. Morgan, L. Godinho, G. Di Cristo, Z. J. Huang, and R. O. Wong. Transient neurites of retinal horizontal cells exhibit columnar tiling via homotypic interactions. *Nature neuroscience*, 12(1):35–43, 2009.

[112] S. Hughes, A. Jagannath, J. Rodgers, M. Hankins, S. Peirson, and R. Foster. Signalling by melanopsin (opn4) expressing photosensitive retinal ganglion cells, 2016.

[113] J. J. Hutsler. The specialized structure of human language cortex: pyramidal cell size asymmetries within auditory and language-associated regions of the temporal lobes. *Brain and Language*, 86(2):226–242, 2003.

[114] N. Itoh and D. M. Ornitz. Fibroblast growth factors: from molecular evolution to roles in development, metabolism and disease. *The Journal of Biochemistry*, 149(2):121–130, 2011.

[115] V. A. Jackson, D. del Toro, M. Carrasquero, P. Roversi, K. Harlos, R. Klein, and E. Seiradake. Structural basis of latrophilin-flrt interaction. *Structure*, 23(4):774–781, 2015.

[116] V. A. Jackson, S. Mehmood, M. Chavent, P. Roversi, M. Carrasquero, D. Del Toro, G. Seyit-Bremer, F. M. Ranaivoson, D. Comoletti, M. S. Sansom, et al. Super-complexes of adhesion gpcrs and neural guidance receptors. *Nature communications*, 7:11184, 2016.

[117] G. H. Jacobs, G. A. Williams, and J. A. Fenwick. Influence of cone pigment co-expression on spectral sensitivity and color vision in the mouse. *Vision research*, 44(14):1615–1622, 2004.

[118] G. Jeyarasasingam, C. J. Snider, G.-M. Ratto, and L. M. Chalupa. Activity-regulated cell death contributes to the formation of on and off α ganglion cell mosaics. *Journal of Comparative Neurology*, 394(3):335–343, 1998.

[119] Z. Jiang, H. Tang, M. Ventura, M. F. Cardone, T. Marques-Bonet, X. She, P. A. Pevzner, and E. E. Eichler. Ancestral reconstruction of segmental duplications reveals punctuated cores of human genome evolution. *Nature genetics*, 39(11):1361, 2007.

[120] K. P. Johnson, L. Zhao, and D. Kerschensteiner. A pixel-encoder retinal ganglion cell with spatially offset excitatory and inhibitory receptive fields. *Cell reports*, 22(6):1462, 2018.

[121] Y. Jossin and J. A. Cooper. Reelin, rap1 and n-cadherin orient the migration of multipolar neurons in the developing neocortex. *Nature neuroscience*, 14(6):697–703, 2011.

[122] X.-C. Ju, Q.-Q. Hou, A.-L. Sheng, K.-Y. Wu, Y. Zhou, Y. Jin, T. Wen, Z. Yang, X. Wang, and Z.-G. Luo. The hominoid-specific gene tbc1d3 promotes generation of basal neural progenitors and induces cortical folding in mice. *Elife*, 5, 2016.

[123] E. E. Karaulanov, R. T. Böttcher, and C. Niehrs. A role for fibronectin-leucine-rich transmembrane cell-surface proteins in homotypic cell adhesion. *EMBO reports*, 7(3):283–290, 2006.

[124] M. Kartagener and A. Horlacher. Bronchiectasien bei situs viscerum inversus. *Schweiz. med. Wchnschr*, 16:782, 1935.

[125] T. Kawauchi, K. Sekine, M. Shikanai, K. Chihama, K. Tomita, K.-i. Kubo, K. Nakajima, Y.-i. Nabeshima, and M. Hoshino. Rab gtpases-dependent endocytic pathways regulate neuronal migration and maturation through n-cadherin trafficking. *Neuron*, 67(4):588–602, 2010.

[126] J. N. Kay, I. De la Huerta, I.-J. Kim, Y. Zhang, M. Yamagata, M. W. Chu, M. Meister, and J. R. Sanes. Retinal ganglion cells with distinct directional preferences differ in molecular identity, structure, and central projections. *Journal of Neuroscience*, 31(21):7753–7762, 2011.

[127] D. A. Keays, G. Tian, K. Poirier, G.-J. Huang, C. Siebold, J. Cleak, P. L. Oliver, M. Fray, R. J. Harvey, Z. Molnár, et al. Mutations in α-tubulin cause abnormal neuronal migration in mice and lissencephaly in humans. *Cell*, 128(1):45–57, 2007.

[128] D. Kennedy, K. O'Craven, B. Ticho, A. Goldstein, N. Makris, and J. Henson. Structural and functional brain asymmetries in human situs inversus totalis. *Neurology*, 53(6):1260–1260, 1999.

[129] I.-J. Kim, Y. Zhang, M. Meister, and J. R. Sanes. Laminar restriction of retinal ganglion cell dendrites and axons: subtype-specific developmental patterns revealed with transgenic markers. *Journal of Neuroscience*, 30(4):1452–1462, 2010.

[130] I.-J. Kim, Y. Zhang, M. Yamagata, M. Meister, and J. R. Sanes. Molecular identification of a retinal cell type that responds to upward motion. *Nature*, 452(7186):478, 2008.

[131] T.-J. Kim and C.-J. Jeon. Morphological classification of parvalbumin-containing retinal ganglion cells in mouse: single-cell injection after immunocytochemistry. *Investigative ophthalmology & visual science*, 47(7):2757–2764, 2006.

[132] M. A. Kingsbury, S. K. Rehen, J. J. Contos, C. M. Higgins, and J. Chun. Non-proliferative effects of lysophosphatidic acid enhance cortical growth and folding. *Nature neuroscience*, 6(12):1292, 2003.

[133] A. J. Klar. Genetic models for handedness, brain lateralization, schizophrenia, and manic-depression. *Schizophrenia research*, 39(3):207–218, 1999.

[134] R. Klein. Eph/ephrin signalling during development. *Development*, 139(22):4105–4109, 2012.

[135] M. Kloc, S. Bilinski, A. Chan, L. Allen, N. R. Zearfoss, and L. Etkin. Rna localization and germ cell determination in xenopus. *International review of cytology*, 203:63–91, 2001.

[136] A. K. Knutsen, C. D. Kroenke, Y. V. Chang, L. A. Taber, and P. V. Bayly. Spatial and temporal variations of cortical growth during gyrogenesis in the developing ferret brain. *Cerebral Cortex*, 23(2):488–498, 2012.

[137] J. Ko, S. Kim, H. S. Chung, K. Kim, K. Han, H. Kim, H. Jun, B.-K. Kaang, and E. Kim. Salm synaptic cell adhesion-like molecules regulate the differentiation of excitatory synapses. *Neuron*, 50(2):233–245, 2006.

[138] B. Kobe and A. V. Kajava. The leucine-rich repeat as a protein recognition motif. *Current opinion in structural biology*, 11(6):725–732, 2001.

[139] S. M. Koch, C. G. D. Cruz, T. S. Hnasko, R. H. Edwards, A. D. Huberman, and E. M. Ullian. Pathway-specific genetic attenuation of glutamate release alters select features of competition-based visual circuit refinement. *Neuron*, 71(2):235–242, 2011.

[140] B. Krieger, M. Qiao, D. L. Rousso, J. R. Sanes, and M. Meister. Four alpha ganglion cell types in mouse retina: Function, structure, and molecular signatures. *PloS one*, 12(7):e0180091, 2017.

[141] J. Kristianto, M. G. Johnson, R. K. Zastrow, A. B. Radcliff, and R. D. Blank. Spontaneous recombinase activity of cre–ert2 in vivo. *Transgenic research*, 26(3):411–417, 2017.

[142] C. D. Kroenke and P. V. Bayly. How forces fold the cerebral cortex. *Journal of Neuroscience*, 38(4):767–775, 2018.

[143] T. Kuwajima, C. A. Soares, A. A. Sitko, V. Lefebvre, and C. Mason. Soxc transcription factors promote contralateral retinal ganglion cell differentiation and axon guidance in the mouse visual system. *Neuron*, 93(5):1110–1125, 2017.

[144] S. E. Lacy, C. G. Bönnemann, E. A. Buzney, and L. M. Kunkel. Identification of flrt1, flrt2, and flrt3: a novel family of transmembrane leucine-rich repeat proteins. *Genomics*, 62(3):417–426, 1999.

[145] C. A. Leamey, S. Merlin, P. Lattouf, A. Sawatari, X. Zhou, N. Demel, K. A. Glendining, T. Oohashi, M. Sur, and R. Fässler. Ten_m3 regulates eye-specific patterning in the mammalian visual pathway and is required for binocular vision. *PLoS biology*, 5(9):e241, 2007.

[146] E.-S. Lee, J.-Y. Lee, and C.-J. Jeon. Types and density of calretinin-containing retinal ganglion cells in mouse. *Neuroscience research*, 66(2):141–150, 2010.

[147] S. Lee, J. Hjerling-Leffler, E. Zagha, G. Fishell, and B. Rudy. The largest group of superficial neocortical gabaergic interneurons expresses ionotropic serotonin receptors. *Journal of Neuroscience*, 30(50):16796–16808, 2010.

[148] W. Levick. Receptive fields and trigger features of ganglion cells in the visual streak of the rabbit's retina. *The Journal of physiology*, 188(3):285–307, 1967.

[149] E. Lewitus, I. Kelava, A. T. Kalinka, P. Tomancak, and W. B. Huttner. An adaptive threshold in mammalian neocortical evolution. *PLoS biology*, 12(11):e1002000, 2014.

[150] E. Leyva-Díaz, D. del Toro, M. J. Menal, S. Cambray, R. Susín, M. Tessier-Lavigne, R. Klein, J. Egea, and G. López-Bendito. Flrt3 is a robo1-interacting protein that determines netrin-1 attraction in developing axons. *Current Biology*, 24(5):494–508, 2014.

[151] W. Li and S. H. DeVries. Bipolar cell pathways for color and luminance vision in a dichromatic mammalian retina. *Nature neuroscience*, 9(5):669, 2006.

[152] S. Lodato and P. Arlotta. Generating neuronal diversity in the mammalian cerebral cortex. *Annual review of cell and developmental biology*, 31:699–720, 2015.

[153] G. Lohmann, D. Y. Von Cramon, and A. C. Colchester. Deep sulcal landmarks provide an organizing framework for human cortical folding. *Cerebral Cortex*, 18(6):1415–1420, 2007.

[154] G. Lohmann, D. Y. von Cramon, and H. Steinmetz. Sulcal variability of twins. *Cerebral Cortex*, 9(7):754–763, 1999.

[155] Y. C. Lu, O. V. Nazarko, R. Sando III, G. S. Salzman, N.-S. Li, T. C. Südhof, and D. Araç. Structural basis of latrophilin-flrt-unc5 interaction in cell adhesion. *Structure*, 23(9):1678–1691, 2015.

[156] J. H. Lui, D. V. Hansen, and A. R. Kriegstein. Development and evolution of the human neocortex. *Cell*, 146(1):18–36, 2011.

[157] J. H. Lui, T. J. Nowakowski, A. A. Pollen, A. Javaherian, A. R. Kriegstein, and M. C. Oldham. Radial glia require pdgfd–pdgfrβ signalling in human but not mouse neocortex. *Nature*, 515(7526):264, 2014.

[158] A. Lukaszewicz, P. Savatier, V. Cortay, P. Giroud, C. Huissoud, M. Berland, H. Kennedy, and C. Dehay. G1 phase regulation, area-specific cell cycle control, and cytoarchitectonics in the primate cortex. *Neuron*, 47(3):353–364, 2005.

[159] M. B. Luskin, A. L. Pearlman, and J. R. Sanes. Cell lineage in the cerebral cortex of the mouse studied in vivo and in vitro with a recombinant retrovirus. *Neuron*, 1(8):635–647, 1988.

[160] T. Ma, C. Wang, L. Wang, X. Zhou, M. Tian, Q. Zhang, Y. Zhang, J. Li, Z. Liu, Y. Cai, et al. Subcortical origins of human and monkey neocortical interneurons. *Nature neuroscience*, 16(11):1588–1597, 2013.

[161] W. Mah, J. Ko, J. Nam, K. Han, W. S. Chung, and E. Kim. Selected salm (synaptic adhesion-like molecule) family proteins regulate synapse formation. *Journal of Neuroscience*, 30(16):5559–5568, 2010.

[162] R. C. Marcus and C. A. Mason. The first retinal axon growth in the mouse optic chiasm: axon patterning and the cellular environment. *Journal of Neuroscience*, 15(10):6389–6402, 1995.

[163] S. Maretto, P.-S. Müller, A. R. Aricescu, K. W. Cho, E. K. Bikoff, and E. J. Robertson. Ventral closure, headfold fusion and definitive endoderm migration defects in mouse embryos lacking the fibronectin leucine-rich transmembrane protein flrt3. *Developmental biology*, 318(1):184–193, 2008.

[164] H. Markram. The blue brain project. *Nature Reviews Neuroscience*, 7(2):153, 2006.

[165] J. H. Marshel, A. P. Kaye, I. Nauhaus, and E. M. Callaway. Anterior-posterior direction opponency in the superficial mouse lateral geniculate nucleus. *Neuron*, 76(4):713–720, 2012.

[166] F. J. Martini, M. Valiente, G. L. Bendito, G. Szabó, F. Moya, M. Valdeolmillos, and O. Marín. Biased selection of leading process branches mediates chemotaxis during tangential neuronal migration. *Development*, 136(1):41–50, 2009.

[167] K. Masuda, T. Toda, Y. Shinmyo, H. Ebisu, Y. Hoshiba, M. Wakimoto, Y. Ichikawa, and H. Kawasaki. Pathophysiological analyses of cortical malformation using gyrencephalic mammals. *Scientific reports*, 5:15370, 2015.

[168] R. L. Matsuoka, Z. Jiang, I. S. Samuels, K. T. Nguyen-Ba-Charvet, L. O. Sun, N. S. Peachey, A. Chédotal, K.-W. Yau, and A. L. Kolodkin. Guidance-cue control of horizontal cell morphology, lamination, and synapse formation in the mammalian outer retina. *Journal of Neuroscience*, 32(20):6859–6868, 2012.

[169] R. L. Matsuoka, K. T. Nguyen-Ba-Charvet, A. Parray, T. C. Badea, A. Chédotal, and A. L. Kolodkin. Transmembrane semaphorin signalling controls laminar stratification in the mammalian retina. *Nature*, 470(7333):259–263, 2011.

[170] H. R. Maturana and S. Frenk. Directional movement and horizontal edge detectors in the pigeon retina. *Science*, 142(3594):977–979, 1963.

[171] J. McGrath, S. Somlo, S. Makova, X. Tian, and M. Brueckner. Two populations of node monocilia initiate left-right asymmetry in the mouse. *Cell*, 114(1):61–73, 2003.

[172] T. McLaughlin, C. L. Torborg, M. B. Feller, and D. D. O'Leary. Retinotopic map refinement requires spontaneous retinal waves during a brief critical period of development. *Neuron*, 40(6):1147–1160, 2003.

[173] S. C. McLoon and R. Barnes. Early differentiation of retinal ganglion cells: an axonal protein expressed by premigratory and migrating retinal ganglion cells. *Journal of Neuroscience*, 9(4):1424–1432, 1989.

[174] M. W. Miller. Maturation of rat visual cortex. iii. postnatal morphogenesis and synaptogenesis of local circuit neurons. *Developmental Brain Research*, 25(2):271–285, 1986.

[175] T. Miyata, A. Kawaguchi, H. Okano, and M. Ogawa. Asymmetric inheritance of radial glial fibers by cortical neurons. *Neuron*, 31(5):727–741, 2001.

[176] G. H. Mochida, M. Mahajnah, A. D. Hill, L. Basel-Vanagaite, D. Gleason, R. S. Hill, A. Bodell, M. Crosier, R. Straussberg, and C. A. Walsh. A truncating mutation of trappc9 is associated with autosomal-recessive intellectual disability and postnatal microcephaly. *The American Journal of Human Genetics*, 85(6):897–902, 2009.

[177] C. A. Moores, M. Perderiset, F. Francis, J. Chelly, A. Houdusse, and R. A. Milligan. Mechanism of microtubule stabilization by doublecortin. *Molecular cell*, 14(6):833–839, 2004.

[178] L. P. Morin and K. M. Studholme. Retinofugal projections in the mouse. *Journal of Comparative Neurology*, 522(16):3733–3753, 2014.

[179] B. Mota and S. Herculano-Houzel. Cortical folding scales universally with surface area and thickness, not number of neurons. *Science*, 349(6243):74–77, 2015.

[180] P.-S. Müller, R. Schulz, S. Maretto, I. Costello, S. Srinivas, E. Bikoff, and E. Robertson. The fibronectin leucine-rich repeat transmembrane protein flrt2 is required in the epicardium to promote heart morphogenesis. *Development*, 138(7):1297–1308, 2011.

[181] J. S. Mumm, P. R. Williams, L. Godinho, A. Koerber, A. J. Pittman, T. Roeser, C.-B. Chien, H. Baier, and R. O. Wong. In vivo imaging reveals dendritic targeting of laminated afferents by zebrafish retinal ganglion cells. *Neuron*, 52(4):609–621, 2006.

[182] B. Nadarajah, J. E. Brunstrom, J. Grutzendler, R. O. Wong, and A. L. Pearlman. Two modes of radial migration in early development of the cerebral cortex. *Nature neuroscience*, 4(2):143–150, 2001.

[183] A. Nath and G. W. Schwartz. Cardinal orientation selectivity is represented by two distinct ganglion cell types in mouse retina. *Journal of Neuroscience*, 36(11):3208–3221, 2016.

[184] A. Nath and G. W. Schwartz. Electrical synapses convey orientation selectivity in the mouse retina. *Nature communications*, 8(1):2025, 2017.

[185] S. C. Noctor, A. C. Flint, T. A. Weissman, R. S. Dammerman, and A. R. Kriegstein. Neurons derived from radial glial cells establish radial units in neocortex. *Nature*, 409(6821):714, 2001.

[186] S. C. Noctor, V. Martínez-Cerdeño, L. Ivic, and A. R. Kriegstein. Cortical neurons arise in symmetric and asymmetric division zones and migrate through specific phases. *Nature neuroscience*, 7(2):136–144, 2004.

[187] M. Nonaka-Kinoshita, I. Reillo, B. Artegiani, M. Á. Martínez-Martínez, M. Nelson, V. Borrell, and F. Calegari. Regulation of cerebral cortex size and folding by expansion of basal progenitors. *The EMBO journal*, 32(13):1817–1828, 2013.

[188] C. W. Nordahl, D. Dierker, I. Mostafavi, C. M. Schumann, S. M. Rivera, D. G. Amaral, and D. C. Van Essen. Cortical folding abnormalities in autism revealed by surface-based morphometry. *Journal of Neuroscience*, 27(43):11725–11735, 2007.

[189] S. Ogata, J. Morokuma, T. Hayata, G. Kolle, C. Niehrs, N. Ueno, and K. W. Cho. Tgf-β signaling-mediated morphogenesis: modulation of cell adhesion via cadherin endocytosis. *Genes & development*, 21(14):1817–1831, 2007.

[190] H. Okawa, L. Della Santina, G. W. Schwartz, F. Rieke, and R. O. Wong. Interplay of cell-autonomous and nonautonomous mechanisms tailors synaptic connectivity of converging axons in vivo. *Neuron*, 82(1):125–137, 2014.

[191] J. A. Osterhout, R. N. El-Danaf, P. L. Nguyen, and A. D. Huberman. Birthdate and outgrowth timing predict cellular mechanisms of axon target matching in the developing visual pathway. *Cell reports*, 8(4):1006–1017, 2014.

[192] J. A. Osterhout, B. K. Stafford, P. L. Nguyen, Y. Yoshihara, and A. D. Huberman. Contactin-4 mediates axon-target specificity and functional development of the accessory optic system. *Neuron*, 86(4):985–999, 2015.

[193] M. L. O'Sullivan, J. de Wit, J. N. Savas, D. Comoletti, S. Otto-Hitt, J. R. Yates, and A. Ghosh. Flrt proteins are endogenous latrophilin ligands and regulate excitatory synapse development. *Neuron*, 73(5):903–910, 2012.

[194] W. Pak, R. Hindges, Y.-S. Lim, S. L. Pfaff, and D. D. O'Leary. Magnitude of binocular vision controlled by islet-2 repression of a genetic program that specifies laterality of retinal axon pathfinding. *Cell*, 119(4):567–578, 2004.

[195] S. Panda, T. K. Sato, A. M. Castrucci, M. D. Rollag, W. J. DeGrip, J. B. Hogenesch, I. Provencio, and S. A. Kay. Melanopsin (opn4) requirement for normal light-induced circadian phase shifting. *Science*, 298(5601):2213–2216, 2002.

[196] J.-J. Pang, F. Gao, and S. M. Wu. Light-evoked excitatory and inhibitory synaptic inputs to on and off α ganglion cells in the mouse retina. *Journal of Neuroscience*, 23(14):6063–6073, 2003.

[197] T. Pang, R. Atefy, and V. Sheen. Malformations of cortical development. *The neurologist*, 14(3):181, 2008.

[198] J. Parnavelas and A. Lieberman. An ultrastructural study of the maturation of neuronal somata in the visual cortex of the rat. *Anatomy and embryology*, 157(3):311–328, 1979.

[199] J. G. Parnavelas. The origin and migration of cortical neurones: new vistas. *Trends in neurosciences*, 23(3):126–131, 2000.

[200] T. J. Petros, A. Rebsam, and C. A. Mason. Retinal axon growth at the optic chiasm: to cross or not to cross. *Annu. Rev. Neurosci.*, 31:295–315, 2008.

[201] C. Pfeiffenberger, J. Yamada, and D. A. Feldheim. Ephrin-as and patterned retinal activity act together in the development of topographic maps in the primary visual system. *Journal of Neuroscience*, 26(50):12873–12884, 2006.

[202] X. Piao, L. Basel-Vanagaite, R. Straussberg, P. E. Grant, E. W. Pugh, K. Doheny, B. Doan, S. E. Hong, Y. Y. Shugart, and C. A. Walsh. An autosomal recessive form of bilateral frontoparietal polymicrogyria maps to chromosome 16q12. 2-21. *The American Journal of Human Genetics*, 70(4):1028–1033, 2002.

[203] X. Piao, B. S. Chang, A. Bodell, K. Woods, B. BenZeev, M. Topcu, R. Guerrini, H. Goldberg-Stern, L. Sztriha, W. B. Dobyns, et al. Genotype–phenotype analysis of human frontoparietal polymicrogyria syndromes. *Annals of neurology*, 58(5):680–687, 2005.

[204] E. M. Pinheiro, Z. Xie, A. L. Norovich, M. Vidaki, L.-H. Tsai, and F. B. Gertler. Lpd depletion reveals that srf specifies radial versus tangential migration of pyramidal neurons. *Nature cell biology*, 13(8):989–995, 2011.

[205] D. M. Piscopo, R. N. El-Danaf, A. D. Huberman, and C. M. Niell. Diverse visual features encoded in mouse lateral geniculate nucleus. *Journal of Neuroscience*, 33(11):4642–4656, 2013.

[206] D. T. Plas, J. E. Lopez, and M. C. Crair. Pretarget sorting of retinocollicular axons in the mouse. *Journal of Comparative Neurology*, 491(4):305–319, 2005.

[207] L. Poggi, M. Vitorino, I. Masai, and W. A. Harris. Influences on neural lineage and mode of division in the zebrafish retina in vivo. *The Journal of cell biology*, 171(6):991–999, 2005.

[208] K. Poirier, D. A. Keays, F. Francis, Y. Saillour, N. Bahi, S. Manouvrier, C. Fallet-Bianco, L. Pasquier, A. Toutain, F. P. D. Tuy, et al. Large spectrum of lissencephaly and pachygyria phenotypes resulting from de novo missense mutations in tubulin alpha 1a (tuba1a). *Human mutation*, 28(11):1055–1064, 2007.

[209] A. A. Pollen, T. J. Nowakowski, J. Chen, H. Retallack, C. Sandoval-Espinosa, C. R. Nicholas, J. Shuga, S. J. Liu, M. C. Oldham, A. Diaz, et al. Molecular identity of human outer radial glia during cortical development. *Cell*, 163(1):55–67, 2015.

[210] P. Rakic. Neuron-glia relationship during granule cell migration in developing cerebellar cortex. a golgi and electonmicroscopic study in macacus rhesus. *Journal of Comparative Neurology*, 141(3):283–312, 1971.

[211] P. Rakic. Mode of cell migration to the superficial layers of fetal monkey neocortex. *The Journal of Comparative Neurology*, 145(1):61–83, 1972.

[212] P. Rakic. Neurons in rhesus monkey visual cortex: systematic relation between time of origin and eventual disposition. *Science*, 183(4123):425–427, 1974.

[213] P. Rakic. Specification of cerebral cortical areas. *Science*, 241(4862):170–176, 1988.

[214] B. G. Rash, S. Tomasi, H. D. Lim, C. Y. Suh, and F. M. Vaccarino. Cortical gyrification induced by fibroblast growth factor 2 in the mouse brain. *Journal of Neuroscience*, 33(26):10802–10814, 2013.

[215] M. A. Raven, S. J. Eglen, J. J. Ohab, and B. E. Reese. Determinants of the exclusion zone in dopaminergic amacrine cell mosaics. *Journal of Comparative Neurology*, 461(1):123–136, 2003.

[216] M. A. Raven, N. C. Orton, H. Nassar, G. A. Williams, W. K. Stell, G. H. Jacobs, N. T. Bech-Hansen, and B. E. Reese. Early afferent signaling in the outer plexiform layer regulates development of horizontal cell morphology. *Journal of Comparative Neurology*, 506(5):745–758, 2008.

[217] M. A. Raven, S. B. Stagg, H. Nassar, and B. E. Reese. Developmental improvement in the regularity and packing of mouse horizontal cells: implications for mechanisms underlying mosaic pattern formation. *Visual neuroscience*, 22(5):569–573, 2005.

[218] B. E. Reese. Development of the retina and optic pathway. *Vision research*, 51(7):613–632, 2011.

[219] C. B. Reid, S. F. Tavazoie, and C. A. Walsh. Clonal dispersion and evidence for asymmetric cell division in ferret cortex. *Development*, 124(12):2441–2450, 1997.

[220] I. Reillo, C. de Juan Romero, M. Á. García-Cabezas, and V. Borrell. A role for intermediate radial glia in the tangential expansion of the mammalian cerebral cortex. *Cerebral Cortex*, 21(7):1674–1694, 2010.

[221] O. Reiner, R. Carrozzo, Y. Shen, M. Wehnert, F. Faustinella, W. B. Dobyns, C. T. Caskey, and D. H. Ledbetter. Isolation of a miller–dicker lissencephaly gene containing g protein β-subunit-like repeats. *Nature*, 364(6439):717, 1993.

[222] D. P. Richman, R. M. Stewart, J. W. Hutchinson, and V. S. Caviness. Mechanical model of brain convolutional development. *Science*, 189(4196):18–21, 1975.

[223] M. Rivlin-Etzion, K. Zhou, W. Wei, J. Elstrott, P. L. Nguyen, B. A. Barres, A. D. Huberman, and M. B. Feller. Transgenic mice reveal unexpected diversity of on-off direction-selective retinal ganglion cell subtypes and brain structures involved in motion processing. *Journal of Neuroscience*, 31(24):8760–8769, 2011.

[224] M. Robinson, M. P. Perez, L. Tebar, J. Palmer, A. Patel, D. Marks, A. Sheasby, C. De Felipe, R. Coffin, F. Livesey, et al. Flrt3 is expressed in sensory neurons after peripheral nerve injury and regulates neurite outgrowth. *Molecular and Cellular Neuroscience*, 27(2):202–214, 2004.

[225] R. W. Rodieck and R. W. Rodieck. *The first steps in seeing*, volume 1. Sinauer Associates Sunderland, MA, 1998.

[226] D. L. Rousso, M. Qiao, R. D. Kagan, M. Yamagata, R. D. Palmiter, and J. R. Sanes. Two pairs of on and off retinal ganglion cells are defined by intersectional patterns of transcription factor expression. *Cell reports*, 15(9):1930–1944, 2016.

[227] M. H. Rowe and J. Stone. The interpretation of variation in the classification of nerve cells. *Brain, behavior and evolution*, 17(2):123–151, 1980.

[228] B. T. Sagdullaev and M. A. Mccall. Stimulus size and intensity alter fundamental receptive-field properties of mouse retinal ganglion cells in vivo. *Visual neuroscience*, 22(5):649–659, 2005.

[229] S. Sakata and K. D. Harris. Laminar structure of spontaneous and sensory-evoked population activity in auditory cortex. *Neuron*, 64(3):404–418, 2009.

[230] P. C. Sallet, H. Elkis, T. M. Alves, J. R. Oliveira, E. Sassi, C. C. de Castro, G. F. Busatto, and W. F. Gattaz. Reduced cortical folding in schizophrenia: an mri morphometric study. *American Journal of Psychiatry*, 160(9):1606–1613, 2003.

[231] J. R. Sanes and R. H. Masland. The types of retinal ganglion cells: current status and implications for neuronal classification. *Annual review of neuroscience*, 38:221–246, 2015.

[232] T. M. Schmidt, N. M. Alam, S. Chen, P. Kofuji, W. Li, G. T. Prusky, and S. Hattar. A role for melanopsin in alpha retinal ganglion cells and contrast detection. *Neuron*, 82(4):781–788, 2014.

[233] J. Schnitzer and A. Rusoff. Horizontal cells of the mouse retina contain glutamic acid decarboxylase-like immunoreactivity during early developmental stages. *Journal of Neuroscience*, 4(12):2948–2955, 1984.

[234] M. L. Schwartz, P. Rakic, and P. S. Goldman-Rakic. Early phenotype expression of cortical neurons: evidence that a subclass of migrating neurons have callosal axons. *Proceedings of the National Academy of Sciences*, 88(4):1354–1358, 1991.

[235] T. A. Seabrook, T. J. Burbridge, M. C. Crair, and A. D. Huberman. Architecture, function, and assembly of the mouse visual system. *Annual review of neuroscience*, 40:499–538, 2017.

[236] E. Seiradake, D. del Toro, D. Nagel, F. Cop, R. Härtl, T. Ruff, G. Seyit-Bremer, K. Harlos, E. C. Border, A. Acker-Palmer, et al. Flrt structure: balancing repulsion and cell adhesion in cortical and vascular development. *Neuron*, 84(2):370–385, 2014.

[237] Y. Shinmyo, Y. Terashita, T. A. D. Duong, T. Horiike, M. Kawasumi, K. Hosomichi, A. Tajima, and H. Kawasaki. Folding of the cerebral cortex requires cdk5 in upper-layer neurons in gyrencephalic mammals. *Cell reports*, 20(9):2131–2143, 2017.

[238] A. Shitamukai, D. Konno, and F. Matsuzaki. Oblique radial glial divisions in the developing mouse neocortex induce self-renewing progenitors outside the germinal zone that resemble primate outer subventricular zone progenitors. *Journal of Neuroscience*, 31(10):3683–3695, 2011.

[239] G. M. Shoukimas and J. W. Hinds. The development of the cerebral cortex in the embryonic mouse: an electron microscopic serial section analysis. *Journal of Comparative Neurology*, 179(4):795–830, 1978.

[240] J. A. Siegenthaler, A. M. Ashique, K. Zarbalis, K. P. Patterson, J. H. Hecht, M. A. Kane, A. E. Folias, Y. Choe, S. R. May, T. Kume, et al. Retinoic acid from the meninges regulates cortical neuron generation. *Cell*, 139(3):597–609, 2009.

[241] S. Siegert, B. G. Scherf, K. Del Punta, N. Didkovsky, N. Heintz, and B. Roska. Genetic address book for retinal cell types. *Nature neuroscience*, 12(9):1197, 2009.

[242] J. I. Simpson. The accessory optic system. *Annual review of neuroscience*, 7(1):13–41, 1984.

[243] D. Snow, M. Watanabe, P. Letourneau, and J. Silver. A chondroitin sulfate proteoglycan may influence the direction of retinal ganglion cell outgrowth. *Development*, 113(4):1473–1485, 1991.

[244] S. Spring, J. P. Lerch, M. K. Wetzel, A. C. Evans, and R. M. Henkelman. Cerebral asymmetries in 12-week-old c57bl/6j mice measured by magnetic resonance imaging. *Neuroimage*, 50(2):409–415, 2010.

[245] D. St Johnston and C. Nüsslein-Volhard. The origin of pattern and polarity in the drosophila embryo. *Cell*, 68(2):201–219, 1992.

[246] M. E. Stabio, S. Sabbah, L. E. Quattrochi, M. C. Ilardi, P. M. Fogerson, M. L. Leyrer, M. T. Kim, I. Kim, M. Schiel, J. M. Renna, et al. The m5 cell: A color-opponent intrinsically photosensitive retinal ganglion cell. *Neuron*, 97(1):150–163, 2018.

[247] R. Stahl, T. Walcher, C. D. J. Romero, G. A. Pilz, S. Cappello, M. Irmler, J. M. Sanz-Aquela, J. Beckers, R. Blum, V. Borrell, et al. Trnp1 regulates expansion and folding of the mammalian cerebral cortex by control of radial glial fate. *Cell*, 153(3):535–549, 2013.

[248] L. A. Stephen, G. M. Davis, K. E. Mcteir, J. James, L. Mcteir, M. Kierans, A. Bain, and M. G. Davey. Failure of centrosome migration causes a loss of motile cilia in talpid3 mutants. *Developmental Dynamics*, 242(8):923–931, 2013.

[249] C. Stone and L. H. Pinto. Response properties of ganglion cells in the isolated mouse retina. *Visual neuroscience*, 10(1):31–39, 1993.

[250] G. F. Striedter, S. Srinivasan, and E. S. Monuki. Cortical folding: when, where, how, and why? *Annual review of neuroscience*, 38:291–307, 2015.

[251] C. A. Stuermer and M. Bastmeyer. The retinal axon's pathfinding to the optic disk. *Progress in neurobiology*, 62(2):197–214, 2000.

[252] U. Sümbül, S. Song, K. McCulloch, M. Becker, B. Lin, J. R. Sanes, R. H. Masland, and H. S. Seung. A genetic and computational approach to structurally classify neuronal types. *Nature communications*, 5:3512, 2014.

[253] L. O. Sun, C. M. Brady, H. Cahill, T. Al-Khindi, H. Sakuta, O. S. Dhande, M. Noda, A. D. Huberman, J. Nathans, and A. L. Kolodkin. Functional assembly of accessory optic system circuitry critical for compensatory eye movements. *Neuron*, 86(4):971–984, 2015.

[254] T. Sun, R. V. Collura, M. Ruvolo, and C. A. Walsh. Genomic and evolutionary analyses of asymmetrically expressed genes in human fetal left and right cerebral cortex. *Cerebral cortex*, 16(suppl_1):i18–i25, 2006.

[255] W. Sun, Q. Deng, W. R. Levick, and S. He. On direction-selective ganglion cells in the mouse retina. *The Journal of physiology*, 576(1):197–202, 2006.

[256] V. Suresh, U. M. Çiftçioğlu, X. Wang, B. M. Lala, K. R. Ding, W. A. Smith, F. T. Sommer, and J. A. Hirsch. Synaptic contributions to receptive field structure and response properties in the rodent lateral geniculate nucleus of the thalamus. *Journal of Neuroscience*, 36(43):10949–10963, 2016.

[257] A. Szel, P. Röhlich, A. Gaffe, B. Juliusson, G. v. Aguirre, and T. Van Veen. Unique topographic separation of two spectral classes of cones in the mouse retina. *Journal of Comparative Neurology*, 325(3):327–342, 1992.

[258] T. Tallinen, J. Y. Chung, F. Rousseau, N. Girard, J. Lefèvre, and L. Mahadevan. On the growth and form of cortical convolutions. *Nature Physics*, 12(6):588, 2016.

[259] S.-S. Tan and S. Breen. Radial mosaicism and tangential cell dispersion both contribute to mouse neocortical development. *Nature*, 362(6421):638, 1993.

[260] D. H. Tanaka, M. Yanagida, Y. Zhu, S. Mikami, T. Nagasawa, J.-i. Miyazaki, Y. Yanagawa, K. Obata, and F. Murakami. Random walk behavior of migrating cortical interneurons in the marginal zone: time-lapse analysis in flat-mount cortex. *Journal of Neuroscience*, 29(5):1300–1311, 2009.

[261] B. Tasic, V. Menon, T. N. Nguyen, T. K. Kim, T. Jarsky, Z. Yao, B. Levi, L. T. Gray, S. A. Sorensen, T. Dolbeare, et al. Adult mouse cortical cell taxonomy revealed by single cell transcriptomics. *Nature neuroscience*, 19(2):335–346, 2016.

[262] E. R. Thomsen, J. K. Mich, Z. Yao, R. D. Hodge, A. M. Doyle, S. Jang, S. I. Shehata, A. M. Nelson, N. V. Shapovalova, B. P. Levi, et al. Fixed single-cell transcriptomic characterization of human radial glial diversity. *Nature methods*, 13(1):87, 2016.

[263] N.-W. Tien, J. T. Pearson, C. R. Heller, J. Demas, and D. Kerschensteiner. Genetically identified suppressed-by-contrast retinal ganglion cells reliably signal self-generated visual stimuli. *Journal of Neuroscience*, 35(30):10815–10820, 2015.

[264] F. Tissir and A. M. Goffinet. Reelin and brain development. *Nature Reviews Neuroscience*, 4(6):496–505, 2003.

[265] T. Toda, S. Ikegawa, K. Okui, E. Kondo, K. Saito, Y. Fukuyama, M. Yoshioka, T. Kumagai, K. Suzumori, I. Kanazawa, et al. Refined mapping of a gene responsible for fukuyama-type congenital muscular dystrophy: evidence for strong linkage disequilibrium. *American journal of human genetics*, 55(5):946, 1994.

[266] M. Torii, K. Hashimoto-Torii, P. Levitt, and P. Rakic. Integration of neuronal clones in the radial cortical columns by epha and ephrin-a signalling. *Nature*, 461(7263):524, 2009.

[267] S. Trenholm, K. Johnson, X. Li, R. G. Smith, and G. B. Awatramani. Parallel mechanisms encode direction in the retina. *Neuron*, 71(4):683–694, 2011.

[268] J. W. Triplett and D. A. Feldheim. Eph and ephrin signaling in the formation of topographic maps. In *Seminars in cell & developmental biology*, volume 23, pages 7–15. Elsevier, 2012.

[269] L. Tsuji, T. Yamashita, T. Kubo, T. Madura, H. Tanaka, K. Hosokawa, and M. Tohyama. Flrt3, a cell surface molecule containing lrr repeats and a fniii domain, promotes neurite outgrowth. *Biochemical and biophysical research communications*, 313(4):1086–1091, 2004.

[270] M. Valiente and O. Marín. Neuronal migration mechanisms in development and disease. *Current opinion in neurobiology*, 20(1):68–78, 2010.

[271] D. C. Van Essen. A tension-based theory of morphogenesis and compact wiring in the central nervous system. *Nature*, 385(6614):313, 1997.

[272] L. N. Vandenberg and M. Levin. Far from solved: a perspective on what we know about early mechanisms of left–right asymmetry. *Developmental Dynamics*, 239(12):3131–3146, 2010.

[273] D. I. Vaney. Territorial organization of direction-selective ganglion cells in rabbit retina. *Journal of Neuroscience*, 14(11):6301–6316, 1994.

[274] D. I. Vaney, B. Sivyer, and W. R. Taylor. Direction selectivity in the retina: symmetry and asymmetry in structure and function. *Nature Reviews Neuroscience*, 13(3):194, 2012.

[275] J. J. Visser, Y. Cheng, S. C. Perry, A. B. Chastain, B. Parsa, S. S. Masri, T. A. Ray, J. N. Kay, and W. M. Wojtowicz. An extracellular biochemical screen reveals that flrts and unc5s mediate neuronal subtype recognition in the retina. *Elife*, page e08149, 2015.

[276] C. H. Waddington et al. The strategy of the genes. a discussion of some aspects of theoretical biology. with an appendix by h. kacser. *The strategy of the genes. A discussion of some aspects of theoretical biology. With an appendix by H. Kacser.*, 1957.

[277] C. Walsh and C. Cepko. Clonally related cortical cells show several migration patterns. *Science*, 241(4871):1342–1345, 1988.

[278] C. Walsh and C. L. Cepko. Clonal dispersion in proliferative layers of developing cerebral cortex. *Nature*, 362(6421):632, 1993.

[279] L. Wang, S. Hou, and Y.-G. Han. Hedgehog signaling promotes basal progenitor expansion and the growth and folding of the neocortex. *Nature neuroscience*, 19(7):888, 2016.

[280] X. Wang, C. Studholme, P. L. Grigsby, A. E. Frias, V. C. C. Carlson, and C. D. Kroenke. Folding, but not surface area expansion, is associated with cellular morphological maturation in the fetal cerebral cortex. *Journal of Neuroscience*, 37(8):1971–1983, 2017.

[281] X. Wang, J.-W. Tsai, B. LaMonica, and A. R. Kriegstein. A new subtype of progenitor cell in the mouse embryonic neocortex. *Nature neuroscience*, 14(5):555, 2011.

[282] M. L. Ware, S. F. Tavazoie, C. B. Reid, and C. A. Walsh. Coexistence of widespread clones and large radial clones in early embryonic ferret cortex. *Cerebral Cortex*, 9(6):636–645, 1999.

[283] H. Wässle, L. Peichl, and B. Boycott. Dendritic territories of cat retinal ganglion cells. *Nature*, 292(5821):344–345, 1981.

[284] W. Wei, A. M. Hamby, K. Zhou, and M. B. Feller. Development of asymmetric inhibition underlying direction selectivity in the retina. *Nature*, 469(7330):402, 2011.

[285] J. Weickenmeier, R. de Rooij, S. Budday, P. Steinmann, T. Ovaert, and E. Kuhl. Brain stiffness increases with myelin content. *Acta biomaterialia*, 42:265–272, 2016.

[286] W. Welker. Why does cerebral cortex fissure and fold? In *Cerebral cortex*, pages 3–136. Springer, 1990.

[287] L. M. Wheldon, B. P. Haines, R. Rajappa, I. Mason, P. W. Rigby, and J. K. Heath. Critical role of flrt1 phosphorylation in the interdependent regulation of flrt1 function and fgf receptor signalling. *PLoS One*, 5(4):e10264, 2010.

[288] K. L. Whitford, P. Dijkhuizen, F. Polleux, and A. Ghosh. Molecular control of cortical dendrite development. *Annual review of neuroscience*, 25(1):127–149, 2002.

[289] L. L. Wong and D. H. Rapaport. Defining retinal progenitor cell competence in xenopus laevis by clonal analysis. *Development*, 136(10):1707–1715, 2009.

[290] G. Xu, A. K. Knutsen, K. Dikranian, C. D. Kroenke, P. V. Bayly, and L. A. Taber. Axons pull on the brain, but tension does not drive cortical folding. *Journal of biomechanical engineering*, 132(7):071013, 2010.

[291] H.-p. Xu, M. Furman, Y. S. Mineur, H. Chen, S. L. King, D. Zenisek, Z. J. Zhou, D. A. Butts, N. Tian, M. R. Picciotto, et al. An instructive role for patterned spontaneous retinal activity in mouse visual map development. *Neuron*, 70(6):1115–1127, 2011.

[292] Q. Xu, I. Cobos, E. De La Cruz, J. L. Rubenstein, and S. A. Anderson. Origins of cortical interneuron subtypes. *Journal of Neuroscience*, 24(11):2612–2622, 2004.

[293] M. Yamagata and J. R. Sanes. Dscam and sidekick proteins direct lamina-specific synaptic connections in vertebrate retina. *Nature*, 451(7177):465–469, 2008.

[294] M. Yamagata and J. R. Sanes. Expanding the ig superfamily code for laminar specificity in retina: expression and role of contactins. *Journal of Neuroscience*, 32(41):14402–14414, 2012.

[295] M. Yamagata, J. A. Weiner, and J. R. Sanes. Sidekicks: synaptic adhesion molecules that promote lamina-specific connectivity in the retina. *Cell*, 110(5):649–660, 2002.

[296] S. Yamagishi, F. Hampel, K. Hata, D. Del Toro, M. Schwark, E. Kvachnina, M. Bastmeyer, T. Yamashita, V. Tarabykin, R. Klein, et al. Flrt2 and flrt3 act as repulsive guidance cues for unc5-positive neurons. *The EMBO journal*, 30(14):2920–2933, 2011.

[297] N. Yamawaki, K. Borges, B. A. Suter, K. D. Harris, and G. M. Shepherd. A genuine layer 4 in motor cortex with prototypical synaptic circuit connectivity. *Elife*, 3, 2014.

[298] L. Yin, R. G. Smith, P. Sterling, and D. H. Brainard. Physiology and morphology of color-opponent ganglion cells in a retina expressing a dual gradient of s and m opsins. *Journal of Neuroscience*, 29(9):2706–2724, 2009.

[299] Y. Yin, F. Bangs, I. R. Paton, A. Prescott, J. James, M. G. Davey, P. Whitley, G. Genikhovich, U. Technau, D. W. Burt, et al. The talpid3 gene (kiaa0586) encodes a centrosomal protein that is essential for primary cilia formation. *Development*, 136(4):655–664, 2009.

[300] K. Yonehara, M. Fiscella, A. Drinnenberg, F. Esposti, S. Trenholm, J. Krol, F. Franke, B. G. Scherf, A. Kusnyerik, J. Müller, et al. Congenital nystagmus gene frmd7 is necessary for establishing a neuronal circuit asymmetry for direction selectivity. *Neuron*, 89(1):177–193, 2016.

[301] K. Yonehara, H. Ishikane, H. Sakuta, T. Shintani, K. Nakamura-Yonehara, N. L. Kamiji, S. Usui, and M. Noda. Identification of retinal ganglion cells and their projections involved in central transmission of information about upward and downward image motion. *PloS one*, 4(1):e4320, 2009.

[302] K. Yonehara, T. Shintani, R. Suzuki, H. Sakuta, Y. Takeuchi, K. Nakamura-Yonehara, and M. Noda. Expression of spig1 reveals development of a retinal ganglion cell subtype projecting to the medial terminal nucleus in the mouse. *PloS one*, 3(2):e1533, 2008.

[303] A. Yoshida, K. Kobayashi, H. Manya, K. Taniguchi, H. Kano, M. Mizuno, T. Inazu, H. Mitsuhashi, S. Takahashi, M. Takeuchi, et al. Muscular dystrophy and neuronal migration disorder caused by mutations in a glycosyltransferase, pomgnt1. *Developmental cell*, 1(5):717–724, 2001.

[304] T. R. Young, M. Bourke, X. Zhou, T. Oohashi, A. Sawatari, R. Fässler, and C. A. Leamey. Ten-m2 is required for the generation of binocular visual circuits. *Journal of Neuroscience*, 33(30):12490–12509, 2013.

[305] Y.-C. Yu, R. S. Bultje, X. Wang, and S.-H. Shi. Specific synapses develop preferentially among sister excitatory neurons in the neocortex. *Nature*, 458(7237):501, 2009.

[306] S. Yuan, L. Zhao, M. Brueckner, and Z. Sun. Intraciliary calcium oscillations initiate vertebrate left-right asymmetry. *Current biology*, 25(5):556–567, 2015.

[307] H. Zeng and J. R. Sanes. Neuronal cell-type classification: challenges, opportunities and the path forward. *Nature Reviews Neuroscience*, 18(9):530–546, 2017.

[308] Y. Zhang, I.-J. Kim, J. R. Sanes, and M. Meister. The most numerous ganglion cell type of the mouse retina is a selective feature detector. *Proceedings of the National Academy of Sciences*, 109(36):E2391–E2398, 2012.

[309] J. Q. Zheng, J. Wan, and M. Poo. Essential role of filopodia in chemotropic turning of nerve growth cone induced by a glutamate gradient. *Journal of Neuroscience*, 16(3):1140–1149, 1996.

[310] K. Zilles, E. Armstrong, A. Schleicher, and H.-J. Kretschmann. The human pattern of gyrification in the cerebral cortex. *Anatomy and embryology*, 179(2):173–179, 1988.

Supplemental figures

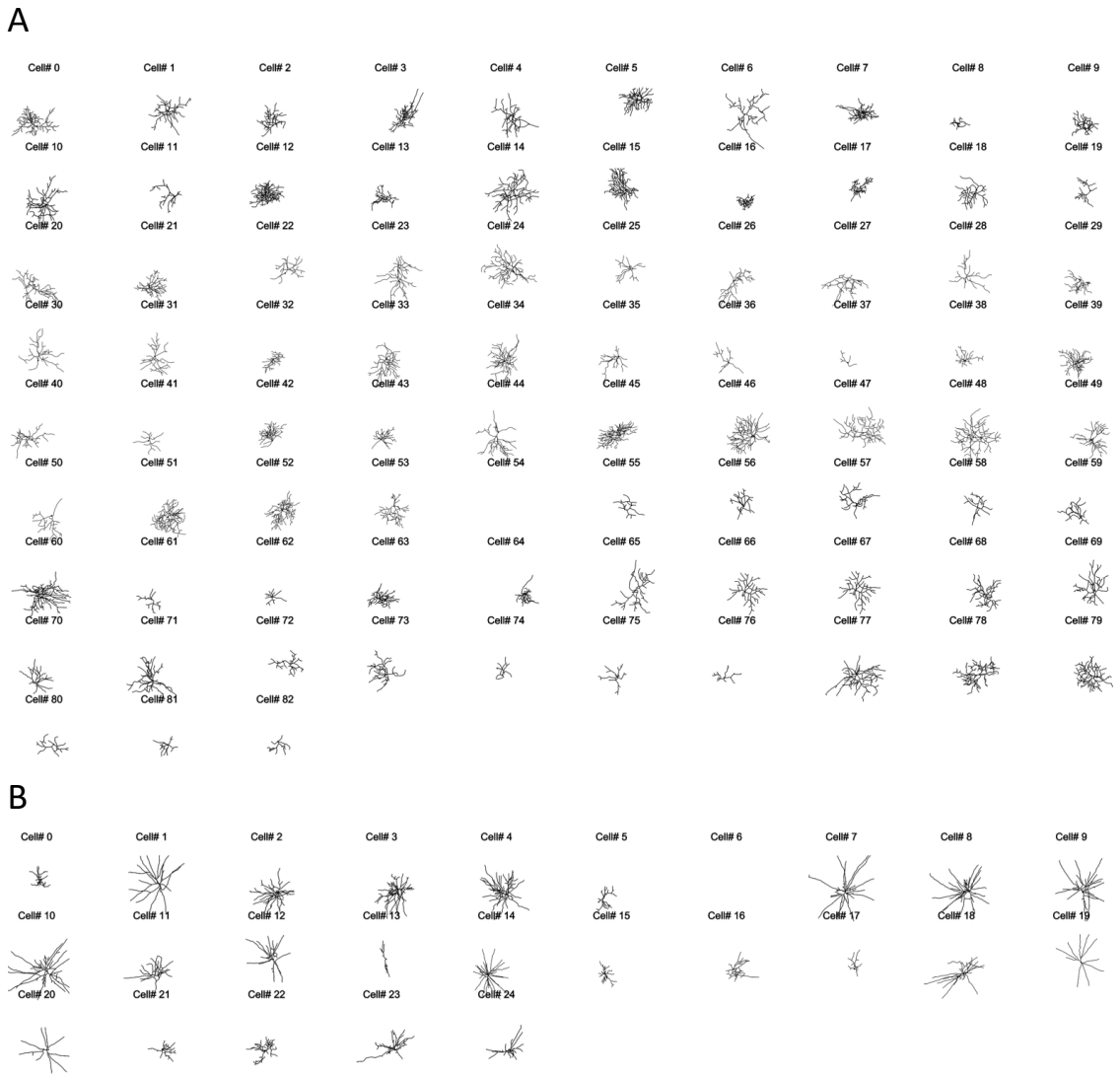

Figure 7.1: Morphology reconstructions of dye injected cells in the ganglion cell layer. A: Morphology reconstruction of all injected retinal ganglion cells. B: Morphology reconstruction of all injected amacrine cells.

Author contribution

In the publication "Regulation of cerebral cortex folding by controlling neuronal migration via FLRT adhesion molecules" I provided the data for Figure 4, Supplemental Figure 2 C, F and G and Supplemental Figure S5. These figures show data that I generated by characterizing the Flrt1 KO, performing in utero electroporations and subsequent time-lapse recordings of organotypic slice cultures and by morphology analysis. Daniel del Toro Ruiz characterized the Flrt1/3 DKO line, performed the neuronal cultures and explants and created the computational model. Erik Cederfjll analysed the Flrt2/3 DKO line and perfomred the bioinformatics analysis of RNA-seq datasets. Goenuel Seyit-Bremer characterized the FLRT1-3 expression and performed the IF assays. Ana Villalba performed in situ hybridization experiments on the ferret sections. The work was supervised by Rdiger Klein and Victor Borrell. The author contributions can also be found in the publication itself.

In the publication " FLRT Structure: Balancing repulsion and adhesion in cortical and vascular development" I provided data for Figure 6 K, N and O. Elena Seiradake generated data for Figure 1,2,3 A, B and F. Daniel del Toro Ruiz generated data for Figure 3 B,D,E, Figure 4 and 5, Figure 6 E, F, G, H, I, J, P, Q, R, S, Figure 7 A, B , C, D, E and F. Daniel Nagel generated data for Figure 6 B and L. Goenuel Seyit-Bremer generated data for Figure 6 A and D. Florian Cop and Ricarda Haertl generated data for Figure 7 G, H, I and J.

In the project "Flrt3 as a potential RGC marker" the following people contributed to the work: Louise Gaitanos and Jana Lindner performed the ES cell cultures, plasmid electroporation and final clone selection. Pilar Alcala Morales designed and cloned the targeting vector and probes for identifying the correct FLRT3-Cre insertion. The transgenic core facility performed pronuclear injections of the FLRT3-Cre Embryonic stem cells. Daniel del Toro Ruiz performed the LacZ staining on P2 and P7 Flrt2/3 LacZ retinas and developed a Fiji macro to extract the sholl profile from the morphological reconstructions. Southern blots to determine correct target vector insertion for clone selection and all remaining data shown in the thesis was performed by me.

Acknowledgements

The successful completion of this thesis would not have been possible without the help of some great scientists, friends and my family. Each of those people helped me through the sometimes stressful but often exciting times of this PhD. I thank all of you. I especially thank,

Ruediger Klein for accepting me in his lab and keeping me focused when my thirst for experimental action diverged too much. I appreciated his patience and support in scientific freedom without unnecessary pressure. This allowed me to explore different branches in neuroscience, learn new methods and develop new time consuming data analysis skills.

Daniel del Toro for being the greatest and most inspiring supervisor I could have ever imagined. I especially thank him for his endless trust in me, for sharing his expertise and enthusiasm in science and his 24/7 support. I thank him for making even the longest working days an enjoyable, fun time and keeping me motivated and positive throughout the most difficult times in my PhD.

Katharina Schulz-Trieglaff for being a person that honestly cares about you. I thank her for many exciting discussions about life in science, justice and future plans, her strategic help in the fellowship application process and for her motivation to think unconventionally.

Hakan Kucuckdereli and Amelia Douglass for being open minded labmates one can discuss about literally anything. Science, technology or the sense of life are just few of the topics we covered during the years we shared an office. I thank Hakan for teaching me Python and introducing me into the art of single cell injections and Amelia for proofreading my thesis.

Erik Cederfjall for being a great motivator in science and sports. Augusto Escalante for being an excellent and reliable source of help in all kind of scientific questions. Irina Doudanova for proofreading my BIF application and being a great source of postdoctoral advice. Elena Seiradake and Victor Borrell for our successful collaborations. Christian Peters for being a very supportive labmate and great bike competitor. Irene Riera Tur, Kerstin Voelkl, Marion Ponserre, Jingyi Gong, Federica Fermani and Sara Brignani for many nice discussions during lunch and coffee breaks. Sara Gutierrez for her excellent and efficient help in Latex. Tom Gaitanos for questioning all my data. Sonia Paixao for her help with the Southern Blots. Ritu Roy Chowdhury for deep scientific discussions. Pilar Alcala Morales, Jana Lindner and Louise Gaitanos for their help in making the Flrt3-Cre mouse. Goenuel Seyit for her excellent technical support. Archana Mishra for nice discussions about life as a scientist and useful advice for my future. Siju Kunhi

Purayil for his accurate market analyses. Alexandra Klein, Daniel Gerlach and Nejc Dolensek for their immediate and excellent help in all lab related issues. The IMPRS coordination office for offering me intellectual, financial and strategic support through workshops, seminars and the obligatory TAC meetings. Andreas Koeckeis for his reliable help with all mouse related work. My TAC members Mark Huebener and Sven Falk for their strategic and scientific help during my TAC meetings. I especially thank Sven Falk for showing me how to prepare and image organotypic slice cultures and sharing his strategic advice.

For financial and intellectual support I thank the Boeringer Ingelheim Fonds represented by Claudia Walther and her team.

Moreover I thank all people that believe in the importance of scientific progress. Through taxes and personal donations they enable the creation of an academic bubble in which people can follow their personal interest in natural sciences without the constraint of profitability or immediate applicability.

I specially thank my sister Tanja Neumayer for her sophisticated Cell paper cake.

Finally, I thank my parents Annemarie und Erich Ruff for their unquestioned support and trust in what I do and believe in. Without their joint efforts to financially support my bachelor and master's degree, this thesis would have never been possible.

Last but not least I thank my girlfriend Victoria Schuhbeck for sharing her adventures and love with me.